Westfälische
Wilhelms-Universität
Münster

Verifiable dark matter with radiative neutrino masses

Master's Thesis

Thede de Boer

Westfälische Wilhelms-Universität Münster
Institute of Theoretical Physics

Supervisor: Prof. Dr. Michael Klasen
Second supervisor: Prof. Dr. Christian Weinheimer

Münster, September 7, 2021

Publications

The work on this thesis has contributed to the following publications:

- T. de Boer et al. "Absolute neutrino mass as the missing link to the dark sector". In: *Phys. Rev. D* 102.5 (2020), p. 051702. DOI: 10.1103/PhysRevD.102.051702. arXiv: 2007.05338 [hep-ph]

- T. de Boer et al. "New constraints on radiative seesaw models from IceCube and other neutrino detectors". In: *Phys. Rev. D* 103.12 (2021), p. 123006. DOI: 10.1103/PhysRevD.103.123006. arXiv: 2103.06881 [hep-ph]

- T. de Boer et al. "Indirect detection constraints on the scotogenic dark matter model". In: *Journal of Cosmology and Astroparticle Physics* 2021.08 (Aug. 2021), p. 038. DOI: 10.1088/1475-7516/2021/08/038. arXiv: 2105.04899 [hep-ph]. URL: https://doi.org/10.1088/1475-7516/2021/08/038

Furthermore the following publication is planned but not yet submitted:

- T. de Boer et al. "Anomaly-free dark matter models with one-loop neutrino masses and a gauged U(1) symmetry".

Contents

1 Introduction

The Standard Model of particle physics describes all known particles and interactions. It has been extremely successful in explaining observed phenomena as well as predicting particles which were then found experimentally. With the discovery of the Higgs boson in 2012 the final piece was found [4, 5]. Despite this success, the Standard Model cannot be a complete description of nature. As it fails to incorporate a description of gravity, the Standard Model must break down at some high energy scale. There are also some phenomena that are not related to quantum gravity, which are not explained by the Standard Model. This thesis is devoted to two of the main open question of particle physics: the nature of dark matter and the question of why the neutrino masses are so tiny.

Astrophysical observations tell us that there must be a large amount of matter in the Universe that does not interact electromagnetically but its presence can be deduced from the gravitational effects. This so called dark matter (DM) makes up the majority of mass in our universe however it is not known what kind of particle makes up dark matter. The Standard Model does not incorporate a fitting candidate. A widely studied concept for the dark matter particle is the so called WIMP (weakly interacting massive particle). Many experiments search for such WIMPs for example collider experiments such as the LHC and direct detection detectors. However no conclusive evidence for WIMPs and their properties has been found.

The Standard Model describes neutrinos as massless Weyl spinors. With the discovery of neutrino oscillations [6, 7] it has been shown that these particles do in fact have masses. The mass differences are known from oscillation experiments but their absolute mass scale is still unknown. The KATRIN experiment is dedicated to probe the mass of the electron neutrino and has set a stringent upper limit of 1.1 eV on the electron neutrino mass [8]. All other fermion masses are generated by the Higgs mechanism and thus have a natural mass scale of $\mathcal{O}(100\text{ GeV})$. The neutrino masses are eleven orders of magnitude below this scale. This raises the question why neutrinos are so light.

For many years the focus of beyond standard model (BSM) physics has been on well motivated but complicated theories with often many free parameters such as the minimal supersymmetric standard model (MSSM) or grand unified theories (GUTs). As there is no experimental evidence found for these theories, the focus has somewhat shifted to a simpler approach. Minimal models do not claim to explain nature at high energy scales such as the GUT scale but try to explain as many open questions of the Standard Model as possible while only introducing few new fields and parameters.

In this thesis we study minimal models that combine both dark matter and neutrino masses. This is done by generating neutrino masses through one loop diagrams where the dark matter particle is running in the loop. The simplest and most famous of these models is Ma's scotogenic model [9] which only requires two new fields, a scalar doublet and three generations of right handed neutrinos. A systematic study of possible minimal models with dark matter and radiative neutrino masses has been carried out in Refs. [10, 11].

This thesis is organized as follows: In Chap. 2 we present the evidences for dark matter and give an overview of the searches for WIMPs. Neutrino masses and oscillations as well as experiments testing those are discussed in Chap. 3. Chapter 4 introduces further experiments that set constraints on our models but do not rely on producing the new particles. The theoretical foundations as well as some conventions are introduced in Chap. 5. In Chap. 6 we introduce the minimal models and their classification. Two specific models i.e. the scotogenic model (T3-B with $\alpha = -1$) and T1-3-B ($\alpha = 0$) are discussed in detail as they are studied further in this work. Chapter 7 covers the findings published in our paper Ref. [1] where we investigated the impact of the absolute neutrino mass on the parameter space of the scotogenic model with fermionic dark matter. A detailed treatment of the WIMP nucleus scattering formalism is given in Chap. 8. Indirect detection constraints are discussed in Chaps. 8 and 9 with Chap. 8 interpolating our paper Ref. [3] and treating scalar dark matter in the scotogenic model while Chap. 9 covers the model T1-3-B ($\alpha = 0$) and is based on our publication Ref. [2]. In Chap. 10 we promote the stabilizing symmetry to a local U(1) and discuss how this affects the phenomenology. We also put these new models in the context of Grand Unified Theories (GUTs). Finally we draw our conclusions in Chap. 11.

Dark matter

2

One of the most intriguing open questions in physics is the nature of dark matter. Over the last 100 years more and more evidence accumulated suggesting that there is a form of mass present in our universe which is not detectable by its interactions with light. Roughly 85% of the mass in the universe is made of a non luminous form of matter, called dark matter. The Standard Model of particle physics, which has been extremely successful in describing high energy physics to high precision, does not encompass a suitable dark matter candidate. This chapter is devoted to a review of the cosmological evidence for dark matter and the experimental status constraining WIMP dark matter.

2.1 Evidence

The history of dark matter goes back to the early 1930's. Fritz Zwicky studied the orbital velocities of galaxies in the Coma cluster. He found that these velocities differ by roughly a factor of ten from the expected velocity calculated by the observed mass in the cluster. To explain this discrepancy Zwicky suggested that there must be large amounts of dark (invisible) matter [12].

The motion of stars and galaxies is decribed by the viral theorem assuming that they are gravitationally bound and in equilibrium. This gives the following estimate of the velocity v

$$v \propto \sqrt{\frac{M}{r}} \tag{2.1.1}$$

where M is the mass of the system and r is the radial distance [14]. Figure 2.1 shows the rotational curve for a galaxy. We can see that the expected curve shows a $\frac{1}{\sqrt{r}}$ behavior for large r as expected from the viral theorem. The observed velocities for such distances are however larger than expected from this theorem. These observation cannot be explained with the amount

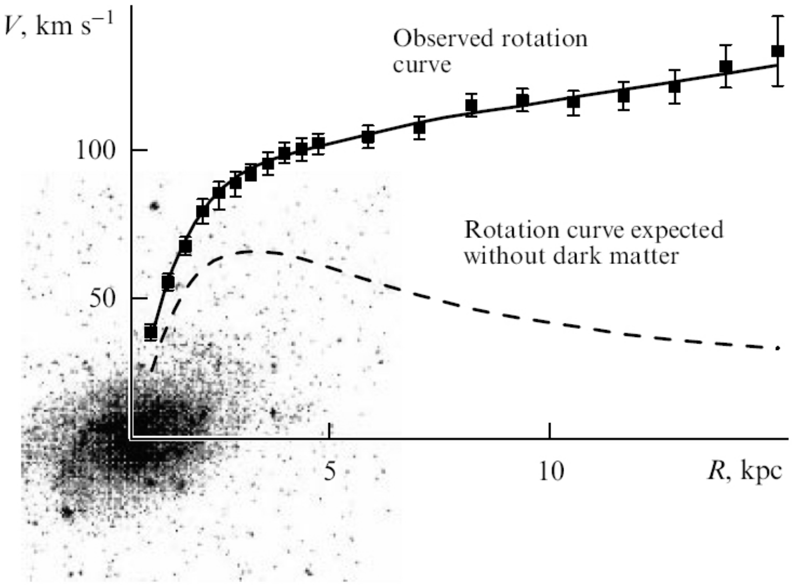

Figure 2.1: Observed rotational curve and expected curve from visible matter for the M33 galaxy. Figure taken from Ref. [13].

and distribution of visible matter. There must be a significant amount dark matter present.

Since the original proposal by Zwicky, more and more evidence that supports the idea of dark matter has been discovered. As known from general relativity, massive objects deflect light. This is known as gravitational lensing. This effect can be used to find mass distributions in galaxies. A figure of the bullet cluster, consisting of two colliding galaxies, is shown in Fig. 2.2. The distribution of hot gas which makes up most of the luminous matter, observed using X-Ray telescopes is highlighted in red. The blue regions indicate the distribution of mass, measured by gravitational lensing. In the collision process the luminous matter (hot gas) interacts electromagnetically and is slowed down. Dark matter on the other hand does not interact electromagnetically and is thus not slowed down. This leads to the separation visible in Fig. 2.2 [15].

Another very compelling piece of evidence can be obtained by measuring the cosmic microwave background (CMB), a nearly uniform background radiation with a temperature of around 2.725 K which originated in the early universe when photons decoupled from thermal equilibrium with matter. The

Figure 2.2: Lensing map of the Bullet Cluster. Red: Distribution of luminous matter from X-Ray emission. Blue: Distribution of mass from gravitational lensing. Figure taken from `https://chandra.harvard.edu/photo/2006/1e0657/`.

CMB shows fluctuations at the scale of 30 μK which are an imprint of primordial density fluctuations. Dark matter can accumulate in over dense regions whereas for electromagnetically interacting matter the radiation pressure counteracts the gravitational potential. The standard cosmological model ΛCDM containing dark energy (Λ) and non relativistic (cold) dark matter can be used for a fit to the measured spectrum. This yields the densities of baryonic matter and non baryonic dark matter. The most recent measurements of the Planck satellite constrain the abundance of dark matter, the so called relic density to $\Omega h^2 = 0.120 \pm 0.001$ [16]. These cosmological observations are nearly independent of the mass, as long as the dark matter is non relativistically. Thus there is no limit on the mass of dark matter.

2.2 WIMPs and other dark matter candidates

Over the years, there have been several suggestions to explain the observations discussed above ranging from modifying gravity such as the MOND theory [17] to MACHOs [18] and primordial black holes [19]. Theories predicting particle dark matter range from Axions [20–23] to Kaluza-Klein excitations [24–26] in compactified extra dimensions. In this work however, we focus on weakly interacting massive particles (WIMPs). It turns out that WIMPs of mass scale $\mathcal{O}(100\ \text{GeV})$ and weak scale interactions yield the correct relic density [27]. This is sometimes called the "WIMP miracle". Such weak scale WIMPs are in the range of current and future detectors and theories predicting such WIMPs are being tested by experiments. A well know example for a theory predicting WIMPs is the minimal supersymmetric standard model (MSSM). Supersymmetric theories often lack predictability due to the high number of unknown parameters and large parts of the parameter space are already excluded by experimental searches [28]. In this thesis, we study WIMPs in minimal models which have only few free parameters and convince through their simplicity.

2.2.1 Properties of dark matter

The cosmological measurements set some constraints on the properties of dark matter. As dark matter is a non luminous type of matter, the coupling to photons must vanish. Thus dark matter does not have an electric charge.[1]

Dark matter is still abundant at the present time. Therefore the decay of WIMPs must be suppressed such that the lifetime of dark matter is long compared to cosmological timescales. Hence the couplings for a decay must be suppressed or forbidden. Usually there is a symmetry which prevents the decay of dark matter. In supersymmetry, R-parity gives a mechanism that stabilizes the lightest supersymmetric particle and thus the dark matter candidate cannot decay. In this work we consider models where the discrete symmetry $\mathbb{Z}_2$ is imposed. All the Standard Model particles have an even charge under this symmetry whereas all new particles have an odd charge. At any vertex there must always be an even number of new particles involved and hence the decay of the lightest new particle is forbidden. We also study the case where the $\mathbb{Z}_2$ is promoted to a continuous group, a local U(1).

The ΛCDM cosmological model required dark matter to move at non relativistic velocities. Standard model neutrinos come close to the desired properties however, due to their small mass, they move relativistically and have been

[1] Note that milli charges arising from gauge kinetic mixing with a dark photon field is possible, however constrained [28].

shown to account for only 0.5% to 1.6% of the non baryonic matter content in our universe [28].

2.2.2 Genesis of dark matter

There are different scenarios, how the relic density was produced in the early universe, the most prominent being the freeze out scenario. More exotic scenarios include the freeze in, where dark matter never reaches thermal equilibrium [29, 30] and dark matter produced at cosmic strings [31]. For the models studies in this thesis, the freeze out scenario is relevant. We briefly sketch the formalism necessary to calculate the relic density in this scenario, following Refs. [27, 32].

The freeze out scenario assumes, that the dark matter density is in thermal equilibrium after the big bang. The number of particles produced is equal to the number of particles annihilating. The number density n_{eq} is proportional to T^3. As the Universe expands, the temperature drops and the energy becomes too low to produce dark matter particles while the annihilation continues. If the expansion of the Universe was so slow that equilibrium was maintained, the number density of dark matter would be given by

$$n_{\text{eq}} = g \left(\frac{m_\chi T}{2\pi}\right)^{\frac{3}{2}} e^{-\frac{m_\chi}{T}} \tag{2.2.1}$$

where T is the temperature, m_χ is the dark matter mass and g is the number of degrees of freedom. Since the Universe does expand fast, n_{eq} does not describe the number density accurately but one must account that, due to the fast expansion, the WIMPs fall out of equilibrium and stop annihilating. This behaviour is described by the Bolzmann equation

$$\dot{n}(t) + 3H(t)n(t) = -\langle\sigma_{\chi\chi}v\rangle \left[n(t)^2 - n_{\text{eq}}(t)^2\right] \tag{2.2.2}$$

where $H(t)$ is the Hubble parameter and $\langle\sigma_{\chi\chi}v\rangle$ is the thermally averaged dark matter self annihilation cross section. Numeric solutions to the Bolzmann equation are shown in Fig. 2.3. Note that the abundance of dark matter is inverse proportional to the annihilation cross section.

The above considerations hold true if only one particle is relevant for the freeze out scenario. Many models predict several new particles which can be close in mass and interact with each other. If at the time of decoupling from

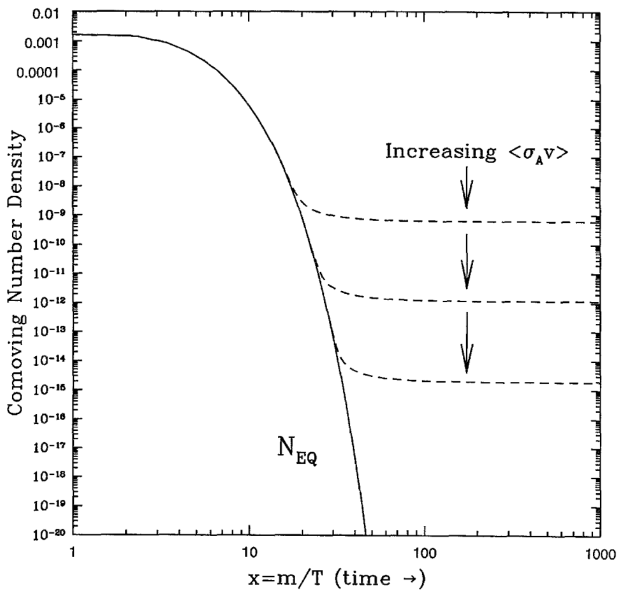

Figure 2.3: The evolution of the dark matter number density over time assuming equilibrium at all times (solid curve) and in the freeze out scenario for different annihilation cross sections (dashed curves). Figure taken from Ref. [27].

equilibrium, several non Standard Model particles are abundant, one must consider all of them. The number density of the particle χ_i at the time of decoupling, with χ_1 being the lightest one, is given by

$$\frac{n_i}{n_1} = \frac{g_i}{g_1}\left(1 + \frac{\Delta m_{i1}}{m_{\chi_1}}\right)^{\frac{3}{2}} e^{-\frac{\Delta m_{i1}}{T}} \tag{2.2.3}$$

where $\Delta m_{i1} = m_{\chi_i} - m_{\chi_1}$. Note how the density of the heavier particles is exponentially suppressed by the mass difference. To calculate the relic density, one must now include the annihilation between $\chi_1\chi_i$ and $\chi_i\chi_i$. Including coannihilations can yield a larger or smaller relic density depending on the details of the model.

2.3 Experimental searches

Different ideas to search for dark matter are pursued. Most of them can be related to the Feynman diagram shown in Fig. 2.4. All three possible ways of

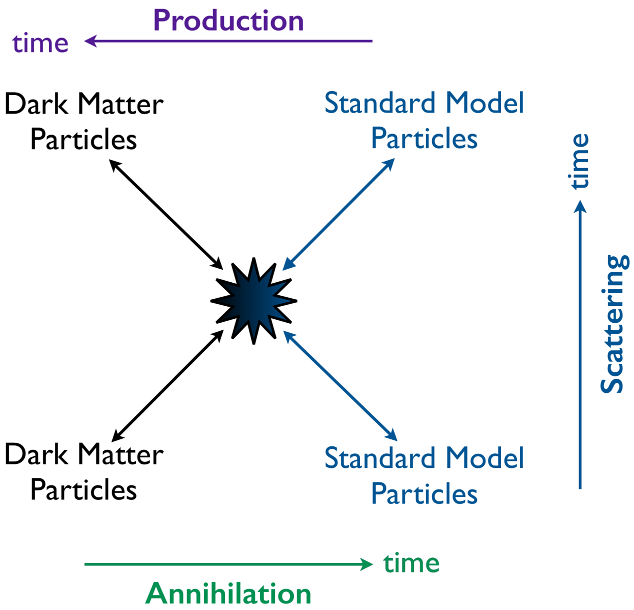

Figure 2.4: Illustration of the different ways to search for WIMP dark matter. Figure taken from `https://particleastro.brown.edu/dark-matter/`.

reading this diagram are being probed.

2.3.1 Direct detection

Direct searches for dark matter probe the diagram in Fig. 2.4 from bottom to top. Dark matter particles scatter on Standard Model particles (quarks and gluons) in nuclei. In this scattering process, energy is transferred to the nucleus and the recoil energy can be measured. The interaction is often mediated by a Higgs or a Z^0 boson in the t-channel. Other types of diagrams can also contribute. In theories where the dark matter particle couples to quarks, s-channel diagrams with colored particles (e.g. squarks in SUSY) as mediator are possible. For WIMPs with masses at the TeV-scale, the velocities in the dark matter halo are of $\mathcal{O}(100\ \text{km/s})$ and thus non relativistically.

The dark matter-nucleus interaction is often classified into spin dependent (SD) and spin independent (SI) interactions. SD interactions couple to the spin of nucleons. For nuclei, the spin is mostly carried by unpaired nucleons. Thus there is no enhancement for heavier nuclei. SI interactions couple to the nucleons in a nucleus coherently. Thus there is a A^2 enhancement for heavy

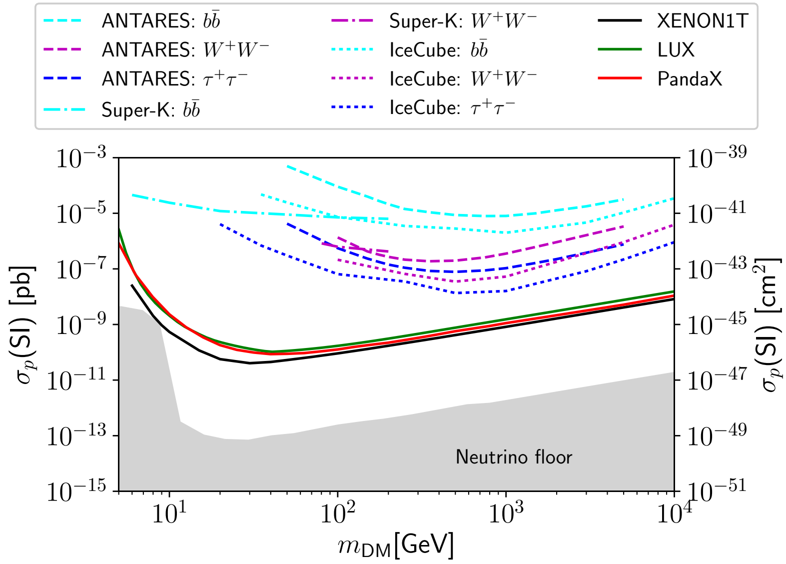

Figure 2.5: Limits on the spin independent scattering cross section on protons set by the direct detection experiments XENON1T[34], LUX [35] and PandaX-II [36] as well as annihilation channel dependent limits set by the neutrino telescopes ANTARES [37], IceCube [38] and Super-Kamiokande [39]. Also shown is the neutrino floor for direct detection experiments [40].

nuclei, assuming that the coupling on protons and neutrons are identical [33]. As a consequence, the limits on the SI cross section are often stronger than the limits on the SD cross section. If the scattering process is mediated by the Standard Model Higgs boson, then it always contributes to SI scattering regardless of the dark matter candidate. In case of scalar dark matter the exchange of a Z^0 boson also contributes to SI scatting. However, for Majorana dark matter, this process generates a SD cross section [33]. In this thesis, only the Higgs and Z^0 boson as mediator as well as the new vector boson called the Z' are relevant.

So far, most direct detection experiments have not detected any signal from dark matter and have thus published upper limits on the dark matter-nucleon scattering cross sections. The limits from XENON1T, LUX and PandaX-II on the spin independent scattering cross section are shown in Fig. 2.5. We also show the WIMP discovery limit (neutrino floor), where the dark matter detectors become sensitive to coherent neutrino scattering. For SI scattering

XENON1T sets the strongest limits in the mass range of $\mathcal{O}$(100 GeV). In Fig. 2.6 we show the limits on the spin dependent cross section set by XENON1T, LUX, PandaX-II and PICO-60. We also show the detector and annihilation channel dependent sensitivity floors where the neutrino telescopes become sensitive to neutrinos from cosmic ray interaction in the sun's atmosphere. For SD scattering on neutrons, XENON1T also imposes the strongest limit whereas for SD scattering on protons PICO-60 sets the most stringent model independent limit. Many other experiments have set limits on dark matter nucleon scattering for different ranges of dark matter masses [28]. The DAMA/LIBRA collaboration reports an annual modulation signal with a confidence level (C.L) of 12.9σ when taking into account the previous results from DAMA/NaI and DAMA/LIBRA-Phase1 [41]. This results are however in strong tension with other direct detection experiments.

2.3.2 Indirect detection

Dark matter annihilating in the cosmos is probed by indirect detection. Figure 2.4 read from left to right represents the annihilation of dark matter particles into Standard Model particles. Indirect detection experiments look for these final state particles. The thermally averaged self annihilation cross section $\langle \sigma v \rangle$ is probed by experiments including the search for gamma rays, cosmic ray anti matter and neutrinos [28].

Indirect detection experiments can also probe the same scattering cross sections on nuclei as direct detection, described in Sec. 2.3.1. Scattering of dark matter in celestial bodies such as the sun can lead to a capture in the gravitational potential and yield an overdensity of dark matter boosting the annihilation rate. Neutrinos produced from this annihilations can then be probed by neutrino telescopes such as IceCube and ANTARES. Limits obtained by these two experiments with the sun as source of neutrinos from dark matter annihilations are also shown in Figs. 2.5 and 2.6. These limits are obtained assuming that the dark matter particles annihilate into the given Standard Model particles (e.g. W^+W^-). The limits on the SI are significantly weaker than the ones set by direct detection experiments. However due to the lack of enhancement for scattering on heavy nuclei and the high abundance of hydrogen in the sun, the SD limits on protons are competitive. Neutrino telescopes are less sensitive to the SD scattering cross section on neutrons since there are

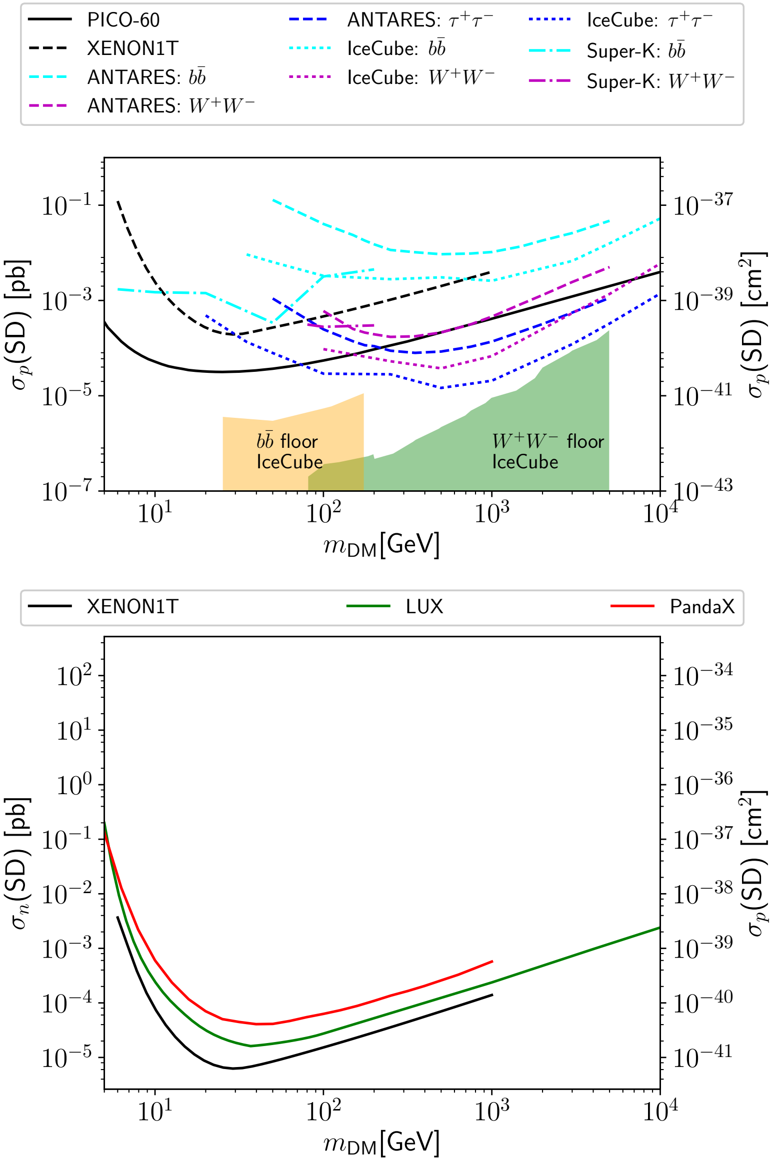

Figure 2.6: Limits on the spin dependent scattering cross section on protons (top) and neutron (bottom) set by the direct detection experiments XENON1T[42], PICO-60 [43], LUX [44] and PandaX-II [45] as well as annihilation channel dependent limits set by the ANTARES [37], IceCube [38] and Super-Kamiokande [39]. Limits from neutrino telescopes and from PICO are only published for scattering on protons. Also shown are the sensitivity floors for the W^+W^- and the $b\bar{b}$ channel for IceCube [46].

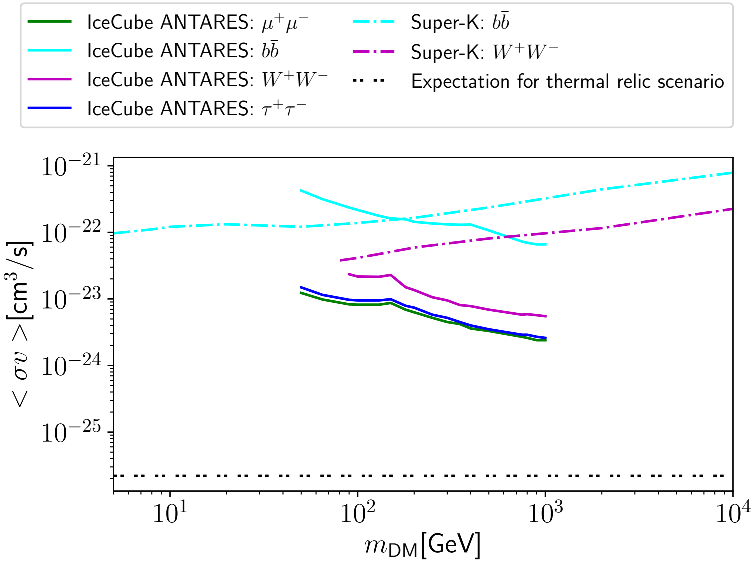

Figure 2.7: Limits on the self annihilation cross section in the galactic center obtained by a combined analysis of ANTARES and IceCube [47]. We show the limits for NFW dark matter halo profile. Limits from Super-Kamiokande [48] are also shown.

fewer neutrons than protons in the sun. We also show the sensitivity floor, where neutrinos from dark matter become indistinguishable from neutrinos produced from cosmic ray interactions with the suns atmosphere [46].

Neutrino telescopes can also probe the dark matter self annihilation cross section using neutrino signals from the galactic center. As dark matter is abundant in the galactic center it can annihilate with itself possibly producing neutrinos. The rate at which such annihilations happen is governed by the density and the self annihilation cross section and the number of neutrino is dependent on the annihilation channel. A combined analysis of IceCube and ANTARES has set the limits on the annihilation cross sections assuming different main annihilation channels. Their results and similar limits obtained by Super-Kamiokande are shown in Fig. 2.7.

2.3.3 Collider searches

The third way to read the diagram in Fig. 2.4 is from right to left representing the search for dark matter at colliders. In the collision of two Standard Model particles with high kinetic energy, new particles with larger mass can be produced. Examples for colliders are the Large Electron-Positron Collider (LEP) and the Large Hadron Collider (LHC). Limits set by the LHC are usually model dependent and obtained making some assumptions on the type of interaction. Thus one need to take care when applying these limits to a specific model. Despite the smaller center of mass energy, the model independent limits on new particles come from LEP since due to the absence of ingoing hadrons there are cleaner signals. The lower limit on the masses of charged fermions obtained by the OPAL collaboration at LEP is 102 GeV and the corresponding lower limit for charged scalar fields is 98 GeV [49].

Neutrinos

3

Neutrinos are some of the most mysterious particles in the Standard Model. They only interact via the weak interaction and are thus hard to detect. About 20 years ago, the fact that at least two of the three neutrinos are massive has been deduced from atmospheric [6] and solar [7, 50] neutrino oscillations. The absolute mass scale and hierarchy are still unknown. Why the neutrino masses are so small or equivalently, how they are generated, is a hot topic in BSM physics.

3.1 Neutrinos in the Standard Model

In the Standard Model, all fermions except neutrinos obtain their mass via interactions with the Higgs vacuum expectation value (vev). This is described by Yukawa interactions which after EWSB take the following form

$$\mathcal{L} \supset y_{ij} \langle H^0 \rangle \psi_L^i \psi_R^j + \text{H. c.} = m_{ij} \psi_L^i \psi_R^j + \text{H. c.}. \tag{3.1.1}$$

where both ψ_L and ψ_R are left handed Weyl spinors. (See Chap. 5 for conventions on the product.) Such mass terms are so called Dirac masses. If one would try to write down a similar interaction for neutrinos, a number of problems arise. First of all, one would need to introduce a right handed neutrino spinor, which is a singlet under the Standard Model gauge group. Such a right handed neutrino would have no electric charge and interact with none of the Standard Model gauge bosons. The only interaction to other Standard Model particles would take place via a Higgs exchange. However such interactions are strongly suppressed, as the Higgs couplings scale with the masses of the particles. Such a right handed neutrino would be practically impossible to detect. More importantly, as the neutrino masses are extremely small compared to the Standard Model Higgs vev of $v = \langle H^0 \rangle \sqrt{2} = 246.22$ GeV [28], the Yukawa couplings must be of $\mathcal{O}(10^{-11})$. As these couplings are dimensionless couplings, one would expect them to be naturally of $\mathcal{O}(1)$ which leaves us with the problem to explain why the couplings are so small. With no appealing way to generate neutrino masses within the Standard Model, neutrinos are described as massless left handed Weyl spinors. There are three neutrinos corresponding to the three generations of charged leptons $l = e, \mu, \tau$ and with all neutrinos massless, the Standard Model has an accidental global lepton flavor symmetry

$$\mathrm{U}(1)_{L_e} \times \mathrm{U}(1)_{L_\mu} \times \mathrm{U}(1)_{L_\tau}. \tag{3.1.2}$$

3.2 Neutrino oscillations and masses

The phenomenon that neutrinos of different flavors can transform into each other is known as neutrino oscillations. This is only possible if the propagating states which are the mass eigenstates differ from the interaction (flavor) eigenstates. Thus the discovery of neutrino oscillations not only shows that lepton flavor is violated but also that neutrinos do in fact have a mass. This section follows the review given in Ref. [28]. It should be noted, that one can assume more than three neutrinos relevant for oscillations, which yield slightly differing formulas. We will restrict ourselves to the case with three neutrinos.

Neutrinos in the weak interaction eigenstates ν_α, which are the eigenstates occuring in charged current interactions involving the lepton l_α, can be written as a linear combination of the propagating (mass) eigenstates ν_i

$$|\nu_\alpha\rangle = \sum_{i=1}^{3} (U^*_{\mathrm{PMNS}})_{\alpha i} \, |\nu_i\rangle. \tag{3.2.1}$$

U_{PMNS} is the Pontecorvo-Maki-Nakagawa-Sakata matrix. After traveling a distance L ($L \approx ct$ for relativistic neutrinos), the state is given by

$$|\nu_\alpha(t)\rangle = \sum_{i=1}^{3} (U^*_{\mathrm{PMNS}})_{\alpha i} \, |\nu_i(t)\rangle \tag{3.2.2}$$

where $|\nu_i(t)\rangle$ are, since they are the propagating states, given by $|\nu_i(t)\rangle = e^{-iE_i t}|\nu_i(0)\rangle$ with the neutrino energy $E_i = \sqrt{p_i^2 + m_i^2}$ and the mass of the propagating eigenstate m_i. The probability that a neutrino of flavor α oscillates

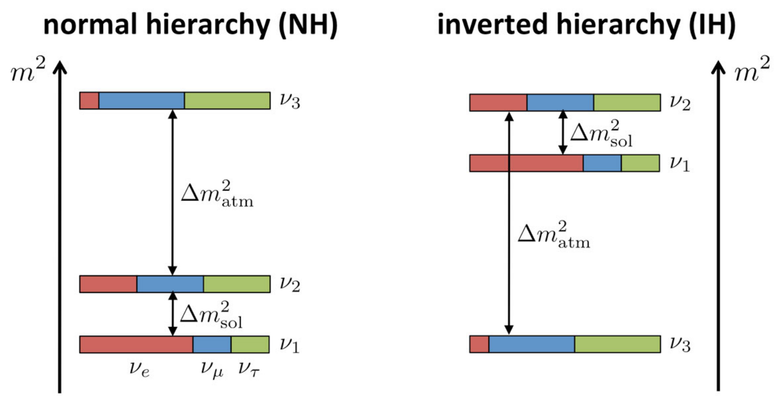

Figure 3.1: An illustration of the neutrino hierarchies. Figure taken from `https://neutrinos.fnal.gov/mysteries/mass-ordering/#moreinfo`.

to a neutrino of flavor β, is given by

$$\begin{aligned} P_{\alpha\beta} =& |\langle \nu_\beta | \nu_\alpha(t) \rangle|^2 \\ =& \delta_{\alpha\beta} - 4 \sum_{i<j}^{3} \text{Re} \left[(U_{\text{PMNS}})_{\alpha i} \, (U^*_{\text{PMNS}})_{\beta i} \, (U^*_{\text{PMNS}})_{\alpha j} \, (U_{\text{PMNS}})_{\beta j} \right] \sin^2(X_{ij}) \\ &+ 2 \sum_{i<j}^{3} \text{Im} \left[(U_{\text{PMNS}})_{\alpha i} \, (U^*_{\text{PMNS}})_{\beta i} \, (U^*_{\text{PMNS}})_{\alpha j} \, (U_{\text{PMNS}})_{\beta j} \right] \sin(2X_{ij}) \end{aligned} \tag{3.2.3}$$

with

$$X_{ij} = \frac{(m_i^2 - m_j^2)L}{4E} \tag{3.2.4}$$

where the approximation for relativistic neutrinos $p_i \approx p_j := p \approx E$ has been made. The expression for anti neutrinos is similar, but with $U_{\text{PMNS}} \to U^*_{\text{PMNS}}$ exchanged. Note how the oscillation depends on the mass difference of the neutrinos as well as the entries of the PMNS matrix but not on the absolute mass scale. The hierarchy of the neutrino masses is still unknown (see Fig. 3.1), however normal hierarchy is favoured in analyses of the full data [28].

In case of three Majorana neutrinos, the PMNS matrix can be parametrized by three angles and three phases. Two of these phases, the Majorana phases can be absorbed into neutrino states leaving one physical phase, the CP phase.

The PMNS matrix can be written as

$$U_{\text{PMNS}} = \begin{pmatrix} c_{12}c_{13} & s_{12}c_{13} & s_{13}e^{-i\delta_{CP}} \\ -s_{12}c_{23} - c_{12}s_{13}s_{23}e^{i\delta_{CP}} & c_{12}c_{23} - s_{12}s_{13}s_{23}e^{i\delta_{CP}} & c_{13}s_{23} \\ s_{12}s_{23} - c_{12}s_{13}c_{23}e^{i\delta_{CP}} & -c_{12}s_{23} - s_{12}s_{13}c_{23}e^{i\delta_{CP}} & c_{13}c_{23} \end{pmatrix} \tag{3.2.5}$$

with $c_{ij} = \cos(\theta_{ij})$, $s_{ij} = \sin(\theta_{ij})$ and the CP phase δ_{CP}.

3.3 Neutrino experiments

There are a number of experiments probing the neutrino oscillation parameters. Historically important are solar neutrinos. In the nuclear fusion cycle in the sun, electron neutrinos are produced. The number of detected neutrinos from the sun on earth is significantly smaller than the theoretical prediction indicating that these neutrinos oscillate into muon and tau neutrinos and are thus not detected. As electron neutrinos are always involved, solar neutrino experiments are sensitive to the upper row of the PMNS matrix and thus can probe the angles θ_{12} and θ_{13}. Solar neutrinos are probed e.g. by Super-Kamiokande and Borexino. Neutrinos produced on earth using accelerators are tested for example with long-baseline experiments such as T2K and NOνA. For these experiments neutrinos are usually produced by colliding a beam of protons with a target producing mostly pions which in turn decay mainly into muon neutrinos and muons. Probing the number of disappearing muon neutrinos gives sensitivity to the angle θ_{23} and Δm^2_{3l} while the number of appearing electron neutrinos allows one to probe the CP-violating phase. Atmospheric neutrinos, stemming from interaction of cosmic rays and the earth atmosphere, are detected for example by IceCube, ANTARES and Super-Kamiokande. Other neutrino sources include nuclear reactors which are being tested by e.g. KamLAND and Daya-Bay. As an overview of experiments for each neutrino source and the parameters they are sensitive to we give Tab. 3.1 which was taken from Ref. [28]. The data from these experiments combined can be used to fit the mixing angles phases and mass differences. The results of such a fit are shown in Tab. 3.2. It is worth mentioning that there are some disagreements between experiments concerning the CP phase. An analysis of the T2K

Table 3.1: Overview of neutrino experiments and the oscillation parameters they are sensitive to with $\Delta m^2_{3l} := \Delta m^2_{31} > 0$ for normal hierarchy and $\Delta m^2_{3l} := \Delta m^2_{32} < 0$ for inverted hierarchy. Table taken from Ref. [28].

Experiment	Dominant	Important
Solar neutrino experiments	θ_{12}	$\Delta m^2_{21}, \theta_{13}$
Reactor long-baseline experiments (KamLAND)	Δm^2_{21}	θ_{12}, θ_{13}
Reactor medium-baseline experiments (Daya-Bay, Reno, D-Chooz)	$\theta_{13}, \lvert\Delta m^2_{3l}\rvert$	
Atmospheric Experiments (Super-Kamiokande, IC-DC)		$\theta_{23}, \lvert\Delta m^2_{3l}\rvert, \theta_{13}, \delta_{\mathrm{CP}}$
Accel LBL $\mu_\mu, \bar{\nu}_\mu$, Disappearing (K2K, MINOS, T2K, NOνA)	$\lvert\Delta m^2_{3l}\rvert, \theta_{23}$	
Accel LBL $\nu_e, \bar{\nu}_e$, Appearing (MINOS, T2K, NOνA)	δ_{CP}	θ_{13}, θ_{23}

Table 3.2: The fit values and the $\pm 3\sigma$ ranges for the neutrino oscillation parameters for both hierarchies with $\Delta m^2_{3l} := \Delta m^2_{31} > 0$ for normal hierarchy and $\Delta m^2_{3l} := \Delta m^2_{32} < 0$ for inverted hierarchy. The values are taken from [51] (with SK-atm).

	Normal hierarchy	Inverted hierarchy
$\sin^2\theta_{12}$	$0.310^{+0.040}_{-0.035}$	$0.310^{+0.040}_{-0.035}$
$\sin^2\theta_{23}$	$0.582^{+0.042}_{-0.154}$	$0.582^{+0.041}_{-0.149}$
$\sin^2\theta_{13}$	$0.02240^{+0.00197}_{-0.00196}$	$0.02263^{+0.00198}_{-0.00196}$
$\delta_{CP}[^\circ]$	217^{+149}_{-82}	280^{+71}_{-84}
$\Delta m^2_{21}[10^{-5}\ \mathrm{eV}^2]$	$7.39^{+0.62}_{-0.60}$	$7.39^{+0.62}_{-0.60}$
$\Delta m^2_{3l}[10^{-3}\ \mathrm{eV}^2]$	$+2.525^{+0.097}_{-0.094}$	$-2.512^{+0.099}_{-0.094}$

data excludes CP-conservation at 95% CL [52] whereas NOνA data does not show significant indication of CP violation [53].

As the absolute neutrino mass scale does not have an impact on neutrino oscillations, the experiments mentioned above are not sensitive to the masses of the neutrinos. The KATRIN experiment is dedicated to the determination of the effective electron neutrino mass. Once this mass is known, the other masses can be calculated using the mass differences known from neutrino oscillations. Recently the KATRIN experiment has published a new upper limit of $m_{\nu_e} \leq 1.1$ eV [8] and aims for a sensitivity of 0.2 eV [54]. Limits on the sum of all three neutrino masses can be obtained from cosmological fits assuming the ΛCDM model with the most recent one being $\sum_i m_{\nu_i} < 0.12$ eV [16, 55].

As described above, the mechanism that generates the neutrino masses is still unknown. In fact it is still unclear whether neutrinos have Majorana or Dirac masses or some contributions of both types. Dirac masses would require right handed neutrinos whereas Majorana masses, predicted e.g. by the see-saw mechanism, violate not only lepton flavor, but also lepton number. The search for neutrinoless double beta decay $0\nu\beta\beta$ probes the Majorana nature of neutrinos. If a nucleus undergoes two beta decays at the same time, then the neutrinos can cancel each other out provided they have Majorana masses. In this process the nucleus emits two electrons but no neutrinos and lepton number is violated by two units. Experiments searching for double beta decay include GERDA and KamLAND-Zen with the strongest bound on the effective Majorana mass being

$$m_{\beta\beta} < 61 - 165 \text{ meV} \tag{3.3.1}$$

set by KamLAND-Zen [56].

4 BSM physics with heavy mediators

Most experiments searching for new particles need either a large enough center of mass energy to produce these particles (e.g. collider searches) or the particles must already exist (e.g. direct dark matter detectors) and are thus limited in the mass region due to the mass threshold or decreasing number densities. However it is also possible to probe new physics without producing the corresponding particles. As quantum field theory tells us, virtual particles can show effects even at energy scales below their mass. Despite the suppression by the mass of the new particles, they can be probed, especially if they induce transitions forbidden or suppressed in the Standard Model.

4.1 Lepton flavor violation

The Standard Model, with massless neutrinos, has an accidental lepton flavor symmetry which forbids decays such as $l_\alpha \to l_\beta \gamma$ and $l_\alpha \to 3l_\beta$[1] for charged leptons $l_\alpha, l_\beta = e, \mu, \tau$. This lepton flavor symmetry is broken by the neutrino mass mixing. This induces flavor violation for charged leptons which is however strongly suppressed by m_{ν_i}. For example the Standard Model decay rate for the branching ratio for $\mu \to e\gamma$ is given by

$$BR(\mu \to e\gamma) = \frac{3\alpha}{32\pi} \left| \sum_i \left(U^*_{\text{PMNS}}\right)_{\mu i} \left(U_{\text{PMNS}}\right)_{ei} \frac{m^2_{\nu_i} - m^2_{\nu_1}}{m^2_W} \right|^2 < 10^{-54} \tag{4.1.1}$$

and thus virtually impossible to detect [28]. As lepton flavor is an accidental symmetry, there is no reason for new physics to obey this symmetry. If the new particles have large masses, the contributions, arising from loop corrections, are suppressed by these masses. As the Standard Model rates are vanishingly small, BSM contributions are dominant and a Lepton Flavor Violation signal would be a clear indication of new physics. Dedicated experiments such as

[1]Note that $3l_\beta \hat{=} l_\beta l_\beta \bar{l}_\beta$ so that electric charge is conserved.

Table 4.1: Current limits and future sensitivities for some LFV observables.

LFV Process	Present Bound	Future Sensitivity
$\mathrm{BR}(\mu \to e\gamma)$	$4.2 \cdot 10^{-13}$[57]	$2 \cdot 10^{-15}$[58]
$\mathrm{BR}(\mu \to 3e)$	$1.0 \cdot 10^{-12}$[59]	10^{-16}[60]
$\mathrm{CR}(\mu - e,\mathrm{Ti})$	$4.3 \cdot 10^{-12}$[61]	10^{-18}[62]

MEG and SINDRUM have set strong limits on LFV. The most stringent limits and future sensitivities are given in Tab. 4.1.

4.2 Muon anomalous magnetic moment

The magnetic moment of leptons is at tree level predicted by the Dirac equation and given by $\vec{M} = g_l \frac{e}{2m_l} \vec{S}$ where $\vec{S}$ is the spin and $g_l = 2$. The "g-factor" g_l receives corrections through loop contributions. The deviation from 2 is called the anomalous magnetic moment and parameterized by

$$a_l := \frac{g_l - 2}{2}. \tag{4.2.1}$$

The most general form of the matrix element relevant for the lepton photon interaction with on shell leptons can be written as [63]

$iM^\mu =$

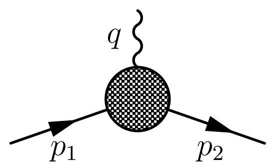

$$= -ie\bar{u}(p_2)\left[\gamma^m u F_E(q^2) + \left(\gamma^\mu - \frac{2m_l q^\mu}{q^2}\right)\gamma^5 F_A(q^2) + i\sigma^{\mu\nu}\frac{q_\nu}{2m_l}F_M(q^2) + \sigma^{\mu\nu}\frac{q_n u}{2m_l}\gamma^5 F_D(q^2)\right] u(p_1). \tag{4.2.2}$$

F_E renormalizes the electric charge while F_A is the anapole moment and F_D is the electric dipole moment. The anomalous magnetic moment is related to the form factor F_M by

$$a_l = F_M(0). \tag{4.2.3}$$

The anomalous magnetic moment for the muon has been calculated up to high loop orders (5-loop for QED). The calculated value can be compared to the experimental results measured at Brookhaven and recently at Fermilab. At the time of the making of this thesis the deviation between the Standard Model prediction and the experimental value is [64]

$$\Delta a_\mu = a_\mu^{\text{exp}} - a_\mu^{\text{SM}} = (251 \pm 59) \cdot 10^{-11} \tag{4.2.4}$$

which has a significance of 4.2σ.[2] New particles running in the loop could give new contributions to the anomalous magnetic moment and in principle explain the deviation from the Standard Model prediction.

4.3 Proton decay

In the Standard Model there is an accidental symmetry that conserves Baryon number. As the proton is the lightest hadron with Baryon number $B = 1$, this symmetry is the reason why the proton is stable. However Baryon number in the Standard Model is not motivated by a deeper principle and there is no reason for new physics to obey such an accidental symmetry. In fact, Grand Unified Theories (GUTs) usually have multiplets containing both leptons and quarks. The corresponding gauge bosons then mediate Baryon number violating transitions.[3]

One can write down effective operators that respect the Standard Model gauge symmetry but violate Baryon number. The lowest order operators with Standard Model fields as external legs are of dimension six and given by [65][4]

$$\begin{aligned}\mathcal{L}_{\text{eff}} \supset &\frac{c_1}{\Lambda^2}\epsilon^{ijk}(\bar{u}_R^c)_i\bar{\sigma}^\mu Q_j \bar{e}_R^c\bar{\sigma}_\mu Q_k + \frac{c_2}{\Lambda^2}\epsilon^{ijk}\left(\bar{u}_R^c\right)_i\bar{\sigma}^\mu Q_j(\bar{d}_R^c)_k\bar{\sigma}_\mu L \\ &+ \frac{c_3}{\Lambda^2}\epsilon^{ijk}(\bar{d}_R^c)_i\bar{\sigma}^\mu Q_j(\bar{u}_R^c)_k\bar{\sigma}_\mu L + \text{H. c.}\end{aligned} \tag{4.3.1}$$

where i, j, k are color indices. For details on gauge and Lorentz invariant products which we have implicitly used see Chap. 5. These operators are suppressed

[2] It is important to mention that there is a ongoing debate about the theoretical value, especially about the hadronic contributions. Thus one needs to take care when interpreting the deviation from the Standard Model.

[3] One should mention that there is also Baryon number violation arising from instanton effect. The rates are however of order 10^{-173} and thus negligible [65].

[4] There are also operators involving non Standard Model fields e.g. right handed neutrinos as external legs.

by the scale Λ which is the given by the mass of the fields mediating the Baryon number violating processes. The above operators allow the proton to decay for example into pions and positrons. The realizations of these operators are model dependent. Following Ref. [65] we make a naive estimate on the proton life time

$$\tau(p \to \pi^0 e^+) \approx \frac{\Lambda^4}{\alpha_{\mathrm{GUT}}^2 m_p^5} \tag{4.3.2}$$

where α_{GUT} is the gauge coupling strength at unification scale and m_p is the proton mass. With the limits on the proton life time for $p \to \pi^0 e^+$ set by Super-Kamiokande $\tau(p \to \pi^0 e^+) > 2.4 \times 10^{34}$ years [66] and assuming $\alpha_{\mathrm{GUT}} \approx 1/25$ we obtain

$$\Lambda \gtrsim 6.5 \times 10^{15} \text{ GeV}. \tag{4.3.3}$$

As the masses of the fields mediating proton decay are usually of the scale where the GUT gauge group is broken, this is often interpreted as a lower limit on the unification scale.

5 Theoretical aspects

5.1 Group theory in BSM physics

One of the most important tool for a model builder are symmetry groups. The standard model Lagrangian can for the most part be built by imposing a number of symmetries and then writing down all possible terms that are allowed by these symmetries[1]. A typical approach to build a new extension of the Standard Model is to add new particles and new symmetries and then define how each particle transforms under the symmetries of the model. The Lagrangian of this model can the simply be found by writing down all terms not forbidden by any symmetry.

Generally one distinguished between to type of symmetries: global and local symmetries. In case of global symmetries, the parameter describing the symmetry transformation does not depend on space time. For local symmetries, also called gauge symmetries, the transformation varies at every space time point. Local symmetries are often considered to be more attractive as they have a physical meaning due to their intrinsic connection to gauge bosons.

5.1.1 Representations of a group

Symmetries are generally described using groups.[2] It is crucial to define how each field in the Lagrangian transforms under a symmetry transformation. This is done by choosing a representation of the group. We will focus on groups that depend continuously on one or several parameter, so called Lie groups. Any element of a Lie group g can be described using the generators

[1] Exceptions include the strong CP-problem, where a CP-violating term in the QCD Lagrangian is allowed from a symmetry perspective but does not seem to be realized in nature.

[2] "Group" is here meant in the mathematical sense, meaning a set together with an operation fulfilling the group axioms.

X^a of the group:

$$g = \exp(\alpha_a X^a). \tag{5.1.1}$$

If X^a is given by a matrix, then exp is the matrix exponential. Conversely the generators can be obtained by taking the derivative regarding α_a. The generators span the Lie algebra and obey the relation

$$\left[X^a, X^b\right] = i f^{abc} X^c \tag{5.1.2}$$

with the structure constants f^{abc}. A representation is now given by a homomorphism[3] D from the Lie group to invertible linear operators acting on a vector space, often represented by matrices $U \in GL(n, K)$ for a vector space of dimension n over K. Since D is a homomorphism, we obtain the following conditions following from the group axioms:

$$D(g_1 \circ g_2) = D(g_1) \cdot D(g_2), \tag{5.1.3}$$
$$D(I) = \mathbb{1} \tag{5.1.4}$$

where I is the identity element of the group and $\mathbb{1}$ the unit matrix. From Eq. (5.1.1) we can define the representation of the Lie algebra $\mathcal{D}$:

$$U = D(g) = D\left(\exp(\alpha_a X^a)\right) := \exp\left(\alpha_a \mathcal{D}(X^a)\right). \tag{5.1.5}$$

The representation of a group is not unique. For example, there is a trivial representation that maps all group elements to 1.

Now we turn our attention to the transformation of fields. As described above a representation projects onto linear operators acting on a vector space. We embed our fields into this vector space by writing them as a vector. Equivalently one can write it componentwise as ϕ_i where i denotes the vector index. The field then transforms under a symmetry transformations as

$$U_{ij}\phi_j = \exp\left(\alpha_a \mathcal{D}(X^a)\right)_{ij} \phi_j \doteq \phi_i + \alpha_a \mathcal{D}(X^a)_{ij}\phi_j \tag{5.1.6}$$

where in the second equality we take the limit for infinitesimal transformations. Note the the vector space and the dimension of this vector space vary depending on which representation we choose. The Lagrangian is required to be invariant under such symmetry transformations with arbitrary α_a. Two of

[3]A homomorphism is a map preserving the group structure.

the most commonly used representations are the fundamental and the adjoint representations. For the symmetry group $SU(N)$ fundamental representation is a N dimensional representation consisting of traceless $N \times N$ matrices. The adjoint representation where the components of the generators are given by the structure constants $(X^a)_{bc} = if^{abc}$.

In case of a local symmetry, the parameter α_a is promoted to have a space time dependence $\alpha_a(x)$. This leads to the introduction of gauge bosons to keep the Lagrangian invariant under the symmetry transformation. With the physical meaning of local symmetries, it is crucial to define the transformation properties of each field under these local symmetries. This can be done by simply choosing a representation of the group. The gauge group of the Standard Model is given by

$$\mathrm{U}(1)_Y \times \mathrm{SU}(2)_L \times \mathrm{SU}(3)_c. \tag{5.1.7}$$

To specify the transformation properties of a particle, we will use the notation (Y, n_L, n_c) where Y denotes the hypercharge and n_L and n_c are the dimensions of the representation under which the particle transforms for $\mathrm{SU}(2)_L$ and $\mathrm{SU}(3)_c$ respectively while the conjugate representations are labeled as $\bar{n}$. For example the transformation of left handed quarks is described by $(\frac{1}{6}, 2, 3)$ whereas the right handed electron transforms as $(-1, 1, 1)$. In this work we only add particles without color charge e.g. in the trivial representation of $\mathrm{SU}(3)_c$ to the Standard Model. If a field transforms under the trivial representation of $\mathrm{SU}(2)_L$ we call it a singlet, whereas particles transforming under the fundamental and adjoint representation are called doublets and triplets respectively. For reference, we give the particles of the Standard Model and the representations in Tab. 5.1. The fields are given in terms of left handed Weyl spinors. For example the right handed electron is given by $\bar{e}_R^c$. This connection is explained in more detail in Sec. 5.2.2.

5.2 Weyl spinors

5.2.1 Representation of the Lorentz group

The group describing Lorentz transformations is given by SO(1,3). As this group has the same Lie algebra as SU(2)×SU(2), the representations of the Lorentz group can be described by (j_1, j_2). The notation for j_i is the same as

Table 5.1: Particle content of the Standard Model. All fields are given in terms of left handed Weyl spinors

Field	Generations	Spin	$U(1)_Y \times SU(2)_L \times SU(3)_c$
$L = \begin{pmatrix} \nu_L \\ e_L \end{pmatrix}$	3	$\frac{1}{2}$	$\left(-\frac{1}{2}, 2, 1\right)$
e_R^c	3	$\frac{1}{2}$	$(1, 1, 1)$
$Q = \begin{pmatrix} u_L \\ d_L \end{pmatrix}$	3	$\frac{1}{2}$	$\left(\frac{1}{6}, 2, 3\right)$
u_R^c	3	$\frac{1}{2}$	$(-\frac{2}{3}, 1, \bar{3})$
d_R^c	3	$\frac{1}{2}$	$(\frac{1}{3}, 1, \bar{3})$
H	1	0	$(\frac{1}{2}, 2, 1)$
B_μ	-	1	$(0, 1, 1)$
W_μ	-	1	$(0, 3, 1)$
G_μ	-	1	$(0, 1, 8)$

for Spin and angular momentum in Quantum mechanics. The nature of a field (scalar, fermion, vector) is fixed by the representation of the Lorentz group. The trivial representation $(0,0)$ describes scalar fields. If one j_i takes the value $\frac{1}{2}$ while the other is zero, this describes two component objects, called Weyl spinors. A field ψ_L in the $(\frac{1}{2}, 0)$ representation is called a left handed Weyl spinor and transforms as

$$\psi_L \rightarrow e^{\frac{1}{2}(i\theta_j - \beta_j)\sigma_j}\psi_L \tag{5.2.1}$$

where θ_j are the rotation angles and β_j are the boost angles. σ_j are given by the Pauli matrices. Similarly, right handed Weyl spinors ψ_R are in the $(0, \frac{1}{2})$ representation and their transformation is given by

$$\psi_R \rightarrow e^{\frac{1}{2}(i\theta_j + \beta_j)\sigma_j}\psi_R. \tag{5.2.2}$$

Left and right handed Weyl spinors can be combined to four component spinors, called Dirac spinors. These are in the $(\frac{1}{2}, 0) \oplus (0, \frac{1}{2})$ representation and with the gamma matrices in the Weyl representation, Dirac spinors Ψ can be written as

$$\Psi = \begin{pmatrix} \psi_L \\ \psi_R \end{pmatrix}. \tag{5.2.3}$$

Finally, vector bosons A^μ live in the $(\frac{1}{2}, \frac{1}{2})$ representation and have four degrees of freedom. They only occur as gauge bosons connected to a local symmetry.

5.2.2 Van der Waerden notation

Writing down fermion fields in terms of Dirac spinors can become confusing when working with particles transforming under $\mathrm{SU}(2)_L$. The left handed components of the Dirac spinors often transform differently under $\mathrm{SU}(2)_L$ than the right handed components. For example the Dirac spinor describing charged leptons contains the e_L component of the lepton doublet as well as e_R^c which is a singlet under $\mathrm{SU}(2)_L$. Often it is more clear to write down the Lagrangian in terms of Weyl spinors. In terms of Dirac spinors the Lagrangian can be obtained by combining the left and right handed Weyl spinors to Dirac spinors and using projection operators whenever necessary. Similar to the component notation for four vectors (with greek indices $\mu, \nu, ...$), one can introduce indices for the two component Weyl spinors to define a Lorentz invariant scalar product. An extensive treatment of this notation can be found in Ref. [67]. For left handed Weyl spinors χ, ξ we use undotted roman letter indices and define the product

$$\chi\xi = \chi^a \xi_a = \chi^1 \xi_1 + \chi^2 \xi_2 \tag{5.2.4}$$

and for right handed spinors $\bar{\chi}, \bar{\xi}$ we use dotted roman letters and the product is defined as[4]

$$\bar{\chi}\bar{\xi} = \bar{\chi}_{\dot{a}} \bar{\xi}^{\dot{a}} = \bar{\chi}_{\dot{1}} \bar{\xi}^{\dot{1}} + \bar{\chi}_{\dot{2}} \bar{\xi}^{\dot{2}}. \tag{5.2.5}$$

[4]One needs to be careful not to confuse notation for right handed Weyl spinors and the bar notation for Dirac spinors $\bar{\Psi} = \Psi^\dagger \gamma^0$. This is however usually clear from context.

We introduce, similar to $\eta^{\mu\nu}$, an invariant tensor to raise and lower the indices as

$$\epsilon^{ab} = \epsilon^{\dot{a}\dot{b}} = +i\sigma_2 = \begin{pmatrix} 0 & 1 \\ -1 & 0 \end{pmatrix}, \tag{5.2.6}$$

$$\epsilon_{ab} = \epsilon_{\dot{a}\dot{b}} = -i\sigma_2 = \begin{pmatrix} 0 & -1 \\ 1 & 0 \end{pmatrix}, \tag{5.2.7}$$

where σ_2 is the second Pauli matrix. These tensors then raise and lower the indices of Weyl spinors as

$$\chi^a = \epsilon^{ab}\chi_b \qquad \chi_a = \epsilon_{ab}\chi^b \qquad \bar{\chi}^{\dot{a}} = \epsilon^{\dot{a}\dot{b}}\bar{\chi}_{\dot{b}} \qquad \bar{\chi}_{\dot{a}} = \epsilon_{\dot{a}\dot{b}}\bar{\chi}^{\dot{b}}. \tag{5.2.8}$$

Since the components of the spinors (operators) anticommute, this yields a symmetric product

$$\chi\xi = \xi\chi \qquad \bar{\chi}\bar{\xi} = \bar{\xi}\bar{\chi}. \tag{5.2.9}$$

As $i\sigma_2\chi^*$ transforms as a right handed spinor, given a left handed spinor χ, it follows that in component notation

$$(\chi^a)^* = \bar{\chi}^{\dot{a}}, \qquad (\bar{\chi}_{\dot{a}})^* = \chi_a. \tag{5.2.10}$$

In this section we will denote Dirac spinors with capital greek letters e.g. Ψ and Weyl spinors with uncapitalised greek letters e.g. ψ. In chiral (Weyl) representation the gamma matrices have the index structure

$$\gamma^\mu = \begin{pmatrix} 0 & (\sigma^\mu)_{a\dot{b}} \\ (\bar{\sigma}^\mu)^{\dot{a}b} & 0 \end{pmatrix} \tag{5.2.11}$$

with

$$\sigma^\mu = (\mathbb{1}, \sigma^i), \qquad \bar{\sigma}^\mu = (\mathbb{1}, -\sigma^i). \tag{5.2.12}$$

A Dirac spinor is then, in component notation, given by

$$\Psi_D = \begin{pmatrix} \psi_a \\ \bar{\chi}^{\dot{a}} \end{pmatrix}, \tag{5.2.13}$$

$$\bar{\Psi}_D = \left(\chi^a, \bar{\psi}_{\dot{a}}\right). \tag{5.2.14}$$

As we will need it later, we give the Fierz replacement which holds true for anticommuting Weyl spinors and can be easily checked:

$$\xi^a(\sigma^\mu)_{a\dot{b}}\bar{\chi}^{\dot{b}} = -\bar{\chi}_{\dot{a}}(\bar{\sigma}^\mu)^{\dot{a}b}\xi_b. \tag{5.2.15}$$

5.3 Some points about Majorana fermions

Feynman rules are derived in many quantum field theory textbooks [68, 69]. Most textbooks focus on the treatment of scalar and vector fields as well as Dirac fermions but only briefly introduce Majorana fermions and do not discuss the Feynman rules for these. This section is devoted to introducing Feynman rules and conventions for Majorana fermions. Some treatment of Majorana fermions can also be found in Ref. [70].

5.3.1 Charge conjugation and Majorana particles

Majorana fermions are defined as being invariant under charge conjugation. The operator that defines the charge conjugation acting on Dirac spinors is

$$C: \quad \Psi \to -i\gamma^2\Psi^* = -i\gamma^2\gamma^0\bar{\Psi}^T. \tag{5.3.1}$$

The condition which defines Majorana fields is given by

$$\Psi_M = C\bar{\Psi}_M^T = -i\gamma^2\gamma^0\bar{\Psi}_M^T. \tag{5.3.2}$$

Note how this condition reduces the degrees of freedom from four to two and the Majorana spinors become their own antiparticles. For the remainder of this section, we will drop the index M as we will almost exclusively work with Majorana spinors. Using

$$C^{-1} = C^\dagger = C^T = -C \tag{5.3.3}$$

the Majorana condition can be rewritten to

$$\bar{\Psi} = \Psi^T C. \tag{5.3.4}$$

Charge conjugation should flip the sign of the charge. By applying C on the Dirac equation and requiring the resulting equation to describe a field with opposite charge, we obtain the relation

$$C(\gamma^\mu)^T C^{-1} = -\gamma^\mu. \tag{5.3.5}$$

From the Majorana condition, it follows that the Dirac spinor describing Majorana fermions is in terms of Weyl spinors given by

$$\Psi_M = \begin{pmatrix} \psi \\ \bar{\psi} \end{pmatrix} \tag{5.3.6}$$

where ψ is a left handed Weyl spinor. Note how only one Weyl spinor is required and thus the degrees of freedom are two.

5.3.2 Majorana Lagrangians

We now turn to the kinetic terms in a Lagrangian describing Majorana fields. We will give the equations in terms of both Dirac and Weyl spinors. To distinguish both notations we will, in this section, use capital letters for Dirac spinors and write the (un)dotted indices for Weyl spinors explicitly. The Lagrangian for free Majorana femions is given by

$$\begin{aligned} \mathcal{L} &= \frac{1}{2}\bar{\Psi}(i\gamma^\mu\partial_\mu - m)\Psi \\ &= \frac{1}{2}\left[\psi^a i(\sigma^\mu)_{a\dot{b}}\partial_\mu\bar{\psi}^{\dot{b}} + \bar{\psi}_{\dot{a}} i(\bar{\sigma}^\mu)^{\dot{a}b}\partial_\mu\psi_b - \psi^a m\psi_a - \bar{\psi}_{\dot{a}} m\bar{\psi}^{\dot{a}}\right]. \end{aligned} \tag{5.3.7}$$

Using Eq. 5.2.15 and partial integration this can be rewritten to

$$\mathcal{L} = \bar{\psi}_{\dot{a}} i(\bar{\sigma}^\mu)^{\dot{a}b}\partial_\mu\psi_b - \frac{m}{2}\left(\psi^a\psi_a + \bar{\psi}_{\dot{a}}\bar{\psi}^{\dot{a}}\right). \tag{5.3.8}$$

The Euler Lagrange equations of motion for $\bar{\psi}_{\dot{a}}$ are then[5]

$$i(\bar{\sigma}^\mu)^{\dot{a}b}\partial_\mu\psi_b - m\bar{\psi}^{\dot{a}} = 0 \tag{5.3.9}$$

or for ψ^a

$$-\partial_\mu\bar{\psi}_{\dot{a}} i(\bar{\sigma}^\mu)^{\dot{a}b} - m\psi^b = 0. \tag{5.3.10}$$

These two differential equations are equivalent as can easily be seen by hermitian conjugation. They represent the so called Majorana equation which describes a Majorana particle of mass m. Now it becomes obvious, why the Lagrangian for Majorana fermions differs from the Dirac Lagrangian by a factor of $\frac{1}{2}$. As Majorana fermions only have half the degrees of freedom compared

[5]Note that $\bar{\psi}$ or rather ψ^* is independent from ψ.

to Dirac fermions and are their own antiparticle, the factor of $\frac{1}{2}$ cancels when taking the derivative[6].

With the Van der Waerden notation one can easily show that Majorana spinors cannot couple to a vector current. We start with the case where both spinors belong to the same field. Then we simply have

$$\begin{aligned}
\bar{\Psi}\gamma^\mu\Psi &= \psi^a(\sigma^\mu)_{a\dot{b}}\bar{\psi}^{\dot{b}} + \bar{\psi}_{\dot{a}}(\bar{\sigma}^\mu)^{\dot{a}b}\psi_b &(5.3.11)\\
&= \psi^a(\sigma^\mu)_{a\dot{b}}\bar{\psi}^{\dot{b}} - \psi^a(\sigma^\mu)_{a\dot{b}}\bar{\psi}^{\dot{b}} &(5.3.12)\\
&= 0 &(5.3.13)
\end{aligned}$$

where we used Eq. (5.2.15) in the second equality. In case of two different spinors Ψ and Ψ', we have the Lagrangian

$$\begin{aligned}
\mathcal{L} =& \frac{1}{2}\bar{\Psi}(i\gamma^\mu\partial_\mu - m)\Psi + \frac{1}{2}\bar{\Psi}'(i\gamma^\mu\partial_\mu - m')\Psi' + g\bar{\Psi}'\gamma^\mu\Psi J_\mu &(5.3.14)\\
=& \bar{\psi}_{\dot{a}}i(\bar{\sigma}^\mu)^{\dot{a}b}\partial_\mu\psi_b - \frac{m}{2}\left(\psi^a\psi_a + \bar{\psi}_{\dot{a}}\bar{\psi}^{\dot{a}}\right)\\
&+ \bar{\psi}'_{\dot{a}}i(\bar{\sigma}^\mu)^{\dot{a}b}\partial_\mu\psi'_b - \frac{m'}{2}\left(\psi'^a\psi'_a + \bar{\psi}'_{\dot{a}}\bar{\psi}'^{\dot{a}}\right)\\
&+ g\left(\psi'^a(\sigma^\mu)_{a\dot{b}}\bar{\psi}^{\dot{b}} + \bar{\psi}'_{\dot{a}}(\bar{\sigma}^\mu)^{\dot{a}b}\psi_b\right)J_\mu &(5.3.15)\\
=& \bar{\psi}_{\dot{a}}i(\bar{\sigma}^\mu)^{\dot{a}b}\partial_\mu\psi_b - \frac{m}{2}\left(\psi^a\psi_a + \bar{\psi}_{\dot{a}}\bar{\psi}^{\dot{a}}\right)\\
&+ \bar{\psi}'_{\dot{a}}i(\bar{\sigma}^\mu)^{\dot{a}b}\partial_\mu\psi'_b - \frac{m'}{2}\left(\psi'^a\psi'_a + \bar{\psi}'_{\dot{a}}\bar{\psi}'^{\dot{a}}\right)\\
&+ g\left(\psi'^a(\sigma^\mu)_{a\dot{b}}\bar{\psi}^{\dot{b}} - \psi^a(\sigma^\mu)_{a\dot{b}}\bar{\psi}'^{\dot{b}}\right)J_\mu &(5.3.16)
\end{aligned}$$

where we used Eq. (5.2.15) in the last equality. Now we calculate the Euler Lagrange equations of motion for $\bar{\psi}_{\dot{a}}$. We obtain

$$0 = i(\bar{\sigma}^\mu)^{\dot{a}b}\partial_\mu\psi_b - m\bar{\psi}^{\dot{a}} + g\left((\sigma^\mu)_{a\dot{b}}\bar{\psi}'^{\dot{b}}\right)J_\mu. \tag{5.3.17}$$

Since ψ and ψ' are different fields, we can decompose this equation to the Majorana equation for ψ_a and

$$g\left((\sigma^\mu)_{a\dot{b}}\bar{\psi}'^{\dot{b}}\right)J_\mu = 0. \tag{5.3.18}$$

Thus the coupling to the vector current must vanish.

[6] This is similar to the case of real scalar field compared to complex ones.

5.3.3 Majorana Feynman rules

The quantized Majorana field is given by

$$\Psi(x) = \sum_s \int \frac{d^3p}{(2\pi)^3} \frac{1}{\sqrt{2\omega_p}} \left[a_p^s u_p^s e^{-ipx} + a_p^{s\dagger} v_p^s e^{ipx} \right], \tag{5.3.19}$$

$$\bar{\Psi}(x) = \sum_s \int \frac{d^3p}{(2\pi)^3} \frac{1}{\sqrt{2\omega_p}} \left[a_p^{s\dagger} \bar{u}_p^s e^{ipx} + a_p^s \bar{v}_p^s e^{-ipx} \right] \tag{5.3.20}$$

with the usual anti-commutation relations for the ladder operators. Note the similarity to Dirac spinors except from the fact that there is only one ladder operator a_p^s. In the Weyl basis, the Dirac spinors u_p^s and v_p^s are as usual given by

$$u_p^s = \begin{pmatrix} \sqrt{p_\mu \sigma^\mu} \xi_s \\ \sqrt{p_\mu \bar{\sigma}^\mu} \xi_s \end{pmatrix}, \qquad v_p^s = \begin{pmatrix} \sqrt{p_\mu \sigma^\mu} \xi_s \\ -\sqrt{p_\mu \bar{\sigma}^\mu} \xi_s \end{pmatrix} \tag{5.3.21}$$

with $\xi_1 = (1,0)^T$ and $\xi_2 = (0,1)^T$. The quantized Weyl spinors can now be deduced

$$\psi_a(x) = \sum_s \int \frac{d^3p}{(2\pi)^3} \frac{1}{\sqrt{2\omega_p}} \left[a_p^s e^{-ipx} + a_p^{s\dagger} e^{ipx} \right] \sqrt{p_\mu (\sigma^\mu)_{a\dot{b}}} \delta_s^{\dot{b}}, \tag{5.3.22}$$

$$\bar{\psi}^{\dot{a}}(x) = \sum_s \int \frac{d^3p}{(2\pi)^3} \frac{1}{\sqrt{2\omega_p}} \left[a_p^s e^{-ipx} - a_p^{s\dagger} e^{ipx} \right] \sqrt{p_\mu (\bar{\sigma}^\mu)^{\dot{a}b}} \delta_b^s. \tag{5.3.23}$$

We can now evaluate the Feynman rules. For in and outgoing Majorana fermions in terms of Dirac spinors we have in momentum space

$\overbracket{\Psi|p}, s\rangle \propto$ 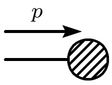 $= u_p^s,$ $\overbracket{\bar{\Psi}|p}, s\rangle \propto$ 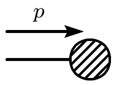 $= \bar{v}_p^s,$ (5.3.24)

$\langle p, \overbracket{s|\Psi} \propto$ 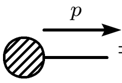 $= v_p^s,$ $\langle p, \overbracket{s|\bar{\Psi}} \propto$ 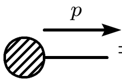 $= \bar{u}_p^s.$ (5.3.25)

In component notation the corresponding Feynman rules are

$\overbracket{\psi_a|p}, s\rangle \propto$ 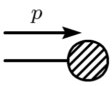 $= \sqrt{p_\mu (\sigma^\mu)_{a\dot{b}}} \delta_s^{\dot{b}},$ $\overbracket{\bar{\psi}^{\dot{a}}|p}, s\rangle \propto$ 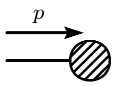 $= \sqrt{p_\mu (\bar{\sigma}^\mu)^{\dot{a}b}} \delta_b^s,$ (5.3.26)

$\langle p, \overbracket{s|\psi_a} \propto$ 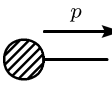 $= \sqrt{p_\mu (\sigma^\mu)_{a\dot{b}}} \delta_s^{\dot{b}},$ $\langle p, \overbracket{s|\bar{\psi}^{\dot{a}}} \propto$ 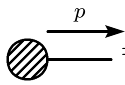 $= -\sqrt{p_\mu (\bar{\sigma}^\mu)^{\dot{a}b}} \delta_b^s.$ (5.3.27)

For propagators, we have the same contraction as for Dirac fermions given by

$$\langle 0|\Psi_a \bar{\Psi}_b|0\rangle \propto \overset{p}{\overline{}} = \frac{i(\not{p}+m)_{ab}}{p^2-m^2+i\varepsilon}, \tag{5.3.28}$$

where a, b denote the components of the spinors. In contrast to Dirac spinors, the following contractions also do not vanish in case of Majorana spinors

$$\langle 0|\bar{\Psi}_a \bar{\Psi}_b|0\rangle = \langle 0|C^{-1}_{ac}\Psi_c \bar{\Psi}_b|0\rangle \propto \overset{p}{\overline{}} = \frac{iC^{-1}_{ac}(\not{p}+m)_{cb}}{p^2-m^2+i\varepsilon}, \tag{5.3.29}$$

$$\langle 0|\Psi_a \Psi_b|0\rangle = \langle 0|C^{-1}_{bc}\Psi_a \bar{\Psi}_c|0\rangle \propto \overset{p}{\overline{}} = \frac{iC^{-1}_{bc}(\not{p}+m)_{ac}}{p^2-m^2+i\varepsilon}, \tag{5.3.30}$$

where we used that $\Psi = C\bar{\Psi}^T$ and $\bar{\Psi}^T = C^{-1}\Psi$ which follows from the Majorana condition. In component notation the relevant propagators are given by

$$\langle 0|\psi_a \psi^b|0\rangle \propto \overset{p}{\overline{}} = \frac{im\delta^b_a}{p^2-m^2+i\varepsilon}, \tag{5.3.31}$$

$$\langle 0|\psi_a \bar{\psi}_{\dot{b}}|0\rangle \propto \overset{p}{\overline{}} = \frac{ip_\mu(\sigma^\mu)_{a\dot{b}}}{p^2-m^2+i\varepsilon}, \tag{5.3.32}$$

$$\langle 0|\bar{\psi}^{\dot{a}} \psi^b|0\rangle \propto \overset{p}{\overline{}} = \frac{ip_\mu(\bar{\sigma}^\mu)^{\dot{a}b}}{p^2-m^2+i\varepsilon}, \tag{5.3.33}$$

$$\langle 0|\bar{\psi}^{\dot{a}} \bar{\psi}_{\dot{b}}|0\rangle \propto \overset{p}{\overline{}} = \frac{im\delta^{\dot{a}}_{\dot{b}}}{p^2-m^2+i\varepsilon}. \tag{5.3.34}$$

All other propagators can be obtained by raising or lowering the indices. Note how the $C^{-1} = i\gamma^2\gamma^0$ in Eqs. (5.3.29) and (5.3.30) operation has a similar effect, as raising and lowering indices.

There are several mathematical expressions for the same graphical line of propagators as well as in and outgoing particles in both Dirac and Weyl spinor notation. Which formula to use can at this point only be determined by writing down all possible contractions as stated in the Wick theorem. However, using the Majorana condition, one can rewrite the contractions in such a way, that the same Feynman rules as for Dirac fermions can be used. To show this, we consider a Lagrangian with interaction terms of the shape

$$\mathcal{L}_{\text{int}} \subset \bar{\Psi}^i_a \Gamma^{ij}_{ab} \Psi^j_b \tag{5.3.35}$$

where we use upper indices to denote different fields and lower indices to denote the spinor structure. Γ^{ij} in general contains scalar or vector fields as well as Gamma matrices. Since Majorana fermions do not have vector interactions, the spinor structure of Γ^{ij} is given by a sum of $\mathbb{1}, \gamma^5$ and $\gamma^\mu\gamma^5$.[7] Using Eq. (5.3.5), it follows that

$$C_{ab}\Gamma^{ij}_{cb}C^{-1}_{cd} = \Gamma^{ij}_{ad}. \tag{5.3.36}$$

This allows us to switch spinors as follows

$$\begin{aligned}
\bar{\Psi}^i_a\Gamma^{ij}_{ab}\Psi^j_b &= \Psi^i_a C_{ab}\Gamma^{ij}_{bc}C_{cd}\bar{\Psi}^j_d & (5.3.37)\\
&= -\bar{\Psi}^j_d C_{ab}\Gamma^{ij}_{bc}C_{cd}\Psi^i_a & (5.3.38)\\
&= \bar{\Psi}^j_d C_{dc}\Gamma^{ij}_{bc}C^{-1}_{ba}\Psi^i_a & (5.3.39)\\
&= \bar{\Psi}^j_d\Gamma^{ij}_{da}\Psi^i_a & (5.3.40)
\end{aligned}$$

where we used the Majorana condition in the first equality, then the anti commutation relation for spinors and finally $C^T = C^{-1} = -C$. This tells us that we can switch the Majorana spinors on both sides of the operator Γ^{ij}. Using this relation, we can write any Wick contracted expression as

$$\mathcal{O}_1\bar{\Psi}^i\Gamma^{ij}\Psi^j\bar{\Psi}^k\Gamma^{kl}\ldots\Gamma^{mn}\Psi^n\bar{\Psi}^o\Gamma^{op}\Psi^p\mathcal{O}_2 \tag{5.3.41}$$

where we do not write the contractions for non Majorana fields (e.g. contained in Γ^{ij}). The operators $\mathcal{O}_i$ in general contain the initial and final states and the corresponding contractions give the expressions for in and out going particles. Note that in case of loops, the fermion field on the left and on the right should be contracted with each other. This case works similar to the case above. All contractions now give the same propagator as known from Dirac Feynman rules. Graphically speaking, ordering the Wick contractions like this corresponds to drawing arrows on the fermions lines (just like for charge flow) and then evaluating the graph just like a graph containing Dirac fermions. In component notation this procedure is equivalent to raising and lowering the indices in such a way, that Eqs. (5.3.26), (5.3.27) and (5.3.31) to (5.3.34) can be used.

[7] The projection operators $P_{R,L}$ are also contained as they are a combination of $\mathbb{1}$ and γ^5.

As Majorana particles are there own anti particles, one needs to take care with interactions where the same field occurs twice such as

$$\mathcal{L}_{\text{int}} \subset \bar{\Psi}\Gamma\Psi. \tag{5.3.42}$$

Say there is a contraction such as

$$\mathcal{O}_1\bar{\Psi}\Gamma\Psi\mathcal{O}_2 \tag{5.3.43}$$

one also needs to include the contraction

$$\mathcal{O}_1\bar{\Psi}\Gamma\Psi\mathcal{O}_2 \tag{5.3.44}$$

which gives the same expression as the first contraction as Eq. (5.3.40) tells us. Thus, for each vertex with the same Majorana field twice, we obtain a factor of two. Similarly to the case of real scalar bosons, we include a factor of $\frac{1}{2}$ in each vertex where a Majorana field occurs twice.

5.4 Gauge invariant products

The Van der Waerden notation introduced in Sec. 5.2.2 defines a Lorentz invariant product. As all products in the Lagrangian should be gauge invariant, it is useful to define a gauge invariant product for $\mathrm{SU}(2)_L$ as well. Similar to the Van der Waerden notation, we introduce a tensor ϵ that raises and lowers the $\mathrm{SU}(2)_L$ indices

$$\epsilon^{ab} = +i\sigma_2 = \begin{pmatrix} 0 & 1 \\ -1 & 0 \end{pmatrix}, \tag{5.4.1}$$

$$\epsilon_{ab} = -i\sigma_2 = \begin{pmatrix} 0 & -1 \\ 1 & 0 \end{pmatrix}. \tag{5.4.2}$$

Fields in different representations have different index structures and must be treated differently. Fields in the trivial representation, so called singlets, do not have any $\mathrm{SU}(2)_L$ index. Doublets are objects with one index which transform as

$$\chi_a \to U_a{}^b\chi_b \tag{5.4.3}$$

$$\tag{5.4.4}$$

where U is the gauge transformation for fields in the fundamental representation of $\mathrm{SU}(2)_L$ given by

$$U = \exp\left(\frac{i}{2}\alpha^i\sigma_i\right). \tag{5.4.5}$$

Using $\epsilon U \epsilon^{-1} = (U^{-1})^T$ we can find the inverse transformation as

$$U^a{}_d = (U^{-1})_d{}^a. \tag{5.4.6}$$

From definition, triplets (i.e. fields on the adjoint representation of $\mathrm{SU}(2)_L$) transform as

$$\phi_j \to \exp\left(\alpha^i T^i_A\right)_{jk}\phi^k \tag{5.4.7}$$

where $(T^i_A)_{jk} = -i\epsilon_{ijk}$ is the $\mathrm{SU}(2)_L$ generator in the adjoint representation whose elements are given by the structure constants. One usually defines triplets as matrices by contracting the fields with the Pauli matrices

$$\Delta = \sigma^j\phi_j. \tag{5.4.8}$$

With the triplets written like this, we can express the gauge transformation as

$$\begin{aligned}
\Delta_a{}^b = (\sigma^j)_a{}^b\phi_j \to & (\sigma^j)_a{}^b \exp\left(\alpha^i T^i_A\right)_{jk}\phi^k && (5.4.9)\\
&\doteq (\sigma^j)_a{}^b\left[\delta_{jk} + \alpha^i (T^i_A)_{jk}\right]\phi^k && (5.4.10)\\
&= \left[(\sigma^k)_a{}^b - i\alpha^i\epsilon_{ijk}(\sigma^j)_a{}^b\right]\phi^k && (5.4.11)\\
&= \left[(\sigma^k)_a{}^b + \frac{1}{2}\alpha^i[\sigma_i,\sigma_k]_a{}^b\right]\phi^k && (5.4.12)\\
&= \left\{\left[\mathbb{1} + \frac{i}{2}\alpha^i\sigma_i\right]\sigma_k\phi^k\left[\mathbb{1} - \frac{i}{2}\alpha^i\sigma_i\right]\right\}_a^{\ b} && (5.4.13)\\
&\doteq U_a{}^c\Delta_c{}^d(U^{-1})_d{}^b. && (5.4.14)
\end{aligned}$$

With the index structure and gauge transformations fixed, we define the product for the $\mathrm{SU}(2)_L$ structure by contracting upper and lower indices, for example for two doublets

$$\chi\xi = \chi^a\xi_a = \chi_b\epsilon^{ba}\xi_a \tag{5.4.15}$$

or for a triplet and a doublet

$$\Delta\chi = \Delta_a{}^b\chi_b. \tag{5.4.16}$$

The gauge transformation for the latter product is

$$\Delta\chi = {\Delta_a}^b \chi_b \to {U_a}^c {\Delta_c}^d {(U^{-1})_d}^b {U_b}^e \chi_e \tag{5.4.17}$$
$$= {U_a}^c {\Delta_c}^d \chi_d. \tag{5.4.18}$$

This is the same transformation as for a single doublet. Similarly one can show, that objects with two indices (e.g. a product of two triplets) transforms the same way as a triplet whereas a product of two doublets (with no free index) transforms trivially. Finally if we have an object with two indices and take the trace, the resulting object transforms trivially since

$${\Delta_a}^a \to {U_a}^b {\Delta_b}^c {(U^{-1})_c}^a = {(U^{-1})_c}^a {U_a}^b {\Delta_b}^c = {\Delta_b}^b. \tag{5.4.19}$$

This should also be expected as after taking the trace there are no free indices.

Every term in the Lagrangian must not only be invariant under $\mathrm{SU}(2)_L$ gauge invariance, but also has to obey the $\mathrm{U}(1)_Y$ group of hypercharge. For a scalar doublet χ one can define a conjugate field $\phi^\dagger$ which has opposite hypercharge but has index structure $(\phi^\dagger)_a$ and transforms as a doublet[8]. Similarly one can define $\Delta^\dagger$ for a scalar triplet. This object transforms as a triplet under $\mathrm{SU}(2)_L$ and again has opposite hypercharge to Δ. For fermion fields we must also make sure that all products are invariant under Lorentz transformations. The corresponding formalism has been introduced in Sec. 5.2.2. In that section we introduced right handed Weyl spinors $\bar{\chi}$ which could be obtained by complex conjugation from left handed Weyl spinors χ. The complex conjugation also ensures that $\bar{\chi}$ has opposite hypercharge to χ. By multiplying with $i\sigma^2$ in $\mathrm{SU}(2)_L$ space, we can make sure that this object transforms under $\mathrm{SU}(2)_L$ as a singlet (i.e. no $\mathrm{SU}(2)_L$ index), a doublet (i.e. a lower $\mathrm{SU}(2)_L$ index) or as a triplet (with one lower and one upper $\mathrm{SU}(2)_L$ index). Note that for fermions one now has the (un)dotted indices from the Warden notation as well as the indices for the $\mathrm{SU}(2)_L$ products. These indices are often not written explicitly but all products in the Lagrangian and simply assumed to be Lorentz and $\mathrm{SU}(2)_L$ invariant.

[8] When one does not define conventions such that all products are gauge invariant, then $\phi^\dagger$ is given by $\tilde{\phi} = i\sigma^2\phi^*$.

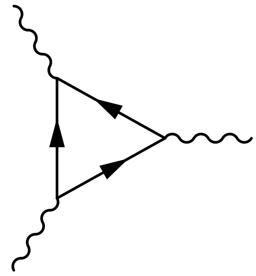

Figure 5.1: Triangle diagram responsible for gauge anomalies.

5.5 Anomalies

For a given Lagrangian one can consider both the classical theory with ordinary fields as well as the quantum theory, where the fields are promoted to operators. The classical theory already describes many features of the model, however it fails to describe effects arising from loops. It turns out that the symmetries of the classical Lagrangian are not necessarily symmetries of the quantum theory. In this case the symmetry is said to be anomalous. In case of global symmetries this does not pose a problem. In fact a number of symmetries in the Standard Model are anomalous, for example Baryon number. Gauge symmetries however cannot be anomalous. In such a case the theory would be unphysical as unitarity breaks down. These so called gauge anomalies are connected to triangle diagrams with three gauge bosons as external legs and a fermion running in the loop. An illustration of such triangle diagrams is shown in Fig. 5.1. The contributions of these diagrams must cancel in order to ensure that a symmetry is gauge anomaly free.

For a triangle diagram where the external vector bosons have indices a, b, c, the contribution is proportional to [69]

$$d_R^{abc} = 2\mathrm{Tr}\left[T_R^a\{T_R^b, T_R^c\}\right] := 2A(R)\mathrm{Tr}\left[T_F^a\{T_F^b, T_F^c\}\right] := 2A(R)d^{abc} \tag{5.5.1}$$

where T_R^i are the generators of the gauge symmetry corresponding to the gauge boson with index $i = a, b, c$ in the representation R where $R = F$ is the fundamental representation. $A(R)$ is the so called anomaly coefficient. From the definition it follows that in the fundamental representation, $A(F) = 1$. The contributions of the triangle diagrams vanish if either $d^{abc} = 0$ or the sum over all fermion fields cancels. The latter case yields the so called anomaly constraints. The anomaly arising from a specific triangle diagram is usually

Table 5.2: Conditions for gauge anomaly cancellation for the Standard Model gauge group $\mathrm{SU}(3)_c \times \mathrm{SU}(2)_L \times \mathrm{U}(1)_Y$. The sums run over all components of fermion fields ψ. Note that all fields are assumed to be left handed Weyl spinors. For $\mathrm{SU}(3)_c$ we assume singlets 1_3 and triplets 3_3 and for $\mathrm{SU}(2)_L$ we consider singlets 1_2, doublets 2_2 and triplets 3_2.

Anomaly	Constraint
$\mathrm{U}(1)_Y^3$	$\sum\limits_{\psi} Y_\psi^3 = 0$
$\mathrm{SU}(3)_c^2 \times \mathrm{U}(1)_Y$	$\sum\limits_{\psi \in 3_3} Y_\psi = 0$
$\mathrm{SU}(2)_L^2 \times \mathrm{U}(1)_Y$	$\sum\limits_{\psi \in 2_2} Y_\psi + 4 \sum\limits_{\psi \in 3_2} Y_\psi = 0$
$\mathrm{grav}^2 \times \mathrm{U}(1)_Y$	$\sum\limits_{\psi} Y_\psi = 0$

denoted by a product of the symmetry groups corresponding to the gauge bosons involved. One also must consider diagrams with the graviton as external legs. These anomalies are then denoted similarly with grav as the symmetry group. For a given gauge symmetry and particle content, we can now calculate whether there are gauge anomalies in this theory. In Tab. 5.2 we give the conditions for anomalies to cancel for the Standard Model gauge group assuming all fields are in the trivial or fundamental representation of $\mathrm{SU}(3)_c$ and for $\mathrm{SU}(2)_L$ we in addition allow for fields in the adjoint representation. As we use the anomaly coefficient for the $\mathrm{SU}(2)_L^2 \times \mathrm{U}(1)_Y$ anomaly with fermions in adjoint representation, we give the calculation of this coefficient. With the $\mathrm{SU}(2)_L$ generators in the adjoint representation $(T_A^a)_{bc} = \epsilon^{abc}$ we have

$$\mathrm{Tr}\left[Y\{T_A^b, T_A^c\}\right] = \mathrm{Tr}\,(Y)\left(\epsilon^{bij}\epsilon^{cji} + \epsilon^{cij}\epsilon^{bji}\right) = -4\delta^{bc}\mathrm{Tr}\,(Y) = 4d^{abc} = A(A)d^{abc} \tag{5.5.2}$$

where we have used $d^{abc} = -\delta^{bc}\mathrm{Tr}\,(Y)$ for the $\mathrm{SU}(2)_L^2 \times \mathrm{U}(1)_Y$ anomaly. It follows that for this anomaly, $A(A) = 4$.

There is one more anomaly which we must consider, the Witten anomaly [71]. It is related to the SU(2) gauge group. For our purposes, it states that there always must be an even number of fermion $\mathrm{SU}(2)_L$ doublets.

In model building one usually makes sure that the model is gauge anomaly free. There is one object that comes in handy when doing so, vector like fermions. Consider two fermions fields ψ, ψ' in the same representation of $\mathrm{SU}(3)_c \times \mathrm{SU}(2)_L$ and opposite U(1) charges.[9] One can easily see these two fields together do not contribute to any gauge anomaly. Both field together form a gauge invariant mass term $m\psi\psi'$. This motivates combining both of them to a Dirac spinor

$$\Psi = \begin{pmatrix} \psi \\ \bar{\psi}' \end{pmatrix}. \tag{5.5.3}$$

5.6 Unification

The parameters in the Lagrangian such as gauge couplings are not constant but depend on the energy scale at which one measures them. When calculating loops, divergences occur which are then absorbed into the bare quantities in the Lagrangian. This renormalization procedure makes the physically measurable couplings dependent on the energy scale μ. In this section we are particularly interested in the scale dependence of the Standard Model gauge couplings. How these couplings run, depends on the particles contributing in the loop. Given the particle content of the Standard Model, we can calculate the running of the three gauge couplings. Their running is shown in Fig. 5.2. We see that the coupling strengths of all three couplings are running towards each other. This motivates the so called Grand Unified theories (GUTs). Should all three gauge couplings intersect at one point, it is plausible, that at this energy scale the Standard Model gauge group is embedded into a larger symmetry, which is spontaneously broken at this scale. The differences in the coupling strengths we now measure, would then simply arise from the fact that these coupling run differently. All Standard Model fields must then be placed into multiplets of this larger symmetry so that at energy scales above the unification scale the models is invariant under this grand unified gauge symmetry. From Fig. 5.2 it becomes obvious that the Standard Model coupling do not unify at one point. As mentioned above the running of couplings depends on the fields running in the loop. Should there be additional fields at a low energy scale, then the running would change possibly leading to a unification of all three

[9]To be precise for triplets under $\mathrm{SU}(3)_c$ one field must be in the 3 representation and the other in the $\overline{3}$. In general ψ and ψ' must be in representations conjugate to one another.

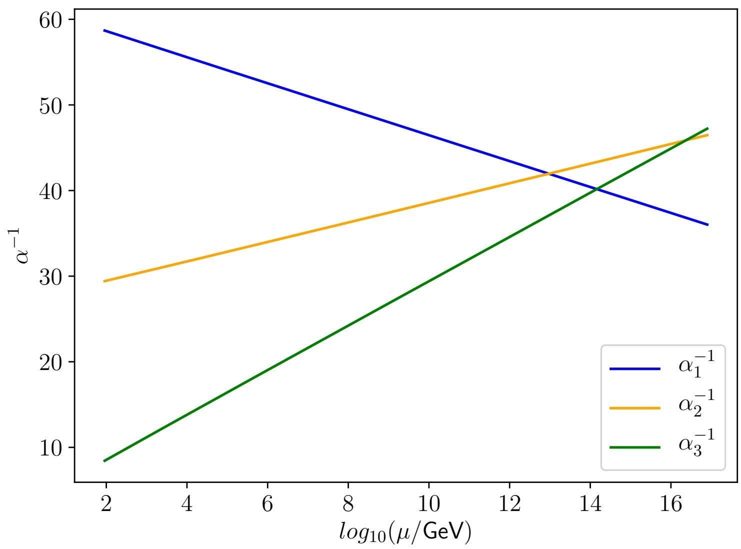

Figure 5.2: Running of couplings in the Standard Model. The RGEs have been calculated using SARAH [72, 73] at two loop. The couplings are set to $\alpha_1(m_{Z^0}) = 0.01704, \alpha_2(m_{Z^0}) = 0.03399$ and $\alpha_3(m_{Z^0}) = 0.1185$ with $m_{Z^0} = 91.1876$ GeV and the Yukawa coupling of the top-quark has been set to one. The parameters have been chosen as in Ref. [74].

gauge couplings at one point. It is worth mentioning, that the particle content of the MSSM with superpartners at TeV scale does lead to unification [75–77].

5.7 Neutrino Masses

The generation of the neutrino masses cannot be explained with the Standard Model. As explained in Chap. 3, the neutrinos cannot obtain their masses via the Standard Model Higgs mechanism, as their masses are extremely small compared to the Higgs vev. In this section we discuss how Majorana neutrino masses can be generated by new physics at high energy scales.

5.7.1 Dimension 5 Weinberg operator

In order to systematically study the generation of Majorana neutrino masses, one can introduce the $d = 5$ Weinberg operator [78] which in Weyl spinor notation is given by

$$\mathcal{L} \supset -\frac{c_{\alpha\beta}}{\Lambda}\left(L_\alpha H\right)\left(L_\beta H\right) + \text{H. c.} \tag{5.7.1}$$

$c_{\alpha\beta}$ is a coefficient obtained by integrating out new physics and Λ is the energy scale of new physics introduced to make $c_{\alpha\beta}$ dimensionless. After EWSB this expression turns into a Majorana mass term for neutrinos

$$\begin{aligned}\mathcal{L} &\supset -\frac{c_{\alpha\beta}}{\Lambda}\langle H^0\rangle^2\left[\nu_L^\alpha \nu_L^\beta + \bar{\nu}_L^\alpha \bar{\nu}_L^\beta\right] \\ &:= -\frac{1}{2}\left(M_\nu\right)_{\alpha\beta}\left[\nu_L^\alpha \nu_L^\beta + \bar{\nu}_L^\alpha \bar{\nu}_L^\beta\right]\end{aligned} \tag{5.7.2}$$

with the Higgs vev $v = \langle H^0\rangle\sqrt{2} = 246.22$ GeV [28]. The neutrino mass matrix $\left(M_\nu\right)_{\alpha\beta}$ is then proportional to $1/\sqrt{\Lambda}$. As the $d = 5$ Weinberg operator has mass dimension 5, this term is non renormalizable and thus needs an UV completion. With new physics at high energy scales, the neutrino masses are automatically suppressed, hence the name seesaw mechanism. Assuming c_{α_β} of $\mathcal{O}(1)$, we find that new physics should occur at a mass scale of $\mathcal{O}(10^{15}$ GeV). Such mass scales for new physics coincide with the mass scales expected from grand unified theories. Loop realisations of the $d = 5$ operator can lower the mass scale of new physics to the TeV scale as $c_{\alpha\beta}$ is then small since it arises from a loop.

5.7.2 Seesaw Type I-III

There are three ways to realize the $d = 5$ Weinberg operator at tree level [79] called the seesaw mechanism type I-III. The seesaw type I requires three right handed neutrinos, singlets under SU(2), for three massive Standard Model neutrinos. With these right handed neutrinos N one can write down a Yukawa interaction

$$\mathcal{L} \supset -\, y_{\alpha i} L_\alpha H N_i + \text{H. c.} \tag{5.7.3}$$

which after EWSB turns into a Dirac mass term

$$\begin{aligned}\mathcal{L} &\supset -y_{\alpha i}\langle H^0\rangle\left[\nu_L^\alpha N_i + \bar{\nu}_L^\alpha \bar{N}_i\right] \\ &:= -\left(M_D\right)_{\alpha i}\left[\nu_L^\alpha N_i + \bar{\nu}_L^\alpha \bar{N}_i\right].\end{aligned} \tag{5.7.4}$$

As the right handed neutrinos have zero hypercharge and are singlets under all Standard model gauge groups, one can write down a Majorana mass term

$$\mathcal{L} \supset -\frac{1}{2}\left(M_M\right)_{ij}\left[N_i N_j + \bar{N}_i \bar{N}_j\right]. \tag{5.7.5}$$

Note that the Standard Model neutrinos cannot have a Majorana mass (before EWSB) as this would break SU(2) invariance explicitly. Putting this together into one (Majorana) mass matrix for both left as well as right handed neutrinos, we obtain

$$M = \begin{pmatrix} 0 & M_D^T \\ M_D & M_M \end{pmatrix}. \tag{5.7.6}$$

The diagonalization of such a 6×6 matrix is quite tedious. For illustrative purposes we now assume only one generation for both the left and right handed neutrinos. Then the matrix has eigenvalues

$$m_{1,2} = \frac{1}{2}\left[M_M \pm \sqrt{M_M^2 - 4M_D^2}\right] \tag{5.7.7}$$

which in the limit of $M_N \gg M_D$, keeping only the leading order, turns into

$$m_1 = M_M, \tag{5.7.8}$$

$$m_2 = \frac{M_D^2}{M_M}. \tag{5.7.9}$$

Note how one of the masses is suppressed which explains the smallness of the neutrino masses.

To realize the seesaw type II, a scalar triplet with hypercharge $Y = 1$ needs to be introduced. This triplet can obtain a naturally small vacuum exception value suppressed by the mass of the triplet [80]. Interactions with this vev generate Majorana neutrino masses. Note that only one triplet is required to generate three massive neutrinos.

Replacing the right handed neutrinos in the seesaw type I by a fermion triplets with zero hypercharge yields the seesaw type III. The mass suppression works similar to seesaw type I.

5.7.3 Radiative Seesaw

The $d = 5$ Weinberg operator can be realized not only at tree level, but also by loop corrections. The tree level contributions will dominate unless suppressed or forbidden. Assuming that there are no tree level contributions, the neutrino masses can be generated at loop level[10] which gives an additional suppression by the masses of the particles running in the loop. One loop realizations of the $d = 5$ operator allow for new physics at the electro weak scale making it accessible to current experiments. Such one loop realizations have been systematically studied in Ref. [10]. In order to have only loop contributions to the neutrino masses often a symmetry prohibiting the tree level seesaw is required. This symmetry could also be connected to the stability of dark matter. Radiative seesaw and the connection to dark matter is described in more detail in Chap. 6.

[10]Note that the neutrino loop diagrams must not be divergent as there are no tree level quantities in the Lagrangian that can absorb the divergences.

Minimal Models with radiative neutrino masses 6

The main goal of this thesis is to study minimal extensions of the Standard Model which can explain both the dark matter phenomenon as well as the smallness of neutrino masses. Following previous work [11], we require the number of new fields to be less than (or equal to) four to fulfill the minimality criterion. The neutrino masses are generated at one loop with the tree level contribution being forbidden by a $\mathbb{Z}_2$ symmetry. The case where the $\mathbb{Z}_2$ symmetry is promoted to a local $U(1)$ is considered in Chap. 10. In this chapter we give an overview of the models in general and discuss two models in detail.

6.1 Classification of minimal dark matter models with radiative neutrino masses

The possible realizations of the dimension 5 Weinberg operator at one loop are categorized in Ref. [10]. Ref. [11] gives a list of 35 models that, integrating out the new particles, yield the dimension 5 Weinberg operator and also contain viable dark matter candidates. The number of new fields is required to be maximally four with at least two being necessary to generate neutrino masses at loop level. All fields transform under the $SU(2)_L$ either trivially (singlets) or are in the fundamental (doublet) or adjoint (triplet) representation. All new particles are odd under a discrete $\mathbb{Z}_2$ symmetry with all standard model particles having an even charge. This symmetry forbids any vertex where one new particle couples to any number of Standard Model particles and therefore prevents tree level contributions to the neutrino masses as well as the decay of dark matter. In Ref. [11] they find four different topologies for the loops that give rise to neutrino masses. These topologies are shown in Fig. 6.1. The possible models are named after the neutrino topology with a roman letter (A,B,C...) appended for numeration. The neutrino masses are naturally small due to the suppression from the masses in the propagators. In contrast to

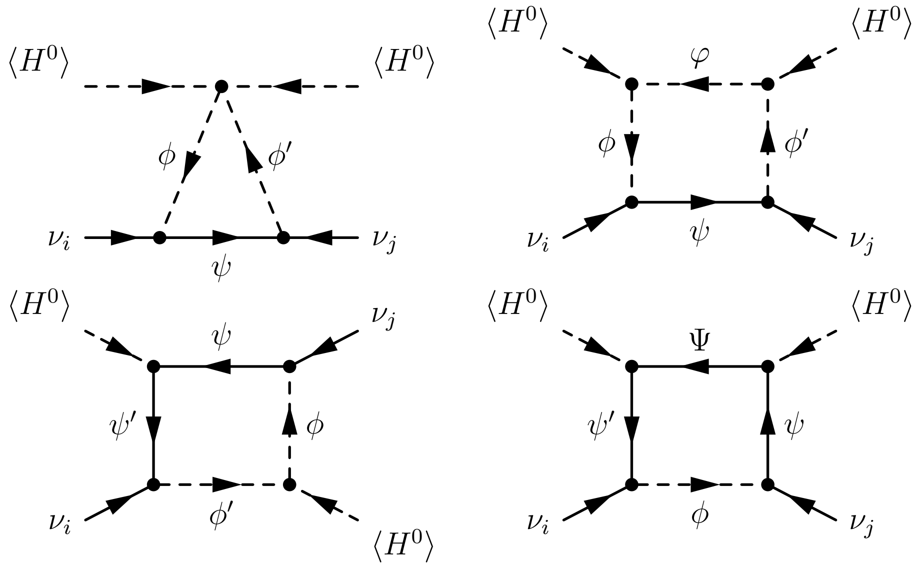

Figure 6.1: Topologies for neutrino mass generation at one loop. With the notation on Ref. [11] from left to right and top to bottom: T3, T1-1, T1-2 and T1-3 topology.

models with tree level seesaw where the right handed neutrinos must have a mass scale of $\mathcal{O}(10^{15}\text{ GeV})$, the radiative seesaw mechanism allows the masses of the new particles to be at electroweak scale making them accessible by current and near future experiments e.g. collider experiments such as the LHC and direct detection experiments such as XENON1T. The neutrino loop also allows for lepton flavor violating processes yielding a way to test them. The limits on the neutrino mass set e.g. by KATRIN and the mixing parameters known from neutrino oscillations can be taken into account by inverting the formula for the neutrino mass matrix obtained by the one loop calculation. This so called Casas-Ibarra parametrization yields a formula for the Yukawa couplings [81].

We will investigate the phenomenology of two specific models in this work. The remainder of this chapter is dedicated to describing those models in detail.

6.2 Scotogenic Model

The scotogenic model, proposed by Ernest Ma in 2006 [9], is the simplest and most famous of the minimal extensions described above. It explains neutrino

Table 6.1: Particle content of the scotogenic model.

Field	Generation	Spin	$\mathrm{U}(1)_Y \times \mathrm{SU}(2)_L \times \mathrm{SU}(3)_c$	$\mathbb{Z}_2$
η	1	0	$(\frac{1}{2}, 2, 1)$	-1
N	3	$\frac{1}{2}$	$(0, 1, 1)$	-1
SM particles	-	-	-	$+1$

masses with the T3 topology and dark matter while containing only two new fields. In Ref. [11] this model is denoted by T3-B with $\alpha = -1$. In this section we give a model description which interpolates the description given in our papers Refs. [1, 3].

6.2.1 Particle content

The scotogenic model extends the Standard Model by three generation of singlet fermion fields (right handed neutrinos) and one complex scalar $SU(2)_L$-doublet [9]. All new particles are odd under a $\mathbb{Z}_2$ symmetry whereas the Standard Model particles have an even charge (see Tab. 6.1). This implies that the lightest new particle, either a fermion or a scalar, must be stable. If this particle is electrically neutral, it is a Dark Matter candidate. The Lagrangian for the fermions reads

$$\mathcal{L}_N = -\frac{m_{N_i}}{2} N_i N_i + y_{i\alpha} (\eta L_\alpha) N_i + \text{H. c.}, \tag{6.2.1}$$

where L_α is the $SU(2)_L$-doublet for the α'th lepton generation. The fermions are defined in terms of Weyl spinors. The scalar potential is given by

$$\begin{aligned} V =& m_H^2 H^\dagger H + m_\eta^2 \eta^\dagger \eta + \frac{\lambda_1}{2} (H^\dagger H)^2 + \frac{\lambda_2}{2} (\eta^\dagger \eta)^2 + \lambda_3 (H^\dagger H)(\eta^\dagger \eta) \\ &+ \lambda_4 (H^\dagger \eta)(\eta^\dagger H) + \frac{\lambda_5}{2} \left[(H^\dagger \eta)^2 + (\eta^\dagger H)^2 \right]. \end{aligned} \tag{6.2.2}$$

H is the Standard Model Higgs-doublet. Therefore m_H and λ_1 are given by the Standard Model Higgs potential. We assume that η does not acquire a vev.[1] Thus λ_2 only induces self-interactions and has little effect on the

[1]Such a vev would break the $\mathbb{Z}_2$ symmetry and thus allow for dark matter decay and tree level seesaw.

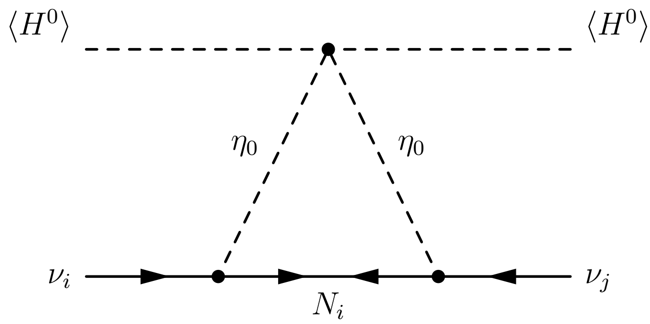

Figure 6.2: Neutrino mass generation in the scotogenic model.

phenomenology. After electroweak symmetry breaking, there are four scalar particles, the physical Standard Model Higgs boson, the charged component η^+ and the two neutral components $\eta^0 = (\eta_R + i\eta_I)/\sqrt{2}$ of the inert doublet. The masses are given by

$$m_{\eta^+}^2 = m_\eta^2 + \lambda_3 \langle H^0 \rangle^2, \tag{6.2.3}$$
$$m_R^2 = m_\eta^2 + (\lambda_3 + \lambda_4 + \lambda_5)\langle H^0 \rangle^2, \tag{6.2.4}$$
$$m_I^2 = m_\eta^2 + (\lambda_3 + \lambda_4 - \lambda_5)\langle H^0 \rangle^2, \tag{6.2.5}$$

where $\langle H^0 \rangle = \frac{v}{\sqrt{2}}$ with the Higgs vev $v = 246.22$ GeV [82]. To ensure that the vacuum is stable, the following conditions for the scalar couplings must be fulfilled [83]

$$\lambda_1 > 0, \quad \lambda_2 > 0, \quad \lambda_3 > -\sqrt{\lambda_1 \lambda_2}, \tag{6.2.6}$$
$$\lambda_3 + \lambda_4 - |\lambda_5| > -\sqrt{\lambda_1 \lambda_2}. \tag{6.2.7}$$

6.2.2 Neutrino masses

Neutrino masses are generated by the radiative seesaw mechanism via one-loop interactions with the Higgs vev (see Fig. 6.2). Tree-level contributions are forbidden by the $\mathbb{Z}_2$ symmetry. The neutrino mass matrix is then given by

$$(M_\nu)_{\alpha\beta} = \sum_{i=1}^{3} \frac{y_{i\alpha} y_{i\beta} m_{N_i}}{32\pi^2} \left[\frac{m_R^2}{m_R^2 - m_{N_i}^2} \log\left(\frac{m_R^2}{m_{N_i}^2}\right) - (R \to I) \right] \tag{6.2.8}$$
$$:= (y^T \Lambda y)_{\alpha\beta} \tag{6.2.9}$$

where we define the diagonal matrix Λ in the second equality. Note that this formula differs by a factor of $\frac{1}{2}$ from the original formula given in [9] as explained in [84]. If λ_5 were zero, the mass difference $m^2_{\eta_R} - m^2_{\eta_I} = 2\lambda_5\langle H^0\rangle$ would vanish and according to Eq. (6.2.8) there would be no neutrino masses. In this case, there would be a larger symmetry, since the Majorana masses of the neutrinos violate lepton number conservation. Therefore it is natural for λ_5 to be small. Expanding Eq. (6.2.8) for small λ_5, we obtain with $m_R^2 \approx m_I^2 \equiv m^2_{R,I}$

$$(M_\nu)_{\alpha\beta} \approx 2\lambda_5\langle H^0\rangle \sum_{i=1}^{3} \frac{y_{i\alpha}y_{i\beta}m_{N_i}}{32\pi^2(m^2_{R,I} - m^2_{N_i})}\left[1 + \frac{m^2_{N_i}}{m^2_{R,I} - m^2_{N_i}} \log\left(\frac{m^2_{N_i}}{m^2_{R,I}}\right)\right]. \tag{6.2.10}$$

Equation (6.2.8) is diagonalized by the PMNS matrix U_{PMNS},

$$\hat{m}_\nu = \text{diag}(m_{\nu_1}, m_{\nu_2}, m_{\nu_3}) = U_{\text{PMNS}} M_\nu U^T_{\text{PMNS}}. \tag{6.2.11}$$

The Yukawa matrix y can be calculated using the Casas-Ibarra parametrization [81]

$$y = \sqrt{\Lambda}^{-1} R\sqrt{\hat{m}_\nu} U^\dagger_{\text{PMNS}}, \tag{6.2.12}$$

where R is an orthogonal matrix.

6.2.3 Lepton flavor violation

The scotogenic model allows for LFV at one-loop level. The contributing diagrams leading to $l_\alpha \to l_\beta\gamma$ are shown in Fig. 6.3. For the process $l_\alpha \to 3l_\beta$ one has similar diagrams, but the photon decays into $l_\beta \bar{l}_\beta$. In addition one can replace the photon by a Z-boson. Moreover there are box diagrams and Higgs-penguins contributing to this process [85]. LFV tends to be an important constraint for the scotogenic model. Generally the most stringent limits come from the diagrams with $l_\alpha = \mu$ and $l_\beta = e$. The experimental constraints are discussed in Chap. 4 and Tab. 4.1 shows the current limit and future sensitivities for these processes. The impact of the current and future LFV limits has been studied in Refs. [85, 86].

6.2.4 Nucleon scattering

As described above, the scotogenic model can provide either a fermionic (N_i) or scalar (η_R, η_I) dark matter candidate, whichever is the lightest particle of

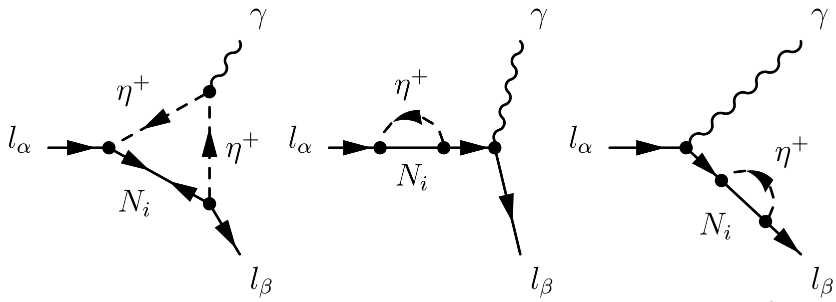

Figure 6.3: 1-loop Feynman diagrams leading to the lepton flavor violating process $l_\alpha \to l_\beta \gamma$.

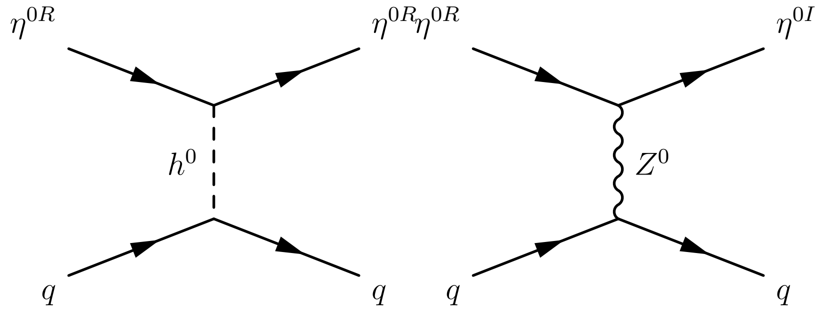

Figure 6.4: Feynman diagrams of the elastic (left) and inelastic (right) scalar dark matter-nucleon scattering processes in the scotogenic model. If η^{0I} is the dark matter candidate, η^{0R} and η^{0I} change their roles. For mass splittings larger than a few hundred keV, the right diagram is kinematically forbidden.

the $\mathbb{Z}_2$ odd sector. The fermionic dark matter candidate is a singlet under the Standard Model gauge group and thus does not give rise to dark matter-nucleon scattering cross sections, neither in the spin-dependent nor the spin-independent case rendering it undetectable for direct detection experiments. Scalar dark matter, on the other hand, has a non-zero spin-independent dark matter-nucleon cross section.

The diagrams for scalar dark matter scattering off nucleons are shown in Fig. 6.4. Usually these scattering processes are described by diagrams with the same in- and outgoing dark matter particle. This is the elastic case. However, as originally pointed out in Ref. [87], the existence of a slightly heavier state allows also for inelastic scattering of the dark matter particle, provided that the mass splitting between the two states $\delta = |m_{\eta^{0R}} - m_{\eta^{0I}}|$ fulfills

$$\delta < \frac{\mu v^2}{2}, \tag{6.2.13}$$

where μ is the WIMP nucleus reduced mass and v is the relative velocity.

Thus inelastic scattering with typical dark matter velocities is only possible for tiny mass splittings of $\mathcal{O}(100\ \text{keV})$. In the scotogenic model, the mass splitting between the neutral scalar components is governed by λ_5. Since λ_5 is naturally small (see above), the mass splitting is small as well and can be approximated by

$$\delta \approx \frac{\lambda_5 \langle \phi^0 \rangle^2}{m_{\eta^{0R,I}}}. \tag{6.2.14}$$

Therefore we need to consider the inelastic scattering case in addition to the "standard" elastic case. Note that the inelastic scattering is mediated by the Z^0 boson and thus governed by gauge couplings. Hence this process tends to give large scattering cross sections if kinematically allowed. The formalism for elastic and inelastic scattering of nucleons is described in detail in Chap. 8.

6.3 T1-3-B($\alpha = 0$)

The models in Ref. [11] contain a number of multiplets ranging from two to four. Fewer multiplets are generally more attractive as they introduce fewer unknown parameters. There are only two viable models with two new multiplets: The above described scotogenic model [9] and a modification of this model with a fermion triplet [88]. The next option is to add three multiplets to the Standard Model with 15 such models given in [11]. Four of these models allow for spin dependent scattering on nucleons while the corresponding dark matter candidate being not excluded by direct detection. We choose the model T1-3B($\alpha = 0$) for further investigation. This model has been studied before in Ref. [89]. The model description given in this section is based on our paper Ref. [2].

6.3.1 Particle content

The model T1-3-B extents the Standard Model by fermion singlet and doublet and scalar triplet fields. α denotes the hypercharge convention established in Ref. [11] and we use the model with $\alpha = 0$. The neutrino masses are generated via the T1-3 topology (see Fig. 6.1). The fields that are added to the Standard Model in this case are listed in Tab. 6.2. Componentwise these fields are given

Table 6.2: New fields in the model T1-3-B with $\alpha = 0$.

Field	Type	Generations	$\mathrm{U}(0)_Y \times \mathrm{SU}(2)_L \times \mathrm{SU}(3)_C$	$\mathbb{Z}_2$
Ψ	Majorana spinor	1	$(0, 1, 1)$	-1
ψ	Weyl spinor	1	$\left(\frac{1}{2}, 2, 1\right)$	-1
ψ'	Weyl spinor	1	$\left(-\frac{1}{2}, 2, 1\right)$	-1
ϕ	Real scalar	2	$(0, 3, 1)$	-1

by

$$\Psi = \Psi^0, \quad \psi = \begin{pmatrix} \psi^0 \\ \psi^- \end{pmatrix}, \quad \psi' = \begin{pmatrix} \psi'^+ \\ \psi'^0 \end{pmatrix}, \quad \phi_i = \begin{pmatrix} \frac{1}{\sqrt{2}}\phi_i^0 & \phi_i^+ \\ \phi_i^- & -\frac{1}{\sqrt{2}}\phi_i^0 \end{pmatrix}, \tag{6.3.1}$$

where the index i denotes the generations of the scalar triplet and the superscripts denote the electric charge. We assume only one generation for each fermion field. The scalar triplet has zero hypercharge and therefore its neutral component is a real scalar while the two charged components can, after EWSB, be combined to one charged field. The two fermion doublets form a vector-like doublet and we can build Dirac spinors as follows:

$$\psi_{\mathrm{D}}^0 = \begin{pmatrix} \psi^0 \\ \bar{\psi}'^0 \end{pmatrix}, \quad \psi_{\mathrm{D}}^- = \begin{pmatrix} \psi^- \\ \bar{\psi}'^+ \end{pmatrix}. \tag{6.3.2}$$

However, throughout this work we stick to using Weyl spinors instead of these Dirac spinors.

Following the notation of Refs. [89, 90], the Lagrangian of the model is given by

$$\begin{aligned} \mathcal{L} =& \mathcal{L}_{\mathrm{SM}} + \mathcal{L}_{\mathrm{kin}} - \frac{1}{2}(M_\phi^2)^{ij} Tr(\phi_i \phi_j) - \left(\frac{1}{2} M_\Psi \Psi\Psi + \mathrm{H.\ c.}\right) - (M_{\psi\psi'}\psi\psi' + \mathrm{H.\ c.}) \\ & - (\lambda_1)^{ij}(H^\dagger H) Tr(\phi_i\phi_j) - (\lambda_3)^{ijkm} Tr(\phi_i\phi_j\phi_k\phi_m) \\ & - \left(\lambda_4(H^\dagger\psi')\Psi + \mathrm{H.\ c.}\right) - (\lambda_5(H\psi)\Psi + \mathrm{H.\ c.}) - \left((\lambda_6)^{ij} L_i \phi_j \psi' + \mathrm{H.\ c.}\right). \end{aligned} \tag{6.3.3}$$

The λ_6 term couples the Standard Model leptons L_i to the new fields, which allows the neutrinos to obtain their masses. $M_\phi^2 > 0$ is required so that the scalar triplets do not aquire a vacuum expectation value (vev). Therefore the λ_3 term only induces self interactions which have no significant impact on the phenomenology. Hence λ_3 is set to zero in this work. The scalar triplets couple to the Standard Model Higgs H through the λ_1 term. The λ_4 and λ_5 terms are similar to Yukawa terms and link the new fermions to the Standard Model Higgs field. After electroweak symmetry breaking (EWSB) these terms will appear in the mass matrix of the fermions and induce mixing between the fermion singlet and the vector-like doublet.

To obtain the physical states (mass eigenstates), the mass matrices must be diagonalized. After EWSB, the mass matrix for the neutral fermions is given by

$$M_f = \begin{pmatrix} M_\Psi & \frac{\lambda_5 v}{\sqrt{2}} & \frac{\lambda_4 v}{\sqrt{2}} \\ \frac{\lambda_5 v}{\sqrt{2}} & 0 & M_{\psi\psi'} \\ \frac{\lambda_4 v}{\sqrt{2}} & M_{\psi\psi'} & 0 \end{pmatrix}, \tag{6.3.4}$$

and it is diagonalized by the unitary mixing matrix U_χ. This results in three Majorana mass eigenstates with masses $m_{\chi_i^0}$, given by

$$\begin{pmatrix} \chi_1^0 \\ \chi_2^0 \\ \chi_3^0 \end{pmatrix} = U_\chi \begin{pmatrix} \Psi^0 \\ \psi^0 \\ \psi'^0 \end{pmatrix}. \tag{6.3.5}$$

Due to the interaction of the scalar triplet with the Standard Model Higgs boson, the scalar mass matrix also obtains a contribution through EWSB

$$M_{\phi^0}^2 = M_{\phi^\pm}^2 = M_\phi^2 + \lambda_1 v^2. \tag{6.3.6}$$

The scalar mass matrix is diagonalized by O_η, which yields the squared masses of the scalar components $m^2_{\eta_i^{0,\pm}}$. The mass eigenstates are defined by

$$\begin{pmatrix} \eta_1^{0,\pm} \\ \eta_2^{0,\pm} \end{pmatrix} = O_\eta \begin{pmatrix} \phi_1^{0,\pm} \\ \phi_2^{0,\pm} \end{pmatrix}. \tag{6.3.7}$$

In this work we choose M_ϕ^2 and λ_1 to be diagonal and thus neglect mixing between the two generations of scalar particles, as this does not affect the phenomenology. Note that the neutral and charged components have equal masses at tree level. Loop corrections induce a mass splitting between both components, making the charged component 166 MeV heavier at one loop [91]. This ensures that the lightest scalar is always neutral and viable as a dark matter candidate.

6.3.2 Neutrino masses

The neutrino loop can be calculated analytically resulting in the following formula for the neutrino mass matrix:

$$\begin{aligned}(M_\nu)_{ij} &= \frac{1}{32\pi^2}\sum_{l=1}^{n_\mathrm{s}} \lambda_6^{im}\lambda_6^{jn}(O_\eta)_{ln}(O_\eta)_{lm}\sum_{k=1}^{n_\mathrm{f}}{(U_\chi)_{k3}^*}^2\frac{m_{\chi_k^0}^3}{m_{\eta_l^0}^2-m_{\chi_k^0}^2}\frac{m_{\chi_k^0}^2}{m_{\eta_l^0}^2}\\ &=: \frac{1}{32\pi^2}\sum_{l=1}^{n_\mathrm{s}}\lambda_6^{im}\lambda_6^{jn}(O_\eta)_{ln}(O_\eta)_{lm}\,A_l. \end{aligned} \tag{6.3.8}$$

Here, n_s is the number of neutral scalars and n_f is the number of neutral fermions. In our model with two generations of a real scalar triplet, $n_\mathrm{s} = 2$. This implies that the rank of the matrix $M_\nu \leq 2$. Thus this model only allows for two massive neutrinos. One could consider the case with three massive neutrinos, which requires a minimum of $n_\mathrm{s} = 3$. For our model with two massive neutrinos, Eq. (6.3.8) can be inverted leading to the Casas-Ibarra parameterization [81]

$$\lambda_6^{im} = U_{\mathrm{PMNS}}^{ij}\sqrt{m_{\nu_j}}R^{jl}\sqrt{A_l}^{-1}O_\eta^{lm}. \tag{6.3.9}$$

m_{ν_j} are the eigenvalues of the neutrino mass matrix M_ν, and U_PMNS the PMNS matrix [28]. R is a 3×2 matrix fulfilling the condition

$$RR^T = \begin{pmatrix} 0 & 0 & 0\\ 0 & 1 & 0\\ 0 & 0 & 1\end{pmatrix}, \tag{6.3.10}$$

meaning that R can be parameterized as

$$R = \begin{pmatrix} 0 & 0\\ \cos(\theta) & -\sin(\theta)\\ \sin(\theta) & \cos(\theta)\end{pmatrix} \tag{6.3.11}$$

by an angle θ, which is allowed to take any value between 0 and 2π.

6.3.3 Spin independent and spin dependent cross sections

Both dark matter candidates can scatter on nucleons and the cross sections can be tested by experiments. In Ref. [89] impact of current and future limits from XENON1T has been investigated.

Scalar dark matter can only scatter via the SI process through the Higgs boson. Contributions with a Z^0-boson as mediator are not present here, resulting in a lower cross section. As we will show later, this has a clear effect on the IceCube event rate. For fermionic dark matter there is one diagram contributing to the SI and SD cross sections each [27]. The diagram for spin (in)dependent scattering is a t-channel diagram with a (Higgs-) Z^0-boson as mediator. Scattering processes through s-channel diagrams are not possible, since none of the new particles couples to quarks. As it turns out, the SI and SD cross sections are correlated with each other, as both are dependent on the mixing between the fermion singlet and doublet, governed by λ_4 and λ_5. We will now discuss the explicit Feynman rules for the dark matter-mediator vertices as well as the impact of singlet-doublet mixing on the cross sections.

The spin (in)dependent cross sections mainly depend on the three point vertex between two dark matter particles and the (Higgs-) Z^0-boson. We focus on the fermion dark matter case since the spin dependent cross section for a scalar triplet is always zero and its coupling to the Higgs boson is given by λ_1. The vertices for the mass eigenstates of the fermions can be calculated by SARAH [72, 73]:

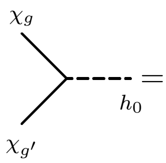

$$
\begin{aligned}
= &-\frac{1}{\sqrt{2}} i \left\{ (U_\chi)^*_{g1} \left[\lambda_4 (U_\chi)^*_{g'3} + \lambda_5 (U_\chi)^*_{g'2} \right] + \lambda_4 (U_\chi)^*_{g3} (U_\chi)^*_{g'1} + \right. \\
&\left. + \lambda_5 (U_\chi)^*_{g2} (U_\chi)^*_{g'1} \right\} P_\mathrm{L} \\
&- \frac{1}{\sqrt{2}} i \left\{ (U_\chi)_{g1} \left[\lambda_4 (U_\chi)_{g'3} + \lambda_5 (U_\chi)_{g'2} \right] + \lambda_4 (U_\chi)_{g3} (U_\chi)_{g'1} + \right. \\
&\left. + \lambda_5 (U_\chi)_{g2} (U_\chi)_{g'1} \right\} P_\mathrm{R}, \qquad (6.3.12)
\end{aligned}
$$

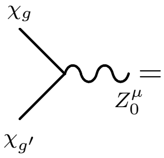

$$= -\frac{1}{2} i \left[g_1 \sin(\theta_{\mathrm{W}}) + g_2 \cos(\theta_{\mathrm{W}}) \right] \left[(U_\chi)_{g2} (U_\chi)^*_{g'2} - (U_\chi)_{g3} (U_\chi)^*_{g'3} \right] \gamma^\mu P_{\mathrm{L}}$$
$$+ \frac{1}{2} i \left[g_1 \sin(\theta_{\mathrm{W}}) + g_2 \cos(\theta_{\mathrm{W}}) \right] \left[(U_\chi)_{g'2} (U_\chi)^*_{g2} - (U_\chi)_{g'3} (U_\chi)^*_{g3} \right] \gamma^\mu P_{\mathrm{R}}. \tag{6.3.13}$$

Since the three mass eigenstates are generally not mass degenerate, only the elastic case where $g = g'$, with χ_g being dark matter, contributes to the spin (in)dependent cross section. Both vertices depend on the mixing matrix U_χ between the fermion singlet and doublet. Since the singlet-doublet mixing is induced by $\lambda_{4,5}$ as can be seen from the fermionic mass matrix in Eq. (6.3.4), the mixing matrix U_χ depends on $\lambda_{4,5}$.

Diagonalizing the fermionic mass matrix proves to be difficult and gives quite unwieldy results. We can however, expand the problem for small λ_4,

$$M_f = M_0 + \lambda_4 M_\lambda = \begin{pmatrix} M_\Psi & 0 & 0 \\ 0 & 0 & M_{\psi\psi'} \\ 0 & M_{\psi\psi'} & 0 \end{pmatrix} + \lambda_4 \begin{pmatrix} 0 & \frac{\tilde{\lambda} v}{\sqrt{2}} & \frac{v}{\sqrt{2}} \\ \frac{\tilde{\lambda} v}{\sqrt{2}} & 0 & 0 \\ \frac{v}{\sqrt{2}} & 0 & 0 \end{pmatrix} \tag{6.3.14}$$

and then (keeping $\tilde{\lambda} = \frac{\lambda_5}{\lambda_4}$ fixed) use perturbation theory to diagonalize this matrix approximately.[2] At second order in λ_4 we obtain for the mixing matrix

[2]Time independent perturbation theory from quantum mechanics is basically a recipe for approximate matrix diagonalization.

$$
\begin{aligned}
U_\chi = &\begin{pmatrix} 1 & 0 & 0 \\ 0 & -\frac{1}{\sqrt{2}} & \frac{1}{\sqrt{2}} \\ 0 & \frac{1}{\sqrt{2}} & \frac{1}{\sqrt{2}} \end{pmatrix} + \\
&\begin{pmatrix} 0 & -\frac{(\lambda_4-\lambda_5)v}{2(M_\Psi+M_{\psi\psi'})} & -\frac{(\lambda_4+\lambda_5)v}{2(M_\Psi-M_{\psi\psi'})} \\ \frac{\left(\lambda_4 M_{\psi\psi'}+\lambda_5 M_\Psi\right)v}{\sqrt{2}(M_\Psi-M_{\psi\psi'})(M_\Psi+M_{\psi\psi'})} & 0 & 0 \\ \frac{\left(\lambda_4 M_\Psi+\lambda_5 M_{\psi\psi'}\right)v}{\sqrt{2}(M_\Psi-M_{\psi\psi'})(M_\Psi+M_{\psi\psi'})} & 0 & 0 \end{pmatrix} + \qquad (6.3.15) \\
&\begin{pmatrix} \frac{\frac{\lambda_5^2+\lambda_4^2}{4}\left(M_\Psi^2+M_{\psi\psi'}^2\right)+\lambda_4\lambda_5 M_\Psi M_{\psi\psi'}}{(M_\Psi-M_{\psi\psi'})^2(M_\Psi+M_{\psi\psi'})^2} & 0 & 0 \\ 0 & \frac{\left(\lambda_4^2-\lambda_5^2\right)\frac{M_\Psi}{2M_{\psi\psi'}}+\lambda_4(\lambda_4-\lambda_5)}{4\sqrt{2}\left(M_\Psi+M_{\psi\psi'}\right)^2} & \frac{\left(\lambda_4^2-\lambda_5^2\right)\frac{M_\Psi}{2M_{\psi\psi'}}-\lambda_4(\lambda_4+\lambda_5)}{4\sqrt{2}\left(M_\Psi-M_{\psi\psi'}\right)^2} \\ 0 & \frac{\left(\lambda_4^2-\lambda_5^2\right)\frac{M_\Psi}{2M_{\psi\psi'}}+\lambda_5(\lambda_4-\lambda_5)}{4\sqrt{2}\left(M_\Psi+M_{\psi\psi'}\right)^2} & \frac{\left(\lambda_5^2-\lambda_4^2\right)\frac{M_\Psi}{2M_{\psi\psi'}}-\lambda_5(\lambda_5+\lambda_4)}{4\sqrt{2}\left(M_\Psi-M_{\psi\psi'}\right)^2} \end{pmatrix} v^2
\end{aligned}
$$

and for the diagonalized mass matrix

$$
\begin{pmatrix} M_\Psi + \frac{v^2\left(\lambda_5^2 M_\Psi+2\lambda_4\lambda_5 M_{\psi\psi'}+\lambda_4^2 M_\Psi\right)}{2(M_\Psi-M_{\psi\psi'})(M_\Psi+M_{\psi\psi'})} & 0 & 0 \\ 0 & -M_{\psi\psi'} - \frac{(\lambda_4-\lambda_5)^2 v^2}{2(M_\Psi+M_{\psi\psi'})} & 0 \\ 0 & 0 & M_{\psi\psi'} - \frac{(\lambda_4+\lambda_5)^2 v^2}{2(M_\Psi-M_{\psi\psi'})} \end{pmatrix}. \qquad (6.3.16)
$$

One can see that in the case $M_\Psi < M_{\psi\psi'}$ (assuming $\lambda_{4,5}^2 v^2 < M_{\psi\psi'}^2 - M_\Psi^2$) [3], χ_1 is the lightest fermion whereas in the case $M_{\psi\psi'} < M_\Psi$, χ_3 is the lightest one. Now we can use the result for U_χ to calculate how the vertices depend on $\lambda_{4,5}$ and the mass parameters $M_\Psi, M_{\psi\psi'}$. We expand the results again for small $\lambda_{4,5}$, omitting all terms that contain higher orders than λ_4^2, λ_5^2 or $\lambda_4\lambda_5$.

[3] Otherwise a more careful analysis is required. E.g. if $\lambda_4\lambda_5 > 0$ or $\lambda_{4,5} < \lambda_{5,4}\frac{M_\Psi}{M_{\psi\psi'}}$, the statement above is also true.

The results are:

$$\chi_1\chi_1 h^0: \quad -\frac{iv\left(M_\Psi\lambda_5^2 + 2M_{\psi\psi'}\lambda_5\lambda_4 + M_\Psi\lambda_4^2\right)}{M_\Psi^2 - M_{\psi\psi'}^2} + \mathcal{O}\left(\lambda_{4,5}^3\right), \tag{6.3.17}$$

$$\chi_2\chi_2 h^0: \quad \frac{iv\left(\lambda_4 - \lambda_5\right)^2}{2(M_\Psi + M_{\psi\psi'})} + \mathcal{O}\left(\lambda_{4,5}^3\right), \tag{6.3.18}$$

$$\chi_3\chi_3 h^0: \quad \frac{iv\left(\lambda_4 + \lambda_5\right)^2}{2(M_\Psi - M_{\psi\psi'})} + \mathcal{O}\left(\lambda_{4,5}^3\right), \tag{6.3.19}$$

$$\chi_1\chi_1 Z_0^\mu: \quad \left[g_1\sin(\theta_\mathrm{W}) + g_2\cos(\theta_\mathrm{W})\right]\frac{iv^2}{4\left(M_\Psi^2 - M_{\psi\psi'}^2\right)}\times \\ \times\left(\lambda_4^2 - \lambda_5^2\right)\gamma^5\gamma^\mu + \mathcal{O}\left(\lambda_{4,5}^3\right), \tag{6.3.20}$$

$$\chi_2\chi_2 Z_0^\mu: \quad \left[g_1\sin(\theta_\mathrm{W}) + g_2\cos(\theta_\mathrm{W})\right]\frac{-iv^2}{8M_{\psi\psi'}(M_\Psi + M_{\psi\psi'})}\times \\ \times\left(\lambda_4^2 - \lambda_5^2\right)\gamma^5\gamma^\mu + \mathcal{O}\left(\lambda_{4,5}^3\right), \tag{6.3.21}$$

$$\chi_3\chi_3 Z_0^\mu: \quad \left[g_1\sin(\theta_\mathrm{W}) + g_2\cos(\theta_\mathrm{W})\right]\frac{iv^2}{8M_{\psi\psi'}(M_\Psi - M_{\psi\psi'})}\times \\ \times\left(\lambda_4^2 - \lambda_5^2\right)\gamma^5\gamma^\mu + \mathcal{O}\left(\lambda_{4,5}^3\right). \tag{6.3.22}$$

We include the vertices for χ_2 even though χ_2 is never the lightest fermion and thus not abundant. The spin dependent cross section becomes zero if $|\lambda_4| = |\lambda_5|$. If χ_3 is the dark matter candidate, then the spin independent cross section vanishes for $\lambda_4 = -\lambda_5$. For χ_1 the spin independent cross section vanishes for $\lambda_4 = \lambda_5\left(\pm\sqrt{\left(\frac{M_{\psi\psi'}}{M_\Psi}\right) - 1} - \frac{M_{\psi\psi'}}{M_\Psi}\right)$. We can compare these results with the cross sections calculated by SPheno 4.0.3 [92, 93] and micrOMEGAs 5.0.8 [94]. Fig. 6.5 shows the numerical results and our rescaled vertex factors squared. For χ_3 the results agree remarkably well. For χ_1 the qualitative behavior is the same, but we see some deviations, which become larger for larger $|\lambda_4|$. This is not surprising since we expanded the vertex factors for small $\lambda_{4,5}$ and thus our formulas are only correct for $\lambda_{4,5}^2 \ll 1$.

From Eqs. (6.3.17)-(6.3.22) it is clear that, except from special cases such as $|\lambda_4| = |\lambda_5|$, both cross sections scale with the larger of the two Yukawa couplings $\lambda_{4,5}$. This yields a correlation between the spin dependent and spin independent cross section. This correlation can be made explicit using the data from the scan described in in Chap. 9 as shown in Fig. 6.6. Note that this data contains points from a random scan over the entire parameter space and no special relation between the parameters is enforced. The points scatter

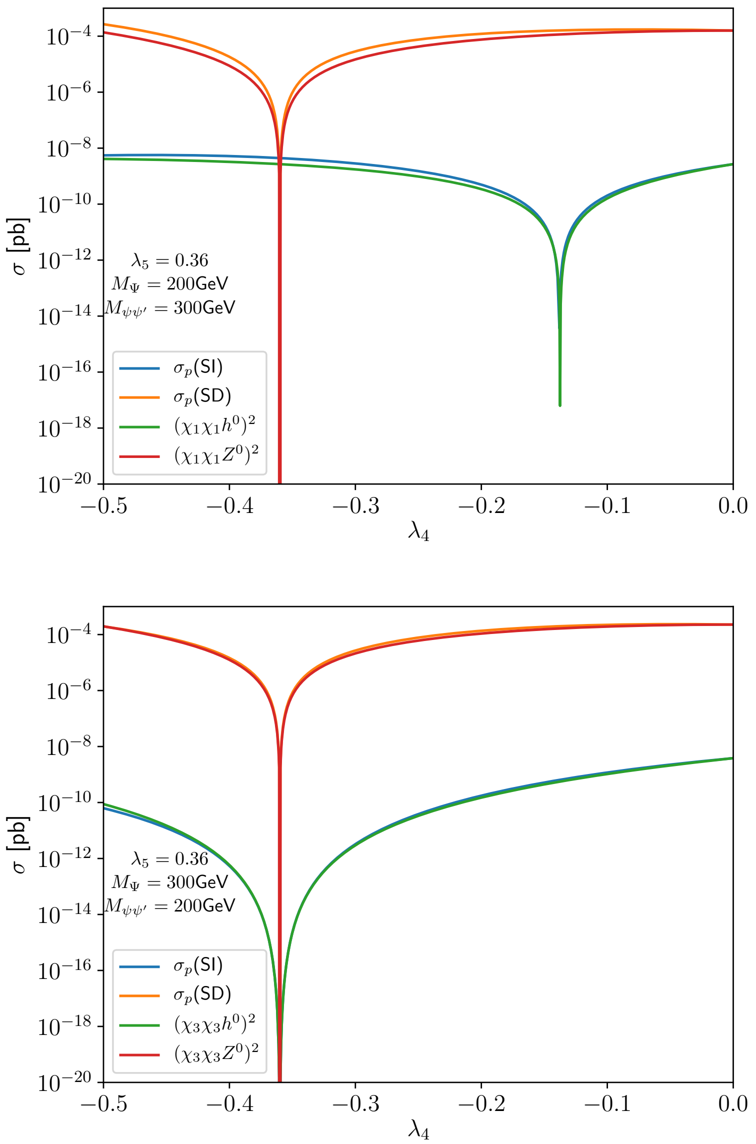

Figure 6.5: Spin dependent (orange) and independent (blue) cross sections calculated numerically and the vertex factors squared (red and blue) for both χ_1 (top) and χ_3 (buttom) as dark matter. The vertex factors have been rescaled so they agree with the cross sections at $\lambda_4 = 0$. The scalar singlet has been decoupled by setting $m_\phi = 10\,\text{TeV}$ and λ_1 has been set to zero (cf. Ref. [90], Fig. 7.1).

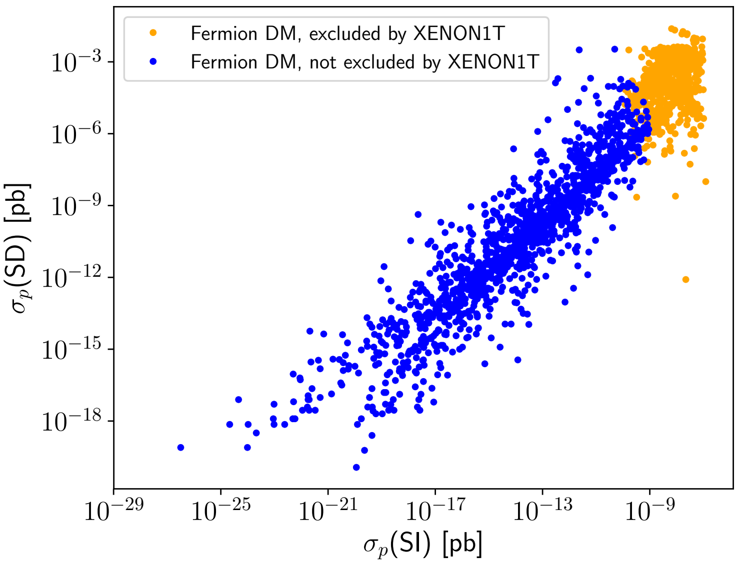

Figure 6.6: Dependence of the spin dependent cross section on the spin independent cross section using the data from Chap. 9.

around a linear relation. In (finetuned) scenarios where the correlation is lifted, the points depart from the points following the linear relation. This relation explains how the limits on the spin independent cross section set by XENON1T also indirectly restrict the spin dependent cross section. Note that the derivation for the vertices is independent of the dark scalar sector and the neutrino loop and our results thus are true for general models with singlet-doublet mixing.

7 Absolute neutrino mass in the scotogenic model

In this chapter we investigate the phenomenology of the scotogenic model introduced in Sec. 6.2. We focus on the case where the fermion singlet is the dark matter candidate and investigate how the absolute neutrino mass influences the parameter space and observables. Scalar dark matter yields a different phenomenology. This chapter extends the results published in our paper Ref. [1] which was created in joint work together with *Sybrand Zeinstra, Caroline Rodenbeck* and *Michael Klasen*.

7.1 Motivation

In the scotogenic model, the Standard Model neutrinos ν obtain mass by one loop contributions arising from a dark sector odd under a discrete $\mathbb{Z}_2$ symmetry, which contains one additional scalar doublet η and (for three massive Standard Model neutrinos) three generations of fermion singlets N_i (sterile neutrinos with $i = 1, 2, 3$) [9]. The parameter space is therefore much smaller than, e.g., the one of supersymmetry and can be better constrained with neutrino oscillation data via the Casas-Ibarra method [81], limits on lepton flavor violation (LFV) [85], and measurements of the dark matter relic density [86]. Nevertheless, these previous analyses found that the dark scalar/fermion masses as well as their scalar and Yukawa couplings could still vary over several orders of magnitude.

We scan over the parameter space and demonstrate that a determination of the absolute electron neutrino mass, which has now come into reach, will provide additional stringent constraints on the dark sector of the scotogenic model in a way that is almost independent of the neutrino hierarchy and CP phase. In particular, we determine the linear relation between the absolute electron neutrino mass and the scalar coupling associated with the mass splitting of the dark neutral scalars. This linear dependence induces correlations among the other parameters of the model, i.e. the dark matter and scalar masses and their Yukawa couplings, which we can also quantify. Together, current neutrino mass and future LFV experiments can then probe almost the entire fermion dark matter parameter space.

7.2 Experimental constraints

The scotogenic model can be tested with a number of experiments. We require our parameter points to yield a phenomenology that is in compliance with current experiments.

Lepton flavor violating processes, forbidden in the standard model, occur in the scotogenic model (see Sec. 6.2). The experimental situation for LFV is discussed in Chap. 4 and we impose the current limits on the branching ratios BR($\mu \to e\gamma$), BR($\mu \to 3e$) and the conversion rate CR($\mu - e$,Ti) given in Tab. 4.1.

The dark matter relic density measured by Planck is $\Omega h^2 = 0.12 \pm 0.001$ [16]. We allow a theoretical uncertainty of 0.02 to account for theoretical and numerical uncertainties. In the standard freeze in scenario, the relic density results from dark matter annihilation in the early Universe.

The neutrino masses and mixing parameter constrain the parameter space of the scotogenic model through the Casas-Ibarra parametrization given in Eq. (6.2.8). KATRIN has recently published a new upper limit on the electron neutrino mass of 1.1 eV [8] and ultimately aims for a sensitivity of 0.2 eV [54]. Assuming Normal Hierarchy and the ΛCDM cosmological constraints impose an upper limit on the sum of the neutrino masses $\sum_i m_{\nu_i} < 0.12$ eV [55] whereas the minimal value from neutrino oscillation is $\sum_i m_{\nu_i} < 0.06$ eV [16]. In addition the neutrino mass differences and mixing angles, for which we use the 3σ ranges [51], enter the Casas-Ibarra parametrization.

7.3 Numerical results

In this section we study how the experimental constraints limit the parameter space of the scotogenic model. We sample the lightest neutrino mass and use the mass differences [51] to calculate the masses of the remaining neutrinos. The orthogonal matrix R in the Casas-Ibarra parametrization is parametrized by three random angles $0 < \theta_i < 2\pi$. Unless specifically mentioned otherwise, the CP violating phase is set to zero $\delta_{CP} = 0$. We impose a pertubativity limit on the Yukawa and dark sector-Higgs couplings and the Yukawa couplings $|\lambda_{3,4}|, |y_{i\alpha}|^2 < 4\pi$. We use the Casas-Ibarra parametrization to calculate the Yukawa couplings and then calculate the branching ratios (BRs) and conversion rates (CRs) with SPHENO 4.0.3 [92, 93] and the relic density with MICROMEGAS 5.0.8 [94]. The required model files have been generated with SARAH-4.13.0 [73].

7.3.1 Fermionic dark matter without CP-Violation

The scalar coupling λ_5 affects both the LFV processes as well as the relic density. Larger values of λ_5 increase the relic density and suppress LFV. This can be seen in Fig. 7.1. Increasing the neutrino mass has the opposite effect. This is true for both Normal and Inverted Hierarchy. From Eq. (6.2.10), it can be seen that for fixed masses increasing λ_5 decreases the Yukawa couplings. Similarly for increasing neutrino masses, the couplings increase. The main dark matter annihilation processes are topologically similar to the loop diagram Fig. 6.2 when cut on the internal fermion line and therefore the cross section scales with the Yukawa couplings. The LFV processes scale with the Yukawa coupling as well, as apparent from Fig. 6.3. Hence there is an interplay between the observables, the neutrino mass and λ_5. This interplay still holds, when one varies the masses of the new particles and all scalar couplings as we will show next.

We scan over the entire parameter space of the scotogenic model in the following ranges

$$100 \text{ GeV} < M_i < 10 \text{ TeV}, \tag{7.3.1}$$

$$100 \text{ GeV} < m_\eta < 10 \text{ TeV}, \tag{7.3.2}$$

$$\lambda_2 = 0.5, \tag{7.3.3}$$

$$|\lambda_{3,4}| < 4\pi, \tag{7.3.4}$$

$$10^{-12} < |\lambda_5| < 10^{-08}, \tag{7.3.5}$$

$$4 \cdot 10^{-3} < m_{\nu_{1,3}} < 2 \text{ eV}. \tag{7.3.6}$$

Collider searches require the scalar masses to be above 100 GeV [49]. For most of the parameter space the scalar masses dominate over $\langle H^0 \rangle$ and therefore

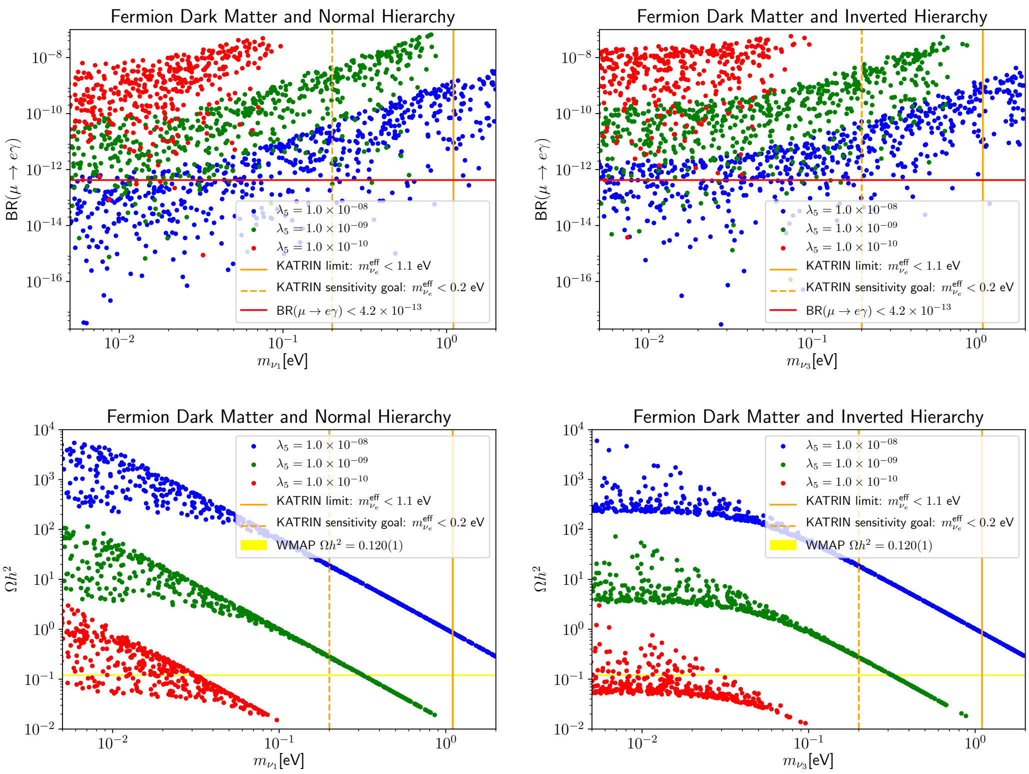

Figure 7.1: Dependence of the BR($\mu \to e\gamma$) (top) and relic density (bottom) on the lightest neutrino mass. Vertical lines show the current limits on the neutrino masses set by KATRIN (solid orange line) and sensitivity goal of KATRIN (dashed orange line). Left for NH and right for IH. The masses of the right handed neutrinos have been set to $m_{N_i} = [1, 4, 8]$ TeV, the scalar mass to $m_\eta = 2$ TeV and the scalar couplings to $\lambda_3 = 0.5$ and $\lambda_4 = -0.5$.

the scalar particles are all close in mass. As mentioned earlier, λ_2 only induces self interactions an has little effect on the phenomenology. Therefore we can fix it to one value without loosing generality. We require coannihilations to contribute less than 1% since they require a unexplained degeneracy of the masses. Generally coannihilations alter the phenomenology resulting i.e. in smaller BRs for LFV as shown in [86].

We find that for NH there are viable models for any neutrino mass in our range. For IH there there are no model with $m_{\nu_3} \lesssim 1 \cdot 10^{-2}$ eV. This is mostly related to the relatively small statistics for the models that meet all

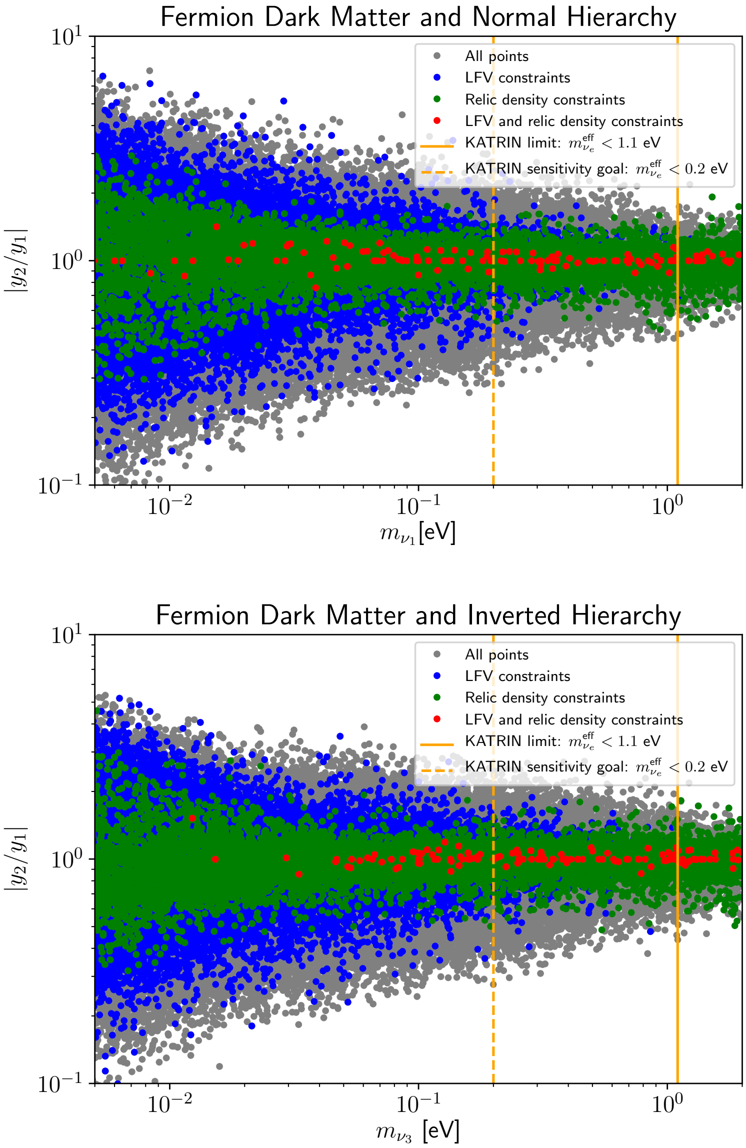

Figure 7.2: Ratio of the eigenvalues of the Yukawa matrix as a function of the lightest neutrino mass with neutrino mass differences and mixing (grey), current LFV constraints (blue), yielding the right relic density (green). The red point fulfill all experimental constraints. Vertical lines show the current limits on the (effective) electron neutrino mass set by KATRIN (solid orange line) and sensitivity goal of KATRIN (dashed orange line). Left for normal hierarchy and right for inverted hierarchy.

experimental constraints (see Fig. 7.2 and 7.3). In addition for both hierarchies the number of valid models decreases for $m_{\nu_{1,3}} \lesssim 5 \cdot 10^{-2}$ eV.

In case of large m_{ν_1} the neutrino mass differences play only small role resulting in nearly degenerate neutrino masses. This leads to the same eigenvalues of the Yukawa matrix as can be seen in Fig. 7.2. The ratio $|y_2/y_1|$ varies only slightly at large $m_{\nu_{1,3}}$ and over two orders of magnitude for small neutrino masses. LFV processes impose upper limits on both Yukawa eigenvalues and limit the ratio further. The relic density constraint requires the coupling to be not too small. This results that the combination of all constraints leads to $|y_2/y_1| \approx 1$. We have checked that this is true for all possible ratios of eigenvalues of the Yukawa matrix.

In Eq. (6.2.10) there is a linear dependence between the neutrino mass matrix M_ν and λ_5. If the lightest neutrino mass dominates over the mass differences, the neutrino mass matrix is approximately diagonal (since all eigenvalues are the same) and the dependence reduces to a linear relation between $m_{\nu_{1,3}}$ and λ_5. The slope of this linear relation depends on the masses of the new particles and the Yukawa couplings which are both varied in the scan. This dependence reemerges in a scan over the entire parameter space once one imposes the relic density constraint as can be seen in Fig. 7.3. For small neutrino masses the mass differences play an important role and therefore the dependence changes, giving a wider constant band. Since the LFV constraints require small Yukawa couplings and thus larger λ_5, the point fulfilling both constraints are on the upper range of this band. For these points λ_5 is a constant. We fit a linear function for large neutrino masses and a constant for small $m_{\nu_{1,3}}$ to the points fulfilling all constraints. At 90% C.L. we obtain

$$|\lambda_5| = \begin{cases} 1.6 \pm 0.7 \cdot 10^{-10} & \text{for } m_{\nu_1} < 0.052 \text{ eV} \\ 3.08 \pm 0.05 \cdot 10^{-9} m_{\nu_1} \text{ eV}^{-1} & \text{for } m_{\nu_1} > 0.052 \text{ eV} \end{cases} \tag{7.3.7}$$

for NH and

$$|\lambda_5| = \begin{cases} 1.7 \pm 1.5 \cdot 10^{-10} & \text{for } m_{\nu_3} < 0.056 \text{ eV} \\ 3.11 \pm 0.06 \cdot 10^{-9} m_{\nu_3} \text{ eV}^{-1} & \text{for } m_{\nu_3} > 0.056 \text{ eV} \end{cases} \tag{7.3.8}$$

for IH. Thus, once the absolute neutrino mass scale is known we can predict the dark sector-Higgs coupling λ_5. The sign of λ_5 is arbitrary.

We will now focus on the points that meet all constraints. For these points $m_{\nu_{1,3}}/|\lambda_5|$ is constant. Thus the Yukawa couplings become correlated with the

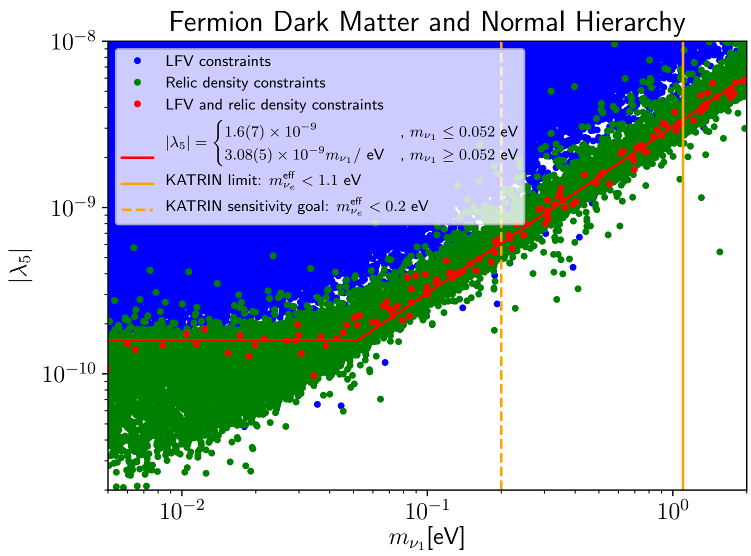

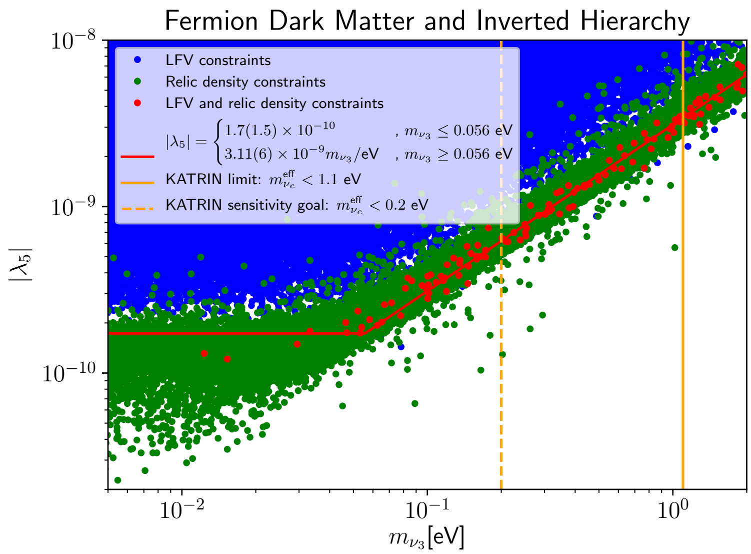

Figure 7.3: The dark sector-Higgs coupling $|\lambda_5|$ as a function of the lightest neutrino mass. The blue points fulfill the current LFV constraints, the green point yield the right relic density and the red point fulfill all experimental constraints. Vertical lines show the current limits on the (effective) electron neutrino mass set by KATRIN (solid orange line) and sensitivity goal of KATRIN (dashed orange line). Left for normal hierarchy and right for inverted hierarchy.

masses of the new particles. All tree level dark matter annihilation processes involve a dark sector scalar in the t-channel. Thus for scalar masses much larger than the dark matter mass, the annihilation processes are suppressed. On the other hand, if the scalar particle has a mass too close to the dark matter mass, there will be coannihilations and we disregard all points with coannihilations. From Fig. 7.4 it is apparent, that the ratio $m_{R,I}/m_{N_i} \sim 1.5$. With this ratio fixed and assuming a diagonal Yukawa matrix (since all eigenvalues are the same) $m_{\nu_{1,3}}/|\lambda_5|$ becomes proportional to $|y_1|^2/m_{N_1}$ as can be seen from Eq. (6.2.10) when neglecting $|y_{2,3}|^2/m_{N_{2,3}}$ since we can assume $m_{N_1} \ll m_{N_{2,3}}$. This is just a rough assessment of the relation, so we do not expect the points to follow this dependence very closely. Remembering that $m_{\nu_{1,3}}/|\lambda_5|$ is constant, we fit this dependence obtaining at 90% CL

$$|y_1| = \begin{cases} 0.078 \pm 0.021\sqrt{m_{N_1}/\text{ GeV}} & \text{for NH} \\ 0.081 \pm 0.012\sqrt{m_{N_1}/\text{ GeV}} & \text{for IH} \end{cases} . \tag{7.3.9}$$

The points and fit are shown in Fig. 7.4. This finding allows us to predict the Yukawa couplings and the scalar masses, if the dark matter mass is known.

The parameter space of the scotogenic model will be almost completely tested with future experiments on LFV and the absolute neutrino mass, as can be seen in Fig. 7.5. Currently the limit on BR($\mu \to e\gamma$) imposes a stronger bound than BR($\mu \to 3e$). With future sensitivities this is expected to change (see Tab. 4.1). The future limits will restrict the parameter space considerably. If the neutrino masses indeed reach into the cosmological favoured region of $\sum_i m_{\nu_i} < 0.12$ eV, they will restrict the parameter space in an orthogonal way, excluding, in combination with the future BR($\mu \to 3e$) limit, almost the entire parameter space.

7.3.2 Fermionic dark matter with CP-Violation

The T2K experiment has published the finding of CP-Violation at 95% CL in the weak sector [52]. We now want to find out how the CP violating phase δ_{CP} affects our findings. Figure 7.6 shows the relic density as a function of δ_{CP}. The masses of the three right handed neutrinos have been set to $m_{N_i} = [1, 4, 8]$ TeV, the scalar mass to $m_\eta = 2$ TeV and the scalar couplings to $\lambda_3 = 2$, $\lambda_4 = 3$ and $\lambda_5 = 1 \cdot 10^9$. In addition, we have set $m_{\nu_{1,3}} = 0.315$ eV. We see that the relic density in fact changes, when δ_{CP} is varied. The CP phase has no effect

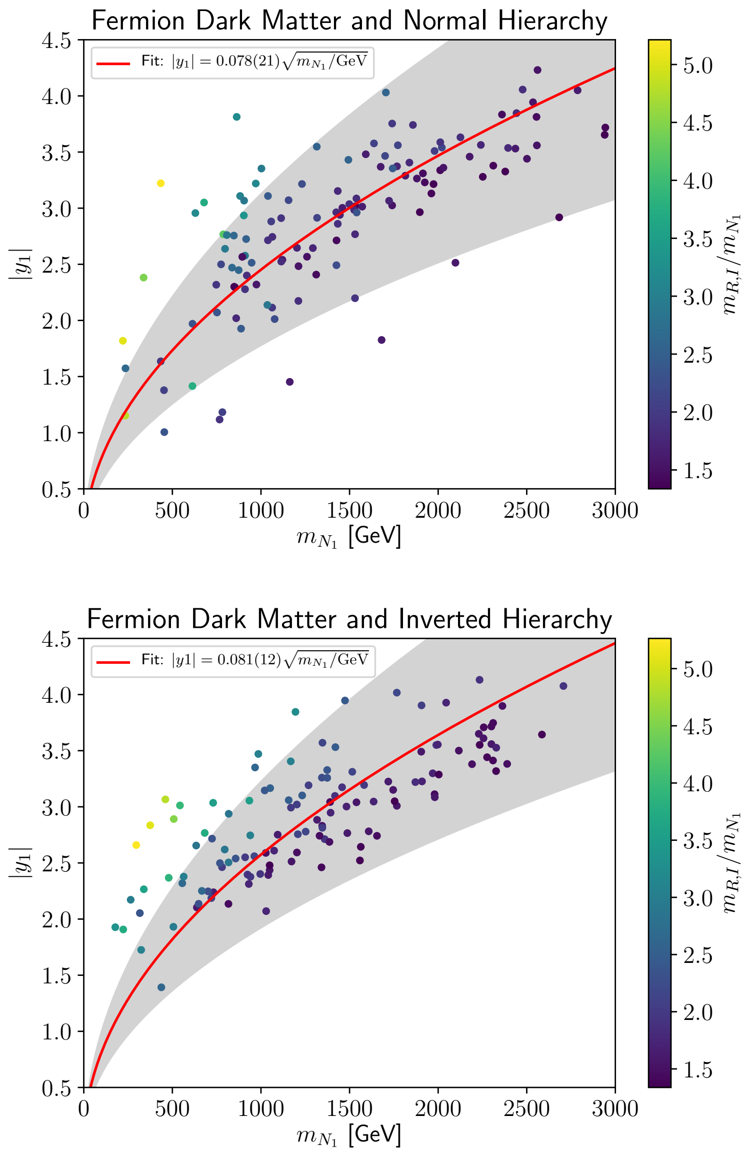

Figure 7.4: The first eigenvalue of the Yukawa matrix as a function of the dark matter mass. Ratio of neutral scalar masses to dark matter mass are given on the temperature scale. The points fulfill all experimental constraints. Left for normal hierarchy and right for inverted hierarchy.

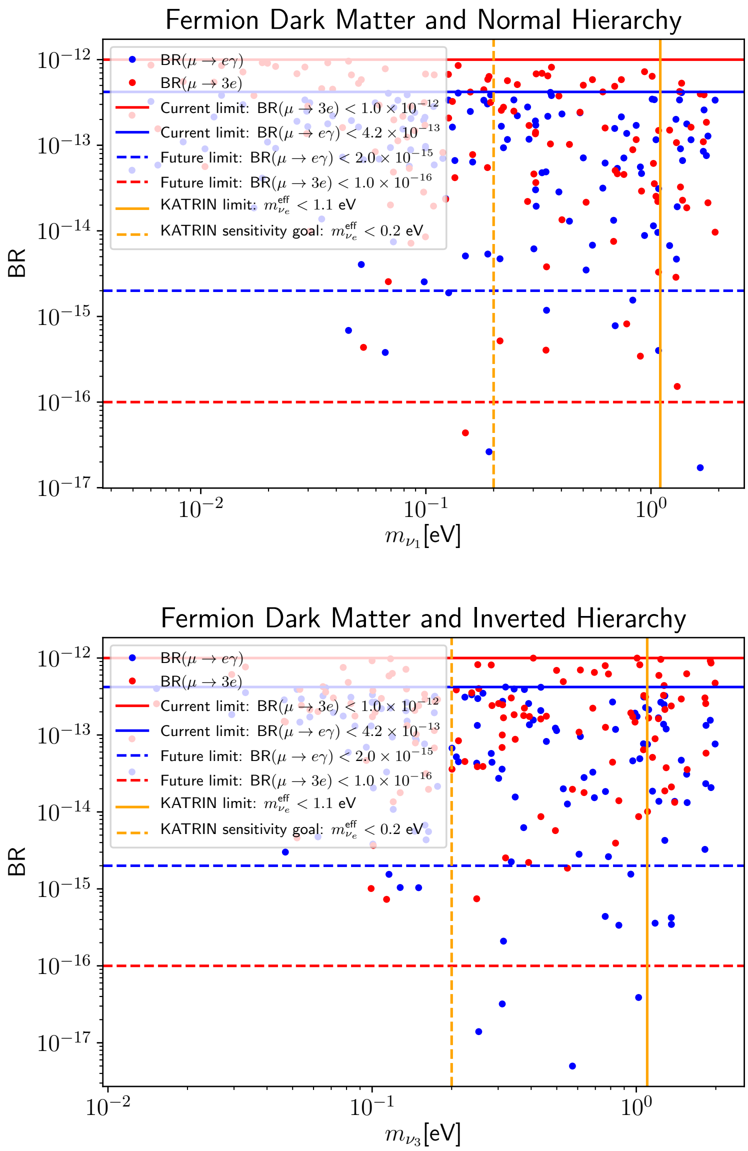

Figure 7.5: The branching ratios BR($\mu \to e\gamma$) (blue Points) and BR($\mu \to 3e$) (red points) as a function of the lightest neutrino mass. Horizontal solid lines show the current LFV limits and dashed lines the future limits. Vertical lines show the current limits on the (effective) electron neutrino mass set by KATRIN (solid orange line) and sensitivity goal of KATRIN (dashed orange line). The point fulfill all experimental constraints. Left for normal hierarchy and right for inverted hierarchy.

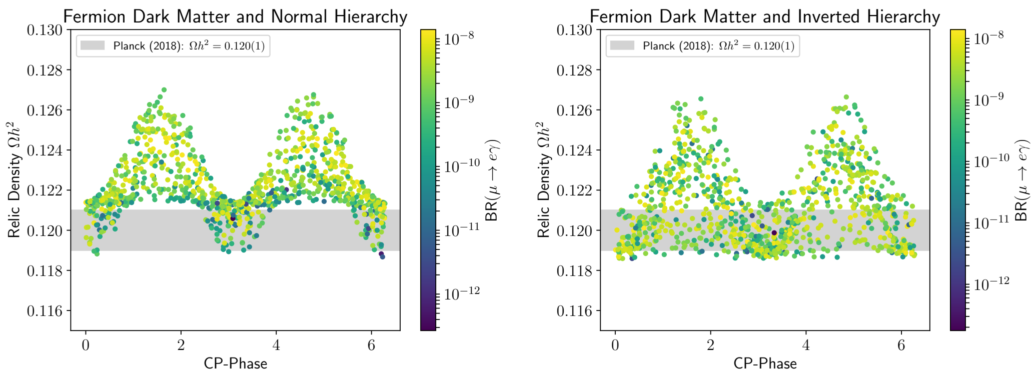

Figure 7.6: The relic density as a function of the CP violating phase δ_{CP}. The masses of the new particles, the neutrino masses and the scalar couplings have been fixed. (See text for details.) The BR($\mu \to e\gamma$) is given on the temperature scale.Left for normal hierarchy and right for inverted hierarchy.

on the BR($\mu \to e\gamma$). It varies randomly as can be seen on the temperature scale. The points scatter due to the three random angles in the Casas-Ibarra parametrization changing the elements of the Yukawa matrix. When varying δ_{CP}, the relic density changes up to ~ 0.01. In comparision, if one varies λ_5 the relic density changes up to several orders of magnitude as can be seen in Fig. 7.1. Similarly this is true for changes of the absolute neutrino mass. We see that even small changes in λ_5 or $m_{\nu_{1,3}}$ overshadow the δ_{CP} dependence. Due to the almost insignificant dependence on δ_{CP}, the results from Sec. 7.3.1 generalize to the case where the CP phase is varied as well. We have checked this explicitly for the behavior in Fig. 7.3. The determination of the CP phase does not restrict the parameter space of the scotogenic model further.

7.3.3 The effect of coannihilations

In this chapter we have, until now, disregarded all points, where coannihilations plays a non negligible role. Coannihilation's occur when the masses of two particles are nearly degenerate and are exponentially suppressed by the mass difference. The $N_1 - N_1$ annihilation process is described by diagrams quadratic in the Yukawa couplings. In case of N_1-η coannihilations there are also diagrams linear in the Yukawa couplings contributing to the relic density. This changes the relic density and allows for smaller Yukawa couplings and

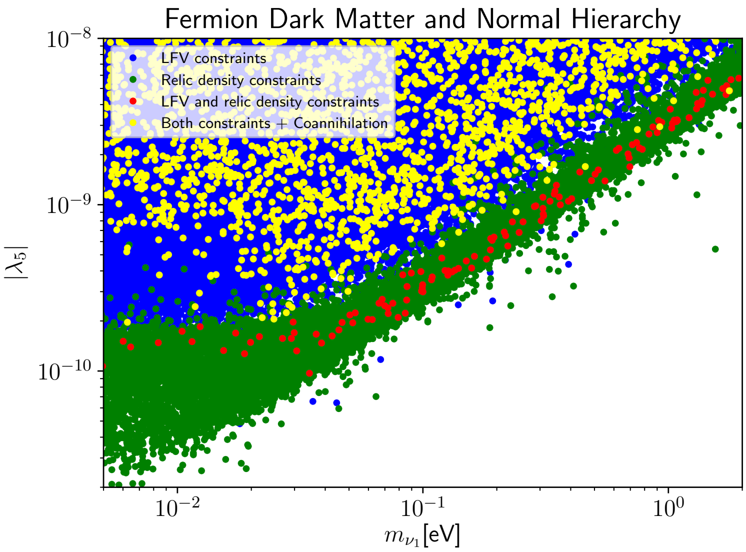

Figure 7.7: The dark sector-Higgs coupling $|\lambda_5|$ as a function of the lightest neutrino mass. The yellow point fulfill all experimental constraints but were previously disregarded due to coannihilations. Left for normal hierarchy and right for inverted hierarchy.

in turn LFV is suppressed [86]. The mass splitting between the dark matter particle and the second lightest dark particle now has as major impact on the phenomenology. In Fig. 7.7 we show the points we previously disregarded due to coannihilations. We still require them to yield the correct relic density and to be not excluded by LFV experiments. These points scatter randomly over the space allowed by LFV and our previously found relation does not hold in this case. Due to the sensitive dependence on the mass splitting, previously dominant dependencies are now less important.

8 Neutrino signals from scotogenic dark matter

In this chapter we study the prospect of detecting scalar dark matter at IceCube in the framework of the scotogenic model. We compute expected event rates in the 86-string configuration for neutrino signals from dark matter annihilating in the sun. Dark matter nucleon scattering allows for capture and accumulation of dark matter in the sun resulting in an overdensity. Since the mass splitting between both neutral scalar components in naturally small, we have to take inelastic scattering into account. As the relative dark matter nucleon velocity is larger in the sun as on earth, the suppression due to the inelasticity is less important for the accumulation of dark matter in the sun allowing neutrino telescopes to probe larger mass splittings than direct detection experiments on earth. This chapter extends the work presented in our paper Ref. [3] with a focus on the formalism for dark matter nucleus scattering. The paper was created together with *Raffaela Busse, Alexander Kappes, Michael Klasen* and *Sybrand Zeinstra*.

8.1 Motivation

In radiative seesaw models, dark matter in the form of WIMPs can annihilate either directly into neutrinos or via the decays of other intermediately produced Standard Model particles. Previous work focused on monochromatic neutrinos from direct decays, as they are easier to distinguish from the background [95–98]. Here, we consider both direct as well as secondary neutrinos from the decays of intermediate other Standard Model particles.

In order to boost the amount of WIMP annihilations, one can consider regions with a local overdensity [27]. Since our solar system is embedded in the galactic dark matter halo, WIMPs can accumulate in large celestial bodies like the Sun, which we focus on in this chapter. Upon scattering with a nucleus inside the Sun, a WIMP can lose enough kinetic energy to be captured by the

Sun's gravitational potential. Thus the WIMP-nucleon scattering cross section plays an important role in this capture process. We go beyond the standard scenario of elastic dark matter-nucleon scattering by considering also inelastic scattering processes, in which a WIMP up-scatters to a slightly heavier state. This so-called inelastic dark matter had originally been proposed by Smith and Weiner [87] to explain the annual modulation signal at DAMA/LIBRA [41, 99]. While these authors considered the sneutrino as a specific dark matter candidate, they concluded generally that due to the larger dark matter velocity, the inelasticity is in fact less relevant in the Sun than at direct detection experiments, leaving ample room for indirect detection experiments.

Other previous work that considered the prospect of detecting inelastic dark matter indirectly includes Refs. [100–102]. Their work was motivated by the DAMA/LIBRA signal and principally considered the parameter space that fitted this signal. A comparison between IceCube and direct detection experiments in a more general inelastic scenario has been carried out within the context of effective field theory in Ref. [103]. There it was found that neutrino telescopes should place stronger limits than direct detection experiments for mass splittings larger than about 200 keV for dark matter particles of mass 1 TeV.

Of the many models that connect neutrinos masses and dark matter, the scotogenic model is the best-known example [9]. Its main strength is the relatively simple extension of the Standard Model with only two new fields, whilst still providing enough interesting phenomenology, in particular naturally occurring inelastic dark matter. The neutrino masses are generated at loop level through the radiative seesaw mechanism, whereas the tree level seesaw is forbidden by a $\mathbb{Z}_2$ symmetry under which all new particles have an odd charge. In this chapter we focus on the scotogenic model with scalar dark matter. For a similar model, extended by a real scalar singlet to account for inflation, elastic scattering in the Sun was found to produce neutrino signals at least two orders of magnitude below the current sensitivity of neutrino telescopes [104].

As the largest neutrino telescope worldwide, the IceCube Observatory [105] is predestined to search for neutrino signals from annihilating WIMPs and thereby contribute to the search for physics beyond the Standard Model. We investigate the parameter space of the scotogenic model for a detectable neutrino flux in IceCube from WIMP annihilations in the Sun and Galactic Center, which could therefore be used to constrain the scotogenic parameter space with dedicated IceCube data analyses.

8.2 Scattering and capture of dark matter

In this subsection we review the capture rate of dark matter. For the general formula and the elastic case, we follow closely the original derivation by Gould [106]. Gould initially assumes an isotropic velocity distribution. The derived formulas are correct in the general case as explained by Gould in the same paper.

8.2.1 General considerations for the capture rate

First consider a sphere with radius R which is large enough to neglect gravity at surface. The flux of dark matter going into the sphere is given by [107]

$$\frac{1}{4} f(u) u \; du \; d\cos^2\theta, \tag{8.2.1}$$

where θ is the angle between the radial direction and the velocity and u is the WIMP velocity. $f(u)$ is the velocity distribution function. In this work we always assume a Maxwell-Bolzmann distribution. If we substitute angular momentum per unit mass

$$J = Ru\sin\theta \tag{8.2.2}$$

and integrate over the surface of the sphere, we obtain the total number of WIMPs entering the region per unit time:

$$\int_0^{2\pi}\int_{-1}^{1}\frac{1}{4} f(u) u \; du \; d\cos^2\theta \; d\phi_s \; d\cos\theta_s = 4\pi R^2 \frac{1}{4} f(u) u \; du \frac{dJ^2}{R^2 u^2}. \tag{8.2.3}$$

Now consider a thin shell of material (e.g. a layer of the sun). The velocity u of a WIMP at the shell is given by

$$w^2 = u^2 + v_{\text{esc}}^2 \tag{8.2.4}$$

where u is the velocity at infinity and v_{esc} is the velocity needed to escape the gravitational potential starting from the shell. If the WIMP scatters to a velocity lower than v_{esc}, the particle is captured. The probability for this is given by

$$\Omega_v^- \frac{dl}{w}. \tag{8.2.5}$$

dl is the distance the WIMP travels through the material of the shell given by

$$dl = \left[1 - \left(\frac{J}{rw}\right)^2\right]^{-\frac{1}{2}} 2\ dr\ \theta(rw - J). \tag{8.2.6}$$

dr is the thickness of the shell. The factor of two arises since the WIMP passes the shell twice and the theta function appears since, if rw is smaller than the angular momentum, the WIMP cannot reach the shell. The capture rate for a shell per unit velocity can now be obtained by multiplying the number of WIMP entering the sphere Eq. (8.2.3) with the capture probability Eq. (8.2.5) and integrating over all angular momenta. This gives

$$4\pi r^2 w \Omega_v^- \frac{f(u)\ du}{u} dr. \tag{8.2.7}$$

After integrating over all velocities, we can rewrite this to the capture rate per shell volume

$$\frac{dC}{dV} = \int_0^\infty du \frac{f(u)}{u} w \Omega_v^-. \tag{8.2.8}$$

This formula describes the capture rate for both the elastic and inelastic case. The velocity distribution function $f(u)$ for an observer moving with $v_\odot$ is given by

$$f(u)\ du = \frac{4\rho_\chi}{m_\chi \pi^{\frac{1}{2}}} x^2 e^{-x^2-\eta^2} \frac{\sinh(2x\eta)}{2x\eta} dx \tag{8.2.9}$$

where ρ_χ is the local dark matter density, m_χ is the dark matter mass, $x^2 = u^2/v_0^2$ and $\eta^2 = v_\odot^2/v_0^2$. v_0 is connected to the WIMP velocity dispersion $\bar{v}$ by $v_0^2/\bar{v}^2 = 2/3$.

8.2.2 Capture of elastic dark matter

Now we focus on the case where dark matter particles scatter elastically on nucleons. From non relativistic kinematics, we know that the energy transfer Q in a scattering process with a WIMP and a nucleus in the nucleus rest frame must be in the interval

$$0 \leq Q \leq Q_{\max} = \frac{1}{2} m_\chi w^2 \frac{4 m_N m_\chi}{(m_N + m_\chi)^2}, \tag{8.2.10}$$

where m_N denotes the nucleus mass. To be captured the velocity after the scattering process must be smaller than the escape velocity. This requires a momentum energy transfer of

$$Q > Q_{\text{cap}} = \frac{1}{2} m_\chi (w^2 - v_{\text{esc}}^2). \tag{8.2.11}$$

The scattering function Ω_v^- is given by the total rate of scattering $\sigma_N n_N w$ multiplied with the probability that the WIMP has a velocity smaller that the escape velocity. σ_N is the WIMP-nucleus cross section and n_N is the number density of nuclei. Finally, if the nucleus is not a proton or nucleon, we need to add a nuclear form factor $F(Q)$, to take the inner structure of the nucleus into account. We obtain

$$\Omega_v^- = \frac{\sigma_N n_N w}{Q_{\text{max}}} \int_{Q_{\text{cap}}}^{Q_{\text{max}}} dQ F(Q) \theta(Q_{\text{max}} - Q_{\text{cap}}). \tag{8.2.12}$$

8.2.3 Capture of inelastic dark matter

In the previous section, we considered elastic scattering. In most scenarios this is the only contributing case. However, if there is an excited state of the dark matter particle with a small mass splitting of $\mathcal{O}(100 \text{ keV})$, the dark matter particle can upscatter into the heavier particle. This scenario has originally been proposed by Thucker-Smith and Weiner [87] to explain the annual modulation signal at DAMA and the absence of signals in CDMS. However, for more recent results of DAMA-LIBRA the tension with other direct detection experiments cannot (or only partially for $m_\chi \approx 10$ GeV) be relieved by inelastic scattering [108]. In the scotogenic model such small mass splittings occur naturally for scalar dark matter. In this subsection we examine how the formulas for the capture rate change for the inelastic scenario. We follow the derivations given in [100, 101].

The derivation in Sec. 8.2.1 does not depend on the scattering process itself. Only the considerations for the scattering function Ω_v^- in Sec. 8.2.2 need to be altered. The differential cross section in not effected by the inelasticity [101]

$$\frac{d\sigma_{\text{elastic}}}{dE_R} = \frac{d\sigma_{\text{inelastic}}}{dE_R}, \tag{8.2.13}$$

where E_R is the recoil energy. Assuming an inelasticity of δ and approximating $m_\chi + \delta = m_\chi$, non relativistic kinematics yield the minimal and maximal energy transfer in the nucleon rest frame

$$Q_{\max} = \frac{1}{2} m_\chi w^2 \left(1 - \frac{\mu^2}{m_N^2}\left(1 - \frac{m_N}{m_\chi}\sqrt{1 - \frac{\delta}{\mu w^2/2}}\right)^2\right) - \delta, \tag{8.2.14}$$

$$Q_{\min} = \frac{1}{2} m_\chi w^2 \left(1 - \frac{\mu^2}{m_N^2}\left(1 + \frac{m_N}{m_\chi}\sqrt{1 - \frac{\delta}{\mu w^2/2}}\right)^2\right) - \delta, \tag{8.2.15}$$

where μ is the WIMP-nucleus reduced mass. The minimal energy transfer required for capture is given by

$$Q_{\text{cap}} = \frac{1}{2} m_\chi (w^2 - v_{\text{esc}}^2) - \delta. \tag{8.2.16}$$

The boundaries on the energy transfer $Q_{\max}, Q_{\min}$ together with Eq. (8.2.13) yield for the total cross section

$$\sigma_{\text{inelastic}} = \sqrt{1 - \frac{\delta}{\mu w^2/2}}\,\sigma_{\text{elastic}}. \tag{8.2.17}$$

The scattering function Ω_v^- is again given by the total rate of scattering multiplied by the capture probability. Including a nuclear form factor we obtain

$$\Omega_v^- = \frac{\sigma_{N,\text{inel}} n_N w}{Q_{\max} - Q_{\min}} \int_{Q'_{\min}}^{Q_{\max}} dQ F(Q) \theta(Q_{\max} - Q_{\text{cap}}), \tag{8.2.18}$$

where $Q'_{\min} = max(Q_{\text{cap}}, Q_{\min})$. $\sigma_{N,\text{inel}}$ is the cross section for inelastic scattering off nucleons (see Eq. (8.2.17)). Note that the lower integration boundary differs from [100] as pointed out in [102].

8.2.4 Scattering cross sections

In this section, we describe how to obtain the cross section for WIMP scattering on nuclei from the high energy Lagrangian. We will focus on interactions with Higgs and Z^0 bosons as mediator as they are the most relevant for our models and carry out the calculation at tree level. The formalism described also generalizes to other WIMP nucleus interactions. The scattering cross sections are relevant for direct detection experiments (see Chap. 2) as well as for the capture rate in celestial bodies. In this section, we consider both scalar as well as fermion dark matter which we denote with ϕ_i and χ_i respectively. We allow the outgoing particle to be different from the ingoing particle in order to incorporate inelastic scattering, while approximating the masses to be the same. We largely follow the derivation for the WIMP nucleon cross section in the zero momentum transfer limit given in [33] while generalizing for inelastic dark matter and working out some details.

Scattering on quarks

The starting point is the Lagrangian of the full theory (after EWSB) which describes the coupling of WIMPs to Higgs and Z^0 bosons and the coupling of these bosons to quarks. Note that we use Dirac spinors instead of Weyl spinors throughout this section. The interaction terms in the Lagrangian are

$$\mathcal{L}_\phi \supset + g_{\phi^2 h}\frac{1}{2}\phi^2 h + g_{\bar{q}qh}\bar{q}qh, \tag{8.2.19}$$

$$\begin{aligned}\mathcal{L}_{\phi_{12}} \supset &+ g_{\phi_1\phi_2 Z^0}(\partial^\mu\phi_1\phi_2 - \phi_1\partial^\mu\phi_2)Z^0_\mu + \bar{q}\gamma^\mu(g_{\bar{q}qZ^0,V} + g_{\bar{q}qZ^0,A}\gamma^5)qZ^0_\mu \\ &+ g_{\phi_1\phi_2 h}\phi_1\phi_2 h + g_{\bar{q}qh}\bar{q}qh\end{aligned} \tag{8.2.20}$$

for real scalar fields ϕ, ϕ_1 and ϕ_2. In case of complex scalar fields, one can split them into two real fields and then obtain similar Lagrangian. Note that there is no elastic interaction vertex between the Z^0 boson and a real scalar field.

Now we turn to possible Lagrangians involving fermions. For Dirac dark matter we have

$$\begin{aligned}\mathcal{L}_D \supset &+ \bar{\chi_1}\gamma^\mu(g_{\bar{\chi_1}\chi_2 Z^0,V} + g_{\bar{\chi_1}\chi_2 Z^0,A}\gamma^5)\chi_2 Z^0_\mu + \bar{q}\gamma^\mu(g_{\bar{q}qZ^0,V} + g_{\bar{q}qZ^0,A}\gamma^5)qZ^0_\mu \\ &+ \bar{\chi_1}(g_{\bar{\chi_1}\chi_2 h,S} + g_{\bar{\chi_1}\chi_2 h,P}\gamma^5)\chi_2 h + g_{\bar{q}qh}\bar{q}qh\end{aligned} \tag{8.2.21}$$

where χ_1 can be equal or different from χ_2 and for Majorana dark matter we have

$$\begin{aligned}\mathcal{L}_M \supset &+ \frac{1}{2}g_{\chi\chi Z^0,A}\bar{\chi}\gamma^\mu\gamma^5\chi Z^0_\mu + \bar{q}\gamma^\mu(g_{\bar{q}qZ^0,V} + g_{\bar{q}qZ^0,A}\gamma^5)qZ^0_\mu \\ &+ \frac{1}{2}\bar{\chi}(g_{\chi\chi h,S} + g_{\chi\chi h,P}\gamma^5)\chi h + g_{\bar{q}qh}\bar{q}qh\end{aligned} \tag{8.2.22}$$

in case of elastic scattering. Since both fermions in the interaction are identical a factor of $\frac{1}{2}$ should be added. For the inelastic case we have

$$\begin{aligned}\mathcal{L}_{M_{12}} \supset &+ g_{\chi_1\chi_2 Z^0,A}\bar{\chi_1}\gamma^\mu\gamma^5\chi_2 Z^0_\mu + \bar{q}\gamma^\mu(g_{\bar{q}qZ^0,V} + g_{\bar{q}qZ^0,A}\gamma^5)qZ^0_\mu \\ &+ \bar{\chi_1}(g_{\chi_1\chi_2 h,S} + g_{\chi_1\chi_2 h,P}\gamma^5)\chi_2 h + g_{\bar{q}qh}\bar{q}qh.\end{aligned} \tag{8.2.23}$$

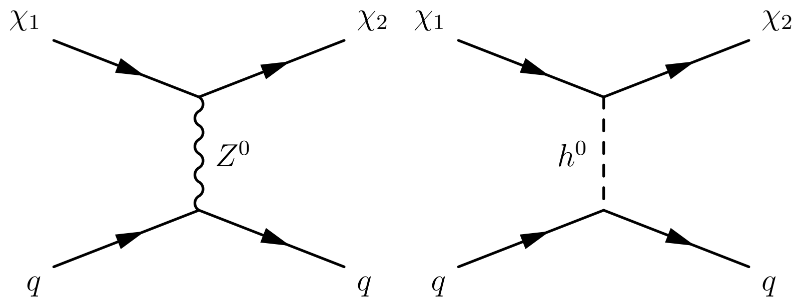

Figure 8.1: Feynman diagrams for dark matter scattering on quarks (nucleons) through Z^0 (left) and Higgs boson exchange (right). Both scalar and fermion dark matter are denoted by χ_i.

Note that Majorana fermions do not have vector interactions (see Sec. 5.3, Ref. [33]).

The Feynman diagrams relevant for WIMP nucleon scattering following from these Lagrangians are given in Fig. 8.1. One can obtain the effective Lagrangian for this theory, by integrating out the mediator. Another more descriptive and for our purposes equivalent possibility is to write down the scattering amplitude and take the zero momentum transfer limit in the propagator. Then the effective coupling can be read of from this expression, leading to the following effective Lagrangians for scalar dark matter:

$$\mathcal{L}_{\text{eff},\phi} \supset + \frac{g_{\phi^2 h} g_{\bar{q}qh}}{m_h^2} \frac{1}{2} \phi^2 \bar{q} q, \tag{8.2.24}$$

$$\mathcal{L}_{\text{eff},\phi_{12}} \supset + \frac{g_{\phi_1\phi_2 Z^0} g_{\bar{q}qZ^0,V}}{m_Z^2} (\partial_\mu \phi_1 \phi_2 - \phi_1 \partial_\mu \phi_2) \bar{q}\gamma^\mu q + \frac{g_{\phi_1\phi_2 h} g_{\bar{q}qh}}{m_h^2} \phi_1\phi_2 \bar{q} q. \tag{8.2.25}$$

Combinations of a derivative ∂_μ and the bilinear $\bar{q}\gamma^\mu\gamma^5 q$ vanish in the non relativistic limit and thus the corresponding term (there is only one) in the Lagrangian is dropped. For Dirac and Majorana dark matter the terms $\bar{\chi_1}\gamma^5\chi_2$, $\bar{\chi_1}\gamma^\mu\gamma^5\chi_2\bar{q}\gamma^\mu q$ and $\bar{\chi_1}\gamma^\mu\chi_2\bar{q}\gamma^\mu\gamma^5 q$ vanish in the non relativistic limit (see e.g.

Ref. [109]). The effective Lagrangians are then

$$\begin{aligned}
\mathcal{L}_{\text{eff},D} \supset &+ \frac{g_{\bar{\chi}_1\chi_2 Z^0,V}\, g_{\bar{q}qZ^0,V}}{m_{Z^0}^2}\bar{\chi}_1\gamma_\mu\chi_2\bar{q}\gamma^\mu q + \frac{g_{\bar{\chi}_1\chi_2 Z^0,A}\, g_{\bar{q}qZ^0,A}}{m_{Z^0}^2}\bar{\chi}_1\gamma_\mu\gamma^5\chi_2\bar{q}\gamma^\mu\gamma^5 q \\
&+ \frac{g_{\bar{\chi}_1\chi_2 h,S}\, g_{\bar{q}qh}}{m_h^2}\bar{\chi}_1\chi_2\bar{q}q, \qquad (8.2.26)\\
\mathcal{L}_{\text{eff},M} \supset &+ \frac{g_{\chi\chi Z^0,A}\, g_{\bar{q}qZ^0,A}}{2m_{Z^0}^2}\bar{\chi}\gamma_\mu\gamma^5\chi\bar{q}\gamma^\mu\gamma^5 q + \frac{g_{\chi\chi h,S}\, g_{\bar{q}qh}}{2m_h^2}\bar{\chi}\chi\bar{q}q, \qquad (8.2.27)\\
\mathcal{L}_{\text{eff},M_{12}} \supset &+ \frac{g_{\chi_1\chi_2 Z^0,A}\, g_{\bar{q}qZ^0,A}}{m_{Z^0}^2}\bar{\chi}_1\gamma_\mu\gamma^5\chi_2\bar{q}\gamma^\mu\gamma^5 q + \frac{g_{\chi_1\chi_2 h,S}\, g_{\bar{q}qh}}{m_h^2}\bar{\chi}_1\chi_2\bar{q}q \qquad (8.2.28)
\end{aligned}$$

for Dirac, elastic and inelastic Majorana dark matter. Note that it is not actually necessary to go to an effective theory. One can calculate the amplitudes on nuclei in the full theory. We choose to give the formulas for the effective theory to make connection with the operator based approach used e.g. by MICROMEGAS [94].

Scattering on nucleons and nuclei

The WIMPs scatter on quarks bound in a nucleon. Thus the initial and final states are given by nucleons and not by quarks. To account for this we need to recall how the Feynman rules for in- and outgoing fermions are obtained.

The Dirac fermion field is given by

$$\Psi(x) = \sum_s \int \frac{d^3p}{(2\pi^3)}\frac{1}{\sqrt{2\omega_p}}\left(a_p^s u_p^s e^{-ipx} + b_p^{s\dagger} v_p^s e^{ipx}\right). \qquad (8.2.29)$$

The Majorana field can be obtained from the Dirac field by setting $a_p^s = b_p^s$. We however only need the Dirac field since quarks a Dirac fermions. The Feynman rules for in- and outgoing fermions arise out of the Wick contraction of the field operators with the initial or final state particle as follows [110]:

$$\Psi|p,s\rangle = u^s(p), \qquad \langle p,s|\bar{\Psi} = \bar{u}^s(p), \qquad (8.2.30)$$

$$\bar{\Psi}|k,s\rangle = \bar{v}^s(k), \qquad \langle k,s|\Psi = v^s(k). \qquad (8.2.31)$$

For quarks bound in a nucleon, the initial and final state particles are given by a nucleon which we denote by $|\tilde{N},s\rangle$. To calculate Feynman diagrams with in- and outgoing nucleons, we now need to use contractions of the quark operators with the state $|\tilde{N},s\rangle$ instead of Dirac spinors for the Feynman rules.

For the Lagrangians in Eqs. (8.2.24)-(8.2.28), the possible terms, arising from the quark part of the diagram are

$$\langle \tilde{N}, s|\bar{q}q|\tilde{N}, s'\rangle, \qquad \langle \tilde{N}, s|\bar{q}\gamma^\mu q|\tilde{N}, s'\rangle, \qquad \langle \tilde{N}, s|\bar{q}\gamma^\mu\gamma^5 q|\tilde{N}, s'\rangle. \tag{8.2.32}$$

To make connection to the literature (e.g. Ref. [27]), we write these expressions in term on non relativistically normalized nucleon states $|N\rangle = \sqrt{\frac{1}{2\omega_p}}|\tilde{N}, s\rangle$ and we will from now on drop the contraction lines. These matrix elements all need to be evaluated differently. Before we discuss these matrix elements further, we first bring the scattering amplitudes into the same shape.

First we focus on amplitudes containing the nucleon matrix element $\langle N|\bar{q}q|N\rangle$. Each of the effective Lagrangians can yield amplitudes containing such matrix elements. Using our newly found Feynman rules for in- and outgoing nucleons, we obtain

$$i\mathcal{M}_\phi = \sum_q 2m_N \frac{g_{\phi^2 h} g_{\bar{q}qh}}{m_h^2}\langle N|\bar{q}q|N\rangle, \tag{8.2.33}$$

$$i\mathcal{M}_{\phi_{12}} = \sum_q 2m_N \frac{g_{\phi_1\phi_2 h} g_{\bar{q}qh}}{m_h^2}\langle N|\bar{q}q|N\rangle, \tag{8.2.34}$$

$$i\mathcal{M}_D = \sum_q 2m_N \frac{g_{\bar{\chi}_1\chi_2 h,S} g_{\bar{q}qh}}{m_h^2}\bar{u}^s_{\chi_1} u^{s'}_{\chi_2}\langle N|\bar{q}q|N\rangle, \tag{8.2.35}$$

$$i\mathcal{M}_M = \sum_q 2m_N \frac{g_{\chi\chi h,S} g_{\bar{q}qh}}{m_h^2}\bar{u}^s_{\chi} u^{s'}_{\chi}\langle N|\bar{q}q|N\rangle, \tag{8.2.36}$$

$$i\mathcal{M}_{M_{12}} = \sum_q 2m_N \frac{g_{\chi_1\chi_2 h,S} g_{\bar{q}qh}}{m_h^2}\bar{u}^s_{\chi_1} u^{s'}_{\chi_2}\langle N|\bar{q}q|N\rangle. \tag{8.2.37}$$

Note how the factors of $\frac{1}{2}$ in the scalar and Majorana Lagrangian cancelled with the symmetry factor of 2! that arises from the two identical fields and how each matrix element got a factor of $2m_N$ from the non relativistic normalisation. In the zero momentum transfer (and equal mass) limit, $\bar{u}^s u^{s'} = 2m_\chi \delta ss'$ where m_χ is the dark matter mass. This leads to

$$i\mathcal{M}_D = \sum_q 4m_N m_\chi \frac{g_{\bar{\chi}_1\chi_2 h,s} g_{\bar{q}qh}}{m_h^2}\langle N|\bar{q}q|N\rangle, \tag{8.2.38}$$

$$i\mathcal{M}_M = \sum_q 4m_N m_\chi \frac{g_{\chi\chi h,s} g_{\bar{q}qh}}{m_h^2}\langle N|\bar{q}q|N\rangle, \tag{8.2.39}$$

$$i\mathcal{M}_{M_{12}} = \sum_q 4m_N m_\chi \frac{g_{\chi_1\chi_2 h,s} g_{\bar{q}qh}}{m_h^2}\langle N|\bar{q}q|N\rangle \tag{8.2.40}$$

where we dropped the spin delta function which will later vanish due to the spin average over initial and sum over final spin. Now all five amplitudes have the same structure. This allows us to work with a general amplitude given by

$$i\mathcal{M} = \sum_q 4m_N m_\chi a_q \langle N|\bar{q}q|N\rangle \tag{8.2.41}$$

from now on.[1] The quark current in $\langle N|\bar{q}q|N\rangle$ couples to the quark content in the nucleon. For light quarks $q = u, d, s$ we can evaluate this as

$$\langle N|m_q\bar{q}q|N\rangle = m_N f_q^{(N)}, \tag{8.2.42}$$

where m_q is the quark mass and m_N is the mass of the nucleon. For heavy quarks $q' = c, b, t$ the matrix element is given by

$$\langle N|m_{q'}\bar{q}'q'|N\rangle = \frac{2}{27}m_N\left(1 - \sum_{q=u,d,s} f_q^{(N)}\right). \tag{8.2.43}$$

In this work we use the values for $f_q^{(N)}$ shown in Tab. 8.1 as they are default in micrOMEGAs 5.0.8 [94]. We can now define

$$\frac{f_N}{m_N} = \sum_{q=u,d,s} f_q^{(N)}\frac{a_q}{m_q} + \frac{2}{27}\left(1 - \sum_{q=u,d,s} f_q^{(N)}\right)\sum_{q=c,b,t}\frac{a_q}{m_q} \tag{8.2.44}$$

which is the effective coupling of the WIMP to the nucleon $N = p, n$. In case of nuclei with more than one nucleon we must sum over the contribution from each nucleon. The cross section at zero momentum transfer for scattering on a nucleus N is then given by

$$\sigma_N = \frac{\mu^2}{\pi}\left[Zf_p + (A-Z)f_n\right]^2 \tag{8.2.45}$$

where μ is the WIMP nucleus reduced mass. Since the contributions from each nucleon add up coherently, this cross section contributes to spin independent scattering.

Scattering amplitudes from our effective Lagrangians containing $\langle N|\bar{q}\gamma^\mu q|N\rangle$ can only arise from scalar and Dirac dark matter since for Majorana fermions there are no vector bilinear in the Lagrangian. The amplitudes are

$$i\mathcal{M}_{\phi_{12}} = \sum_q 2m_N\frac{g_{\phi_1\phi_2Z^0}g_{\bar{q}qZ^0,V}}{m_{Z^0}^2}(P_{\phi_1,\mu} + P_{\phi_2,\mu})\langle N|\bar{q}\gamma^\mu q|N\rangle, \tag{8.2.46}$$

$$i\mathcal{M}_D = \sum_q 2m_N\frac{g_{\bar{\chi}_1\chi_2Z^0,V}g_{\bar{q}qZ^0,V}}{m_{Z^0}^2}\bar{u}_{\chi_1}^s\gamma_\mu u_{\chi_2}^{s'}\langle N|\bar{q}\gamma^\mu q|N\rangle. \tag{8.2.47}$$

[1]Note that we absorbed a factor of $(2m_\chi)^{-1}$ into the effective coupling for scalar fields.

Table 8.1: Nucleon form factors for quark and spin content in nucleons. Values taken from [94].

	proton	neutron		proton	neutron
$f_d^{(N)}$	0.0191	0.0273	Δd	-0.427	0.842
$f_u^{(N)}$	0.0153	0.011	Δu	0.842	-0.427
$f_s^{(N)}$	0.0447	0.0447	Δs	-0.085	-0.085

In the non relativistic and zero momentum transfer limit, $P_{\phi_1,\mu} + P_{\phi_2,\mu} \approx 2m_\chi \delta^0_\mu$ and $\bar{u}^s_{\chi_1}\gamma_\mu u^{s'}_{\chi_2} \approx 2m_\chi \delta^0_\mu \delta ss'$. Dropping the spin delta function again, the scattering amplitudes are given by

$$i\mathcal{M}_{\phi_{12}} = \sum_q 4m_N m_\chi \frac{g_{\phi_1\phi_2 Z^0} g_{\bar{q}qZ^0,V}}{m^2_{Z^0}} \delta^0_\mu \langle N|\bar{q}\gamma^\mu q|N\rangle, \tag{8.2.48}$$

$$i\mathcal{M}_D = \sum_q 4m_N m_\chi \frac{g_{\bar{\chi}_1\chi_2 Z^0,V} g_{\bar{q}qZ^0,V}}{m^2_{Z^0}} \delta^0_\mu \langle N|\bar{q}\gamma^\mu q|N\rangle. \tag{8.2.49}$$

As these amplitudes have the same structure, we again work with a general scattering amplitude given by

$$i\mathcal{M} = \sum_q 4m_N m_\chi b_q \delta^0_\mu \langle N|\bar{q}\gamma^\mu q|N\rangle. \tag{8.2.50}$$

Since the vector current couples to the valence quarks only, we can make the connection to the proton (neutron) spinors u_N as follows

$$2m_N\langle N|\bar{q}\gamma^\mu q|N\rangle = 2\bar{u}_N\gamma^\mu u_N \quad \text{for } q = u(d), \tag{8.2.51}$$

$$2m_N\langle N|\bar{q}\gamma^\mu q|N\rangle = \bar{u}_N\gamma^\mu u_N \quad \text{for } q = d(u). \tag{8.2.52}$$

where u, d denote the up and down quark. Once we take the non relativistic limit for the nucleon spinors $\bar{u}_N\gamma^\mu u_N \approx 2m_N\delta^\mu_0$, the scattering amplitude turns into

$$i\mathcal{M} = 4m_N m_\chi b_N \tag{8.2.53}$$

where $N = p, n$ denotes the proton and neutron and b_N is given by

$$b_p = 2b_u + b_d, \tag{8.2.54}$$

$$b_n = 2b_d + b_u. \tag{8.2.55}$$

For nuclei with more than nucleon, we must sum over all valence quarks from each nucleon. Thus the WIMP nucleon cross section at zero momentum transfer is again given by

$$\sigma_N = \frac{\mu^2}{\pi}\left[Zb_p + (A-Z)b_n\right]^2 \tag{8.2.56}$$

where μ is the WIMP nucleon reduced mass.

Both processes discussed up to this point contribute to the spin independent cross section. Note that some literature assumes the coupling on protons and neutrons to be equal. For scalar interactions (Higgs boson as mediator) this is a reasonable approximation. However for vector interactions this approximation fails. The contribution from protons and neutrons often have different signs and differ significantly in value.

The axial vector interaction contributes to the spin dependent interaction which couples to the spin of the nucleus and the contribution of the nucleon will not simply add up as for the spin independent interaction. It is useful to work with nucleus states instead of the nucleon states for the derivation. The possible scattering amplitudes arising from the Lagrangians above are

$$\mathcal{M}_D = \sum_q 2m_N \frac{g_{\bar{\chi}_1\chi_2Z^0,A}\, g_{\bar{q}qZ^0,A}}{m_{Z^0}^2}\bar{u}^s_{\chi_1}\gamma_\mu\gamma^5 u^{s'}_{\chi_2}\langle N|\bar{q}\gamma^\mu\gamma^5 q|N\rangle, \tag{8.2.57}$$

$$\mathcal{M}_M = \sum_q 2m_N \frac{g_{\chi\chi Z^0,A}\, g_{\bar{q}qZ^0,A}}{2m_{Z^0}^2}\bar{u}^s_{\chi}\gamma_\mu\gamma^5 u^{s'}_{\chi}\langle N|\bar{q}\gamma^\mu\gamma^5 q|N\rangle, \tag{8.2.58}$$

$$\mathcal{M}_{M_{12}} = \sum_q 2m_N \frac{g_{\chi_1\chi_2Z^0,A}\, g_{\bar{q}qZ^0,A}}{m_{Z^0}^2}\bar{u}^s_{\chi_1}\gamma_\mu\gamma^5 u^{s'}_{\chi_2}\langle N|\bar{q}\gamma^\mu\gamma^5 q|N\rangle. \tag{8.2.59}$$

m_N is now the mass of the nucleus. In the non relativistic limit $\bar{u}^s_{\chi_1}\gamma_\mu\gamma^5 u^{s'}_{\chi_2} \approx 2m_\chi\sigma^i_{ss'}\delta^i_\mu := 2m_\chi 2S^i_{\chi,ss'}\delta^i_\mu$. We drop the indices s, s' of the WIMP spin operator for now. The scattering amplitudes are now given by

$$\mathcal{M}_D = \sum_q 4m_N m_\chi \frac{g_{\bar{\chi}_1\chi_2Z^0,A}\, g_{\bar{q}qZ^0,A}}{m_Z^2} 2S^i_\chi\delta^i_\mu\langle N|\bar{q}\gamma^\mu\gamma^5 q|N\rangle, \tag{8.2.60}$$

$$\mathcal{M}_M = \sum_q 4m_N m_\chi \frac{g_{\chi\chi Z^0,A}\, g_{\bar{q}qZ^0,A}}{2m_{Z^0}^2} 2S^i_\chi\delta^i_\mu\langle N|\bar{q}\gamma^\mu\gamma^5 q|N\rangle, \tag{8.2.61}$$

$$\mathcal{M}_{M_{12}} = \sum_q 4m_N m_\chi \frac{g_{\chi_1\chi_2Z^0,A}\, g_{\bar{q}qZ^0,A}}{m_{Z^0}^2} 2S^i_\chi\delta^i_\mu\langle N|\bar{q}\gamma^\mu\gamma^5 q|N\rangle. \tag{8.2.62}$$

We again treat all these matrix element together by defining

$$\mathcal{M} = \sum_q 4m_N m_\chi d_q 2S^i_\chi\delta^i_\mu\langle N|\bar{q}\gamma^\mu\gamma^5 q|N\rangle. \tag{8.2.63}$$

The nuclear matrix element in the non relativistic limit becomes

$$\langle N|\bar{q}\gamma^\mu\gamma^5 q|N\rangle = 2\left(\langle N|S_{p,i}\Delta^p q|N\rangle + \langle N|S_{n,i}\Delta^n q|N\rangle\right)\delta_i^\mu \tag{8.2.64}$$

where p, n denote the proton and neutron respectively and Δq denotes the nucleon spin content carried by the quark q. The numerical values are given in Tab. 8.1. $S_{p,n}$ are the spin operators for protons and neutron are the spin operators for protons and neutrons. The nuclear matrix element can then be rewritten in terms of the total nuclear angular momentum J_N by using the Wigner-Eckart theorem:

$$\langle N|S_{p,i}\Delta^p q|N\rangle + \langle N|S_{n,i}\Delta^n q|N\rangle = \lambda_q\langle N|J_{N,i}|N\rangle. \tag{8.2.65}$$

When the spin of the nucleus is carried by a single nucleon, λ_q can be evaluated in the single-particle shell model. In case of an unpaired proton (neutron), we have

$$\lambda_q = \frac{1}{2}\Delta^{p(n)}q\left[1 - \frac{L_{p(n)}(L_{p(n)}+1) - S_{p(n)}(S_{p(n)}+1)}{J_N(J_N+1)}\right] \tag{8.2.66}$$

where $L_{p(n)}$ is the orbital angular momentum and $S_{p(n)}$ is the spin of the unpaired nucleon. The single-particle shell model can however only applied if only the last odd nucleon contributes to the spin. Thus we leave λ_q variable in the rest of this derivation. After substituting the results for the matrix element, the scattering amplitude is given by

$$\mathcal{M} = \sum_{q=u,d,s} 4m_N m_\chi d_q 4S_\chi^i \lambda_q\langle N|J_{N,i}|N\rangle. \tag{8.2.67}$$

Note that only the light quarks contribute, since the contibution from the heavy quaks to the spin content is neglectable. To calculate the squared and spin averaged over initial and spin summed over final states matrix element we show the WIMP spin indices s, s' and make the difference between nucleus initial and final state explicit:

$$\begin{aligned}|\bar{\mathcal{M}}|^2 := \sum_{s,s',N_i,N_f}\frac{|\mathcal{M}|^2}{2(2J_N+1)} =& \frac{256m_N^2m_\chi^2}{2(2J_N+1)}\left[\sum_{q=u,d,s} d_q\lambda_q\right]^2\sum_{s,s'}S^j_{\chi,ss'}S^i_{\chi,s's}\times \\ &\times\sum_{N_i,N_f}\langle N_f|J_{N,j}|N_i\rangle\langle N_i|J_{N,i}|N_f\rangle.\end{aligned} \tag{8.2.68}$$

The sum over $i, k = 1, 2, 3$ is implicit. Now we carry out the sum over the initial nucleus states using the completeness relation and we carry out the WIMP spin sum using

$$\sum_{s,s'} S^j_{\chi,ss'} S^i_{\chi,s's} = \frac{1}{4} Tr(\sigma^j \sigma^i) = \frac{1}{4} Tr(\delta_{ij} \mathbb{1} + i\epsilon_{ijk}\sigma^k) = \frac{1}{2}\delta_{ij}. \tag{8.2.69}$$

We obtain

$$|\bar{\mathcal{M}}|^2 = \frac{64 m_N^2 m_\chi^2}{(2J_N + 1)} \left[\sum_{q=u,d,s} d_q \lambda_q \right]^2 \sum_{N_f} \langle N_f | J_N^2 | N_f \rangle. \tag{8.2.70}$$

Finally we can evaluate J^2 to be $J_N(J_N + 1)$ and carry out the sum over initial polarisations which gives a factor of $2J_N + 1$. The squared matrix element for the axial current is then

$$|\bar{\mathcal{M}}|^2 = 64 m_N^2 m_\chi^2 \left[\sum_{q=u,d,s} d_q \lambda_q \right]^2 J_N(J_N + 1) \tag{8.2.71}$$

and the scattering cross section in the zero momentum transfer limit is given by

$$\sigma_N = \frac{4\mu^2}{\pi} \left[\sum_{q=u,d,s} d_q \lambda_q \right]^2 J_N(J_N + 1). \tag{8.2.72}$$

Spin (in)dependent scattering and nuclear form factors

At this point we take a step back and discuss the distinction between spin dependent and spin independent scattering. For spin independent scattering, once we figure out the effective couplings to protons and neutrons, we can write down the scattering cross section. The contribution from the nucleons simply add up:

$$\sigma_N = \frac{\mu^2}{\pi} \left[Z b_p + (A - Z) b_n \right]^2. \tag{8.2.73}$$

For scalar interaction one can approximate the coupling to the proton and neutron to be equal. Then the cross section scales as A^2. The spin independent cross section leads to large couplings to heavy nuclei. This allows direct detection experiments with elements in the detector such as XENON1T to set stringent limits on the spin independent scattering cross section. For spin dependent scattering there is no such enhancement. The WIMP couples to the spin of the nucleus, which is 0 or $\frac{1}{2}$ for most nuclei and only few elements have higher spin. The coupling to protons is of a similar order of magnitude as the coupling to e.g. Xenon. Thus direct detection limits on the spin dependent cross section are significantly weaker than those for spin independent scattering. Indirect detection experiments are, due to the high abundance of protons in the sun, similarly sensitive to both cross sections and competitive in setting limits on spin dependent scattering.

Up to this point, we simply calculated the scattering cross sections in the zero momentum transfer limit. This works fine for protons and neutrons. For heavier elements, we need to introduce form factors to account for loss of coherence at finite momentum transfer. These form factors have already been mentioned in Sec. 8.2.2 and 8.2.3. There are a number of different ways to express these form factors (see e.g. [111] for a discussion). For our purposes it is sufficient to stick to Gaussian form factors which can be integrated analytically. We include the form factors in the differential cross section:

$$\frac{d\sigma_N}{d|\mathbf{q}|^2} = \frac{\sigma_N(E_R = 0)}{4\mu v^2} F(E_R). \tag{8.2.74}$$

$E_R = |\mathbf{q}|^2/(2m_N)$ denotes the recoil energy and $\sigma_N(E_R = 0)$ are the cross sections in the zero momentum transfer and zero mass splitting limit calculated above. μ is the WIMP nucleus reduced mass and v is the relative velocity.[2] For spin independent scattering the form factor is given by [106]

$$F(E_R) = exp\left(-\frac{E_R 2 m_N R^2}{3}\right) \tag{8.2.75}$$

with

$$R = \left[0.91\left(\frac{m_N}{\text{GeV}}\right)^{\frac{1}{3}} + 0.3\right] \times 10^{-13}. \tag{8.2.76}$$

For spin dependent scattering there is also a Gaussian form factor as discussed in Ref. [111] given by

$$F(E_R) = exp\left(-\frac{E_R m_N R_A^2}{2}\right) \tag{8.2.77}$$

[2]Note that the above formula is not in conflict with Eq. (8.2.18) even though this is not apparent at first sight.

with

$$R_A = 1.7A^{\frac{1}{3}} - 0.28 - 0.78\left(A^{\frac{1}{3}} - 3.8 + \left[(A^{\frac{1}{3}} - 3.8)^2 + 0.2\right]^{\frac{1}{2}}\right). \qquad (8.2.78)$$

8.2.5 Numeric calculation of capture rate

To calculate the capture rate for inelastic dark matter, we manipulate existing DarkSUSY-6.2.3 [112] routines, namely *dssenu_capsunnum* and the routines therein, to encompass the inelastic scenario described in Sec. 8.2.3. We use the respective Gaussian form factors described in Sec. 8.2.4 for both spin dependent and spin independent scattering. The Gaussian form factors can be integrated analytically. Note that some references, e.g. [101] use different form factors such as the Helm form factor. The different form factors can explain some minor deviations between our results and results in the literature. For spin dependent scattering we also use the DarkSUSY routines to utilize the internal spin structure functions for whose we set the momentum transfer q to zero and then use the Gaussian form factors.

We first test our routine by reproducing Fig. 2. from the DarkSUSY manual [112]. Our results are shown in Fig. 8.2. The only difference worth mentioning is that for for spin dependent scattering the elements Na and 13N are swapped. Additionally 14N does not show up in the DarkSUSY manual. The bumps show up when $m_\chi \approx m_N$. In the equal mass limit, the energy transfer is generally larger. Note that for spin independent scattering for $m_\chi \gtrsim 100$ GeV the main contribution to the capture rate is from heavy elements even though these are less abundant. Since for light elements the energy transfer is small, the WIMPs do not lose enough kinetic energy and can still escape the suns gravitational field.

In order to test our code in the inelastic case, we reproduce some results from Ref. [101] as shown in Fig. 8.3. In this reference the Helm form factor is used. This explains the (small) deviations from our results. In Fig. 8.3 we see the capture rate due to different elements as a function of the mass splitting. For light elements such as H and He the capture rate decreases already for small mass splittings. For heavy elements such as Fe the capture rate increases slightly before falling of at $\delta \approx 200$ keV. The right hand side of Fig. 8.3 shows the suppression of the capture rate due to the inelasticity δ. For small dark matter masses the inelastic case is strongly suppressed. For heavier WIMPs ($m_\chi \approx 200$ GeV) the inelastic scenario is less suppressed. Note that

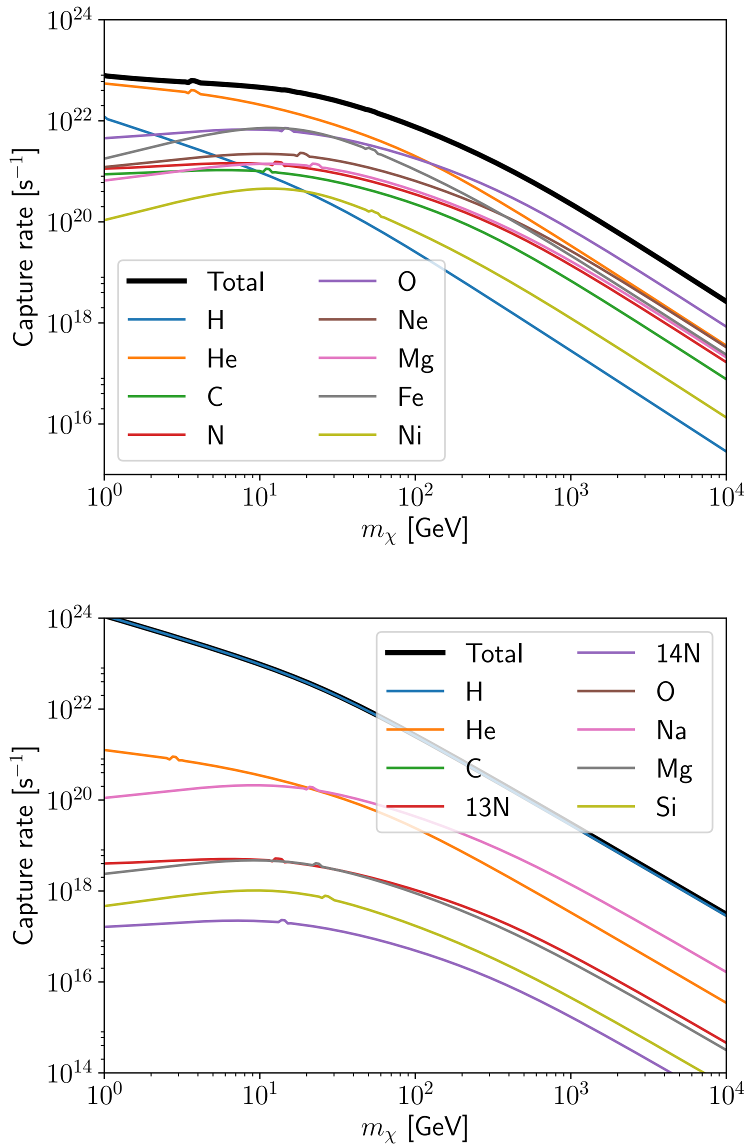

Figure 8.2: The capture rate due to different elements in the elastic limit ($\delta = 0$) for both spin independent (top) and spin dependent (bottom). The respective cross sections are $\sigma_{\mathrm{SI}} = 10^{-43}$ cm^2 and $\sigma_{\mathrm{SD}} = 10^{-41}$ cm^2 as in the DarkSUSY manual, Fig. 2 [112].

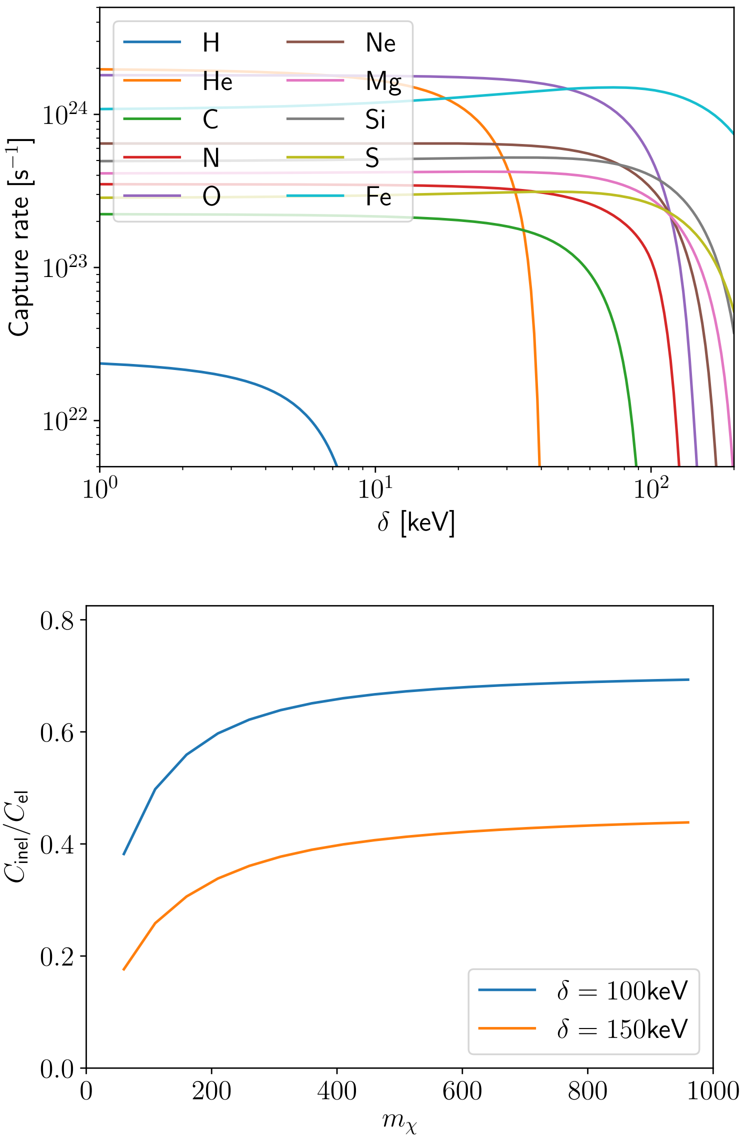

Figure 8.3: (top) The contributions to capture rate the capture rate from different elements as a function of the mass splitting δ. The dark matter mass is set to $m_\chi = 100$ GeV. The (spin independent) cross section is $\sigma_{\text{SI}} = 10^{-40}$ cm^2. (bottom) Ratio of the capture rates for the inelastic and the elastic scenario for the mass splittings $\delta = 100, 150$ keV. These figures are reproductions of Fig. 3 & 4 in Ref. [101].

in Ref. [101] Eq. (25) is incorrect and it should read $E_{\text{max}}^{\text{elastic}} = 4\mu^2 w^2/(2m_N)$.[3]

Figure 8.4 shows the dependence of the capture rate on the dark matter mass and the mass splitting similar to Fig. 3 in Ref. [100]. The solid lines correspond to the case where the lower integration bound in Eq. (8.2.18) is given by $Q'_{\text{min}} = max(Q_{\text{cap}}, Q_{\text{min}})$. As explained in Sec. 8.2.3 this is the correct way, since it takes the case where minimal energy transfer allowed for inelastic scattering is larger than the energy transfer needed for capture into account. This is also mentioned in Ref. [102]. The dashed lines correspond to the (incorrect) lower integration limit given in Ref. [100]. These lines reproduce the results of Ref. [100].

Finally we can reproduce Fig. 1. in Ref. [102]. Since this plot is similar to Fig. 8.3 (top), it is not shown here.

8.2.6 Annihilation rate and neutrino flux

The evolution of the number of WIMPs in the sun N is given by [113]

$$\dot{N} = C - 2\Gamma_A - C_E N \qquad \text{with} \qquad \Gamma_A = \frac{C_A N^2}{2}, \tag{8.2.79}$$

where C is the capture rate, Γ_A is the annihilation rate and $C_E N$ is the evaporation rate which we savely neglect since we study heavy dark matter candidates. Assuming the system is in equilibrium [114] ($\dot{N} = 0$) there is a linear relation between the capture rate and the annihilation rate

$$\Gamma_A = \frac{C}{2}. \tag{8.2.80}$$

The assumption of a sufficiently large scattering cross section is not trivial in case of inelastic scattering. The case in which purely inelastic scattering is present is discussed in Ref. [114]. There it was found that for an inelastic scattering cross section of $\sigma_p \approx 10^{-6}$ pb, dark matter masses above 100 GeV and $\delta > 200$ keV equilibrium is not reached. For our model we have a much larger inelastic cross section of $\sigma_p \approx 10^{-4}$ pb which allows for faster settlement to equilibrium. As we also have elastic scattering cross sections, WIMPs can be captured through an inelastic scattering process and subsequently thermalise

[3] In Ref. [101] Fig. 5 (bottom left) and Fig. 6. are inconsistent with Fig. 4 in the same reference. The authors have been contacted to resolve these deviations, however no explanation was found.

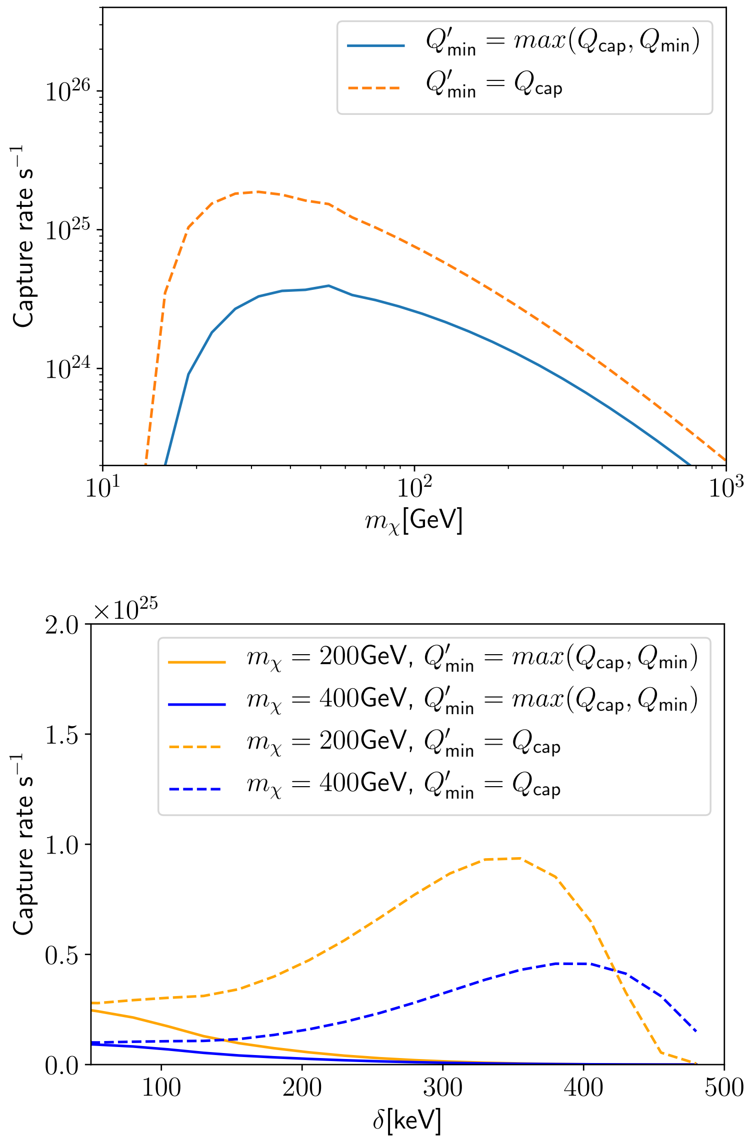

Figure 8.4: Capture rate as a function of the dark matter mass with δ = 125 keV (top) and as a function of δ for $m_\chi = 200, 400$ GeV (bottom). The lower integration bound in Eq. (8.2.18) is chosen according to Ref. [102] (solid) and Ref. [100] (dashed). (See text for details.) The scattering cross section is $\sigma_{\text{SI}} = 10^{-40}$ cm^2. These figures are similar to Fig. 3 in Ref. [100]. Note that DarkSUSY uses $v_\odot = 220$ km/s.

via elastic scattering. This case has been discussed in Ref. [101], where it was reported that for elastic scattering cross sections of approximately 10^{-12} pb equilibrium is reached. It should be stressed that, while for most models the assumption of equilibrium is safely fulfilled, there are parts of the parameter space, namely for large mass splittings and small elastic scattering cross sections, where this is not the case. If equilibrium is not reached, the annihilation rate and thus the IceCube event rate would be suppressed.

In Secs. 8.2.2, 8.2.3 we saw a linear relation between the scattering cross section σ and the capture rate. Thus the annhilation rate Γ_A is also propotional to σ. When two dark matter particles annihilate, neutrinos can be produced either direcly or in the subsequent decay chain. The resulting neutrino flux from the sun depends greatly on the scattering cross section σ in addition to a depedence on the annihilation channels.

8.3 Indirect detection of (in)elastic dark matter in the Sun with IceCube

Our numerical analysis of elastic and inelastic dark matter and in particular of the expected neutrino signals at IceCube from dark matter annihilations in the Sun is based on an implementation of the model described in Sec. 6.2 in Sarah 4.14.0 [72]. The physical mass spectrum and branching ratios, in particular those for LFV processes, are computed with SPheno 4.0.3 [92, 93]. The dark matter relic density, direct detection cross sections and neutrino event rates are obtained from micrOMEGAs 5.0.8 [94].

Assuming equilibrium of capture and annihilation in the core of the Sun ($\Gamma = C/2$), the differential flux of neutrinos or antineutrinos on Earth is given by [27, 115]

$$\frac{d\phi_\nu}{dE_\nu} = \frac{1}{4\pi d_\odot^2}\Gamma \sum_f Br_{f\bar{f}} \frac{dN_f}{dE_\nu}, \tag{8.3.1}$$

where $d_\odot$ is the distance Earth-Sun, $Br_{f\bar{f}}$ are the branching fractions into particle-antiparticle final states $f\bar{f}$, and dN_f/dE_ν are the corresponding neutrino (antineutrino) energy spectra. In micrOMEGAs, the latter are computed based on tables and feature neutrino propagation and oscillation in the Sun and in vacuum. The function `neutrinoFlux` automatizes the process of calculating the capture rate, the annihilation branching ratios and spectra of the respective channels and provides the total neutrino flux at Earth. Since the inelastic scenario was not implemented in micrOMEGAs, we used CalcHEP 3.7 [116] to compute the corresponding dark matter-quark scattering matrix elements and cross sections as described in the previous section. We then use the modified routine `dssenu_capsunnum` in DarkSUSY 6.2.3 [112] to obtain the inelastic capture rate, which was then fed back to micrOMEGAs.

For the prediction of the neutrino flux in the IC86 detector we use the neutrino flux at the surface of the Earth, Eq. (8.3.1), convolved with the IC86 effective area as described later in this paragraph. That means that we make no effort to propagate the neutrino flux through the Earth's medium, so that matter effects in the Earth's interior like absorption and tau-regeneration are ignored. These effects are expected to have only a small impact on the result, but should be considered in an analysis which goes beyond the theoretical approach of this study.

The differential number of signal events in the detector is given by [115]

$$\frac{dN_s}{dE} = t_e \left(\frac{d\phi_{\nu_\mu}}{dE} A_{\nu_\mu}(E) + \frac{d\phi_{\bar{\nu}_\mu}}{dE} A_{\bar{\nu}_\mu}(E) \right) , \tag{8.3.2}$$

where t_e is the exposure time and $A_{\nu_\mu(\bar{\nu}_\mu)}$ is the muon neutrino (muon antineutrino) effective area of the detector. A routine for the effective area of the now obsolete configuration IC22 (where 22 is the number of data-taking strings), `IC22nuAr`, was already implemented in micrOMEGAs. We updated this routine using the data from Ref. [38] for the effective area of IC86. Eight DeepCore strings are part of the IC86 configuration. Including their effective area lowers the energy threshold to 10 GeV. We extrapolated the data points linearly to fit our energy range, as shown in Fig. 8.5. The corresponding data points have been taken from Ref. [38]. In the region where both selections overlap, we use the IceCube effective area, as it is larger than the one of the DeepCore selection.

IceCube is sensitive to both ν_μ and $\bar{\nu}_\mu$. However, the corresponding energy dependent deep-inelastic scattering cross sections with nucleons in the detector are slightly different. Since Ref. [38] provides only the combined ν_μ+$\bar{\nu}_\mu$ effective area, we calculate the individual effective areas by taking into account the different cross sections $\sigma_{\nu_\mu(\bar{\nu}_\mu)}$ given in Ref. [117] with the relation

$$A_{\nu_\mu(\bar{\nu}_\mu)} = \frac{A_{\text{combined}}}{1 + \frac{\sigma_{\bar{\nu}_\mu(\nu_\mu)}}{\sigma_{\nu_\mu(\bar{\nu}_\mu)}}} . \tag{8.3.3}$$

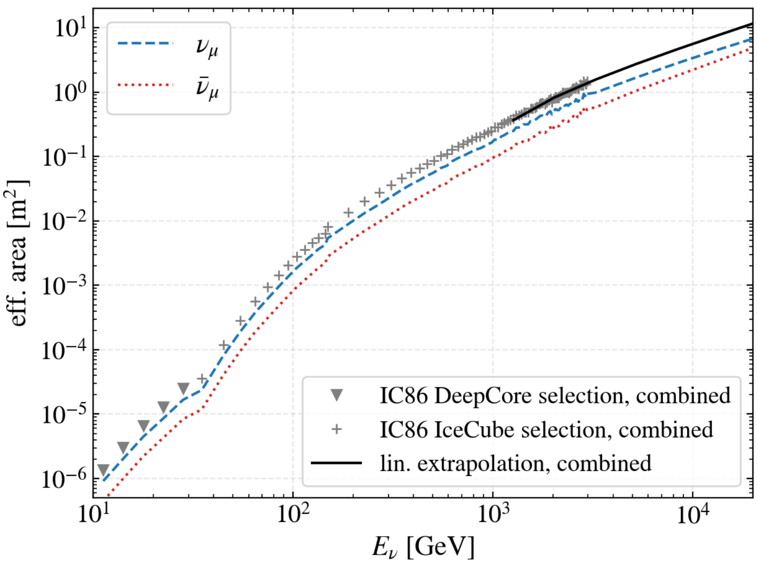

Figure 8.5: The ν_μ and $\bar{\nu}_\mu$ effective areas of the DeepCore detector and the IceCube detector configuration IC86 as a function of the neutrino energy. The data for the combined effective area is taken from Ref. [38] (triangles and crosses) and linearly extrapolated (solid black line). The individual effective areas for neutrinos (dashed blue line) and antineutrinos (dotted red line) are calculated with the deep inelastic scattering cross sections taken from Ref. [117]. Both the IceCube and DeepCore selections of the effective area are used in our work.

As there are now quite a number of tools involved for the numerical evaluation, we show an illustration of the toolchain in Fig. 8.6 and repeat the steps involved. This toolchain can easily be adapted to analyse different (minimal) models. The Lagrangian of the model can be generated using minimal-lagrangians [118]. The files generated by minimal-lagrangians can then be used to run SARAH [72, 73] which generated the code necessary to implement the model in SPheno [92, 93] and micrOMEGAs [94]. The steps up to this point only need to be executed once, whereas the following steps must be done for every point in the parameter space. We use a Python routine to operate the different pieces of code. First a random point in parameter space is generated and written into a SLHA file. Then SPheno is used in order to calculate the mass spectrum as well as observables such as the anomalous

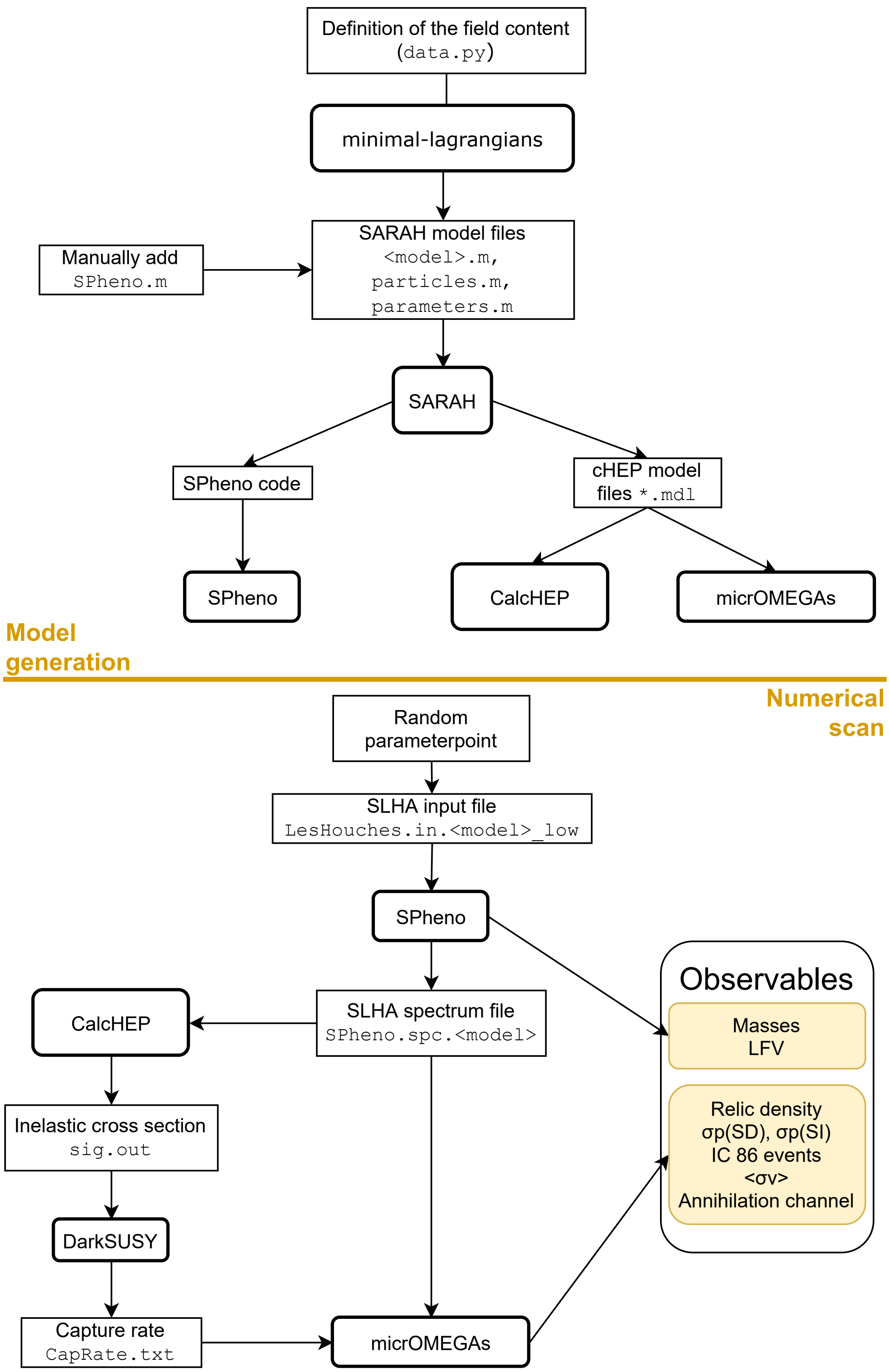

Figure 8.6: Illustration of the toolchain used in this work.

Table 8.2: Parameters of the scotogenic model for our benchmark point BPA. Shown are the coupling parameters λ_i, the squared mass m_η^2 of the new scalar doublet, the (diagonal) mass matrix m_N for the three new fermion singlets, and the real and imaginary parts of the Yukawa matrix, y^R and y^I.

λ_1	λ_2	λ_3	λ_4	λ_5	m_η^2	m_{N_1}	m_{N_2}	m_{N_3}
0.26	0.50	0.56	-0.14	$2.00 \cdot 10^{-7}$	$1.00 \cdot 10^{6}$	$1.32 \cdot 10^{3}$	$3.13 \cdot 10^{3}$	$3.44 \cdot 10^{3}$

$y^R/10^{-2}$	$y^I/10^{-3}$
$\begin{pmatrix} -17.20 & 2.07 & -6.91 \\ -4.94 & 9.41 & 15.17 \\ 5.22 & 15.98 & -8.20 \end{pmatrix}$	$\begin{pmatrix} 2.58 & 4.46 & 5.10 \\ -6.88 & 2.02 & 2.30 \\ -2.08 & -1.23 & -1.40 \end{pmatrix}$

magnetic moment of the muon, LFV and decay branching ratios. In order to implement inelastic scattering, a custom CalcHEP routine is used to calculate the inelastic quark nucleon scattering cross section in the non relativistic limit. These cross sections are then used by the DarkSUSY [112] routine `dssenu_capsunnum` and the routines therein which we modified in order to encompass the inelastic scattering scenario. This routine calculates the capture rate, which is then fed back into micrOMEGAs where it is used to calculate the neutrino flux at earth. This flux is then multiplied with the IC86 effective area in order to calculate the expected event rates a IceCube. micrOMEGAs is also used to calculate dark matter related observables such as the elastic dark matter nucleon scattering cross sections, the relic density, the thermally averaged annihilation cross section and the event rate at IceCube stemming from elastic scattering in the sun.

We illustrate the expected neutrino fluxes at Earth and event rates in IceCube for a specific benchmark point BPA in the scotogenic model which has been chosen randomly, and is representative for the parameter space of the model. The corresponding parameters are listed in Tab. 8.2. With these parameters, we obtain the correct relic density of $\Omega h^2 = 0.1217$ for the scalar dark matter candidate η^{0I} with mass 1007.38 GeV. In descending order of importance, the dark matter annihilation channels are W^+W^- (58.36%), Z^0Z^0 (23.51%), hh (12.30%) and $W^+W^-\gamma$ (4.99%), i.e. W^+W^- pairs (plus an accompanying photon) represent the dominant channel with a branching fraction of over 63%, as is the case for most points in the parameter space with $m_{\eta^{0R,I}} > m_W$. Direct annihilation into neutrinos is suppressed by both the small Yukawa couplings $y_{i\alpha}$ and the large neutrino propagator masses m_{N_i}.

We show the differential neutrino and antineutrino fluxes at BPA for both elastic (blue) and inelastic (red) scattering in the Sun in Fig. 8.7 (top). The differences in differential fluxes between neutrinos (full) and antineutrinos (dashed lines) that show up at high energies are due to absorption (also oscillation and regeneration) effects taking place inside the Sun [119]. Because there is no annihilation into neutrinos directly, we do not observe a monochromatic neutrino line in the spectrum, but instead a sharp cut-off at the dark matter mass of about 1 TeV. The differential number of expected signal events per year in IC86 is shown in Fig. 8.7 (bottom). After integration over the neutrino energy, BPA yields a total number of only 0.07 expected events per year in IC86 in the elastic case, but $8.65 \cdot 10^4$ in the inelastic case.

8.4 Numerical scan

Using the tool chain described in the previous chapter, we now perform a numerical scan of the scotogenic parameter space by means of random sampling. To comply with the requirements of vacuum stability, perturbativity and that the lightest scalar must be neutral, the scalar couplings are varied within the ranges

$$\lambda_3 \in \left[-\sqrt{\lambda_1\lambda_2}, 4\pi\right] \ , \tag{8.4.1}$$

$$\lambda_4 \in \left[\max\{-\sqrt{\lambda_1\lambda_2} - \lambda_3 + |\lambda_5|\,, -4\pi\}, 0\right] \ , \tag{8.4.2}$$

$$|\lambda_5| \in \left[10^{-10}, 10^{-3}\right] \tag{8.4.3}$$

As was mentioned in Sec. 6.2, λ_5 is naturally small, since the Standard Model neutrino masses would vanish and the symmetry of the Lagrangian increase if it were exactly zero. The mass parameter of the new scalar doublet is varied in the range

$$m_\eta \in [1 \text{ GeV}, 10 \text{ TeV}]\,. \tag{8.4.4}$$

The masses m_{N_i} of the new fermion singlets are required to be larger than the mass of the lightest scalar, but below 10 TeV. In a second scan, we choose this mass difference to be small (i.e. 0.1 GeV) in order to demonstrate the impact

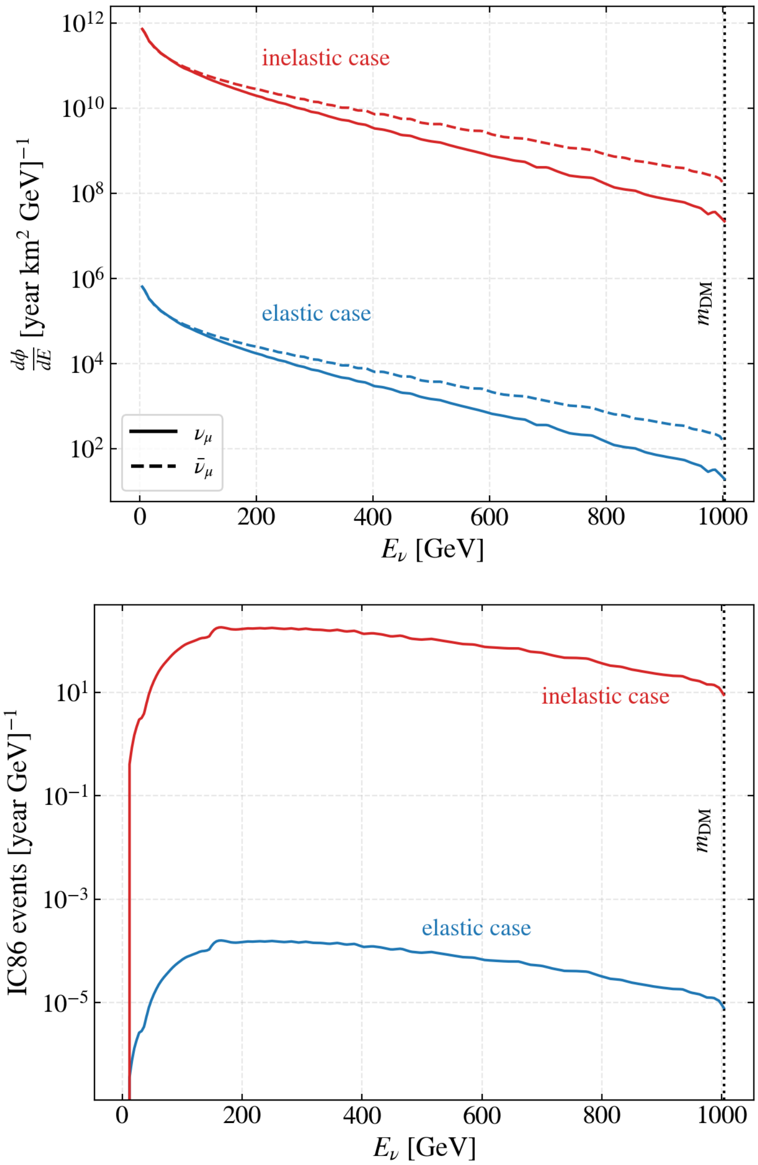

Figure 8.7: Top: Elastic (blue) and inelastic (red) muon neutrino (full) and antineutrino (dashed) fluxes at Earth as a function of the neutrino energy, calculated with the modified function `neutrinoFlux` in MICROMEGAS at the parameter point BPA. The mass of the dark matter particle η^{0I} is 1007.38 GeV. Bottom: Expected number of signal events in IC86 per year as a function of the neutrino energy.

of coannihilation processes [120]. The Standard Model neutrino oscillation parameters are taken from Ref. [51] in the 3σ range, assuming normal ordering. The CP violating phase δ_{CP} is varied from zero to 2π, and the lightest neutrino mass is varied in the interval $[10^{-4}, 1.1]$ eV in accordance with the most recent limit set by KATRIN [8]. All mass parameters, as well as λ_5 are sampled uniformly in log space, as they are varied over several orders of magnitude. All remaining parameters are sampled uniformly in a linear fashion. The Yukawa couplings are then calculated using the Casas-Ibarra parametrization and required to satisfy $|y_{i\alpha}|^2 < 4\pi$.

The scotogenic model is further constrained by a number of other experimental measurements. In particular, we impose the relic density measurement by PLANCK [16] with a relatively loose margin of $\Omega h^2 = 0.12 \pm 0.02$ in order to account for theoretical uncertainties [121]. We also impose the LFV branching ratios (BR) and conversion rate (CR) of

$$\begin{aligned} \mathrm{BR}\,(\mu \to e + \gamma) &< 4.2 \cdot 10^{-13}, \\ \mathrm{BR}\,(\mu \to 3e) &< 1.0 \cdot 10^{-12}, \\ \mathrm{CR}\,(\mu - e, \mathrm{Ti}) &< 4.3 \cdot 10^{-12}, \end{aligned} \tag{8.4.5}$$

published by the MEG [57], SINDRUM [59] and SINDRUM II [61] collaborations. Furthermore, we apply limits on the new physics invisible decay width of the Z^0 boson from LEP [122]

$$\mathrm{BR}(Z^0 \to \mathrm{new}) < 0.008, \tag{8.4.6}$$

which effectively excludes $m_{\mathrm{DM}} < m_{Z^0}/2$ [123, 124], and on the invisible decay width of the Standard Model Higgs boson from ATLAS (CMS) at the LHC [125, 126]

$$\mathrm{BR}(h \to \mathrm{inv.}) < 0.11\ (0.19), \tag{8.4.7}$$

as well as on the elastic and inelastic scattering cross section from direct searches with XENON1T [34], XENON100 [127, 128] and PANDAX-II [129]. The possible signal from DAMA/LIBRA [41, 99], its ongoing verification [130–132], previous limits on indirect detection from dark matter annihilation into neutrinos in the Sun [37–39] and the Galactic Center [47, 48, 133, 134], and expected event rates for neutrinos from the Sun in the current ICECUBE configuration with 86 strings (IC86) are also discussed in the following.

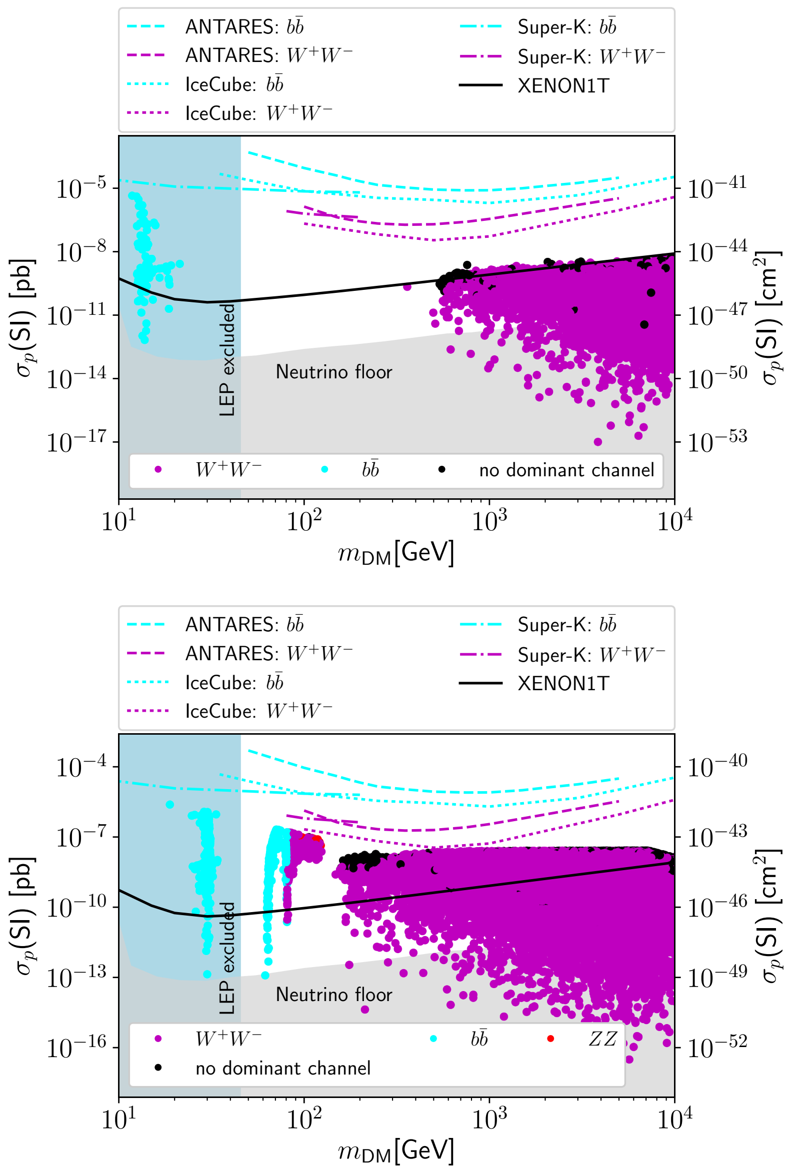

Figure 8.8: The spin independent (SI) elastic cross section with ANTARES [37], IceCube [38], Super-Kamiokande [39] and XENON1T [34] exclusion limits as a function of the dark matter mass. All points and lines are color coded according to the main annihilation channel, provided there is one with a branching ratio of over 50%. Also shown are the LEP exclusion from the invisible Z^0 boson width [123, 124] and the neutrino floor [40]. In the lower plot, coannihilation processes are enhanced by the small scalar-fermion mass difference.

8.4.1 Limits on the elastic cross section

Our spin independent elastic cross section results for scalar dark matter in the scotogenic model are shown in Fig. 8.8. Apart from the larger mass range of our scan and considering that we imposed updated constraints from the Higgs mass, dark matter relic density, neutrino masses/mixings and LFV, our results agree with those in Fig. 9 in Ref. [120]. In particular, models with low mass dark matter contain sufficiently heavy charged scalars to evade the corresponding LEP2 bound [49], but are excluded by the LEP limit on the invisible Z^0 decay width [123, 124]. Since there are no viable models with $m_{Z^0}/2 < m_{\rm DM} < m_h/2$, there are no additional constraints from the invisible h decay width [125, 126]. Otherwise and as well known, the correct relic density requires the dark matter to be larger than about 500 GeV (top). Fermion coannihilation processes reduce this lower mass limit to about 200 GeV (bottom) [120]. The sampled points are color coded according to the dominant annihilation branching ratio. A point is marked as having no dominant channel when no single branching ratio reaches 50%. Above the W boson threshold, mostly annihilation into W boson pairs occurs. The channel-dependent constraints derived from indirect dark matter detection with ANTARES [37], IceCube [38] and Super-Kamiokande [39] are considerably weaker than the direct detection constraints from XENON1T [34]. Only the latter constrain the parameter space, and in particular the coannihilation region. Since the Higgs coupling to the quarks in the nucleon is relatively small, the elastic cross sections are small as well. A significant part of the parameter space for dark matter masses beyond 1 TeV results even in cross sections below the atmospheric and diffuse supernova background (DSNB) neutrino "floor" [40], which may render dark matter direct detection difficult.

8.4.2 Limits on the inelastic cross section

The observation of an annual modulation signal by DAMA/LIBRA [41, 99], its interpretation as dark matter of low or (relatively) higher mass of about 10 and 50 GeV [135, 136] and the tension with other direct detection experiments have led to the speculation that dark matter might only undergo inelastic scattering off nuclei in DAMA/LIBRA, to which other experiments would not be sensitive [87]. To fit the DAMA/LIBRA observation, the inelastic nucleon cross section was usually assumed to be 10^{-4} pb [100–102]. This value

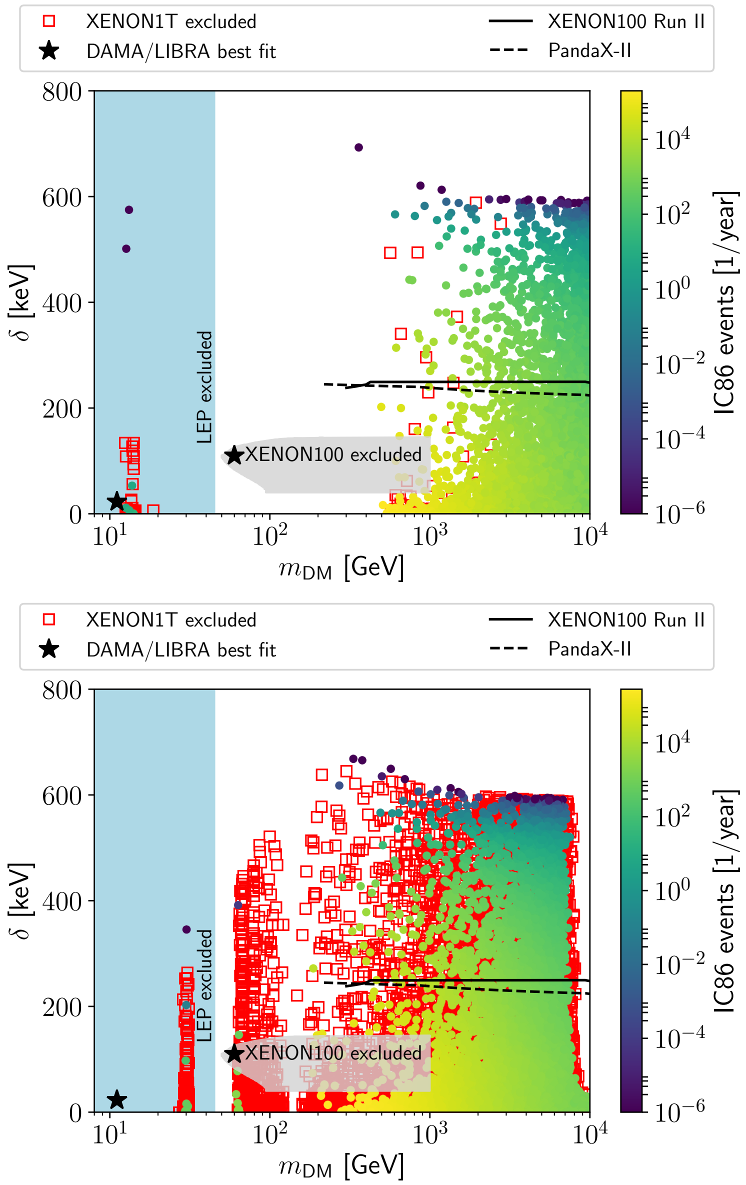

Figure 8.9: Scotogenic models in the plane dark matter mass vs. neutral scalar mass splitting, color coded for expected IC86 events (temperature scale) and elastic scattering exclusion by XENON1T (red boxes) [34]. Also shown are the exclusion of the low- (sodium) [108] and high-mass (iodine) DAMA/LIBRA preferred regions [41, 99] by LEP and XENON100 [127] and the upper limits on the mass splitting from the XENON100 Run II data [128] and by the PandaX-II experiment with smaller recoil energy window and larger background [129]. In the lower plot, coannihilation processes are enhanced by the small scalar-fermion mass difference.

is indeed close to the proton cross section of $1.7 \cdot 10^{-4}$ pb in the scotogenic model, where the mediator is not a Higgs (h) boson, but an electroweak gauge (Z^0), which violates isospin by $b_n/b_p = 1/(4\sin^2\theta_W - 1) \simeq -6.6$.[4] It also corresponds to typical cross sections in the inert doublet model, which is in fact the only model with a *single* scalar dark matter multiplet that allows for naturally small neutral component mass splittings at the renormalizable level [137].

In Fig. 8.9, we plot all scotogenic model points that survive Higgs mass, dark matter relic density, neutrino mass/mixing and LFV constraints in the plane dark matter mass and neutral scalar mass splitting. The points are color coded for expected IC86 events (temperature scale) and exclusion of elastic scattering by XENON1T (red boxes) [34]. Following the observations by DAMA/LIBRA [41, 99], several other experiments have specifically searched for inelastic dark matter. In a first analysis of 100.9 live days of data with a fiducial volume containing 48 kg of liquid xenon, XENON100 (grey shaded areas) excluded the high mass (iodine) preferred region with mass splittings up to 140 keV [127]. The Run II data with 224.6 live days of data with a fiducial volume containing 34 kg of liquid xenon was later reanalyzed in the context of effective field theory (EFT) using the correspondence

$$\sigma_N^0 = (C_1^N)^2 \frac{\mu_N^2}{\pi}, \tag{8.4.8}$$

where μ_N is the dark matter-nucleon reduced mass and C_1^N is the coefficient of the spin-independent operator [128]. Since in our case the interaction is not isospin-conserving, we translate the limits on C_1^N from Ref. [128] to the proton cross section as [138]

$$\sigma_p^0 = \sigma_N^0 \left[\frac{Z}{A} + \left(1 - \frac{Z}{A}\right)\frac{b_n}{b_p}\right]^{-2}, \tag{8.4.9}$$

assuming for simplicity $A = 132$ for the xenon isotope with the largest abundance. This excludes the mass region above 300 GeV with mass splittings up to 250 keV (full black lines). PandaX-II, who analyzed 79.6 live days of data with a fiducial volume containing 329 kg of liquid xenon, presented their results only for fixed dark matter masses of 1 and 10 TeV [129]. When interpolated and translated for isospin violation, they give a similar, but slightly

[4] The neutron cross section $1/(2\pi)G_F^2 m_N^2 = 74.3 \cdot 10^{-4}$ pb is therefore significantly larger [104, 137].

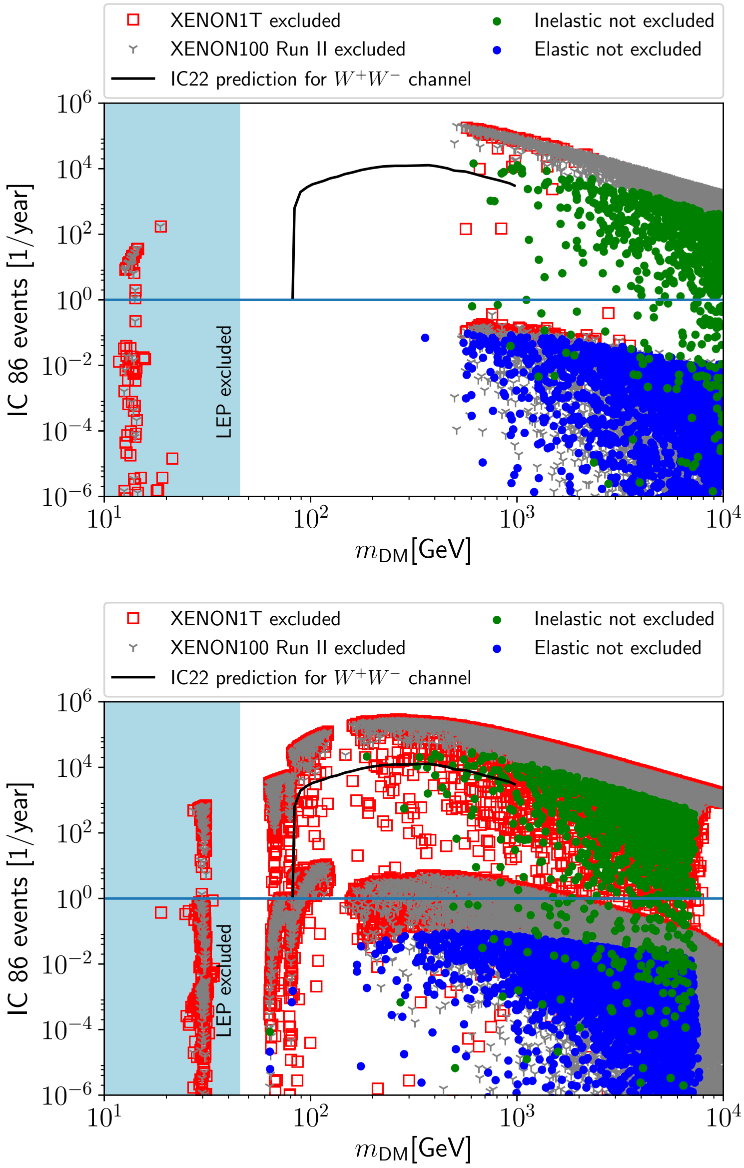

Figure 8.10: The expected number of events per year in the current IceCube configuration with 86 strings (IC86) as a function of the dark matter mass from inelastic and elastic dark matter scattering in the Sun. The black line marks the number of expected events in the W^+W^- channel for IC22 [102]. The blue line marks one event per year for orientation. Also shown are the points excluded by XENON1T [34], XENON100 [127, 128] and LEP from the invisible Z^0 boson width [123, 124]. In the lower plot, coannihilation processes are enhanced by the small scalar-fermion mass difference.

weaker exclusion curve (dashed black lines) as/than Xenon100 due to the smaller recoil energy window and larger background. The exclusion of larger mass splittings with direct detection experiments is limited by the maximum recoil energy and would require much larger cross sections than expected from electroweak interactions [139]. The low-mass (sodium) point (black stars), to which a good fit is still possible, albeit with a large cross section of 10^{-2} pb and different isospin violation $b_n/b_p \simeq -0.7$ [136, 140], as well as the (already excluded) high-mass (iodine) point to the DAMA/LIBRA signal [108] are under intense scrutiny by the DM-Ice17 [130], COSINE-100 [131, 141], SABRE [142] and ANAIS-112 [132] experiments, which are expected to provide a 3σ C.L. test of this signal by autumn 2022.

8.4.3 Expected IC86 event rates from (in)elastic dark matter scattering in the Sun

The expected number of events in the current IceCube configuration with 86 strings (IC86) was already shown by color coding in Fig. 8.9. It ranges from less than 10^{-6} to more than 10^5 per year. For both the random and the coannihilation scan, at least ten events are expected for neutral scalar mass splittings $\delta \leq (500 \pm 20)$ keV. Points below 250 keV were already excluded by XENON100 [128], but half of the parameter space could be tested with IC86 for the first time. From Eq. (6.2.14), the non-observation of the predicted events would set a lower bound on

$$\lambda_5 \gtrsim 1.6 \cdot 10^{-5} \cdot m_{\mathrm{DM}}/\mathrm{TeV}. \tag{8.4.10}$$

In the following, we analyze the expected event rates in more detail. Fig. 8.10 shows the expected number of events per year as a function of the dark matter mass for both inelastic and elastic dark matter scattering in the Sun, i.e. when both occurs two points are shown. Points excluded by XENON1T [34], XENON100 [127, 128] and LEP from the invisible Z^0 boson width [123, 124] are also shown. The black line shows a previous estimate of the number of expected inelastic events in the W^+W^- channel for IC22 [102], which scales roughly as expected with our IC86 predictions. Note that this and other previous analyses of indirect detection of inelastic dark matter were motivated by the high-mass (iodine) DAMA/LIBRA best fit point with $\delta = (125 \pm 25)$ keV [100–102]. In our Fig. 8.10, the blue line marks one event per year for orientation. As one can see, the expected event rates for models with only elastic scattering stay below this line. In the lower plot, where coannihilation processes are enhanced by the small scalar-fermion mass difference, models with larger elastic scattering rates are already excluded by direct detection experiments. Nevertheless, inelastic scattering allows for a large region of the scalar dark matter parameter space with and without coannihilation to be tested by IC86.

Fig. 8.11 shows the expected number of events per year as a function of the neutral scalar mass splitting δ. Although we scan values above $\lambda_5 \geq 10^{-10}$, the neutrino masses constrain λ_5 to be larger than 10^{-9}. In addition, in the coannihilation scenario the relic density mostly requires values above 10^{-8}. From Fig. 8.9 we know that direct detection experiments exclude neutral scalar mass splittings below 250 keV, which for $m_{\mathrm{DM}} \geq 500$ (200) GeV in the normal (coannihilation) scan translates through Eq. (6.2.14) to a limit of $\lambda_5 \gtrsim 4.1$ (1.7) $\cdot 10^{-6}$. With IC86, mass splittings up to 500 keV and at least two more orders of magnitude in λ_5 could be tested up to $1.6 \cdot 10^{-4}$ (or beyond) for $m_{\mathrm{DM}} = 10$ TeV (or larger). While the event rate falls quickly for inelastic scattering towards the kinematic edge, it is of course independent of both δ and λ_5 in the elastic case. This is illustrated in Fig. 8.12, where the event rate due to inelastic and elastic processes have been summed. For higher values of δ, the elastic process is dominant. In the other regions inelastic scattering dominates by several orders of magnitude, such that the total event rate is in practice determined by the inelastic scattering process alone. The scattered points below the main bulk correspond to points with lower masses, where the inelastic scattering rate is lower, as can be seen in Fig. 8.10.

8.4.4 Limits from dark matter annihilations in the Galactic Center

Neutrino telescopes are also used to set bounds on the self annihilation of dark matter in the Galactic Center. We test the scotogenic model with the limits on the thermally averaged self annihilation cross section $\langle \sigma v \rangle$ set by a joint analysis of ANTARES and IceCube [47], assuming a NFW halo profile [143]. The results are shown in Fig. 8.13. All points are color coded for their dominant annihilation channel (i.e. $b\bar{b}$ quark, W^+W^- and Z^0Z^0 boson pairs). Points with no branching ratio larger than 50% are marked as "no

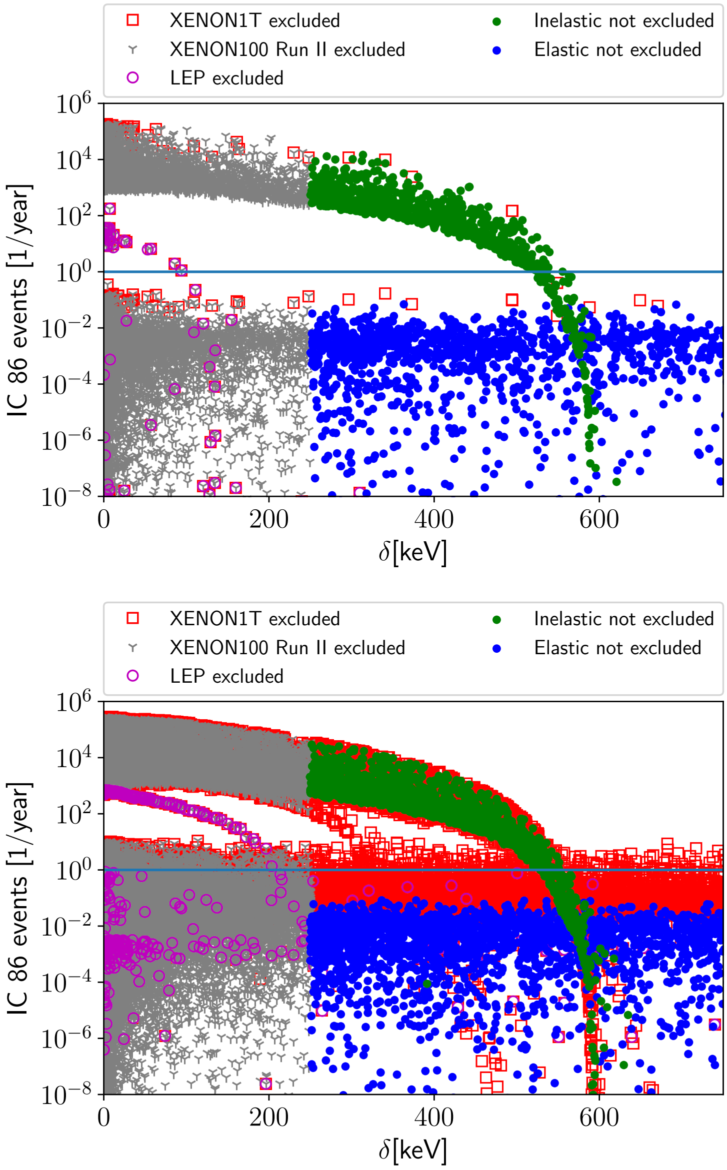

Figure 8.11: Same as Fig. 8.10 as a function of the neutral scalar mass splitting δ.

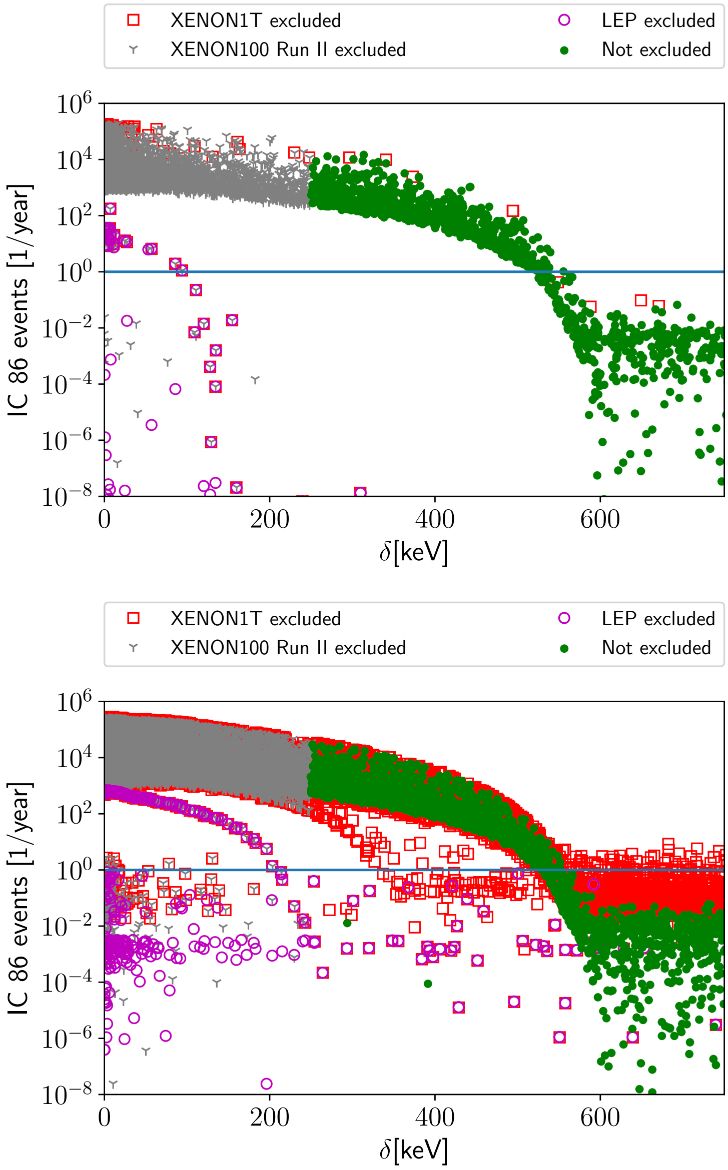

Figure 8.12: Same as Fig. 8.11, where the inelastic and eleastic event rates have been summed.

dominant channel". The predictions agree roughly with the naive expectation for a thermal relic [144], but can be considerably larger in the coannihilation scenario, where the coannhiliation processes increase rather than decrease the predicted dark matter relic density [120]. Contrary to dark matter annihilation in the Sun, the direct detection experiments XENON1T [34] and XENON100 [127, 128] now exclude points with *lower* expected rates, while *larger* rates remain viable. This can be attributed to the fact that the dark matter density in the Galactic Center is now fixed by the NFW profile and not determined by (in)elastic scattering and the capture rate. Low-mass points annihilating mostly into $b\bar{b}$ quarks are already excluded by the direct detection experiments and LEP from the invisible Z^0 boson width [123, 124], whereas the limits from Super-Kamiokande [39] are much weaker. For high-mass points, dark matter annihilation into W^+W^- bosons is dominant. While the points from our random scan lie still considerably below the limits set by ANTARES and IceCube [47], those from our coannihilation scan are less than an order of magnitude smaller and should be within reach of the next IC86 analysis. It would be particularly interesting to extend the mass range of this analysis from 1 to 10 TeV and beyond.

8.5 Summary

To summarize, we have investigated in this chapter the indirect detection prospects of scalar dark matter in the scotogenic model. We have focused on dark matter annihilation into neutrinos in the Sun, but also in the Galactic Center. After a brief review of the particle content, interactions and neutrino mass generation in the scotogenic model, we described in detail the elastic and inelastic dark matter scattering processes induced by Higgs and Z^0 boson exchanges in the Sun, which determine the WIMP capture rate and thus also the annihilation rate into neutrinos and particles that decay into them. We then implemented the capture rate from inelastic scattering in DarkSUSY 6.2.3 and interfaced it with micrOMEGAs 5.0.8 and our updated routine for the expected neutrino fluxes on Earth and the effective area of the IceCube detector in its current 86-string configuration.

We then performed two large numerical scans spanning the theoretically allowed parameter space, i.e. a random scan and one with enhanced scalar-fermion coannihilation from a small dark matter-sterile neutrino mass splitting,

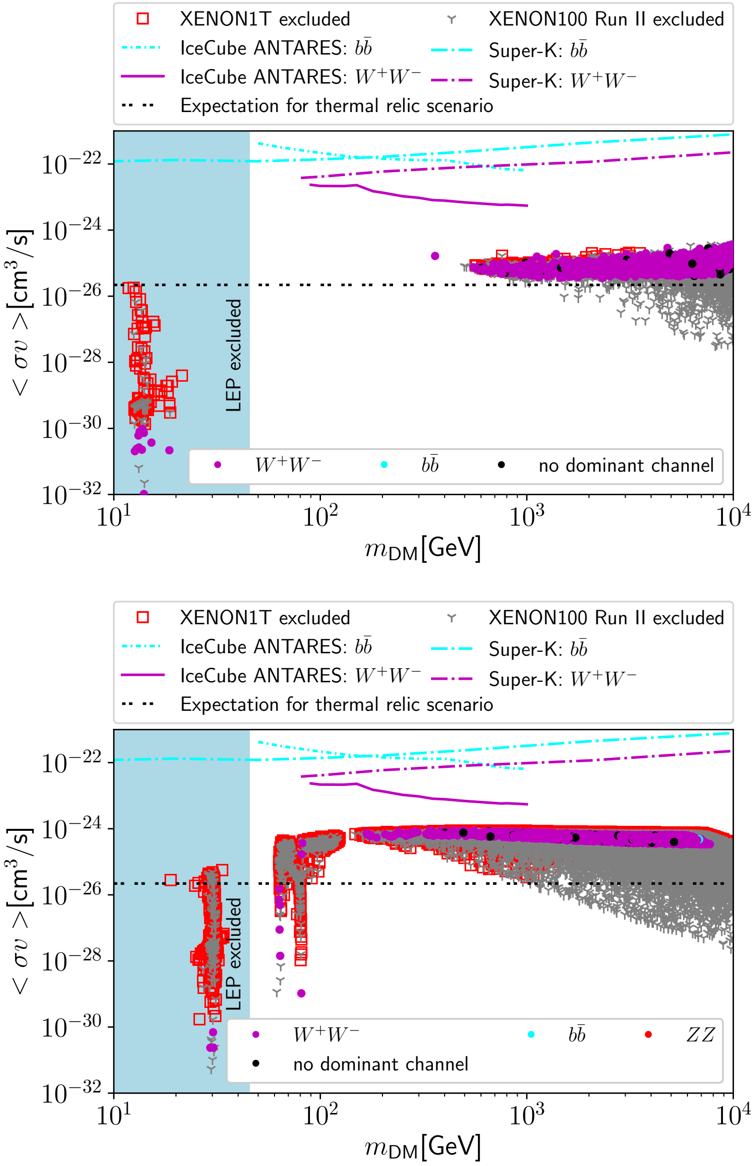

Figure 8.13: Thermally averaged cross section $\langle \sigma v \rangle$ with combined IceCube ANTARES [47] and Super-Kamiokande [48] exclusion limits as a function of the dark matter mass. All points are colored according to the main annihilation channel, provided there is one with a branching ratio of over 50%. Also shown are the points excluded by XENON1T [34], XENON100 [127, 128] and LEP from the invisible Z^0 boson width [123, 124] as well as the expected cross section for a thermal relic [144]. In the lower plot, coannihilation processes are enhanced by the small scalar-fermion mass difference.

which is known to increase the relic density and extend the viable scalar dark matter mass region from above 500 GeV to above 200 GeV. Experimental constraints were imposed from the known neutrino mass differences and mixing angles, LFV, the searches for new neutral and charged scalars at LEP and LEP2, the LHC measurements of the Higgs boson mass and invisible width, and from direct and previous indirect dark matter searches.

First, we found that direct, but not indirect detection experiments constrain the spin-independent elastic scattering cross section, in particular in the coannihilation scenario. We also found that a considerable fraction of the models lie below the neutrino floor, which may render direct detection difficult. We then showed that direct detection experiments cover only half of the parameter space for inelastic scattering, i.e. inelasticities up to 250 keV. The higher kinetic energy of dark matter in the Sun therefore leaves ample room for a dedicated analysis with IC86, that would cover inelasticities up to at least 500 keV. The expected rates extend well beyond 10^3 per year. The non-observation of the predicted neutrino events would translate into a lower limit on the scalar coupling $\lambda_5 \gtrsim 1.6 \cdot 10^{-5} \cdot m_{\mathrm{DM}}/\mathrm{TeV}$. For larger couplings, only elastic scattering has to be considered. In this case, the expected event rates for models that are not yet excluded by the direct detection experiments do not exceed 0.1 per year. We reminded the reader that the coupling λ_5 has to be naturally small, since if it was exactly zero, the neutrinos would be massless and lepton number would be conserved, leading to a larger symmetry of the Lagrangian.

Models with elastic and inelastic scattering can also be tested with dark matter annihilation in the Galactic Center, assuming e.g. a NFW dark matter profile. Here, we found that direct detection experiments exclude mostly models with lower thermally averaged cross sections. This could be attributed to the fact that the dark matter density in the Galactic Center was fixed by the NFW profile and not determined by (in)elastic scattering and the capture rate. Low-mass points annihilating mostly into $b\bar{b}$ quarks were already excluded by direct detection experiments and LEP, whereas the limits from Super-Kamiokande were much weaker. For high-mass points, dark matter annihilation into W^+W^- bosons was dominant. There, a previous combined analysis by ANTARES and IceCube led to limits that were two orders of magnitude above our predictions. For the coannihilation scenario, our predictions are, however, less than an order of magnitude smaller and thus within reach of the next IC86 analysis, in particular for TeV-scale dark matter.

Our results generalize to models with several scalar multiplets where the mass splitting between the neutral components is small. A particularly interesting case for future study would be the AMEND model with small singlet-triplet scalar mass splitting, which could again be small due to an otherwise larger symmetry of the Lagrangian [145].

9 Indirect detection constraints on the model T1-3-B

In this chapter we perform a similar analysis as in Chap. 8 but focus on a different model. The model studied here does not allow for the rather exotic scenario of inelastic scattering and thus the results generalize more easily to a wider class of models. It also encompasses both spin dependent and spin independent scattering allowing us to study the effect of both scattering types on the IceCube event rates. As the limits on spin dependent scattering set by direct detection experiments are generally weaker than the limits on spin independent scattering, indirect detection is especially competitive in the former case. For a detailed description of the model, we refer to Sec. 6.3. This chapter is based on our paper [2] which was created in collaboration with *Raffaela Busse, Alexander Kappes, Michael Klasen* and *Sybrand Zeinstra*.

9.1 Motivation

Dark matter and neutrinos are inherently linked in our model allowing for dark matter annihilations into neutrinos. With dark matter being heavy, such annihilations can lead to high energy neutrinos which are being searched for with neutrino telescopes such as the IceCube detector. The annihilation processes can lead to two different neutrino spectra. In particular, direct annihilation into neutrino pairs will result in a clear, distinct line at $E_\nu \simeq m_{\rm DM}$, whereas neutrinos produced from the decays of other Standard Model particles created by annihilations result in a continuous spectrum. Direct annihilation into neutrinos has been studied in Refs. [95–98]. Here, we will study the general case, where both scenarios are taken into consideration.

Monochromatic neutrinos provide a clear and distinct signal compared to a continuous spectrum. Since we also take into account the latter type of signals, we consider the case where the annihilation rate is enhanced by a local boost in the relic density. We focus on annihilations due to an increased relic density in the Sun. Other astrophysical objects that have been considered in the literature are e.g. the Earth [146, 147], the Galactic Center [47, 48, 133, 134], or super massive black holes [97].

As our solar system moves through the galactic halo, dark matter in the form of a weakly interacting massive particle (WIMP) can scatter off nuclei in the Sun. If enough of the kinetic energy of the WIMP is transferred in these scatterings, the WIMP will be gravitationally captured by the Sun [106, 148]. This will lead to an accumulation of WIMPs in the Sun's core, enhancing the local relic density and leading to a boost in annihilations. The capture rate depends chiefly on the WIMP-nucleon scattering cross section, on which direct and indirect detection experiments have put stringent constraints [28, 34, 37–39, 42, 43, 149, 150].

For definiteness, we consider here the radiative seesaw model T1-3-B with $\alpha = 0$ [89, 90], following the notation in Ref. [11], that can contain either a scalar or a fermionic dark matter candidate. The model is explained in all detail in Sec. 6.3 with a special emphasis on the spin (in)dependent scattering cross sections. Previous studies have shown that triplet scalar [91, 151–154] and singlet-doublet fermion dark matter [155–158] can both reproduce the relic density in agreement with the PLANCK satellite data [16].

9.2 Detecting neutrinos from dark matter in the Sun with IceCube

For our numerical analysis, we use the same routine already described in Chap. 8. As the model T1-3-B does not have naturally small mass splittings, inelastic scattering does not occur. Thus we do not need the routines specific to inelastic scattering and can use micrOMEGAs to calculate the scattering cross sections and the capture rate instead of our custom DarkSUSY routine.

We start by examining a typical benchmark point in order to illustrate procedure and show the neutrino energy spectrum. The parameters used for this point which gives rise to fermionic dark matter are given in Tab. 9.1 with the couplings chosen in such way, that the neutrino masses are correct. Figure 9.1 shows the differential (anti) neutrino flux as well as the expected event rates at IceCube for different neutrino energies. The neutrino flux is sharply cut of at $E_\nu = m_{\rm DM}$ as for non relativistic dark matter the kinetic energy

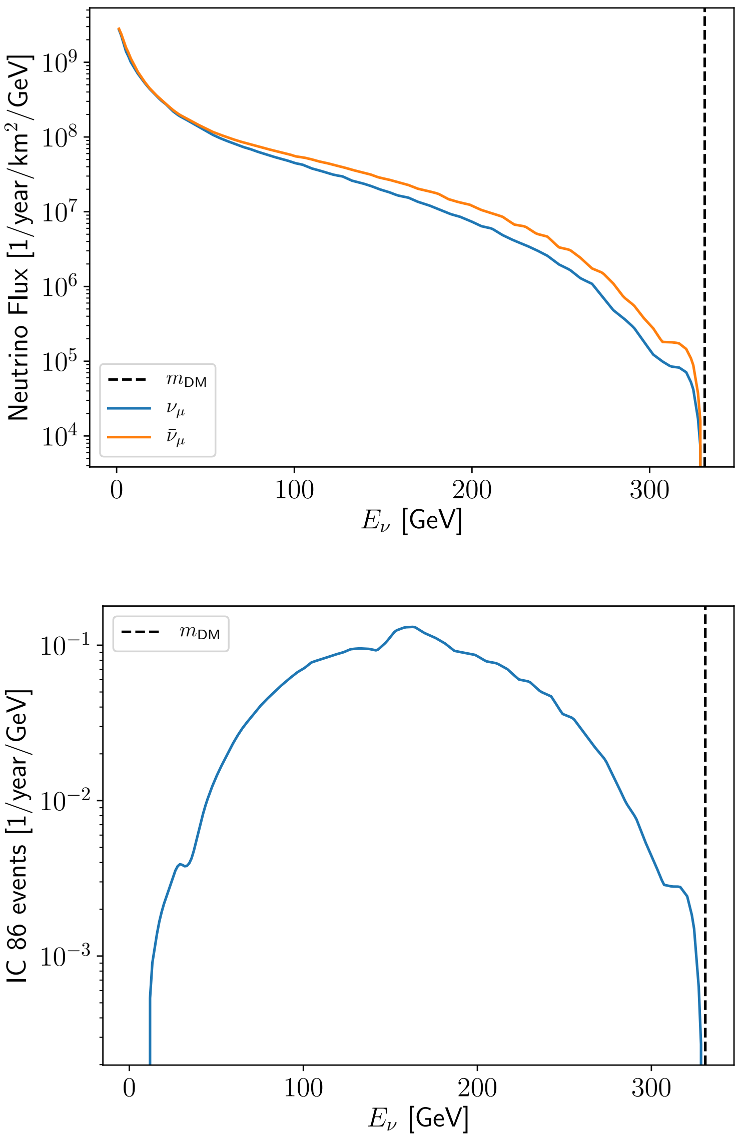

Figure 9.1: (Anti-)neutrino flux from the Sun (left) and expected event rate at IceCube (right) for the benchmark point given in Tab. 9.1. The dashed lines indicate the value of the dark matter mass.

Table 9.1: Parameters used for our benchmark point (masses in GeV). The matrix elements not mentioned (e.g. $\left(M_\phi^2\right)_{12}$) are set to zero.

M_Ψ	$M_{\psi\psi'}$	$(M_\phi^2)_{11}$	$(M_\phi^2)_{22}$
362	614	$2.4 \cdot 10^6$	$4.3 \cdot 10^7$

λ_4	λ_5	λ_1	λ_6
-0.17	-0.65	$\begin{pmatrix} 0.011 & 0 \\ 0 & 0.012 \end{pmatrix}$	$\begin{pmatrix} -1.74 & -5.28 \\ 0.90 & -18.67 \\ 5.36 & 11.91 \end{pmatrix} \cdot 10^{-5}$

of the neutrinos is limited by the dark matter mass. Furthermore for such a typical point, there are only few monochromatic neutrinos as the annihilation into gauge bosons or quark pairs dominates. Such annihilation channels yield several neutrinos in the subsequent decay chain. Annihilation into leptons is suppressed by the Yukawa couplings λ_6 which are restricted to be small in order for the model to yield the correct neutrino masses and comply with LFV constraints [89]. Therefore we do not expect to measure a monochromatic neutrino line at IceCube but a continuous neutrino spectrum. The neutrino flux is highest for energies smaller that 50 GeV. Multiplying the neutrino flux with the IceCube effective area for the 86 string configuration, we obtain the expected event rates. As the effective area declines for small neutrino energies, the expected event rates peak at roughly half the dark matter mass. Integrating the differential rates, we obtain a prediction of 16 events per year for this model. For this benchmark point, the SI cross section is $\sigma_p(\text{SI}) = 1.75 \cdot 10^{-8}$ pb and already excluded by the XENON1T limits. We will see in the following, there are parts of the parameter space which are not excluded but yield sizeable event rates.

9.3 Numerical results

We use the tool chain described in Chap. 8 in order to explore the parameter space of our model by means of a numerical scan. As inelastic scattering does not occur naturally in the model T1-3-B ($\alpha = 0$), the routines specific to this case are omitted. We now scan over the parameter space of the model. The mass parameters $M_{\Psi,\psi\psi',\phi}$ are varied between 100 GeV and 10 TeV. As was mentioned before, M_ϕ^2 is chosen to be diagonal. The couplings $|\lambda_{1,4,5}|$ are varied between $1 \cdot 10^{-3}$ and 10, where λ_1 is chosen to be diagonal. The signs of these couplings are chosen randomly. λ_6 is calculated using the Casas-Ibarra parameterization Eq. (6.3.9), which requires the other model parameters as input. The neutrino mass differences and the PMNS angles are varied in the 3σ ranges [51], where we assume Normal Ordering. The angle θ from the Casas-Ibarra parameterization is varied from zero to 2π. In addition we require the Higgs mass to be (125 ± 2.5) GeV. Lepton Flavor Violation (LFV) constrains the parameter space further. We impose the current limits on $\text{BR}(\mu \to e\gamma) < 4.2 \cdot 10^{-13}$ [57] and $\text{BR}(\mu \to 3e) < 1.0 \cdot 10^{-12}$ [59], as they usually impose the most stringent constraints. We require the relic density to be $\Omega h^2 = 0.12$ [16], allowing it to vary by ± 0.02. As a cross check, we have reproduced the results shown in Figs. 7 and 10 of Ref. [89].

9.3.1 Spin independent scattering

Our spin independent cross section results for both fermion (below about 1 TeV) and scalar (above about 1 TeV) dark matter are shown in Fig. 9.2. The two kinds of dark matter are clearly divided by their allowed mass ranges. In the case of scalar triplet dark matter, the thermally-averaged cross section in the early Universe is dominated by the annihilations of the triplet components into the electroweak gauge bosons, e.g. $\eta_1^0\eta_1^0 \to W^+W^-$, but co-annihilation processes with the charged component such as $\eta_1^0\eta_1^+ \to Z^0W^+$ need also to be included due to the small mass splitting between the triplet components. An extensive overview of the possible (co)-annihilation diagrams is given in Ref. [153]. For this case, Ref. [91] computed the thermally-averaged cross section as well as the dark matter abundance and freeze-out temperature for a general $SU(2)_L$ n-plet, resulting in a dark matter mass of 2.0 ± 0.05 TeV for $n = 3$. The freeze-out temperature $X_f = m_{\text{DM}}/T_f \sim 26$ is in line with the results of micrOMEGAs for this model of $X_f \approx 26$. In principle, annihilation into two Higgs bosons is also possible, but it only starts to become relevant for dark matter masses above 2 TeV [151]. Nonetheless, the triplet-Higgs coupling λ_1 does affect the mass range for which the dark matter satisfies the relic density

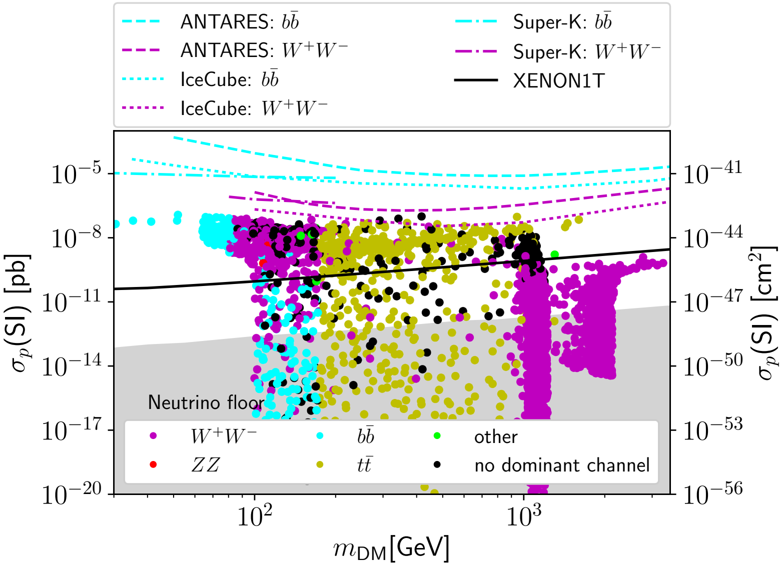

Figure 9.2: The spin independent (SI) cross section in pb with ANTARES [37], IceCube [38], Super-Kamiokande [39] and XENON1T [34] exclusion limits as a function of the dark matter mass for both fermion (below about 1 TeV) and scalar dark matter (above). All points and lines are color coded according to the main annihilation channel, provided there is one with a branching ratio of over 50%. Also shown is the neutrino floor [40].

constraint already at smaller masses. This has been observed in Refs. [89, 91, 152, 153], all of which placed the scalar triplet dark matter in a mass range around 2 TeV.

For singlet-doublet fermion dark matter the situation is dependent on the mixing between the fermion fields. This scenario is similar to MSSM neutralino dark matter, in the case the Bino mixes with the Higgsinos. In the early Universe, the thermally-averaged annihilation cross section is dominated by the coupling of the fermions to the Higgs and Z^0 boson. Through s-channel processes the dark matter can annihilate into Standard Model quarks. These couplings depend on the parameters λ_4 and λ_5, as is shown in Sec. 6.3. Further processes include the direct annihilation of the neutral doublet component into W boson pairs through the t-channel exchange of the charged doublet component, as well as co-annihilations between the neutral and charged doublet components into a W boson, of which the cross sections are given in Ref. [158].

Additionally, an expression for the relic density depending on the cross section is given. The masses presented in Ref. [158] are in the range of a few hundred GeV. However, as a Higgs mass of 500 GeV was assumed making a direct comparison difficult. An overview of annihilation diagrams, as well as the relation to direct detection is presented in Ref. [155], which also placed a lower bound on the mass range of the doublet component of ~ 1 TeV. Moreover, it was found that in the case where the dark matter is mostly doublet in nature, the relic density constraint is satisfied for masses ~ 1.1 TeV. More generally, the authors presented a numerical scan satisfying relic density constraints in the 40 GeV to 500 GeV mass range. The results obtained in Ref. [89] extend further in both directions, from around 10 GeV up to the purely doublet case around 1.1 TeV. Taking into account a slightly different spread of the points due to differing scan ranges and the already imposed LFV limits, the results agree with those in Figs. 7 and 10 of Ref. [89].

For indirect detection purposes the branching ratios of dark matter annihilations in the galactic halo are important. Hence the points in Fig. 9.2 are color coded according to their dominant decay channel. A point is marked by its dominant channel when a single branching ratio exceeds 50%. If this is not the case, then a point is marked as having no dominant channel.

The scalar dark matter candidates, all located around 2 TeV, mainly decay into a pair of W-bosons. For fermionic dark matter the situation is mixed. At masses below the W boson mass, the main channel is through $b\bar{b}$ production, after which the dominant channel becomes W^+W^-. For masses above the top mass, there is mainly $t\bar{t}$ production, except for the points around 1 TeV, where W-boson production is the only dominant channel. This can be explained by the singlet-doublet nature of the fermionic dark matter, where the parameter points located around 1 TeV are those that have a large doublet contribution and therefore couple more strongly to the electroweak gauge bosons. In contrast, the points for which the dark matter candidate is mainly a singlet with only a small doublet admixture couple less to the gauge bosons and relatively more to the top quark via the Standard Model Higgs boson. The charged fermions are always heavier than 102 GeV, so that the limits by the LEP experiments [49] do not restrict the parameter space. We see that the previous limits by the ANTARES [37], IceCube [38] and Super-Kamiokande [39] collaborations from dark matter annihilations in the Sun are several orders of magnitude weaker than the XENON1T [34] direct detection bound, with the

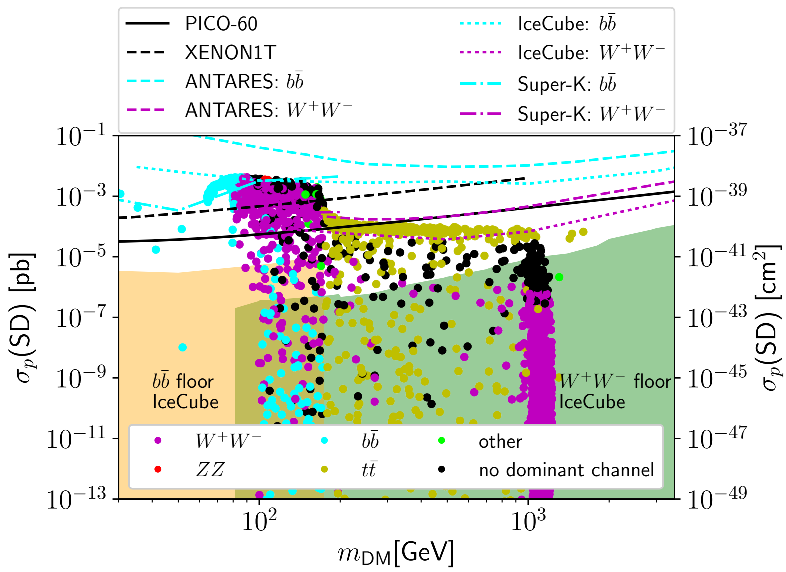

Figure 9.3: The spin dependent (SD) cross section in pb with PICO-60 [43], XENON1T [42], ANTARES [37], IceCube [38] and Super-Kamiokande [39] exclusion limits as a function of the dark matter mass for singlet-doublet fermion dark matter. All points and lines are color coded according to the main annihilation channel, provided there is one with a branching ratio of over 50%. Also shown is the neutrino floor for $b\bar{b}$ final states [159].

$b\bar{b}$ limits being less stringent compared to the W^+W^- ones. We also show the atmospheric and diffuse supernova background (DSNB) neutrino "floor" [40], which may render dark matter direct detection difficult.

9.3.2 Spin dependent scattering

In Fig. 9.3 we show the spin dependent cross section for singlet-doublet fermion dark matter in our model and compare it to direct and indirect detection limits. Different annihilation channels are again color coded as before. For certain channels, ANTARES [37] and IceCube [38] impose stronger constraints than XENON1T [42], while the full data set of PICO-60 [43] has similar sensitivity as the indirect detection experiments. In a combined analysis, IceCube and PICO-60 have removed the Standard Halo Model assumption and published velocity independent limits following the suggestion in Ref. [160], which are

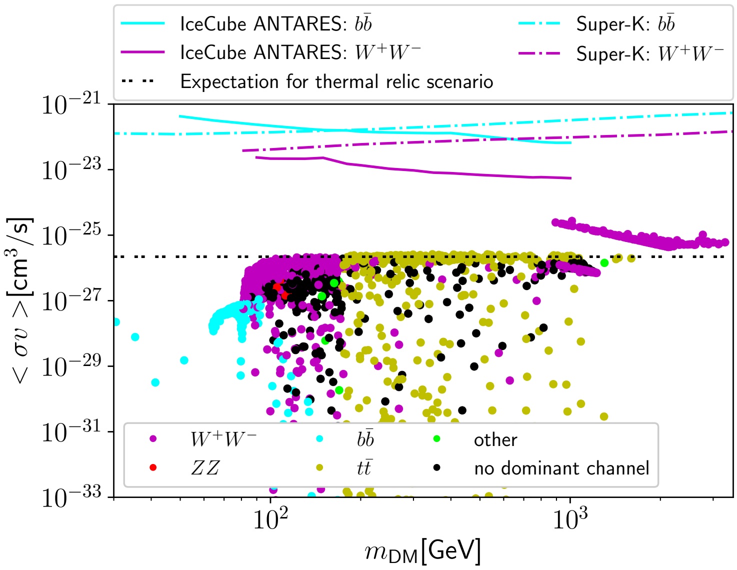

Figure 9.4: Thermally averaged cross section $\langle \sigma v \rangle$ with combined IceCube ANTARES [47] and Super-Kamiokande [48] exclusion limits as a function of the dark matter mass for both fermion (below about 1 TeV) and scalar dark matter (above). All points are colored according to the main annihilation channel, provided there is one with a branching ratio of over 50%. Also shown is the expected cross section for a thermal relic [144].

however significantly weaker [161]. Also shown is the neutrino floor for $b\bar{b}$ final states due to high-energy neutrinos from cosmic-ray interactions with the solar atmosphere, which may render indirect detection difficult [159] and leaves little room for the $b\bar{b}$ channel at low mass beyond the PICO-60 limits.

9.3.3 Limits from the Galactic Center

Fig. 9.4 shows the thermally averaged cross section $\langle \sigma v \rangle$ for the same points with fermionic and scalar dark matter as in Fig. 9.2. Here, we assume the NFW dark matter halo profile [143]. The expectation for a thermal relic is indicated by a dashed line [144]. For fermionic dark matter, it represents an upper limit, while for scalar dark matter it is rather a lower limit. All points are several orders of magnitude below the bounds established by IceCube [134], ANTARES [133] and their combination [47] as well as by Super-

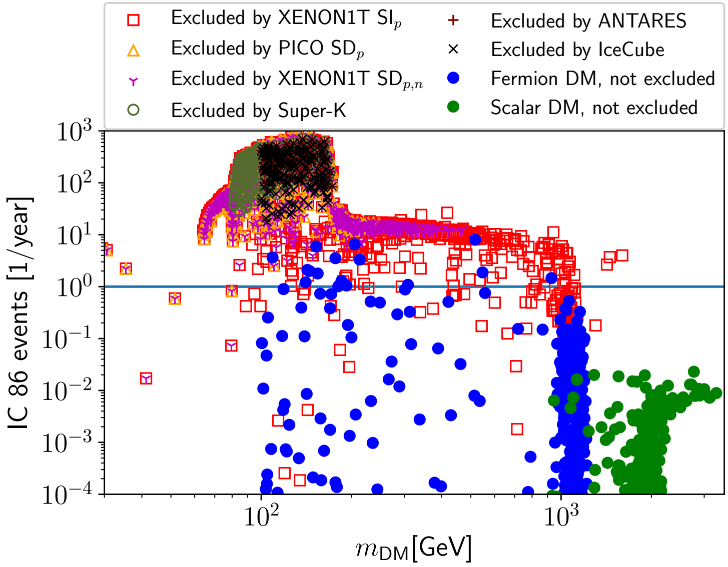

Figure 9.5: The expected number of events per year in the current IceCube configuration with 86 strings (IC86) as a function of the dark matter mass for singlet-doublet fermion (blue) and triplet scalar (green) dark matter. Allowed points are shown together with points excluded by direct and indirect detection (other colors and symbols). The blue line marks one event per year for orientation.

Kamiokande [48], meaning that these measurements do not constrain the model. For heavy scalar dark matter, the IceCube ANTARES sensitivity must be improved less than for lighter fermion dark matter, i.e. by only a few orders of magnitude.

9.3.4 Expected IceCube event rates

In Fig. 9.5 we show the expected event rate at IceCube for all model points of our numerical scan. For the triplet scalar dark matter case (green points), the spin dependent cross section is always zero. Thus in our model the accumulation of scalar dark matter in the Sun is only determined by the spin independent cross section, which lies below the current XENON1T bound. As can be seen, this leads to less than one event per year in the current IceCube configuration with 86 strings (IC86), whose sensitivity would therefore have to be improved by a few orders of magnitude.

For singlet-doublet fermion dark matter (blue and other points), the expected event rates reach values of up to 1000 events per year. However, we have to impose all previous direct and indirect detection constraints, marked by different symbols and colors in Fig. 9.5. Not shown previously, but also imposed are the XENON1T limits on spin dependent scattering off neutrons, which occurs rarely in the Sun. For indirect detection, we have always used the limits for the main annihilation channel. As expected, viable models (blue) lie in particular below the rates excluded previously by IceCube (black x symbols). They can reach rates of up to ten events per year at IC86, making indirect detection competitive with respect to the direct detection limits imposed in particular by PICO-60 (orange triangles). A considerable fraction of the parameter space with high rates is excluded by the limits on the spin independent cross section set by XENON1T (red squares) due to the correlation of the spin dependent and spin independent cross sections through λ_4 and λ_5 (see Sec. 6.3). Note, however, that the correlation of spin dependent and spin independent cross sections is absent in fine-tuned scenarios where the relation between λ_4 and λ_5 is fixed.

9.4 Summary

To summarize, we have studied in this chapter the prospects to probe radiative seesaw models with neutrino signals from dark matter annihilation and detectors such as ANTARES, Super-Kamiokande and in particular IceCube, focusing on the model T1-3-B with $\alpha = 0$ with either scalar triplet or singlet-doublet fermion dark matter. Both dark matter candidates can in principle directly annihilate into neutrinos. However, the relevant Yukawa couplings involved are usually strongly constrained to be small from neutrino masses and LFV processes, which are always present in these models. A sharp neutrino line at an energy corresponding to the dark matter mass is therefore not expected.

Continuous neutrino spectra are, however, produced from dark matter annihilation into decaying Standard Model particles such as W and Z^0 bosons, b and t quarks as well as (at least in principle) μ and τ leptons. When boosted through dark matter accumulation in celestial bodies such as the Earth, the Sun or the Galactic Center, the rates are observable in neutrino telescopes. Focusing on the most promising case of the Sun, we performed a detailed analysis of the expected event rates in IceCube. In the case of scalar triplet dark matter, there exists no spin dependent scattering process, and the spin independent scattering cross section is too small to obtain enough accumulation inside the Sun. Because of this, the event rate of neutrino signals in IceCube would lie below one event per year, making scalar triplet dark matter currently undetectable with neutrino telescopes.

For singlet-doublet fermionic dark matter, the situation is different. In this scenario, the dark matter candidate can scatter via both the spin independent as well as the spin dependent process, leading to rates of up to 1000 events per year. Through our approximation of the fermion mixing matrix for small Yukawa couplings $\lambda_{4,5}$, we then showed that the dark matter-mediator vertices in the spin (in)dependent processes, i.e. with Z^0 (Higgs) bosons, both depend on these Yukawa couplings, so that the two scattering processes become correlated. This was confirmed in a numerical scan and resulted in a considerable fraction of the parameter space with large event rates being excluded by the stringent XENON1T limits on the spin independent cross section. Previously obtained results by ANTARES, IceCube and Super-Kamiokande from the Sun and the Galactic Center were instead found to be much weaker. Constraints on the spin dependent cross section from PICO-60 and previous analyses by IceCube and ANTARES limited the viable models further to event rates of up to ten per year, leaving indirect detection with the IceCube neutrino telescope still competitive with respect to direct detection experiments.

Our results generalize to models with either real scalar triplet dark matter or fermion dark matter with singlet doublet mixing only, where scattering in the Sun is governed by similar relationships. The model points of our scan are available at `https://github.com/nechnif/T13Balpha0`.

10 Anomaly free scotogenic models with a hidden local U(1)

In this chapter we systematically study minimal models that allow for dark matter and Majorana neutrino masses while being stabilized by a local U(1) symmetry. All gauge anomalies are required to cancel. We then discuss important aspects of the phenomenology and investigate the unification hypothesis for these models. As of the time of writing this thesis, the results are not yet published. A publication is however planned and this chapter is based on an early manuscript. The results given in this chapter have been produced in collaboration with *Sybrand Zeinstra* and *Michael Klasen*.

10.1 Motivation and overview

Minimal models explaining neutrino masses and dark matter such as those studied in this work require a symmetry in order to stabilize the dark sector. This symmetry is needed in order to prevent tree level seesaw contributions to the neutrino masses and ensure that dark matter is stable. Often this symmetry is assumed to be a discrete $\mathbb{Z}_2$ symmetry as this is the simplest and most minimal possibility. However a $\mathbb{Z}_2$ symmetry lacks a fundamental theoretical reason. Replacing the discrete symmetry group by a local U(1) group, which is inherently connected to a new gauge boson, does give a physical meaning to the stabilization of the dark sector.

The goal of this chapter is to systematically investigate models that allow for Majorana neutrino masses at one loop as well as viable dark matter candidates. Our considerations extend the previous work of Refs. [10, 11]. All possible minimal realizations of the $d = 5$ Weinberg operator have been found and classified in Ref. [10]. The models found have then been examined whether they contain a viable dark matter candidate in Ref. [11]. They find 35 viable models which are all assumed to be stabilized by a discrete $\mathbb{Z}_2$ symmetry. In this chapter we promote this $\mathbb{Z}_2$ symmetry to a gauged U(1). When doing so there are a number of theoretical and phenomenological constraints which need to be taken into consideration. These constraints are imposed and discussed in this chapter.

Previous work has considered a global U(1) with neutrino masses at 1 [162, 163] or 2 loops [164, 165], where a Z_n symmetry then arises after spontaneous symmetry breaking [166]. Some of the models we find in this chapter have already been proposed in the literature, namely the $\mathrm{U}(1)_D$ scotogenic model (T3-B) [167] and the model T3-A which has a singlet-triplet scalar sector [168]. Models that predict Dirac neutrino masses with a local U(1) group have been studied in more detail for example with B-L charge assignments [169–174] or with a lepton number $\mathrm{U}(1)_L$ assignment [175, 176]. A systematic analysis of models with Dirac neutrino masses has been carried out in Ref. [177].

The addition of a new gauge group as well as the spontaneous breaking of this group gives rise to a new phenomenology, mainly the phenomenology of the Z' boson but also an extended Higgs sector. Gauge kinetic mixing between hypercharge and the new gauge group allows for many ways the test our models. Model independent discussions of the Z' phenomenology can be found for example in Refs. [178, 179]. The prospects of collider searches for a similar gauge and Higgs sector can be found for example in Ref. [180]. The Higgs sector is mainly constrained by the Higgs measurements and the new parameters are not tightly restricted [181–183].

We first give an overview of the models and the procedure. The derivation of the models and the phenomenology are then discussed in the following sections.

We first discuss realizations of the Weinberg operator. A brief overview was already presented in Chap. 6. As a reminder we repeat some arguments and put them in a more general context. Neutrino masses can be generated through interactions with new particles, which can be conveniently classified by means of effective operators that are obtained by integrating out the new physics. We focus on Majorana neutrino masses with the $d = 5$ Weinberg operator given by

$$\mathcal{L} \supset -\frac{c_{\alpha\beta}}{\Lambda}\left(L_\alpha H\right)\left(L_\beta H\right) + \mathrm{H.\,c.} \tag{10.1.1}$$

where Λ is the mass scale of the new particles and $c_{\alpha\beta}$ is obtained by integrating

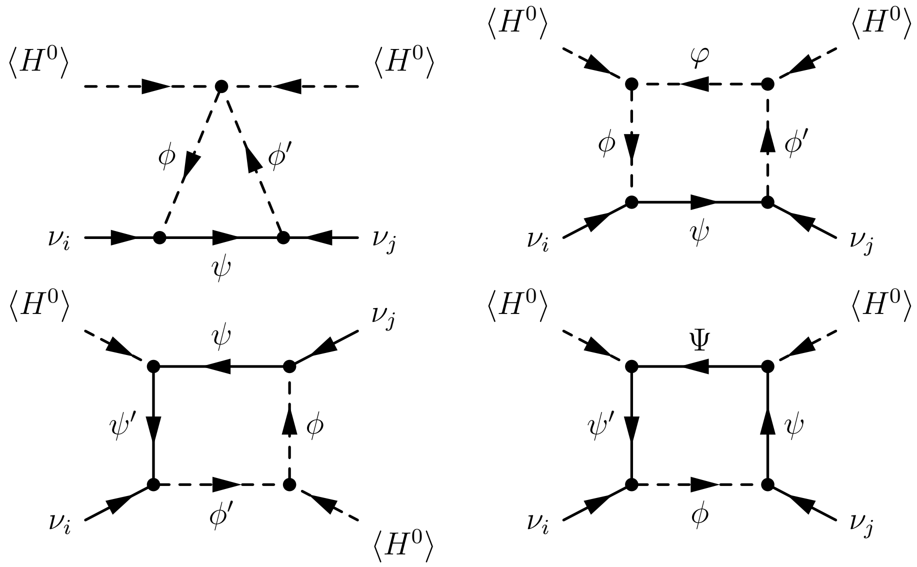

Figure 10.1: Topologies for neutrino mass generation at one loop. With the notation on Ref. [11] from left to right and top to bottom: The T3, T1-1, T1-2 and T1-3 topology.

out the new fields. After EWSB, this operator turns into a Majorana mass term for the Standard Model neutrinos

$$\mathcal{L} \supset -\frac{c_{\alpha\beta} v^2}{2\Lambda} \nu_L^\alpha \nu_L^\beta + \text{H. c.} \tag{10.1.2}$$

which is suppressed by the scale of new physics. The $d = 5$ Weinberg operator can be realized at one loop. As the loop integrals yield a suppression of the neutrino masses, this case allows for physics in a broad range from the GeV scale to several TeV, making it accessible to current particle physics experiments. The possible realizations of this operator at the one loop level have been systematically studied in Ref. [10] under the assumption that the number of new field multiplets is ≤ 4. There it was found that there exist four different topologies which are shown in Fig. 10.1.[1] For each of the topologies, all possible particle contents that can generate radiative neutrino masses through the one loop realization of the Weinberg operator were given, with the requirement that all new fields multiplets are singlets under $\mathrm{SU}(3)_c$ and singlets, doublets

[1]To be precise, they find more topologies, however, following previous work [11], we do not consider the T4 topologies as realizations that do not allow for tree level seesaw require lepton number conserving couplings which may be difficult to implement.

or triplets under $SU(2)_L$. A discrete $\mathbb{Z}_2$ symmetry is proposed as otherwise some models would allow for tree level contributions to the neutrino mass. In Ref. [11] all of these models that contain a viable dark matter candidate have been classified. In this case the $\mathbb{Z}_2$ symmetry is always needed in order to ensure dark matter stability.

The objective of this work is to replace the $\mathbb{Z}_2$ symmetry by a gauged U(1) symmetry which may or may not be broken. In doing so some subtleties occur. In a consistent theory all gauge anomalies should cancel, however this condition is not trivially satisfied when extending the Standard Model gauge group and particle content. A simple way to add new fermions without having new contributions to gauge anomalies is to make these fermions vector like[2]. It turns out that for our models all fermions must be vector like as no other possibilities exist that fulfill the requirements for our models. It is also crucial to make sure that the Standard Model Yukawa interactions do not violate the new $U(1)_X$ symmetry and that dark matter is stable. In order to keep the models minimal, we, similar to Refs. [10, 11], do not allow for more than four new fields in addition to one field ζ that is needed to break the $U(1)_X$ symmetry. In the following sections, we argue that with these requirements, the Standard Model must have zero charge under $U(1)_X$ and all new fermions must be vector like.

We allow for the $U(1)_X$ symmetry to be broken by a scalar field ζ. This field must be a singlet under the Standard Model gauge group as it should only break the new gauge symmetry. If the vev of ζ is small compared to the scale of new physics $v_\zeta \ll \Lambda$, then the neutrino masses are simply generated by the $d = 5$ operator given above. In this case, charge conservation implies that all fields running in the loop must have the same $U(1)_X$ charge. One can also consider the case where $v_\zeta \approx \Lambda$. In this case, the effective operator

$$\mathcal{L} \supset -\frac{c_{\alpha\beta}}{\Lambda^{1+2n}} \left(L_\alpha H\right) \left(L_\beta H\right) |\zeta|^{2n} + \text{H. c.} \tag{10.1.3}$$

is not suppressed for $n \neq 0$ as, once ζ obtains a vev, this turns into the usual $d = 5$ operator. In order to find all models, we also need to consider this case. As after $U(1)_X$ breaking we end up with the $d = 5$ Weinberg operator, we can still use the results of Refs. [10, 11] as a complete classification. However all mass dimension 3 vertices can violate $U(1)_X$ charge by one unit of charge of X_ζ,

[2]This means introducing for each new fermion an additional field in the conjugate representation of the gauge group. These two fields then form a mass term.

where X_ζ denotes the $\mathrm{U}(1)_X$ charge of ζ. Also the propagators can violate the $\mathrm{U}(1)_X$ charge by one (or two units in case of two scalar fields) as ζ obtaining a vev can induce mixing between fields in the same Standard Model gauge group representation. All possible charge assignments and a more extensive discussion in this case are given in the following section where we also give list of models with these charge assignments.

10.2 One-loop scotogenic models with local U(1) symmetry

10.2.1 Theoretical conditions

We will now discuss the different constraints that need to be taken into account when adding an extra $\mathrm{U}(1)_X$ gauge symmetry to a radiative seesaw model. The aim is to obtain general statements and restrictions on the charge assignment, such that these can then be applied to more specific cases. We will consider several factors that need to be taken into account in assigning the new $U(1)_X$ charges. As a gauge invariance must not be explicitly broken, the Yukawa terms in the Standard Model Lagrangian must not violate the $\mathrm{U}(1)_X$ charges. Similarly, the $d = 5$ Weinberg operator should be allowed as well as the couplings relevant for the neutrino loop. Furthermore all gauge anomalies should cancel among the new fields and the Standard Model fields. Finally we require the models to have a dark matter candidate which is stabilized by the gauged $\mathrm{U}(1)_X$ symmetry. We constrain ourselves to a maximum of four new fields running in the neutrino loop in addition to the new gauge boson and a scalar field required to break the $\mathrm{U}(1)_X$ gauge group. All four new fields should have no color charge and be singlets, doublets or triplets under $\mathrm{SU}(2)_L$. Once all general constraints on the charge assignment are found, we can apply these on models that realize the $d = 5$ Weinberg operator at one loop and also contain a viable dark matter candidate. The particle content of these models can be found in Ref. [11].

Yukawa couplings

The interactions in the Standard Model should not change. While the couplings to gauge bosons is dictated by the representation of the fields and do not change when extending the gauge group, we must ensure that the Yukawa terms

$$\mathcal{L} \supset -\frac{y_d}{\sqrt{2}} Q H^\dagger d_R^c - \frac{y_u}{\sqrt{2}} Q H u_R^c - \frac{y_e}{\sqrt{2}} L H^\dagger e_R^c + \text{H. c.} \tag{10.2.1}$$

do not violate the $\mathrm{U}(1)_X$ charge. The neutrino masses are generated by the effective operator

$$\mathcal{L} \supset -\frac{c_{\alpha\beta}}{\Lambda^{1+2n}} \left(L_\alpha H\right) \left(L_\beta H\right) |\zeta|^{2n} + \text{H. c.} \tag{10.2.2}$$

which also must not be forbidden by gauge invariance. ζ is an singlet under the Standard Model gauge group that is used to eventually break the $U(1)_X$ symmetry. After ζ obtains a vev, we are left with the $d = 5$ Weinberg operator. If $v_\zeta \ll \Lambda$, only the case with $n = 0$ i.e. the $d = 5$ Weinberg operator contributes whereas for $v_\zeta \approx \Lambda$ also $n \geq 1$ contribute. From the Yukawa couplings and the neutrino mass operator we obtain the following conditions for the $U(1)_X$ charges X_ψ for a field ψ[3]

$$\begin{aligned} X_Q - X_H + X_{d_R^c} &= 0, & (10.2.3)\\ X_Q + X_H + X_{u_R^c} &= 0, & (10.2.4)\\ X_L - X_H + X_{e_R^c} &= 0, & (10.2.5)\\ X_L + X_H &= 0. & (10.2.6) \end{aligned}$$

These can be brought to the following form

$$\begin{aligned} X_{d_R^c} &= -X_Q - X_L, & (10.2.7)\\ X_{u_R^c} &= -X_Q + X_L, & (10.2.8)\\ X_{e_R^c} &= -2X_L. & (10.2.9) \end{aligned}$$

Anomaly conditions

As we require the model to be anomaly free with the given particle content, the next constraints come from gauge anomaly cancellation. The conditions for all gauge anomalies to cancel in case of the Standard Model gauge group extended by a local U(1) are listed in Tab. 10.1. In order to make some following arguments more comprehensible, we calculate the contributions of

[3]Note that all Standard Model generations are assumed to have the same $\mathrm{U}(1)_X$ charge.

Table 10.1: Conditions for gauge anomaly cancellation for the gauge group $\mathrm{SU}(3)_c\times\mathrm{SU}(2)_L\times\mathrm{U}(1)_Y\times\mathrm{U}(1)_X$. Note that all fields are assumed to be left handed Weyl spinors. For $\mathrm{SU}(3)_c$ we assume singlets 1_3 and triplets 3_3 and for $\mathrm{SU}(2)_L$ we consider singlets 1_2, doublets 2_2 and triplets 3_2. The sums run over all components of fermion fields ψ.

Anomaly	Constraint
$\mathrm{U}(1)_Y^3$	$\sum_\psi Y_\psi^3 = 0$
$\mathrm{U}(1)_X^3$	$\sum_\psi X_\psi^3 = 0$
$\mathrm{U}(1)_Y^2\times\mathrm{U}(1)_X$	$\sum_\psi Y_\psi^2 X_\psi = 0$
$\mathrm{U}(1)_X^2\times\mathrm{U}(1)_Y$	$\sum_\psi X_\psi^2 Y_\psi = 0$
$\mathrm{SU}(3)_c^2\times\mathrm{U}(1)_Y$	$\sum_{\psi\in 3_3} Y_\psi = 0$
$\mathrm{SU}(3)_c^2\times\mathrm{U}(1)_X$	$\sum_{\psi\in 3_3} X_\psi = 0$
$\mathrm{SU}(2)_L^2\times\mathrm{U}(1)_Y$	$\sum_{\psi\in 2_2} Y_\psi + 4\sum_{\psi\in 3_2} Y_\psi = 0$
$\mathrm{SU}(2)_L^2\times\mathrm{U}(1)_X$	$\sum_{\psi\in 2_2} X_\psi + 4\sum_{\psi\in 3_2} X_\psi = 0$
$\mathrm{grav}^2\times\mathrm{U}(1)_Y$	$\sum_\psi Y_\psi = 0$
$\mathrm{grav}^2\times\mathrm{U}(1)_X$	$\sum_\psi X_\psi = 0$

the Standard Model fields to gauge anomalies. Using Eqs. (10.2.7-10.2.9), we find the following contributions:

$$\mathrm{SU}(3)_c^2 \times \mathrm{U}(1)_X: \quad 0, \tag{10.2.10}$$
$$\mathrm{SU}(2)_L^2 \times \mathrm{U}(1)_X: \quad 6\,[3X_Q + X_L]\,, \tag{10.2.11}$$
$$\mathrm{grav}^2 \times \mathrm{U}(1)_X: \quad 0, \tag{10.2.12}$$
$$\mathrm{U}(1)_Y^2 \times \mathrm{U}(1)_X: \quad -\frac{3}{2}\,[3X_Q + X_L]\,, \tag{10.2.13}$$
$$\mathrm{U}(1)_Y \times \mathrm{U}(1)_X^2: \quad 6X_L\,[3X_Q + X_L]\,, \tag{10.2.14}$$
$$\mathrm{U}(1)_X^3: \quad -6X_L^2\,[3X_Q + X_L]\,. \tag{10.2.15}$$

The contributions of the new fields must then cancel with those given above. Finally we also need to consider the Witten anomaly which cancels if there is an even number of fermion doublets.

New fermions

Now we turn our attention to the charges of the new fields. The conditions for the Standard Model charges can be used to make some observations in special cases with only few new fermions. We state these observations and give an argument why they hold true. Then we argue that models with one, two and three fermions can contain only vector like fermions.

Observation 1 *Only fermions that are not vector like contribute to the anomaly cancellation conditions.*

Argument: All gauge anomaly contributions from vector like fermions vanish due to opposite contributions from the other vector like component.

Observation 2 *If there is a single new fermion ψ that is not a priori part of a vector like fermion, ψ must be made vector like.*

Argument: From the Witten anomaly it is clear that if ψ is a doublet, it must be made vector like as we must add a second doublet. If ψ is a singlet or a triplet, the anomalies associated with hypercharge must cancel. As the Standard Model and other new vector like fermions do not contribute to the hypercharge anomalies, ψ must either be vector like or have zero hypercharge. However, if a singlet or triplet has zero hypercharge, it must have a non zero $\mathrm{U}(1)_X$ charge as otherwise seesaw types I or III are possible.[4] In this case the $\mathrm{grav}^2 \times \mathrm{U}(1)_X$ anomaly, which has no contributions from the Standard Model, must cancel. This is only possible if ψ is vector like.

Observation 3 *If there are two or more new fermions that are relevant in the neutrino loop, at least one of these fermions must be a doublet and at least one fermion must be a singlet or triplet.*

[4] Note that this argument works even in the Standard Model neutrino is charged under $\mathrm{U}(1)_X$ as $X_L = -X_H$.

Argument: In any minimal model with more than one fermion, there must be a coupling of the two fermions to the Higgs doublet. This is not possible, unless one of the new fermions is a doublet. One also needs a fermionic triplet or singlet to complete the vertex in an $\mathrm{SU}(2)_L$ invariant way.

Observation 4 *If there are two fermion fields that are either singlets or triplets under $SU(2)_L$, then they must both be vector like or identified with each other in order to form a vector like field.*

Argument: In order to cancel the hypercharge anomalies, both fields must be vector like, identified with each other or have zero hypercharge. In these cases there is no BSM contribution to the $\mathrm{U}(1)_Y \times \mathrm{U}(1)_X^2$. From this condition, it can easily be seen that the Standard Model cannot contribute to the $\mathrm{U}(1)_X$ anomalies. It follows that all BSM contributions to the $\mathrm{U}(1)_X$ anomalies must cancel amongst themselves. As the singlets and triplets with zero hypercharge must have a $\mathrm{U}(1)_X$ charge in order to avoid seesaw type I and III, one finds that both must be vector like or identified with each other.

With these general considerations for the fermionic sector in mind, we will now discuss the consequences for neutrino models with different number of fermions in more detail.

Models with one new fermion (T1-1, T3) From Observation 2 it follows that the fermion must be vector like.

Models with two new fermions (T1-2) From Observation 3 it is clear that one of these fermions must be a doublet and the other one is either a singlet or a triplet. As the doublet must be vector like in order to cancel the Witten anomaly, from Observation 2 it follows that the second fermion is also vector like.

Models with three new fermions (T1-3) The discussion for three fermion fields is a bit more involved. We start with the case with only one fermion doublet, which must be vector like following from the Witten anomaly. Then it follows from Observation 4 that the two remaining fermions must be vector like or identified with each other. The only combinations left are the cases of two doublets and one singlet/triplet. From the anomaly cancellation conditions for hypercharges $\mathrm{grav}^2\times\mathrm{U}(1)_Y$ and $\mathrm{SU}(2)_L^2\times\mathrm{U}(1)_Y$, one quickly finds that both doublets must have opposite hypercharge or both be vector like[5]. Similarly the singlet/triplet must have zero hypercharge or be vector like. If both doublets are vector like, the argument is reduced to the one given for one fermion. Finally if the doublets are not vector like (e.g. have different $\mathrm{U}(1)_X$ charge), one needs to specifically calculate the anomaly cancellation conditions $\mathrm{SU}(2)_L^2\times\mathrm{U}(1)_X$, $\mathrm{U}(1)_Y^2\times\mathrm{U}(1)_X$ and $\mathrm{grav}^2\times\mathrm{U}(1)_X$. Doing so, one quickly finds, that the singlet/triplet must be vector like and both doublets must have opposite $\mathrm{U}(1)_X$ charge[6] in order to have no tree level seesaw mechanism.[7]

To sum up, we find that all new fermions must be either vector like, or be combined with another fermion to form a vector like fermion.

Standard Model is uncharged

Because the fermions in the BSM particle content are all vector like, the conditions for gauge anomaly cancellation are simplified. Having only vector like fermions, makes the conditions for anomaly cancellation easy. As every Weyl spinor has a partner with opposite $\mathrm{U}(1)_{X,Y}$ charge, all conditions in Tab. 10.1 vanish separately for each vector like fermion. Thus all contributions to the gauge anomalies are zero if one only sums over the BSM particle content. As the BSM contributions all vanish separately, we can now use the results given in Ref. [69] (Chap. 30.4) for the possibilities to assign hypercharges and a second U(1) symmetry. They find that the new charges either must be a copy of the hypercharge or the $B-L$ charges

$$X_L = -X_{e_R^c} = -X_{\nu_R^c} = -1, \qquad X_Q = -X_{u_R^c} = -X_{d_R^c} = \frac{1}{3}, \tag{10.2.16}$$

where $X_{\nu_R^c}$ is the $\mathrm{U}(1)_X$ of a right handed neutrino. This charge assignment does not allow for the $d=5$ Weinberg operator.[8] Thus this possibility is ruled out for our models.

[5]There are no doublets with zero hypercharge in Ref. [11] as this case does not allow for an electrically neutral dark matter candidate.

[6]This allows us to combine both doublets to one vector like doublet.

[7]Solutions with irrational values for hypercharge are excluded here as they do not allow for electrically neutral dark matter.

[8]A right handed neutrino with such quantum numbers would also allow for Dirac neutrino masses of $\mathcal{O}(100\text{ GeV})$ arising from the Higgs interactions i.e. tree level seesaw type I.

In principle one can assign a $\mathrm{U}(1)_X$ charge to all Standard Model particles that is proportional to the hypercharge by a factor λ. In this case the Standard Model does not contribute to the anomaly conditions. In order to conserve the neutrino loop all new fields must also have a $\mathrm{U}(1)_X$ charge proportional to their hypercharge as well as a independent value that is conserved in the loop and only violated by $\mathrm{U}(1)_X$ breaking. The latter value is required in order to ensure dark matter stability and prevent tree level seesaw. The charges of the BSM particles inside the neutrino loop can be parameterized as

$$X_\psi = \lambda Y_\psi + X'_\psi \quad \text{for all fields.} \tag{10.2.17}$$

Note that such a charge assignment has a similar effect to gauge kinetic mixing as the new gauge boson couples to the hypercharge. For the case of two U(1) groups one is free to make a basis change. Such a change of basis can be used to shift the $\mathrm{U}(1)_X$ charge by $-\lambda Y_\psi$ for every field. This leaves us with the case that the Standard Model is uncharged under $\mathrm{U}(1)_X$ whereas all new fields have a charge of $X_\psi = X'_\psi$.

Dark matter stability

We require our model to contain a viable dark matter candidate. The stability of dark matter requires that none of the new particles has zero charge under the new symmetry as in that case, one could cut the neutrino loop at the dark matter propagator and the propagator of the uncharged particle which would allow for dark matter to decay. Thus all new particles must have non zero $\mathrm{U}(1)_X$ charge. If a new field has the same $\mathrm{U}(1)_X$ charge as ζ, the neutrino loop dictates that there must always exist a scalar field ϕ with $X_\phi = \pm X_\zeta$. Such a charge assignment will generally lead to ways for the dark matter candidate to decay and/or to mixing between Standard Model fields and new fields. Thus none of the new fields should have the same charge as ζ.

Mixing

Depending on the representations and $\mathrm{U}(1)_X$ charges of the fields, mixing can be induced by $\mathrm{U}(1)_X$ breaking. Through the vev of ζ[9] the following interactions

[9] One can also replace any of these fields by their conjugate field as long as gauge and Lorentz invariance allows this.

that give rise to mixing after $\mathrm{U}(1)_X$ breaking are possible

$$\psi\psi'\zeta, \qquad \phi\phi'\zeta, \qquad \phi\phi'\zeta\zeta. \tag{10.2.18}$$

The fields $\psi(\phi)$ and $\psi'(\phi')$ must be in $\mathrm{SU}(3)_c\times$ $\mathrm{SU}(2)_L\times$ $\mathrm{U}(1)_Y$ representations conjugate to one another. If they have zero hypercharge, one can have the additional case of $\psi = \psi'$ or $\phi = \phi'$. However the vertex

$$\phi\phi\zeta\zeta \tag{10.2.19}$$

is not possible as it requires $X_\phi = \pm X_\zeta$ which does not allow for stable dark matter. For $X_\psi = -\frac{X_\zeta}{2}$ the following interactions are possible

$$\psi\psi\zeta, \qquad \phi\phi\zeta. \tag{10.2.20}$$

10.2.2 General solutions

After discussing all factors that are relevant in assigning $\mathrm{U}(1)_X$ charges, we now want to find all possible charge assignments such that neutrino masses at one-loop level can still be generated. There is always the possibility that all fields which run in the loop have the same $\mathrm{U}(1)_X$ charge. For $v_\zeta \ll \Lambda$, with Λ being the mass scale of the new fields, this is the only possibility. For $v_\zeta \approx \Lambda$, higher dimensional operators (see Eq. (10.1.3)) are not suppressed. The $\mathrm{U}(1)_X$ symmetry is broken by the vev of a scalar field ζ which is a singlet under the Standard Model gauge group. The breaking induces mixing and $\mathrm{U}(1)_X$ violating vertices, which must not violate the Standard Model gauge symmetry. The $\mathrm{U}(1)_X$ violation must always occur in units of X_ζ. We will now discuss the different possibilities for the charge assignment for each of the topologies which are found by allowing $\mathrm{U}(1)_X$ violation in propagators via mixing and vertices as described above. We differentiate different values of the hypercharge parameter α as some values of this parameter fields have zero hypercharge which allows for mixing with the conjugate field which is not possible in the general case. At the end of each section we give a list of non equivalent models for the respective topology.

T1-1

Both vertices that couple to the Higgs can violate $\mathrm{U}(1)_X$. Thus for any α one can have the distributions

$$X_\psi = X_{\phi'} = X_\varphi = X_\phi, \tag{10.2.21}$$

$$X_\psi = X_{\phi'} = X_\varphi \pm X_\zeta = X_\phi. \tag{10.2.22}$$

$\underline{\alpha = 1}$ In the case of $\alpha = 1$, the scalar ϕ' has zero hypercharge. All new possible charge assignments can be found from the above ones by redefining $\phi' \to (\phi')^\dagger$.
$\underline{\alpha = -1}$ ϕ has zero hypercharge. The new possibilities for charge assignments are equivalent to the ones already found once one redefines $\phi \to (\phi)^\dagger$.
$\underline{\alpha = 0}$ Both ψ and φ have zero hypercharge. There is one more non equivalent charge assignment given by

$$X_\psi = -X_{\phi'} = X_\varphi = X_\phi = \pm\frac{X_\zeta}{2}. \tag{10.2.23}$$

If ϕ and ϕ' are in the same representation of $\mathrm{SU}(2)_L$, mixing between ϕ and $(\phi')^\dagger$ can be introduced by the breaking of $\mathrm{U}(1)_X$. This allows for the following new non equivalent charge assignments for this model

$$X_\psi = X_\phi = X_{\phi'} \pm 2X_\zeta = -X_\varphi = \pm\frac{X_\zeta}{2}, \tag{10.2.24}$$

$$X_\psi = X_\phi = X_{\phi'} \pm 2X_\zeta = X_\varphi \pm 2X_\zeta = \pm\frac{X_\zeta}{2}. \tag{10.2.25}$$

If ϕ and ϕ' are in the same $\mathrm{SU}(2)_L$ representation, and have opposite $\mathrm{U}(1)_X$ charges, we can identify them with each other by defining $\phi' = \phi^\dagger$. However in order to have at least two massive neutrinos, there must be two generations of either ψ or ϕ. The latter case is equivalent to the case where the fields are not identified with each other.

Equivalent models can be found by redefining $\varphi \to \varphi^\dagger$ and/or $\psi \to \psi^c$ and if possible $\phi' \to \phi^\dagger$.

List of models T1-1 We give a complete list of all the models found in Tab. 10.2. X_ζ is set to 2 while models with other charges of ζ are equivalent and can be obtained by rescaling the $\mathrm{U}(1)_X$ gauge coupling. The parameter a must be $\neq 0, \pm 2$. Note that if a scalar doublet has the charge $X = \pm 4$ there may be mixing of the new scalar doublet and the Higgs doublet making the dark matter candidate unstable.

Table 10.2: Non equivalent models with Topology T1-1. X_ζ is set to 2.

Model	α	φ	ϕ'	ψ	ϕ	X_φ	$X_{\phi'}$	X_ψ	X_ϕ
T1-1-A	± 2	1^S_2	2^S_1	1^F_2	2^S_3	a	a	a	a
T1-1-A	± 2	1^S_2	2^S_1	1^F_2	2^S_3	$a \pm 2$	a	a	a
T1-1-A	0	1^S_0	2^S_{-1}	1^F_0	2^S_1	a	a	a	a
T1-1-A	0	1^S_0	2^S_{-1}	1^F_0	2^S_1	$a \pm 2$	a	a	a
T1-1-A	0	1^S_0	2^S_{-1}	1^F_0	2^S_1	1	-1	1	1
T1-1-A	0	1^S_0		1^F_0	2^S_1	1		1	1
T1-1-A	0	1^S_0	2^S_{-1}	1^F_0	2^S_1	$1, -3$	-3	1	1
T1-1-B	± 2	1^S_2	2^S_1	3^F_2	2^S_3	a	a	a	a
T1-1-B	± 2	1^S_2	2^S_1	3^F_2	2^S_3	$a \pm 2$	a	a	a
T1-1-B	0	1^S_0	2^S_{-1}	3^F_0	2^S_1	a	a	a	a
T1-1-B	0	1^S_0	2^S_{-1}	3^F_0	2^S_1	$a \pm 2$	a	a	a
T1-1-B	0	1^S_0	2^S_{-1}	3^F_0	2^S_1	1	-1	1	1
T1-1-B	0	1^S_0		3^F_0	2^S_1	1		1	1
T1-1-B	0	1^S_0	2^S_{-1}	3^F_0	2^S_1	$1, -3$	-3	1	1
T1-1-C	± 1	2^S_1	1^S_0	2^F_1	1^S_2	a	a	a	a
T1-1-C	± 1	2^S_1	1^S_0	2^F_1	1^S_2	$a \pm 2$	a	a	a
T1-1-D	1	2^S_1	1^S_0	2^F_1	3^S_2	a	a	a	a
T1-1-D	1	2^S_1	1^S_0	2^F_1	3^S_2	$a \pm 2$	a	a	a
T1-1-D	-1	2^S_{-1}	1^S_{-2}	2^F_{-1}	3^S_0	a	a	a	a
T1-1-D	-1	2^S_{-1}	1^S_{-2}	2^F_{-1}	3^S_0	$a \pm 2$	a	a	a
T1-1-F	± 1	2^S_1	3^S_0	2^F_1	3^S_2	a	a	a	a
T1-1-F	± 1	2^S_1	3^S_0	2^F_1	3^S_2	$a \pm 2$	a	a	a
T1-1-G	± 2	3^S_2	2^S_1	1^F_2	2^S_3	a	a	a	a
T1-1-G	± 2	3^S_2	2^S_1	1^F_2	2^S_3	$a \pm 2$	a	a	a
T1-1-G	0	3^S_0	2^S_{-1}	1^F_0	2^S_1	a	a	a	a
T1-1-G	0	3^S_0	2^S_{-1}	1^F_0	2^S_1	$a \pm 2$	a	a	a
T1-1-G	0	3^S_0	2^S_{-1}	1^F_0	2^S_1	1	-1	1	1
T1-1-G	0	3^S_0		1^F_0	2^S_1	1		1	1
T1-1-G	0	3^S_0	2^S_{-1}	1^F_0	2^S_1	$1, -3$	-3	1	1
T1-1-H	± 2	3^S_2	2^S_1	3^F_2	2^S_3	a	a	a	a
T1-1-H	± 2	3^S_2	2^S_1	3^F_2	2^S_3	$a \pm 2$	a	a	a
T1-1-H	0	3^S_0	2^S_{-1}	3^F_0	2^S_1	a	a	a	a
T1-1-H	0	3^S_0	2^S_{-1}	3^F_0	2^S_1	$a \pm 2$	a	a	a
T1-1-H	0	3^S_0	2^S_{-1}	3^F_0	2^S_1	1	-1	1	1
T1-1-H	0	3^S_0		3^F_0	2^S_1	1		1	1
T1-1-H	0	3^S_0	2^S_{-1}	3^F_0	2^S_1	$1, -3$	-3	1	1

T1-2

Only the three scalar vertex can violate $\mathrm{U}(1)_X$. For any α we can always have the distributions

$$X_\psi = X_{\psi'} = X_\phi = X_{\phi'}. \tag{10.2.26}$$

$\underline{\alpha = -1}$ ψ' and ϕ have zero hypercharge. This allows for the new non equivalent charge assignment of

$$X_\psi = -X_{\psi'} = X_\phi = X_{\phi'} = \pm\frac{X_\zeta}{2}. \tag{10.2.27}$$

$\underline{\alpha = 0}$ ψ and ϕ' have zero hypercharge. We find the new non equivalent charge assignment

$$X_\psi = X_{\psi'} = -X_\phi = X_{\phi'} = \pm\frac{X_\zeta}{2}. \tag{10.2.28}$$

List of models T1-2 In Tab. 10.3, we give a list of the possible non equivalent models. X_ζ has been normalized to 2. Again, the parameter $a \neq 0, \pm 2$ and the assignment $a = \pm 4$ may yield problems with dark matter stability if the Standard Model Higgs mixes with a new scalar doublet.

T1-3

None of the vertices can violate $\mathrm{U}(1)_X$. For any α we can always have the distributions

$$X_\Psi = X_\psi = X_{\psi'} = X_\phi. \tag{10.2.29}$$

$\underline{\alpha = 0}$ Both Ψ and ϕ have zero hypercharge. There is one more non equivalent charge assignment

$$X_\Psi = -X_{\psi'} = X_\psi = X_\phi = \pm\frac{X_\zeta}{2}. \tag{10.2.30}$$

If ψ and ψ' are in the same representation of $\mathrm{SU}(2)_L$, mixing between ψ and $(\psi')^c$ can be introduced by the breaking of $\mathrm{U}(1)_X$. We find the additional possibility

$$-X_\Psi = X_{\psi'} = X_\psi = X_\phi = \pm\frac{X_\zeta}{2}. \tag{10.2.31}$$

Table 10.3: Non equivalent models with Topology T1-2. X_ζ is set to 2.

Model	α	ψ	ϕ	ϕ'	ψ'	X_ψ	X_ϕ	$X_{\phi'}$	$X_{\psi'}$
T1-2-A	0	1^F_0	2^S_1	1^S_0	2^F_1	a	a	a	a
T1-2-A	0	1^F_0	2^S_1	1^S_0	2^F_1	1	-1	1	1
T1-2-A	-2	1^F_{-2}	2^S_{-1}	1^S_{-2}	2^F_{-1}	a	a	a	a
T1-2-B	0	1^F_0	2^S_1	3^S_0	2^F_1	a	a	a	a
T1-2-B	0	1^F_0	2^S_1	3^S_0	2^F_1	1	-1	1	1
T1-2-B	-2	1^F_{-2}	2^S_{-1}	3^S_{-2}	2^F_{-1}	a	a	a	a
T1-2-D	1	2^F_1	1^S_2	2^S_1	3^F_2	a	a	a	a
T1-2-D	-1	2^F_{-1}	1^S_0	2^S_{-1}	3^F_0	a	a	a	a
T1-2-D	-1	2^F_{-1}	1^S_0	2^S_{-1}	3^F_0	1	1	1	-1
T1-2-F	1	2^F_1	3^S_2	2^S_1	3^F_2	a	a	a	a
T1-2-F	-1	2^F_{-1}	3^S_0	2^S_{-1}	3^F_0	a	a	a	a
T1-2-F	-1	2^F_{-1}	3^S_0	2^S_{-1}	3^F_0	1	1	1	-1

If ψ and ψ' are in the same $SU(2)_L$ representation, and have opposite $U(1)_X$ charges, we can combine them to form a vector like doublet instead of making both fields vector like. However in order to have at least two massive neutrinos, there must be two generations of either ϕ or ψ. The latter case is equivalent to the case where the fields are not identified with each other.

List of models T1-3 The explicit models are given in Tab. 10.4. As before X_ζ is set to 2 and the parameter a must be $\neq 0, \pm 2$ and in case of a scalar doublet $a \neq \pm 4$.

T3

None of the vertices can violate $U(1)_X$. For any α we can always have the distributions

$$X_\phi = X_{\phi'} = X_\psi. \tag{10.2.32}$$

$\underline{\alpha = -1}$ ψ has zero hypercharge. There are no more non equivalent charge assignments. If ϕ and ϕ' are in the same representation of $SU(2)_L$, mixing between ϕ and $(\phi')^\dagger$ can be introduced by the breaking of $U(1)_X$. We find no additional possibilities for the charge assignments.

Table 10.4: Non equivalent models with Topology T1-3. X_ζ is set to 2.

Model	α	Ψ	ψ'	ϕ	ψ	X_Ψ	$X_{\psi'}$	X_ϕ	X_ψ
T1-3-A	0	1_0^F	2_1^F	1_0^S	2_{-1}^F	a	a	a	a
T1-3-A	0	1_0^F	2_1^F	1_0^S	2_{-1}^F	1	-1	1	1
T1-3-A	0	1_0^F	2_1^F	1_0^S		1	-1	1	
T1-3-A	0	1_0^F	2_1^F	1_0^S	2_{-1}^F	-1	1	1	1
T1-3-B	0	1_0^F	2_1^F	3_0^S	2_{-1}^F	a	a	a	a
T1-3-B	0	1_0^F	2_1^F	3_0^S	2_{-1}^F	1	-1	1	1
T1-3-B	0	1_0^F	2_1^F	3_0^S		1	-1	1	
T1-3-B	0	1_0^F	2_1^F	3_0^S	2_{-1}^F	-1	1	1	1
T1-3-C	±1	2_1^F	1_2^F	2_1^S	1_0^F	a	a	a	a
T1-3-D	1	2_1^F	1_2^F	2_1^S	3_0^F	a	a	a	a
T1-3-D	-1	2_{-1}^F	1_0^F	2_{-1}^S	3_{-2}^F	a	a	a	a
T1-3-F	±1	2_1^F	3_2^F	2_1^S	3_0^F	a	a	a	a
T1-3-G	0	3_0^F	2_1^F	1_0^S	2_{-1}^F	a	a	a	a
T1-3-G	0	3_0^F	2_1^F	1_0^S	2_{-1}^F	1	-1	1	1
T1-3-G	0	3_0^F	2_1^F	1_0^S		1	-1	1	
T1-3-G	0	3_0^F	2_1^F	1_0^S	2_{-1}^F	-1	1	1	1
T1-3-H	0	3_0^F	2_1^F	3_0^S	2_{-1}^F	a	a	a	a
T1-3-H	0	3_0^F	2_1^F	3_0^S	2_{-1}^F	1	-1	1	1
T1-3-H	0	3_0^F	2_1^F	3_0^S		1	-1	1	
T1-3-H	0	3_0^F	2_1^F	3_0^S	2_{-1}^F	-1	1	1	1

List of models T3 The list of non equivalent models in given in Tab. 10.5. With the normalization $X_\zeta = 2$, the parameter a is again constrained by $a \neq 0, \pm 2$ and if $a = \pm 4$ a new scalar doublet may mix with the Standard Model Higgs boson which makes the dark matter candidate unstable.

10.3 Phenomenology

The models proposed above give rise to a wide variety of new phenomena. Most importantly they introduce dark matter and predict at least two massive neutrinos. Furthermore most of these models allow for LFV at one loop via similar diagrams as the neutrino loop. The above mentioned aspects generally

Table 10.5: Non equivalent models with Topology T1-3. X_ζ is set to 2.

Model	α	ϕ'	ϕ	ψ	$X_{\phi'}$	X_ϕ	X_ψ
T3-A	0	1^S_0	3^S_2	2^F_1	a	a	a
T3-A	-2	1^S_{-2}	3^S_0	2^F_{-1}	a	a	a
T3-B	$1, -3$	2^S_1	2^S_3	1^F_2	a	a	a
T3-B	-1	2^S_{-1}	2^S_1	1^F_0	a	a	a
T3-C	$1, -3$	2^S_1	2^S_3	3^F_2	a	a	a
T3-C	-1	2^S_{-1}	2^S_1	3^F_0	a	a	a
T3-E	$0, -2$	3^S_0	3^S_2	2^F_1	a	a	a

depend on the specific model and also occur in the models with a $\mathbb{Z}_2$ symmetry. We will briefly comment on some of those model dependent phenomena. Introducing a gauged U(1) symmetry and the corresponding breaking mechanism gives rise to a massive Z' boson. The phenomenology of this sector is mostly model independent. We will discuss the main constraints on the parameters that are relevant for the Z' boson. A general review of the phenomenology for heavy Z' can be found in Ref. [184] while massless dark photons are discussed in Ref. [185].

10.3.1 $\mathrm{U}(1)_X$ breaking

The gauge symmetry can be broken through the addition of a new scalar. For this purpose we take a complex scalar ζ, which we allow to develop a vev v_ζ. If v_ζ lies at the same scale as the masses of the new particles, all charge assignments that were listed in the overview in Tabs. 10.2-10.5 are possible. If $v_\zeta \ll \Lambda$, only models with $n = 0$ in the Weinberg operator Eq. (10.2.2) are possible. In this case operators with a contribution of v_ζ are suppressed by the mass of the heavier particles, which are usually around the TeV scale. In this case, only charge assignments where all new fields in the neutrino loop have the same $\mathrm{U}(1)_X$ charge are possible.

Residual symmetry

A residual symmetry can remain after the breaking of the $\mathrm{U}(1)_X$ gauge symmetry. As the charges of the fields only differ in units of X_ζ, the ratio of X_ϕ

and X_ζ can for any new field ϕ be expressed as

$$\frac{X_\phi}{X_\zeta} = r + n(\phi) \tag{10.3.1}$$

where $r \in \mathbb{R}$ and $n \in \mathbb{Z}$. n does depend on the fields ϕ, whereas r is only dependent on the model, but not on the field. The Lagrangian after $\mathrm{U}(1)_X$ breaking has a residual symmetry under the transformation

$$\phi \to \exp{(i2\pi r)}\phi. \tag{10.3.2}$$

For example, if $r = \frac{1}{3}$ one has a $\mathbb{Z}_3$ symmetry, whereas for the charge assignment

$$X_\phi = \left(\frac{1}{2} + n(\phi)\right) X_\zeta \tag{10.3.3}$$

we have $r = \frac{1}{2}$ and thus a $\mathbb{Z}_2$ symmetry just as in Ref. [11][10]. Depending on the specific model, there may also be a larger residual symmetry (usually a global $\mathrm{U}(1)_X$). See for example Ref. [167] in the case $X_\zeta = 3$.

Higgs sector

We will now work out the features of a Higgs sector involving the most general potential containing the Standard Model Higgs doublet H and the new scalar singlet ζ, with charges of 0 and 2 under the new $\mathrm{U}(1)_X$ group respectively. The scalar potential is given by

$$V = -m_H^2(H^\dagger H) - m_\zeta^2(\zeta^\dagger\zeta) + \frac{\lambda}{2}(H^\dagger H)^2 + \frac{\lambda_\zeta}{2}(\zeta^\dagger\zeta)^2 + \lambda_{H\zeta}(H^\dagger H)(\zeta^\dagger\zeta). \tag{10.3.4}$$

In many ways this is similar to a type I 2HDM Higgs sector[11], with the exception that ζ is a singlet instead of a doublet. Therefore terms like $(H^\dagger\zeta)(\zeta^\dagger H)$ and $(H^\dagger\zeta)^2 + \mathrm{H.\,c.}$ do not appear. The first step is to find the minimum of

[10] Note that the particle content still differs from the one given in Ref. [11], as before $\mathrm{U}(1)_X$ breaking all scalar fields are complex and all fermions are vector like. After $\mathrm{U}(1)_X$ breaking, these fields are still there. Also we have a heavy Z' and the real scalar σ.

[11] In these models the second Higgs doublet ϕ_2 is odd under a $\mathbb{Z}_2$ symmetry, as are the right-handed fermions. Thus only ϕ_2 couples to the Standard Model fermions.

the potential, which should be the case when H and ζ obtain their vevs. We denote the vevs of these fields by

$$\langle H\rangle = \begin{pmatrix} 0 \\ \frac{v+h}{\sqrt{2}} \end{pmatrix} \qquad \langle\zeta\rangle = \frac{v_\zeta+\sigma}{\sqrt{2}}. \tag{10.3.5}$$

Inserting these expressions in Eq. (10.3.4) results in the vacuum state of the potential $\langle V\rangle$. Ignoring the fluctuations around the minimum by h and σ, it is given as

$$\langle V\rangle = -\frac{m_H^2}{2}v^2 - \frac{m_\zeta^2}{2}v_\zeta^2 + \frac{\lambda}{8}v^4 + \frac{\lambda_\zeta}{8}v_\zeta^4 + \frac{\lambda_{H\zeta}}{4}v^2 v_\zeta^2. \tag{10.3.6}$$

In order to be a minimum, this must satisfy

$$\frac{\partial\langle V\rangle}{\partial v} = 0, \qquad \frac{\partial\langle V\rangle}{\partial v_\zeta} = 0, \tag{10.3.7}$$

from which one can derive the two minimum equations, which we solve for the mass terms. This results in

$$m_H^2 = \frac{\lambda v^2}{2} + \frac{\lambda_{H\zeta}v_\zeta^2}{2}, \tag{10.3.8}$$

$$m_\zeta^2 = \frac{\lambda_\zeta v_\zeta^2}{2} + \frac{\lambda_{H\zeta}v^2}{2}. \tag{10.3.9}$$

With this relation in place, let us now look at the mass terms that arise. If we consider V, where we now include the terms with h and σ one finds that the terms containing two fields are

$$V = -\frac{m_H^2}{2}h^2 - \frac{m_\zeta^2}{2}\sigma^2 + \frac{3\lambda}{4}v^2h^2 + \frac{3\lambda_\zeta}{4}v_\zeta^2\sigma^2 + \frac{\lambda_{H\zeta}}{4}\left(v_\zeta^2h^2 + v^2\sigma^2 + 4vv_\zeta h\sigma\right), \tag{10.3.10}$$

in which one can substitute the solutions of Eqs. (10.3.8, 10.3.9), so that the m^2 terms drop out of the expression. This results in the mass matrix

$$M = \begin{pmatrix} \lambda v^2 & \lambda_{H\zeta}vv_\zeta \\ \lambda_{H\zeta}vv_\zeta & \lambda_\zeta v_\zeta^2, \end{pmatrix} \tag{10.3.11}$$

with eigenvalues

$$m_{h_1}^2 = \frac{1}{2}\left(\lambda v^2 + \lambda_\zeta v_\zeta^2 - \sqrt{(\lambda v^2 - \lambda_\zeta v_\zeta^2)^2 + 4\lambda_{H\zeta} v^2 v_\zeta^2}\right), \tag{10.3.12}$$

$$m_{h_2}^2 = \frac{1}{2}\left(\lambda v^2 + \lambda_\zeta v_\zeta^2 + \sqrt{(\lambda v^2 - \lambda_\zeta v_\zeta^2)^2 + 4\lambda_{H\zeta} v^2 v_\zeta^2}\right), \tag{10.3.13}$$

that are obtained by diagonalizing M through an orthogonal matrix, with a mixing angle given by

$$\tan 2\alpha = \frac{2\lambda_{H\zeta} v v_\zeta}{\lambda v^2 - \lambda_\zeta v_\zeta^2}. \tag{10.3.14}$$

The mixing in the scalar sector has an effect on the Yukawa couplings. Remember that the Standard Model Yukawa couplings can be written as

$$\mathcal{L} \supset -\frac{y_d}{\sqrt{2}} Q H^\dagger d - \frac{y_u}{\sqrt{2}} Q H u - \frac{y_e}{\sqrt{2}} L H^\dagger e + \text{H. c.} \tag{10.3.15}$$

through which the Standard Model fermions obtain their masses. The Standard Model fermions do not couple to ζ in the unbroken phase, and receive no contribution from v_ζ. In the Standard Model, the couplings of a fermion f can be brought to the form

$$\frac{m_f}{v}, \tag{10.3.16}$$

with which they couple to h. Because of the mixing between h and σ to h_1 and h_2, these couplings get modified. One can rewrite

$$h = \cos\alpha h_1 - \sin\alpha h_2. \tag{10.3.17}$$

We identify h_1 with the Standard Model-like Higgs boson. The couplings of h_1 and h_2 to the Standard Model fermion are then

$$\frac{m_f \cos\alpha}{v} \qquad \frac{m_f \sin\alpha}{v} \tag{10.3.18}$$

respectively. Through mixing, the Standard Model fermions obtain a coupling to h_2. Constraints on the mixing angle have been set by Refs. [181–183, 186]. For example Ref. [186] constrains $\sin^2\alpha$ to be smaller than 0.12.

10.3.2 Gauge sector

Gauge kinetic mixing

Gauge kinetic mixing occurs when there are several abelian gauge groups [187]. As the field strength tensor $F^{\mu\nu}$ itself is gauge invariant, products of different field strength tensors in the kinetic Lagrangian are allowed by gauge invariance. For theories with two abelian gauge groups, the kinetic Lagrangian for the gauge fields can be written as

$$\mathcal{L}_{\text{kin}} = -\frac{1}{4}\tilde{F}_{1\mu\nu}\tilde{F}_1^{\mu\nu} - \frac{1}{4}\tilde{F}_{2\mu\nu}\tilde{F}_2^{\mu\nu} - \frac{\tilde{\epsilon}}{2}\tilde{F}_{1\mu\nu}\tilde{F}_2^{\mu\nu}, \tag{10.3.19}$$

where the final term is allowed and thus present, inducing gauge-kinetic mixing between the field tensors. The form of the covariant derivatives, taking only the $U(1)$ groups into account, is most generally given by

$$D_\mu\phi = \left(\partial_\mu - i\sum_{i,j} Q^i_\phi g_{ij}\tilde{A}^\mu_j\right)\phi. \tag{10.3.20}$$

Here, $Q^i_\phi = X_\phi, Y_\chi$ is the $U(1)$ charge of the particle ϕ under the gauge group $U(1)_i$ $(i = X, Y)$. The coupling g_{ij} thus couples a field with charge Q^i_ϕ to a gauge field A^μ_j. Note that g_{ij} must not be diagonal as also non diagonal entries are allowed by gauge invariance. The interactions of the gauge fields can then be written as

$$\mathcal{L} \supset \begin{pmatrix}\tilde{A}_{1\mu} & \tilde{A}_{1\mu}\end{pmatrix}\begin{pmatrix} g_{11} & g_{12} \\ g_{21} & g_{22}\end{pmatrix}\begin{pmatrix} j^\mu_Y \\ j^\mu_X\end{pmatrix} \tag{10.3.21}$$

with the currents j^μ_Y and j^μ_X defined in terms of the charges

$$\begin{aligned} j^\mu_Y = &\sum_\phi iY_\phi\left(\partial^\mu\phi^\dagger\phi - \phi^\dagger\partial^\mu\phi\right) + Y_\phi\left(\sum_{i,j} Q^i_\phi g_{ij}\tilde{A}^\mu_j\right)|\phi|^2 \\ &+ \sum_\psi Y_\psi\bar{\psi}_{\dot{a}}\left(\bar{\sigma}^\mu\right)^{\dot{a}b}\psi_b, \end{aligned} \tag{10.3.22}$$

$$\begin{aligned} j^\mu_X = &\sum_\phi iX_\phi\left(\partial^\mu\phi^\dagger\phi - \phi^\dagger\partial^\mu\phi\right) + X_\phi\left(\sum_{i,j} Q^i_\phi g_{ij}\tilde{A}^\mu_j\right)|\phi|^2 \\ &+ \sum_\psi X_\psi\bar{\psi}_{\dot{a}}\left(\bar{\sigma}^\mu\right)^{\dot{a}b}\psi_b. \end{aligned} \tag{10.3.23}$$

The spinor sum is taken over Weyl spinors ψ while ϕ denotes scalar fields. The basis of the gauge fields can be freely chosen, whereas it is inconvenient to redefine the currents a priori as the charges are fixed. In order to make the connection with literature, we first transform the coupling matrix into a diagonal form. This is done by decomposing the matrix as follows:

$$\begin{pmatrix} g_{11} & g_{12} \\ g_{21} & g_{22} \end{pmatrix} = \begin{pmatrix} \frac{g_{11}}{g_Y} & \frac{g_{12}}{g_X} \\ \frac{g_{21}}{g_Y} & \frac{g_{22}}{g_X} \end{pmatrix} \begin{pmatrix} g_Y & 0 \\ 0 & g_X \end{pmatrix}. \tag{10.3.24}$$

We now redefine the gauge fields (using a non unitary transformation) by

$$\begin{pmatrix} A_Y^\mu \\ A_X^\mu \end{pmatrix} = \begin{pmatrix} \frac{g_{11}}{g_Y} & \frac{g_{12}}{g_X} \\ \frac{g_{21}}{g_Y} & \frac{g_{22}}{g_X} \end{pmatrix} \begin{pmatrix} \tilde{A}_1^\mu \\ \tilde{A}_2^\mu \end{pmatrix}. \tag{10.3.25}$$

g_X and g_Y need to be chosen in such a way, that the kinetic Lagrangian takes the canonical form as in Eq. (10.3.19).[12] Such a field redefinition also gives new contributions to the kinetic mixing term which shifts $\tilde{\epsilon} \to \epsilon$. The Lagrangian now takes the following form, which is often found in the literature as starting point [179, 188–191]:

$$\mathcal{L} \supset -\frac{1}{4} F_Y^{\mu\nu} F_{Y\mu\nu} - \frac{\epsilon}{2} F_Y^{\mu\nu} F_{X\mu\nu} - \frac{1}{4} F_X^{\mu\nu} F_{X\mu\nu} + \begin{pmatrix} A_{Y\mu} & A_{X\mu} \end{pmatrix} \begin{pmatrix} g_Y & 0 \\ 0 & g_X \end{pmatrix} \begin{pmatrix} j_Y^\mu \\ j_X^\mu \end{pmatrix}. \tag{10.3.26}$$

The kinetic terms in the Lagrangian can be diagonalized by redefining the fields as follows

$$\begin{pmatrix} A_Y^\mu \\ A_X^\mu \end{pmatrix} = \frac{1}{\sqrt{2}} \begin{pmatrix} \frac{1}{\sqrt{1+\epsilon}} & \frac{1}{\sqrt{1-\epsilon}} \\ \frac{1}{\sqrt{1+\epsilon}} & \frac{-1}{\sqrt{1-\epsilon}} \end{pmatrix} \begin{pmatrix} A_1^\mu \\ A_2^\mu \end{pmatrix}. \tag{10.3.27}$$

Note that this is not an orthogonal transformation. The Lagrangian in this basis is given by

$$\mathcal{L} \supset -\frac{1}{4} F_1^{\mu\nu} F_{1\mu\nu} - \frac{1}{4} F_2^{\mu\nu} F_{2\mu\nu} + \frac{1}{\sqrt{2}} \begin{pmatrix} A_{1\mu} & A_{2\mu} \end{pmatrix} \begin{pmatrix} \frac{g_Y}{\sqrt{1+\epsilon}} & \frac{g_X}{\sqrt{1+\epsilon}} \\ \frac{g_Y}{\sqrt{1-\epsilon}} & \frac{-g_X}{\sqrt{1-\epsilon}} \end{pmatrix} \begin{pmatrix} j_Y^\mu \\ j_X^\mu \end{pmatrix}. \tag{10.3.28}$$

[12] The analytic expressions are quite unwieldy and are thus not given here.

The matrix coupling the gauge bosons to the currents can in general not be diagonalized as this would reintroduce the kinetic mixing term into the Lagrangian. However using the QR decomposition it can be transformed to a lower triangular matrix.

$$\frac{1}{\sqrt{2}}\begin{pmatrix} \frac{g_Y}{\sqrt{1+\epsilon}} & \frac{g_X}{\sqrt{1+\epsilon}} \\ \frac{g_Y}{\sqrt{1-\epsilon}} & \frac{-g_X}{\sqrt{1-\epsilon}} \end{pmatrix} = \frac{1}{\sqrt{2}}\begin{pmatrix} \sqrt{1+\epsilon} & \sqrt{1-\epsilon} \\ \sqrt{1-\epsilon} & -\sqrt{1+\epsilon} \end{pmatrix}\begin{pmatrix} g_Y & 0 \\ \frac{-g_Y\epsilon}{\sqrt{1-\epsilon^2}} & \frac{g_X}{\sqrt{1-\epsilon^2}} \end{pmatrix} =: QR \tag{10.3.29}$$

Note that the orthogonal matrix Q has determinant -1 in order to have positive diagonal entries in the lower triangular matrix. We can now rotate the fields with the redefinition

$$\begin{pmatrix} A^\mu \\ A'^\mu \end{pmatrix} := \frac{1}{\sqrt{2}}\begin{pmatrix} \sqrt{1+\epsilon} & \sqrt{1-\epsilon} \\ \sqrt{1-\epsilon} & -\sqrt{1+\epsilon} \end{pmatrix}\begin{pmatrix} A_1^\mu \\ A_2^\mu \end{pmatrix}. \tag{10.3.30}$$

which leaves us with the following Lagrangian

$$\mathcal{L} \supset -\frac{1}{4}F^{\mu\nu}F_{\mu\nu} - \frac{1}{4}F'^{\mu\nu}F'_{\mu\nu} + \begin{pmatrix} A_\mu & A'_\mu \end{pmatrix}\begin{pmatrix} g_Y & 0 \\ \frac{-g_Y\epsilon}{\sqrt{1-\epsilon^2}} & \frac{g_X}{\sqrt{1-\epsilon^2}} \end{pmatrix}\begin{pmatrix} j_Y^\mu \\ j_X^\mu \end{pmatrix}. \tag{10.3.31}$$

This result agrees with case b) in Ref. [191]. If we would have chosen R to be an upper diagonal matrix, we would have ended up with case a) in Ref. [191]. As Q is orthogonal, the kinetic mixing term is not reintroduced. Thus it is, starting from the most general case, always possible to transform into a basis such that the Standard Model gauge boson A_μ couples to the charges Y only. On the other hand, the gauge boson A'_μ picks up a small coupling to the current j_Y^μ as well, but still chiefly couples to j_X^μ.

$Z - Z'$ mixing

The previous section concerned itself with basis transformations inside the gauge kinetic terms. However, because of couplings to the Higgs sector, the U(1) symmetry can be broken, which was shown in Sec. 10.3.1. In this process, the gauge bosons obtain their masses. The covariant derivative for $SU(2)_L \times U(1)_Y \times U(1)_X$ in the basis as in Eq. (10.3.31) is given by

$$D_\mu = \partial_\mu - i\left(g_Y A_\mu + \frac{-\epsilon g_Y}{\sqrt{1-\epsilon^2}}A'_\mu\right)Y - i\frac{g_X}{\sqrt{1-\epsilon^2}}A'_\mu X - ig\tau^a W_\mu^a \tag{10.3.32}$$

where X, Y and τ^a are the generators of $\mathrm{U}(1)_X$, $\mathrm{U}(1)_Y$ and $\mathrm{SU}(2)_L$ respectively. The part of the Lagrangian relevant for the mass of the gauge bosons is given by

$$\mathcal{L} \supset |D_\mu H|^2 + |D_\mu \zeta|^2 . \tag{10.3.33}$$

Expanded around the minimum this expression yields for the neutral gauge bosons

$$\mathcal{L} \supset \frac{v_H^2}{8}\left(g_Y A_\mu + \frac{-\epsilon g_Y}{\sqrt{1-\epsilon^2}} A'_\mu - g W_\mu^3\right)^2 + \frac{v_\zeta^2}{2}\left(\frac{g_X}{\sqrt{1-\epsilon^2}} A'_\mu X_\zeta\right)^2 \tag{10.3.34}$$

$$= \begin{pmatrix} A_\mu & W_\mu^3 & A'_\mu \end{pmatrix} \begin{pmatrix} \frac{g_Y^2 v_H^2}{8} & -\frac{g g_Y v_H^2}{8} & -\frac{\epsilon g_Y^2 v_H^2}{8\sqrt{1-\epsilon^2}} \\ -\frac{g g_Y v_H^2}{8} & \frac{g^2 v_H^2}{8} & \frac{\epsilon g g_Y v_H^2}{8\sqrt{1-\epsilon^2}} \\ -\frac{\epsilon g_Y^2 v_H^2}{8\sqrt{1-\epsilon^2}} & \frac{\epsilon g g_Y v_H^2}{8\sqrt{1-\epsilon^2}} & \frac{\epsilon^2 g_Y^2 v_H^2}{8(1-\epsilon^2)} + \frac{g_X^2 v_\zeta^2 X_\zeta^2}{2(1-\epsilon^2)} \end{pmatrix} \begin{pmatrix} A^\mu \\ W^{3\mu} \\ A'^\mu \end{pmatrix} . \tag{10.3.35}$$

Through the Weinberg angle, A_μ and W_μ^3 mix to form the photon and the Z boson. This results in the following mass matrix

$$\begin{pmatrix} \gamma & \tilde{Z} & A'_\mu \end{pmatrix} \frac{1}{2} \begin{pmatrix} 0 & 0 & 0 \\ 0 & M_{\tilde{Z}}^2 & \Delta \\ 0 & \Delta & \frac{M_X^2}{(1-\epsilon^2)}\left(1 + \epsilon^2 \sin^2\theta_w \frac{M_{\tilde{Z}}^2}{M_X^2}\right) \end{pmatrix} \begin{pmatrix} \gamma \\ \tilde{Z} \\ A'^\mu \end{pmatrix} , \tag{10.3.36}$$

with

$$M_{\tilde{Z}}^2 = \frac{(g^2 + g_Y^2) v_H^2}{4} = \frac{g^2 v_H^2}{4\cos^2\theta_w} \tag{10.3.37}$$

being the Standard Model Z mass, and mixing terms

$$\Delta = \epsilon \frac{g_Y \sqrt{g^2 + g_Y^2}\, v_H^2}{4\sqrt{1-\epsilon^2}} = \frac{\epsilon \sin\theta_w}{\sqrt{1-\epsilon^2}} M_{\tilde{Z}}^2 . \tag{10.3.38}$$

The term in the lower right corner has been rewritten in terms of the mass

$$M_X^2 = g_X^2 X_\zeta^2 v_\zeta^2 \tag{10.3.39}$$

of the new gauge boson in the absence of kinetic mixing. This means the complete term can be written as

$$M_{A'}^2 = \frac{M_X^2}{(1-\epsilon^2)} \left(1 + \epsilon^2 \sin^2\theta_w \frac{M_{\tilde{Z}}^2}{M_X^2}\right) \tag{10.3.40}$$

The remaining non-diagonal part can be diagonalized by a second mixing angle θ', whose value is given by

$$\tan 2\theta' = \frac{2\Delta}{M_{\tilde{Z}}^2 - M_{A'}^2}. \tag{10.3.41}$$

Up to second order in ϵ, the squared masses of γ, Z and Z' are then given by

$$\begin{pmatrix} 0 \\ M_{\tilde{Z}}^2 \left(1 - \epsilon^2 \sin^2\theta_w \frac{M_{\tilde{Z}}^2}{M_X^2 - M_{\tilde{Z}}^2}\right) \\ M_X^2 \left(1 + \epsilon^2 \left(1 + \sin^2\theta_w \frac{M_{\tilde{Z}}^2}{M_X^2 - M_{\tilde{Z}}^2}\right)\right) \end{pmatrix}. \tag{10.3.42}$$

The Z^0 boson mass has been experimentally measured by e.g. the LEP experiment and matches the Standard Model prediction. As the shift in the Z^0 mass that depends on the kinetic mixing and the Z' mass, this can be used to constrain the viable parameter space. We compute the Z^0 mass numerically and show the area in the $m_{Z'} - \epsilon$ plane, where m_Z deviates more than 3σ from the experimental value of $m_Z = 91.1876$ GeV. The results are presented in Fig. 10.2. We also show the limits set by BaBar [192] and NA64 [193] as well the the favored region to explain the anomalous magnetic moment of the muon (see below).

Couplings

The diagonalization of the mass matrix explained above can be expressed with the following transformation

$$\begin{pmatrix} A^\mu \\ W^{3\mu} \\ A'^\mu \end{pmatrix} = \begin{pmatrix} c & -sc' & ss' \\ s & cc' & -cs' \\ 0 & s' & c' \end{pmatrix} \begin{pmatrix} \gamma^\mu \\ Z^\mu \\ Z'^\mu \end{pmatrix} \tag{10.3.43}$$

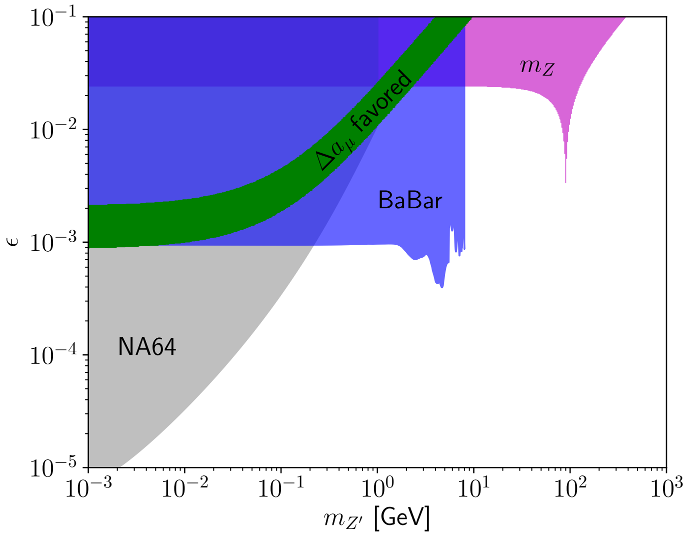

Figure 10.2: Regions excluded by experiments and the determination of the Z mass in the $m_{Z'} - \epsilon$ plane. For the anomalous magnetic moment of the muon a_μ, the region where the Z' boson can explain the discrepancy between the Standard Model and experiment in the 3σ range is highlighted. The parameters are $g_X = 0.1, X_\zeta = 3$ while ϵ and v_ζ are varied.

where $s = \sin(\theta_W)$, $c = \cos(\theta_W)$ and similarly s', c' with the angle being θ'. The interaction term in the Lagrangian with mass eigenstates can then be expressed as

$$\mathcal{L} \supset \begin{pmatrix} \gamma_\mu & Z_\mu & Z'_\mu \end{pmatrix} \begin{pmatrix} c & s & 0 \\ -sc' & cc' & s' \\ ss' & -cs' & c' \end{pmatrix} \begin{pmatrix} g_Y & 0 & 0 \\ 0 & g & 0 \\ \frac{-g_Y \epsilon}{\sqrt{1-\epsilon^2}} & 0 & \frac{g_X}{\sqrt{1-\epsilon^2}} \end{pmatrix} \begin{pmatrix} j_Y^\mu \\ j_{\tau^3}^\mu \\ j_X^\mu \end{pmatrix} \tag{10.3.44}$$

where $j^\mu_{\tau^3}$ is the current belonging to the generator τ^3 of $\mathrm{SU}(2)_L$. We see that the photon does not couple to the $\mathrm{U}(1)_X$ charge which ensures that dark matter does not interact with the Standard Model photon. Both the Z and Z' boson couple to both isospin as well as the $\mathrm{U}(1)_X$ charge. This allows for further ways to test our models.

10.3.3 Anomalous magnetic moment

As the new particles couple to leptons, there are generally new contributions to the anomalous magnetic moment. In $\mathbb{Z}_2$ case these stem from similar loop as the ones relevant for LFV or the neutrino masses. With LFV and neutrino masses supressed, they usually give only small contribution's to the anomalous magnetic moment as has been shown e.g. in Refs. [145, 194]. The Z' boson is not connected to LFV and neutrino masses and must not be heavy. Through kinetic mixing, the Z' boson does couple to leptons. The couplings can be extracted from Eq. (10.3.44). The Z' boson then contributes to the muon anomalous magnetic moment a_μ through similar loops as the Standard Model photon. With

$$g_V = \frac{1}{2}(g_R + g_L), \tag{10.3.45}$$

$$g_A = \frac{1}{2}(g_R - g_L) \tag{10.3.46}$$

the contribution of a neutral vector boson is given by [195]

$$\Delta a_\mu = \frac{m_l^2}{8\pi^2} \int_0^1 dx \frac{g_V^2 2x^2(1-x) + g_A^2 \left[2x(1-x)(x-4) - 4\frac{m_l^2}{m_{Z'}^2} x^3\right]}{(1-x)(m_{Z'}^2 - m_l^2 x) + m_l^2 x}. \tag{10.3.47}$$

We calculate the contribution of the Z' boson numerically and mark the area where solely the contribution of the new gauge boson can explain the discrepancy between Standard Model and experiment in the 3σ range [64] in Fig. 10.2. The entire area is already excluded by other experiments such as BaBar.

10.3.4 Lepton flavor violation

LFV processes are generally present in radiative seesaw models. Mostly these processes occur through diagrams of similar topology as the neutrino mass loop, but then with charged leptons and charged components of the BSM field multiplets. There can also be additional diagrams contributing. However these contributions depend on the details of the specific model.

The coupling of the Z' boson to the leptons is governed by kinetic mixing and the couplings are diagonal in flavor space. Therefore, at one loop, the presence of a Z' boson does not introduce additional LFV processes.

10.3.5 Dark matter phenomenology

One of the main motivations for our models is to explain the dark matter phenomenon. As the lightest of the new fields is expected to be a dark matter candidate, one can also probe these models by considering the dark matter phenomenology. The dark matter phenomenology is dependent on the specific model.

Relic density

The relic density is assumed to be produced in the freeze out scenario. The annihilation process of two dark matter particles can involve the Z' boson or other new particles as mediators. Furthermore the annihilation can have Standard Model fields as mediators or in case of four point vertices, no mediator is required. The diagrams involving the Z' are usually suppressed by the kinetic mixing parameter ϵ and often other (model dependent) annihilation diagrams dominate.

Direct detection

If the hidden sector is stabilized by a $\mathbb{Z}_2$ symmetry, dark matter can scatter on nuclei via Higgs and Z^0 exchange. Whether the WIMPs couple to these bosons is dictated by their Standard Model gauge group representation as well as their Lorentz representation. The coupling to the Higgs boson in given by a new parameter of the model whereas the coupling to the Z^0 boson is given by the Standard Model gauge couplings. If the latter case is not suppressed for example by singlet doublet mixing (see Ref. [2]), the dark matter candidate is usually ruled out by direct detection experiments.

In the case where the $\mathbb{Z}_2$ symmetry is replaced by the $\mathrm{U}(1)_X$ symmetry, we have an additional possibility for dark matter to scatter off nuclei. As the WIMPs are charged under $\mathrm{U}(1)_X$, the coupling of Z' is given by $g_X X_{\mathrm{DM}}$ at leading order in ϵ. Kinetic mixing introduces some corrections so that the Z' boson also couples to hypercharge and weak isospin. Similarly there is always a contribution from the Standard Model Z-boson as kinetic mixing couples the Z boson to the dark matter candidate. If the charge of the dark matter field is $X_{\mathrm{DM}} = \pm\frac{X_\zeta}{2}$, the vev of ζ can introduce a mass splitting between the oppositely charged components of the dark matter field. In this case elastic scattering via the Z' boson in not possible.

As an example for a case where scattering via the Z' exchange is relevant, we consider the case of Dirac dark matter. For simplicity we also assume that the dark matter is a singlet under the Standard Model gauge group. The couplings of the Z and Z' boson to dark matter and to quarks can be extracted from Eq. (10.3.44). The scattering cross section for protons is given by[13] (see e.g. Ref. [33])

$$\sigma_p = \frac{\mu^2}{\pi}|2b_u + b_d|^2 \tag{10.3.48}$$

where μ is the WIMP nucleon reduced mass and

$$b_q = \frac{g_{\bar{\chi}\chi Z',V}\, g_{\bar{q}q Z',V}}{m_{Z'}^2} + \frac{g_{\bar{\chi}\chi Z^0,V}\, g_{\bar{q}q Z^0,V}}{m_{Z^0}^2}. \tag{10.3.49}$$

The $g_{\dots,V}$ are the vector couplings to the two relevant gauge bosons.

To illustrate the impact of the direct detection experiments, we calculate the cross section for different dark matter masses and different values of g_X, but vary the kinetic mixing parameter and v_ζ. We then calculate what parts of the parameter space is excluded by XENON1T [34]. We show our results in Fig. 10.3. One can see that large parts of the parameter space are excluded by XENON1T. A comparison to Fig. 10.2 shows that for most values of g_X, direct detection proves to be the most stringent limit. It is important to stress, that this finding holds true for Dirac dark matter as well as complex scalar dark matter while for Majorana and real scalar fields there is no elastic scattering via the Z' exchange.

Inelastic scattering

Majorana and real scalar dark matter do not allow for elastic scattering off nuclei via the Z' exchange. As in the Lagrangian before symmetry breaking, all fermions are vector like and all scalar fields are complex, Majorana and real scalar fields always stem from Dirac or complex fields where the components obtain a mass splitting in the symmetry breaking process. For small v_ζ, the mass splitting between two components may also be small while EWSB always leads to large mass splittings. For example for vector like fermions with $\mathrm{U}(1)_X$

[13] Note that due to the vector like nature, the coupling to the WIMP is a always a vector coupling.

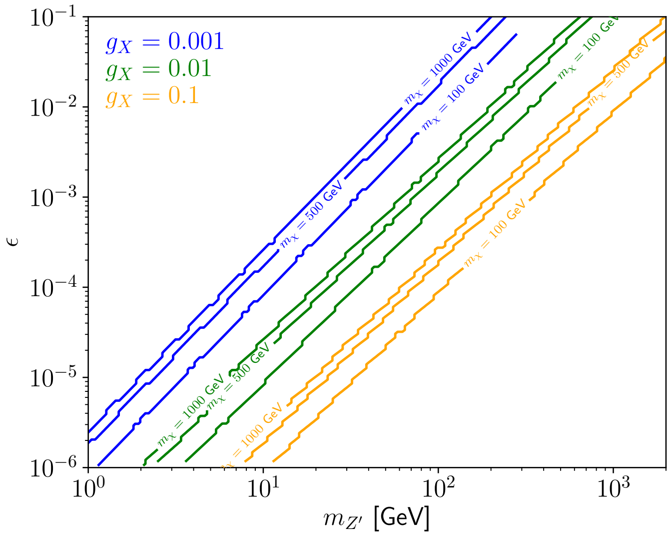

Figure 10.3: XENON1T limits for Dirac dark matter in the $m_{Z'} - \epsilon$ plane for different values of m_{DM} and g_X. The area above the lines is excluded by direct detection. The parameters are $X_{\mathrm{DM}} = 1, X_\zeta = 3$ while ϵ and v_ζ are varied.

charges of $X_\psi = \frac{1}{2} X_\zeta$ and zero hypercharge, the mass matrix is generated by terms in the Lagrangian as

$$\mathcal{L} \supset -m_\psi \psi \psi' - \lambda_\psi \psi \psi \zeta^\dagger - \lambda_{\psi'} \psi' \psi' \zeta + \text{H. c..} \tag{10.3.50}$$

After $\mathrm{U}(1)_X$ breaking this turns into

$$\mathcal{L} \supset -\frac{1}{2} \begin{pmatrix} \psi & \psi' \end{pmatrix} \begin{pmatrix} \sqrt{2} v_\zeta \lambda_\psi & m_\psi \\ m_\psi & \sqrt{2} v_\zeta \lambda_{\psi'} \end{pmatrix} \begin{pmatrix} \psi \\ \psi' \end{pmatrix} + \text{H. c..} \tag{10.3.51}$$

For $v_\zeta \ll m_\psi$, the two mass eigenstates then have a mass splitting of

$$\delta \doteq \sqrt{2} v_\zeta (\lambda_\psi + \lambda_{\psi'}). \tag{10.3.52}$$

Thus for v_ζ at $\mathcal{O}(100 \text{ keV})$ inelastic scattering can occur naturally.

Scalar exchange

Depending on the $\mathrm{U}(1)_X$ charge, there can also be a coupling between the dark matter candidate and ζ. Such a scattering is model dependent, as the coupling of dark matter to σ is a free parameter. Through Higgs mixing, this allows for dark matter scattering on nuclei via this channel, as h and σ mix, see Sec. 10.3.1. If a dark matter candidate is scalar, a direct coupling to the Standard Model Higgs is always possible through a $H^\dagger H \chi^\dagger \chi$ term. For fermion dark matter a direct coupling to the Standard Model Higgs is only possible if there exists a singlet-doublet or triplet-doublet coupling to the Higgs. If no such particle content is available, the only contribution is through Higgs mixing. In this case, the scattering takes place through the exchange of h_2. Compared to the exchange of the Standard Model-like Higgs h_1, its coupling to the quarks is then suppressed by the factor $\sin\alpha$, see Eqs. (10.3.14) and (10.3.18). If h_2 is heavier than h_1, it receives an additional suppression as the scattering cross section scales with $m_{h_2}^{-4}$.

10.3.6 Neutrinos

In this section we discuss how many generations of the new fields are required in order to allow for a least two massive neutrinos. In Ref. [10] the formulas for the neutrino masses arising from each topology are given. We first assume only one generation of each new field. In this case a simple pattern emerges in the neutrino mass formulas. Assuming that the neutrinos have Yukawa interactions with the new fields given by the couplings y, y', the neutrino mass matrix is

$$(M_\nu)_{\alpha\beta} \propto y_\alpha y'_\beta + y'_\alpha y_\beta =: A_{\alpha\beta} + A^T_{\alpha\beta}. \tag{10.3.53}$$

The proportionality factor depends on the masses and couplings of the new fields. It is easy to see that the matrix A has rank 1. The rank of M_ν and thus the number of massive neutrinos can be estimated to be ≤ 2. As the entries of the Yukawa couplings are not fixed a priori, the neutrino matrix will actually have rank two unless two fields in the loop are identified with each other, which yields $y = y'$.[14] Some models allow for the case where two fields are identified with each other. If one does so, the models predict only one massive neutrino unless one introduces several generations of one of the new fields.

[14]Strictly speaking some entries of y and y' could be exactly the same or a special relation to one another. This should not pose a problem since such a scenario would be extremely fine-tuned unless one had a reason for the entries to be the same.

10.4 Unification

Adding new fields to the Standard Model changes the running of the gauge couplings possibly leading to unification of all three Standard Model gauge couplings. Previous work has examined how the models from Ref. [11] stabilized by a $\mathbb{Z}_2$ affect the running of gauge couplings and if the couplings unify with the new particle content [74]. As our models with a gauged $\mathrm{U}(1)_X$ do have a different particle content (for example all scalar fields are complex), the running of coupling differs from the running in the $\mathbb{Z}_2$ case. In Ref. [74] they found that the difference between one and two loop is small (a few %). Thus we restrict ourselves to a analysis at one loop. The scale at which the new fields contribute also introduces some uncertainties.

For the Standard Model gauge couplings with the GUT normalization $g_1 = \sqrt{5/3}g_Y$ the RGEs at one loop are given by [74]

$$\frac{dg_k}{d\ln(\mu)} = b_k \frac{g_k^3}{(4\pi)^2} \tag{10.4.1}$$

where μ is the energy scale. The coefficients depend on the particle content of the model. For the Standard Model they are given by

$$b_k^{\mathrm{SM}} = \begin{pmatrix} \frac{41}{10} \\ -\frac{19}{6} \\ -7 \end{pmatrix}. \tag{10.4.2}$$

If one adds fields to the Standard Model the coefficients can be calculated by

$$b_k = b_k^{\mathrm{SM}} + \sum_i^N n_i b_k^i \tag{10.4.3}$$

where i is the index denoting the fields and n_i is the number of generations of i. b_k^i are the coefficients for the fields which can be calculated from the coefficients for complex scalars b_k^{CS} by

$$b_k^i = b_k^{\mathrm{CS}} \begin{cases} 1 & \text{complex scalar} \\ \frac{1}{2} & \text{real scalar} \\ 2 & \text{Weyl fermion} \\ 4 & \text{Dirac fermion} \end{cases}. \tag{10.4.4}$$

Table 10.6: One loop coefficients for complex scalars. Values taken from [74].

$(\mathrm{U}(1)_Y, \mathrm{SU}(2)_L, \mathrm{SU}(3)_c)$	b_k^{CS}
$(y, 1, 1)$	$\left(\frac{1}{5}y^2, 0, 0\right)$
$(y, 2, 1)$	$\left(\frac{2}{5}y^2, \frac{1}{6}, 0\right)$
$(y, 3, 1)$	$\left(\frac{3}{5}y^2, \frac{2}{3}, 0\right)$

For the U(1) models, all scalars are complex and all fermions are Dirac fermions since they are vector like. The coefficients for complex scalars in the relevant representations are given in Tab. 10.6. At one loop the RGEs can be solved analytically

$$\alpha_k^{-1}(\mu) = \alpha_k^{-1}(\mu_0) - \frac{b_k}{2\pi} \ln \frac{\mu}{\mu_0}. \tag{10.4.5}$$

Now we generalize the formulas to the case of two U(1) gauge groups. The running of coupling in the basis where kinetic mixing is absent (and one off diagonal entry of the coupling matrix is zero) is given by [196]

$$\frac{d}{d\ln(\mu)} g' = \frac{1}{(4\pi)^2} \left(A^{XX} g'^3 + 2A^{XY} g'^2 g_{XY} + A^{YY} g' g_{XY}^2 \right), \tag{10.4.6}$$

$$\frac{d}{d\ln(\mu)} g_Y = \frac{1}{(4\pi)^2} A^{YY} g_Y^3, \tag{10.4.7}$$

$$\frac{d}{d\ln(\mu)} g_{XY} = \frac{1}{(4\pi)^2} \left(A^{YY} g_{XY}(g_{XY}^2 + 2g_Y^2) + 2A^{XY} g'(g_{XY}^2 + g_Y^2) + A^{XX} g'^2 g_{XY} \right), \tag{10.4.8}$$

where A^{ab} takes a similar role as b_k^i and is for complex scalar fields given by

$$A^{ab} = \frac{1}{3} Y^a Y^b. \tag{10.4.9}$$

g' and g_{XY} are related to the couplings in Eq. (10.3.31) by $g' = \frac{g_X}{\sqrt{1-\epsilon^2}}$ and $g_{XY} = \frac{-g_Y \epsilon}{\sqrt{1-\epsilon^2}}$. With the GUT normalization $g_1 = \sqrt{5/3} g_Y$ and $g_4 = \sqrt{3/2} g'$

Table 10.7: One loop coefficients for complex scalars for two U(1) groups.

$(\mathrm{U}(1)_Y, \mathrm{SU}(2)_L, \mathrm{SU}(3)_c, \mathrm{U}(1)_X)$	$b_k^{\mathrm{CS}} \hat{=} \left(b_1, b_2, b_3, b_4, \tilde{b}\right)$
$(y, 1, 1, x)$	$\left(\frac{1}{5}y^2, 0, 0, \frac{2}{9}x^2, \sqrt{\frac{2}{45}}xy\right)$
$(y, 2, 1, x)$	$\left(\frac{2}{5}y^2, \frac{1}{6}, 0, \frac{4}{9}x^2, 2\sqrt{\frac{2}{45}}xy\right)$
$(y, 3, 1, x)$	$\left(\frac{3}{5}y^2, \frac{2}{3}, 0, \frac{6}{9}x^2, 3\sqrt{\frac{2}{45}}xy\right)$

the running of couplings is given by

$$\frac{d}{d\ln(\mu)} g_4 = \frac{1}{(4\pi)^2}\left(b_4 g_4^3 + 2\tilde{b} g_4^2 \tilde{g} + b_1 g_4 \tilde{g}^2\right) \tag{10.4.10}$$

$$\frac{d}{d\ln(\mu)} g_1 = \frac{1}{(4\pi)^2} b_1 g_1^3 \tag{10.4.11}$$

$$\frac{d}{d\ln(\mu)} \tilde{g} = \frac{1}{(4\pi)^2}\left(b_1 \tilde{g}(\tilde{g}^2 + 2g_1^2) + 2\tilde{b} g_4(\tilde{g}^2 + g_1^2) + b_4 g_4^2 \tilde{g}\right) \tag{10.4.12}$$

where we also defined $\tilde{g} = \sqrt{5/3}g_{XY}$. The contributions to the new coefficients b_k are given in Tab. 10.7. Note how at one loop, the running of the Standard Model gauge couplings only depends on the particle content and the representation of the particles, but not on the $\mathrm{U}(1)_X$ charges or the new gauge couplings g_4 and $\tilde{g}$. This allows us to consider the models independent of the $\mathrm{U}(1)_X$ charge assignments. Once the Unification point is found, one can impose at unification scale $\frac{g_4^2}{4\pi} = \alpha_{\mathrm{GUT}}$ and $\tilde{g} = 0$ and run these couplings down to TeV scale.

Similar to Ref. [74] we run the couplings to the scale of new physics $\Lambda_{\mathrm{NP}} = 1$ TeV using b_i^{SM}. For energy scales larger than Λ_{NP}, we use the coefficients calculated using Eq. (10.4.3) and the particle content of each model. The initial values are chosen as in Ref. [74] to allow for comparisons and are given by

$$\alpha_1(m_{Z^0}) = 0.01704, \qquad \alpha_2(m_{Z^0}) = 0.03399, \qquad \alpha_3(m_{Z^0}) = 0.1185 \tag{10.4.13}$$

with $m_{Z^0} = 91.1876$ GeV. As an example we show the running for the model T1-2-A with $\alpha = 0$ and $X_\psi = X_\phi = X_{\phi'} = X_{\psi'} = 1$ and $X_\zeta = 2$ in Fig. 10.4.

In order to quantify how good the couplings unify, we calculate the intersection points. The unification scale in then given by the average (of the

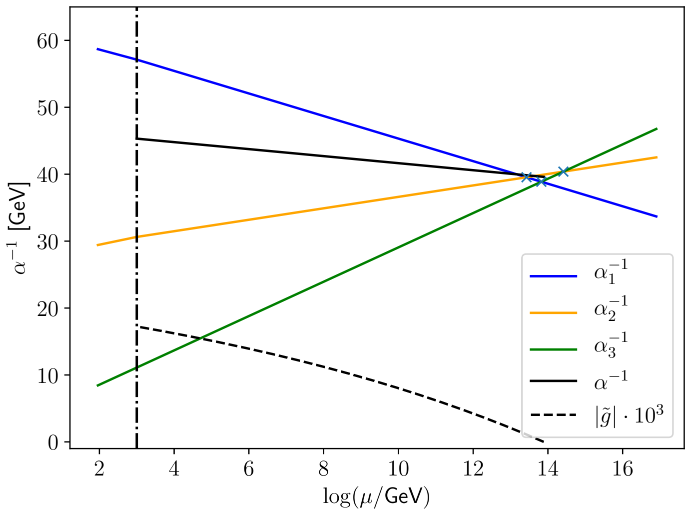

Figure 10.4: Running of coupling for the model T1-2-A with $\alpha = 0$ at one loop. The new particles contribute from $\Lambda_{\mathrm{NP}} = 1$ TeV upwards. Λ_{NP} is shown with the dashed line.

logarithmic values) of all three x-values of the intersection points and the relative error is

$$\frac{\Delta \log_{10}(\Lambda)}{\log_{10}(\Lambda)}. \tag{10.4.14}$$

$\Delta \log_{10}(\Lambda)$ is the separation of the intersection points that are the furthest apart from each other on the Λ-axis. For the couplings we proceed in a similar way with $\log_{10}(\Lambda) \to \alpha^{-1}$. Tables 10.8 to 10.11 show the Unification scale and the coupling at this scale as well as the respective errors for the models with the topologies T1-1, T1-2, T1-3 and T-3.

We find that in some models the couplings unify reasonably well whereas for other models the intersection points lie far apart. The new $\mathrm{U}(1)_X$ coupling can always be chosen in such a way that it unifies (i.e. passes through the middle of the triangle) as it is not fixed by experiments. Similarly the off diagonal coupling can be chosen to be zero at the unification scale. The models that unify do so at a scale of $\mathcal{O}(10^{12}\ \mathrm{GeV}) - \mathcal{O}(10^{14}\ \mathrm{GeV})$. This agrees qualitatively with the findings of Ref. [74]. The scale is lower than the unification scale expected from running with only the Standard Model fields as the running of $\mathrm{SU}(3)_c$ is not changed and the new fields affect the running of $\mathrm{SU}(2)_L$ and

Table 10.8: Unification results for models with Topology T1-1. Models marked with * have two generations of ψ while $\phi' = \phi^\dagger$.

Model	m	Λ [GeV]	$\frac{\Delta \log_{10}(\Lambda)}{\log_{10}(\Lambda)}$ [%]	$\alpha^{-1}(\Lambda)$	$\frac{\Delta\alpha}{\alpha}$ [%]
T1-1-A	2	1.43e+13	35.66	39.54	20.75
T1-1-A	0	2.21e+14	18.47	41.55	10.32
T1-1-A*	0	3.34e+14	22.55	42.27	12.78
T1-1-B	2	3.23e+11	12.12	31.77	6.03
T1-1-B	0	4.99e+14	57.09	34.11	24.94
T1-1-B*	0	3.55e+21	153.25	21.04	201.32
T1-1-C	1	5.37e+13	9.31	39.36	5.04
T1-1-D	1	1.86e+13	4.08	37.10	2.11
T1-1-D	-1	4.01e+13	8.77	37.53	4.47
T1-1-F	1	1.89e+13	20.96	35.43	10.24
T1-1-G	2	3.59e+12	21.33	37.20	11.86
T1-1-G	0	1.27e+14	1.13	39.50	0.59
T1-1-G*	0	1.70e+14	2.45	40.11	1.30
T1-1-H	2	2.04e+11	21.32	30.22	11.76
T1-1-H	0	2.59e+15	77.36	32.03	38.94
T1-1-H*	0	3.94e+28	192.07	9.68	780.08

$U(1)_Y$ in such a way that α^{-1} declines faster than in the Standard Model case.

When all couplings unify one would like to combine the gauge symmetry group to a larger gauge symmetry that is broken at this scale. In this grand unified group quarks and leptons are placed in the same representations and interactions with the gauge bosons of the larger symmetry allow for transitions between both. Such transitions are suppressed by the mass of the gauge bosons

Table 10.9: Unification results for models with Topology T1-2.

Model	m	Λ [GeV]	$\frac{\Delta \log_{10}(\Lambda)}{\log_{10}(\Lambda)}$ [%]	$\alpha^{-1}(\Lambda)$	$\frac{\Delta\alpha}{\alpha}$ [%]
T1-2-A	0	7.74e+13	7.10	39.60	3.82
T1-2-A	-2	1.46e+13	17.48	38.49	9.65
T1-2-B	0	6.07e+13	11.24	37.76	5.69
T1-2-B	-2	4.92e+12	4.39	36.33	2.32
T1-2-D	1	7.56e+11	27.49	30.96	14.37
T1-2-D	-1	4.76e+14	65.96	32.39	31.85
T1-2-F	1	5.47e+11	36.60	29.32	22.36
T1-2-F	-1	3.33e+15	86.49	30.11	51.83

which is given by the scale at which the group is broken. As these processes allow for proton decay, limits on the lifetime of protons can be used to set limits on the unification scale. As discussed in Sec. 4.3, the unification scale should be higher than 10^{15} GeV and thus our values for unification are ruled out. As our models do not claim to be complete models but only minimal explanations for dark matter and neutrino masses, one could imagine more (colored) new particles between the TeV and the GUT scale that change the running of coupling and thus the unification scale.

10.5 Embedding gauged scotogenic models into SO(10)

Additional U(1) gauge symmetries are often motivated by grand unified theories. The well known unification group SO(10) can be broken to the Standard Model gauge group and an additional U(1) symmetry. In this section we investigate whether the Standard Model uncharged under the extra U(1) can be embedded into irreducible representations of SO(10). We use LieART [197] to decompose the irreducible representations of SO(10) into SU(5)×U(1) representations and SU(5) representations into SU(3)×SU(2)×U(1) represen-

Table 10.10: Unification results for models with Topology T1-3. Models marked with * have two generations of ϕ while ψ' is combined with ψ into a vector like doublet.

Model	m	Λ [GeV]	$\frac{\Delta \log_{10}(\Lambda)}{\log_{10}(\Lambda)}$ [%]	$\alpha^{-1}(\Lambda)$	$\frac{\Delta\alpha}{\alpha}$ [%]
T1-3-A	0	3.41e+13	3.16	37.86	1.64
T1-3-A*	0	1.07e+14	10.75	40.23	5.86
T1-3-B	0	3.42e+13	20.59	36.14	10.08
T1-3-B*	0	8.64e+13	26.03	36.58	12.54
T1-3-C	1	1.98e+13	15.53	38.70	8.54
T1-3-D	1	3.57e+13	51.69	31.90	25.70
T1-3-D	-1	1.06e+12	29.78	31.05	15.50
T1-3-F	1	6.17e+13	92.44	23.21	100.62
T1-3-G	0	5.13e+14	74.63	30.64	42.35
T1-3-G*	0	4.77e+14	63.03	32.97	28.84
T1-3-H	0	4.95e+15	95.56	28.10	68.46
T1-3-H*	0	5.78e+16	106.39	27.89	77.93

tations. Putting the results together we find the decompositions of SO(10) irreducible representations into SU(3)×SU(2)×U(1)×U(1). For the SO(10) representations up to $\underline{144}$, we find the following decompositions:

$$\underline{10} = (3,1,2,2)_{\mathrm{VL}} + (1,2,-3,2)_{\mathrm{VL}}, \tag{10.5.1}$$

$$\begin{aligned}\underline{16} =&(3,2,-1,-1) + (\overline{3},1,4,-1) + (1,1,-6,-1)+\\ &(\overline{3},1,-2,3) + (1,2,3,3) + (1,1,0,-5),\end{aligned} \tag{10.5.2}$$

$$\begin{aligned}\underline{45} =&(8,1,0,0) + (3,2,5,0)_{\mathrm{VL}} + (1,3,0,0) + (1,1,0,0)+\\ &(3,2,-1,4)_{\mathrm{VL}} + (\overline{3},1,4,4)_{\mathrm{VL}} + (1,1,-6,4)_{\mathrm{VL}} + (1,1,0,0),\end{aligned} \tag{10.5.3}$$

Table 10.11: Unification results for models with Topology T3.

Model	m	Λ [GeV]	$\frac{\Delta \log_{10}(\Lambda)}{\log_{10}(\Lambda)}$ [%]	$\alpha^{-1}(\Lambda)$	$\frac{\Delta\alpha}{\alpha}$ [%]
T3-A	0	2.35e+13	0.88	37.64	0.46
T3-A	-2	5.04e+13	5.52	38.08	2.85
T3-B	1	1.84e+13	33.96	39.73	19.69
T3-B	-1	2.21e+14	18.47	41.55	10.32
T3-C	1	1.00e+13	34.83	32.98	16.27
T3-C	-1	7.45e+13	46.67	33.59	21.05
T3-E	0	2.23e+13	18.02	35.94	8.89

$$\begin{aligned}\underline{54} =&(8,1,0,0) + (3,2,5,0)_{\mathrm{VL}} + (1,3,0,0) + (1,1,0,0)+\\ &(6,1,4,4)_{\mathrm{VL}} + (3,2,-1,4)_{\mathrm{VL}} + (1,3,-6,4)_{\mathrm{VL}},\end{aligned} \tag{10.5.4}$$

$$\begin{aligned}\underline{120} =&(8,2,-3,2)_{\mathrm{VL}} + (\overline{6},1,2,2)_{\mathrm{VL}} + (3,3,2,2)_{\mathrm{VL}} + (\overline{3},2,7,2)_{\mathrm{VL}}+\\ &(\overline{3},1,-8,2)_{\mathrm{VL}} + (3,1,2,2)_{\mathrm{VL}} + (1,2,-3,2)_{\mathrm{VL}} + (3,2,-1,-6)_{\mathrm{VL}}+\\ &(\overline{3},1,4,-6)_{\mathrm{VL}} + (1,1,-6,-6)_{\mathrm{VL}} + (3,1,2,2)_{\mathrm{VL}} + (1,2,-3,2)_{\mathrm{VL}},\end{aligned} \tag{10.5.5}$$

$$\begin{aligned}\underline{126} =&(8,2,-3,2)_{\mathrm{VL}} + (\overline{6},3,2,2) + (6,1,-8,2) + (\overline{3},2,7,2)_{\mathrm{VL}} + (3,1,2,2)_{\mathrm{VL}}+\\ &(1,1,12,2) + (6,1,-2,-2) + (\overline{3},3,-2,-2) + (3,1,8,-2)+\\ &(1,2,3,-2)_{\mathrm{VL}} + (6,1,4,-6) + (3,2,-1,-6)_{\mathrm{VL}} + (1,3,-6,-6)+\\ &(3,1,-4,6) + (1,1,6,6) + (3,1,2,2) + (1,1,0,10),\end{aligned} \tag{10.5.6}$$

$$\begin{aligned}\underline{144} =&(8,2,3,3) + (6,1,-2,3) + (\overline{3},3,-2,3) + (3,2,-7,3) + (3,1,8,3)+\\ &(\overline{3},1,-2,3) + (1,2,3,3) + (8,1,-6,-1) + (\overline{6},2,-1,-1) + (\overline{3},3,4,-1)+\\ &(3,2,-1,-1) + (\overline{3},1,4,-1) + (1,2,9,-1) + (8,1,0,-5) + (3,2,5,-5)+\\ &(\overline{3},2,-5,-5) + (1,3,0,-5) + (1,1,0,-5) + (6,1,4,-1)+\\ &(3,2,-1,-1) + (1,3,-6,-1) + (3,2,-1,-1) + (\overline{3},1,4,-1)+\\ &(1,1,-6,-1) + (\overline{3},1,-2,3) + (1,2,3,3) + (3,1,2,7) + (1,2,-3,7).\end{aligned} \tag{10.5.7}$$

We marked fields for which also a field in the conjugate representation occurs with the subscript VL as these are vector like fields. The fermions in the Standard Model are for our models in the following representations of $\mathrm{SU}(3)_c{\times}\mathrm{SU}(2)_L{\times}\mathrm{U}(1)_Y{\times}\mathrm{U}(1)_X$

$$Q:\left(3,2,\frac{1}{6},0\right),\quad L:\left(1,2,-\frac{1}{2},0\right), \tag{10.5.8}$$

$$u_R^c:\left(\overline{3},1,-\frac{2}{3},0\right),\quad d_R^c:\left(\overline{3},1,\frac{1}{3},0\right),\quad e_R^c:(1,1,1,0)\,. \tag{10.5.9}$$

As there are two U(1) groups, we are free to make a change of basis (including rescaling) for the two corresponding charges. Usually the Standard Model is embedded into the $\underline{16}$ representation. However one can easily see, that all Standard Model fields then do have a $\mathrm{U}(1)_X$ charge. Looking at higher representations we can find cases where some Standard Model fields do not have $\mathrm{U}(1)_X$ charge. This however fixes the basis and we do not find any basis where all the fields given in Eqs. (10.5.8, 10.5.9) occur at the same time. As for all of our models, the Standard Model fields must be uncharged, it is not possible to embed our models into a grand unified theory with a SO(10) gauge group. If we look at groups of higher rang, e.g. E_6, which has the subgroup SO(10)×U(1), we end up with three abelian groups and more different ways to choose the basis are possible.

Another issue with embedding our models into GUTs is that in many irreducible representations, a right handed neutrino arises. This almost always allows for type I seesaw which can yield to correct neutrino masses if the right handed neutrino has a Majorana mass term of $\mathcal{O}(\Lambda_{\mathrm{GUT}})$.

10.6 Summary and outlook

Minimal extensions of the Standard Model can introduce viable dark matter candidates and generate neutrino masses. To stabilize the dark sector a new symmetry must be introduced. This symmetry can be a local U(1) symmetry. Arguments based on anomaly cancellation and the neutrino topologies restrict the possible charge assignments. We find that the Standard Model must be uncharged under the new gauge group and all new fermions must be vector like. We then give the particle content of all possible models and the charge assignments.

An additional scalar field is introduced in order to break the new U(1) symmetry. The extended gauge and Higgs sector give rise to a number of new phenomena. Especially gauge kinetic mixing which introduces mixing between the Standard Model Z^0 boson and the new Z' boson can be severely constrained by experiments. Other phenomenological aspects such as LFV and the dark matter phenomenology are dependent on the specific particle content of the model.

We run the Standard Model gauge couplings in order to find out whether, with the particle content of the new models, the unification hypothesis is fulfilled. Some models allow for grand unification, however the unification scale is generally to low to comply with the limits on the proton lifetime.

We decompose irreducible representations of SO(10) along the breaking chain SO(10) $\rightarrow$SU(5)$\times$U(1) $\rightarrow$SU(3)$\times$SU(2)$\times$U(1)$\times$U(1) in order to find out whether the new models can be embedded into such a GUT. We find that it seems to be impossible to have an uncharged Standard Model and thus our models cannot be embedded into a SO(10).

As future work it would be interesting to investigate the full phenomenology of some specific models, similarly to the studies of models with a $\mathbb{Z}_2$ symmetry presented in this thesis. As a starting point one could choose models with only three new fields preferably in trivial or fundamental representations such as T3-A or T1-3-A as these are more simple and have less free parameters. Furthermore the case of very light or massless dark photons could be investigated under astrophysical aspects as suggested in Ref. [167]. With the limits on kinetic mixing in this mass range being strong [198] one could also investigate whether the running of this parameter prevents it from being small in all of the relevant energy range and thus gives conflicts with experiments.

11 Conclusion and Outlook

Minimals models can successfully explain both dark matter as well as neutrino masses while being testable by current and near future experiments. New physics at TeV scale including dark matter allows for the correct neutrino masses generated via the radiative seesaw mechanism. With maximally for new fields in the $\mathbb{Z}_2$ case and maximally six new fields for the gauged models, only few unknown parameters are introduced. This simplicity is an advantage over complicated theories such as supersymmetry and allows detailed studies of the entire parameter space.

In Chaps. 2, 3 and 4 we give an introduction to the question about the nature of dark matter and the generation of neutrino masses as well as an overview about relevant experiments and their current constraints.

Chapter 5 is devoted to the theoretical foundations necessary for describing minimal models. Conventions are introduced and theoretical constraints are presented. Furthermore the main mechanisms for neutrino mass generation are discussed.

Minimal models with dark matter and neutrino masses as well as their classification are presented in Chap. 6. Arguably the simplest and most famous of these models, the scotogenic model which extents the Standard model by an inert doublet and three generations of right handed neutrinos is then introduced in detail. Additionally another simple model with three new multiplets is discussed. This model, called T1-3-B ($\alpha = 0$), allows for fermion singlet doublet and scalar triplet dark matter as well as two generations of massive neutrinos.

In Chap. 7 fermionic dark matter in the framework of the scotogenic model is studied. The scalar coupling λ_5, which has a strong impact on the phenomenology, is for models which yield the correct relic density found to be solely dependent on the absolute neutrino mass. A determination of the neutrino mass with the KATRIN experiment would fix this coupling. In addition, the determination of the dark matter mass fixes the value of the Yukawa couplings. Future experiments on LFV and the absolute neutrino mass are shown to exclude the fermionic dark matter if there are no coannihilations.

Chapter 8 treats indirect detection constraints for scalar dark matter in the scotogenic model. As the mass splitting between both neutral scalar components is naturally small, inelastic scatting is kinematically allowed. The corresponding scattering formalism is discussed in detail and a code that calculates the expected event rates at IceCube is introduced. Numerical results show that indirect detection with neutrinos from dark matter in the sun is more sensitive to inelastic scattering than direct detection on earth.

Prospects for neutrino telescopes are further discussed in Chap. 9 where the model T1-3-B ($\alpha = 0$) is studied. This model allows for both spin independent as well as spin dependent scattering of WIMPs on nucleons. Indirect detection is generally more competitive in the case where dark matter accumulates in the sun through spin dependent scattering. The expected event rates at IceCube are calculated and a numerical scan shows that there are points yielding event rates up to 10 events per year which are not excluded by experimental limits. A future analysis of IceCube data might exclude this part of the parameter space.

Finally we promote the stabilizing symmetry to a local U(1) in Chap. 10. The models are constructed in such a way that all gauge anomalies cancel and Majorana neutrino masses are generated at one loop. The phenomenology of these models is discussed with special emphasis on the Z' boson. We investigate the gauge coupling unification for all of these models.

Bibliography

[1] T. de Boer et al. “Absolute neutrino mass as the missing link to the dark sector”. In: *Phys. Rev. D* 102.5 (2020), p. 051702. DOI: 10.1103/PhysRevD.102.051702. arXiv: 2007.05338 [hep-ph].

[2] T. de Boer et al. “New constraints on radiative seesaw models from IceCube and other neutrino detectors”. In: *Phys. Rev. D* 103.12 (2021), p. 123006. DOI: 10.1103/PhysRevD.103.123006. arXiv: 2103.06881 [hep-ph].

[3] T. de Boer et al. “Indirect detection constraints on the scotogenic dark matter model”. In: *Journal of Cosmology and Astroparticle Physics* 2021.08 (Aug. 2021), p. 038. DOI: 10.1088/1475-7516/2021/08/038. arXiv: 2105.04899 [hep-ph]. URL: https://doi.org/10.1088/1475-7516/2021/08/038.

[4] Georges Aad et al. “Observation of a new particle in the search for the Standard Model Higgs boson with the ATLAS detector at the LHC”. In: *Phys. Lett. B* 716 (2012), pp. 1–29. DOI: 10.1016/j.physletb.2012.08.020. arXiv: 1207.7214 [hep-ex].

[5] Serguei Chatrchyan et al. “Observation of a New Boson at a Mass of 125 GeV with the CMS Experiment at the LHC”. In: *Phys. Lett. B* 716 (2012), pp. 30–61. DOI: 10.1016/j.physletb.2012.08.021. arXiv: 1207.7235 [hep-ex].

[6] Y. Fukuda et al. “Evidence for oscillation of atmospheric neutrinos”. In: *Phys. Rev. Lett.* 81 (1998), pp. 1562–1567. DOI: 10.1103/PhysRevLett.81.1562. arXiv: hep-ex/9807003.

[7] Q. R. Ahmad et al. “Direct evidence for neutrino flavor transformation from neutral current interactions in the Sudbury Neutrino Ob-

servatory”. In: *Phys. Rev. Lett.* 89 (2002), p. 011301. DOI: 10.1103/PhysRevLett.89.011301. arXiv: nucl-ex/0204008.

[8] M. Aker et al. “Improved Upper Limit on the Neutrino Mass from a Direct Kinematic Method by KATRIN”. In: *Phys. Rev. Lett.* 123.22 (2019), p. 221802. DOI: 10.1103/PhysRevLett.123.221802. arXiv: 1909.06048 [hep-ex].

[9] Ernest Ma. “Verifiable radiative seesaw mechanism of neutrino mass and dark matter”. In: *Phys. Rev. D* 73 (2006), p. 077301. DOI: 10.1103/PhysRevD.73.077301. arXiv: hep-ph/0601225.

[10] Florian Bonnet et al. “Systematic study of the d=5 Weinberg operator at one-loop order”. In: *JHEP* 07 (2012), p. 153. DOI: 10.1007/JHEP07(2012)153. arXiv: 1204.5862 [hep-ph].

[11] Diego Restrepo, Oscar Zapata, and Carlos E. Yaguna. “Models with radiative neutrino masses and viable dark matter candidates”. In: *JHEP* 11 (2013), p. 011. DOI: 10.1007/JHEP11(2013)011. arXiv: 1308.3655 [hep-ph].

[12] F. Zwicky. “Die Rotverschiebung von extragalaktischen Nebeln”. In: *Helvetica Physica Acta* 6 (Jan. 1933), pp. 110–127.

[13] A V Zasov et al. “Dark matter in galaxies”. In: *Physics-Uspekhi* 60.1 (Jan. 2017), pp. 3–39. DOI: 10.3367/ufne.2016.03.037751. arXiv: 1710.10630. URL: https://doi.org/10.3367/ufne.2016.03.037751.

[14] E. Kolb and M. Turner. *The Early Universe*. Frontiers in physics. Avalon Publishing, 1994. ISBN: 9780813346458. URL: https://books.google.de/books?id=Qwijr-HsvMMC.

[15] Douglas Clowe, Anthony Gonzalez, and Maxim Markevitch. “Weak lensing mass reconstruction of the interacting cluster 1E0657-558: Direct evidence for the existence of dark matter”. In: *Astrophys. J.* 604 (2004), pp. 596–603. DOI: 10.1086/381970. arXiv: astro-ph/0312273.

[16] N. Aghanim et al. “Planck 2018 results. VI. Cosmological parameters”. In: (July 2018). arXiv: 1807.06209 [astro-ph.CO].

[17] Mordehai Milgrom. “Dynamics with a non-standard inertia-acceleration relation: an alternative to dark matter”. In: *Annals Phys.* 229 (1994), pp. 384–415. DOI: 10.1006/aphy.1994.1012. arXiv: astro-ph/9303012.

[18] D. P. Bennett et al. “The MACHO project dark matter search”. In: *ASP Conf. Ser.* 88 (1996), p. 95. arXiv: astro-ph/9510104.

[19] Ya. B. Zel’dovich and I. D. Novikov. “The Hypothesis of Cores Retarded during Expansion and the Hot Cosmological Model”. In: *azh* 43 (Jan. 1966), p. 758.

[20] R. D. Peccei and Helen R. Quinn. “CP Conservation in the Presence of Instantons”. In: *Phys. Rev. Lett.* 38 (1977), pp. 1440–1443. DOI: 10.1103/PhysRevLett.38.1440.

[21] R. D. Peccei and Helen R. Quinn. “Constraints Imposed by CP Conservation in the Presence of Instantons”. In: *Phys. Rev. D* 16 (1977), pp. 1791–1797. DOI: 10.1103/PhysRevD.16.1791.

[22] Frank Wilczek. “Problem of Strong P and T Invariance in the Presence of Instantons”. In: *Phys. Rev. Lett.* 40 (1978), pp. 279–282. DOI: 10.1103/PhysRevLett.40.279.

[23] Steven Weinberg. “A New Light Boson?” In: *Phys. Rev. Lett.* 40 (1978), pp. 223–226. DOI: 10.1103/PhysRevLett.40.223.

[24] Th. Kaluza. “Zum Unitätsproblem der Physik”. In: *Sitzungsber. Preuss. Akad. Wiss. Berlin (Math. Phys.)* 1921 (1921), pp. 966–972. DOI: 10.1142/S0218271818700017. arXiv: 1803.08616 [physics.hist-ph].

[25] Oskar Klein. “Quantum Theory and Five-Dimensional Theory of Relativity. (In German and English)”. In: *Z. Phys.* 37 (1926). Ed. by J. C. Taylor, pp. 895–906. DOI: 10.1007/BF01397481.

[26] Geraldine Servant and Timothy M. P. Tait. “Is the lightest Kaluza-Klein particle a viable dark matter candidate?” In: *Nucl. Phys. B* 650 (2003), pp. 391–419. DOI: 10.1016/S0550-3213(02)01012-X. arXiv: hep-ph/0206071.

[27] Gerard Jungman, Marc Kamionkowski, and Kim Griest. "Supersymmetric dark matter". In: *Physics Reports* 267.5 (1996), pp. 195–373. ISSN: 0370-1573. DOI: https://doi.org/10.1016/0370-1573(95)00058-5. URL: http://www.sciencedirect.com/science/article/pii/0370157395000585.

[28] P.A. Zyla et al. "Review of Particle Physics". In: *PTEP* 2020.8 (2020), p. 083C01. DOI: 10.1093/ptep/ptaa104.

[29] Lawrence J. Hall et al. "Freeze-In Production of FIMP Dark Matter". In: *JHEP* 03 (2010), p. 080. DOI: 10.1007/JHEP03(2010)080. arXiv: 0911.1120 [hep-ph].

[30] Nicolás Bernal et al. "The Dawn of FIMP Dark Matter: A Review of Models and Constraints". In: *Int. J. Mod. Phys. A* 32.27 (2017), p. 1730023. DOI: 10.1142/S0217751X1730023X. arXiv: 1706.07442 [hep-ph].

[31] R. Jeannerot, X. Zhang, and Robert H. Brandenberger. "Non-thermal production of neutralino cold dark matter from cosmic string decays". In: *JHEP* 12 (1999), p. 003. DOI: 10.1088/1126-6708/1999/12/003. arXiv: hep-ph/9901357.

[32] Martin Bauer and Tilman Plehn. *Yet Another Introduction to Dark Matter: The Particle Physics Approach*. Vol. 959. Lecture Notes in Physics. Springer, 2019. DOI: 10.1007/978-3-030-16234-4. arXiv: 1705.01987 [hep-ph].

[33] Prateek Agrawal et al. "A Classification of Dark Matter Candidates with Primarily Spin-Dependent Interactions with Matter". In: (Mar. 2010). arXiv: 1003.1912 [hep-ph].

[34] E. Aprile et al. "Dark Matter Search Results from a One Ton-Year Exposure of XENON1T". In: *Phys. Rev. Lett.* 121.11 (2018), p. 111302. DOI: 10.1103/PhysRevLett.121.111302. arXiv: 1805.12562 [astro-ph.CO].

[35] D. S. Akerib et al. "Results from a search for dark matter in the complete LUX exposure". In: *Phys. Rev. Lett.* 118.2 (2017), p. 021303. DOI: 10.1103/PhysRevLett.118.021303. arXiv: 1608.07648 [astro-ph.CO].

[36] Xiangyi Cui et al. "Dark Matter Results From 54-Ton-Day Exposure of PandaX-II Experiment". In: *Phys. Rev. Lett.* 119.18 (2017), p. 181302. DOI: 10.1103/PhysRevLett.119.181302. arXiv: 1708.06917 [astro-ph.CO].

[37] S. Adrian-Martinez et al. “Limits on Dark Matter Annihilation in the Sun using the ANTARES Neutrino Telescope”. In: *Phys. Lett. B* 759 (2016), pp. 69–74. DOI: 10.1016/j.physletb.2016.05.019. arXiv: 1603.02228 [astro-ph.HE].

[38] M. G. Aartsen et al. “Search for annihilating dark matter in the Sun with 3 years of IceCube data”. In: *Eur. Phys. J. C* 77.3 (2017). [Erratum: Eur.Phys.J.C 79, 214 (2019)], p. 146. DOI: 10.1140/epjc/s10052-017-4689-9. arXiv: 1612.05949 [astro-ph.HE].

[39] K. Choi et al. “Search for neutrinos from annihilation of captured low-mass dark matter particles in the Sun by Super-Kamiokande”. In: *Phys. Rev. Lett.* 114.14 (2015), p. 141301. DOI: 10.1103/PhysRevLett.114.141301. arXiv: 1503.04858 [hep-ex].

[40] J. Billard, L. Strigari, and E. Figueroa-Feliciano. “Implication of neutrino backgrounds on the reach of next generation dark matter direct detection experiments”. In: *Phys. Rev. D* 89.2 (2014), p. 023524. DOI: 10.1103/PhysRevD.89.023524. arXiv: 1307.5458 [hep-ph].

[41] R. Bernabei et al. “First model independent results from DAMA/LIBRA-phase2”. In: *Nucl. Phys. Atom. Energy* 19.4 (2018), pp. 307–325. DOI: 10.15407/jnpae2018.04.307. arXiv: 1805.10486 [hep-ex].

[42] E. Aprile et al. “Constraining the spin-dependent WIMP-nucleon cross sections with XENON1T”. In: *Phys. Rev. Lett.* 122.14 (2019), p. 141301. DOI: 10.1103/PhysRevLett.122.141301. arXiv: 1902.03234 [astro-ph.CO].

[43] C. Amole et al. “Dark Matter Search Results from the Complete Exposure of the PICO-60 C_3F_8 Bubble Chamber”. In: *Phys. Rev. D* 100.2 (2019), p. 022001. DOI: 10.1103/PhysRevD.100.022001. arXiv: 1902.04031 [astro-ph.CO].

[44] D. S. Akerib et al. “Limits on spin-dependent WIMP-nucleon cross section obtained from the complete LUX exposure”. In: *Phys. Rev. Lett.* 118.25 (2017), p. 251302. DOI: 10.1103/PhysRevLett.118.251302. arXiv: 1705.03380 [astro-ph.CO].

[45] Changbo Fu et al. “Spin-Dependent Weakly-Interacting-Massive-Particle–Nucleon Cross Section Limits from First Data of PandaX-II Experiment”. In: *Phys. Rev. Lett.* 118.7 (2017). [Erratum: Phys.Rev.Lett. 120, 049902

(2018)], p. 071301. DOI: 10.1103/PhysRevLett.118.071301. arXiv: 1611.06553 [hep-ex].

[46] C. A. Argüelles et al. "Solar Atmospheric Neutrinos and the Sensitivity Floor for Solar Dark Matter Annihilation Searches". In: *JCAP* 07 (2017), p. 024. DOI: 10.1088/1475-7516/2017/07/024. arXiv: 1703.07798 [astro-ph.HE].

[47] A. Albert et al. "Combined search for neutrinos from dark matter self-annihilation in the Galactic Center with ANTARES and IceCube". In: *Phys. Rev. D* 102.8 (2020), p. 082002. DOI: 10.1103/PhysRevD.102.082002. arXiv: 2003.06614 [astro-ph.HE].

[48] K. Abe et al. "Indirect search for dark matter from the Galactic Center and halo with the Super-Kamiokande detector". In: *Phys. Rev. D* 102.7 (2020), p. 072002. DOI: 10.1103/PhysRevD.102.072002. arXiv: 2005.05109 [hep-ex].

[49] G. Abbiendi et al. "Search for stable and longlived massive charged particles in e+ e- collisions at s**(1/2) = 130-GeV to 209-GeV". In: *Phys. Lett. B* 572 (2003), pp. 8–20. DOI: 10.1016/S0370-2693(03)00639-7. arXiv: hep-ex/0305031.

[50] Q. R. Ahmad et al. "Measurement of the rate of $\nu_e + d \to p + p + e^-$ interactions produced by ^{8}B solar neutrinos at the Sudbury Neutrino Observatory". In: *Phys. Rev. Lett.* 87 (2001), p. 071301. DOI: 10.1103/PhysRevLett.87.071301. arXiv: nucl-ex/0106015.

[51] Ivan Esteban et al. "Global analysis of three-flavour neutrino oscillations: synergies and tensions in the determination of θ_{23}, δ_{CP}, and the mass ordering". In: *JHEP* 01 (2019), p. 106. DOI: 10.1007/JHEP01(2019)106. arXiv: 1811.05487 [hep-ph].

[52] K. Abe et al. "Constraint on the matter–antimatter symmetry-violating phase in neutrino oscillations". In: *Nature* 580.7803 (2020), pp. 339–344. DOI: 10.1038/s41586-020-2177-0. arXiv: 1910.03887 [hep-ex].

[53] M. A. Acero et al. "First Measurement of Neutrino Oscillation Parameters using Neutrinos and Antineutrinos by NOvA". In: *Phys. Rev. Lett.* 123.15 (2019), p. 151803. DOI: 10.1103/PhysRevLett.123.151803. arXiv: 1906.04907 [hep-ex].

[54] G. Drexlin et al. “Current direct neutrino mass experiments”. In: *Adv. High Energy Phys.* 2013 (2013), p. 293986. DOI: 10.1155/2013/293986. arXiv: 1307.0101 [physics.ins-det].

[55] Sunny Vagnozzi et al. “Unveiling ν secrets with cosmological data: neutrino masses and mass hierarchy”. In: *Phys. Rev. D* 96.12 (2017), p. 123503. DOI: 10.1103/PhysRevD.96.123503. arXiv: 1701.08172 [astro-ph.CO].

[56] A. Gando et al. “Search for Majorana Neutrinos near the Inverted Mass Hierarchy Region with KamLAND-Zen”. In: *Phys. Rev. Lett.* 117.8 (2016). [Addendum: Phys.Rev.Lett. 117, 109903 (2016)], p. 082503. DOI: 10.1103/PhysRevLett.117.082503. arXiv: 1605.02889 [hep-ex].

[57] A.M. Baldini et al. “Search for the lepton flavour violating decay $\mu^+ \to \mathrm{e}^+\gamma$ with the full dataset of the MEG experiment”. In: *Eur. Phys. J. C* 76.8 (2016), p. 434. DOI: 10.1140/epjc/s10052-016-4271-x. arXiv: 1605.05081 [hep-ex].

[58] Francesco Renga. “The quest for $\mu \to e\gamma$: present and future”. In: *Hyperfine Interact.* 239.1 (2018), p. 58. DOI: 10.1007/s10751-018-1534-y. arXiv: 1811.05921 [hep-ex].

[59] U. Bellgardt et al. “Search for the Decay mu+ —¿ e+ e+ e-”. In: *Nucl. Phys. B* 299 (1988), pp. 1–6. DOI: 10.1016/0550-3213(88)90462-2.

[60] A. Blondel et al. “Research Proposal for an Experiment to Search for the Decay $\mu \to eee$”. In: (Jan. 2013). arXiv: 1301.6113 [physics.ins-det].

[61] C. Dohmen et al. “Test of lepton flavor conservation in mu —¿ e conversion on titanium”. In: *Phys. Lett. B* 317 (1993), pp. 631–636. DOI: 10.1016/0370-2693(93)91383-X.

[62] *A Letter of Intent on Nuclear and Particle Physics Experiments at the J-PARC 50 GeV Proton Synchrotron.* URL: http://j-parc.jp/researcher/Hadron/en/pac_0606/pdf/p20-Kuno.pdf.

[63] Friedrich Jegerlehner. *The Anomalous Magnetic Moment of the Muon.* Vol. 274. Cham: Springer, 2017. DOI: 10.1007/978-3-319-63577-4.

[64] B. Abi et al. “Measurement of the Positive Muon Anomalous Magnetic Moment to 0.46 ppm”. In: *Phys. Rev. Lett.* 126.14 (2021), p. 141801. DOI: 10.1103/PhysRevLett.126.141801. arXiv: 2104.03281 [hep-ex].

[65] Pran Nath and Pavel Fileviez Perez. "Proton stability in grand unified theories, in strings and in branes". In: *Phys. Rept.* 441 (2007), pp. 191–317. DOI: 10.1016/j.physrep.2007.02.010. arXiv: hep-ph/0601023.

[66] A. Takenaka et al. "Search for proton decay via $p \to e^+\pi^0$ and $p \to \mu^+\pi^0$ with an enlarged fiducial volume in Super-Kamiokande I-IV". In: *Phys. Rev. D* 102.11 (2020), p. 112011. DOI: 10.1103/PhysRevD.102.112011. arXiv: 2010.16098 [hep-ex].

[67] Herbi K. Dreiner, Howard E. Haber, and Stephen P. Martin. "Two-component spinor techniques and Feynman rules for quantum field theory and supersymmetry". In: *Phys. Rept.* 494 (2010), pp. 1–196. DOI: 10.1016/j.physrep.2010.05.002. arXiv: 0812.1594 [hep-ph].

[68] M.E. Peskin and D.V. Schroeder. *An Introduction To Quantum Field Theory*. Frontiers in Physics. Avalon Publishing, 1995. ISBN: 9780813345437.

[69] M.D. Schwartz. *Quantum Field Theory and the Standard Model*. Cambridge University Press, 2013. ISBN: 9781108976336.

[70] M. Srednicki. *Quantum Field Theory*. Cambridge University Press, 2007. ISBN: 9781139462761.

[71] Edward Witten. "An SU(2) Anomaly". In: *Phys. Lett. B* 117 (1982). Ed. by Mikhail A. Shifman, pp. 324–328. DOI: 10.1016/0370-2693(82)90728-6.

[72] Florian Staub. "SARAH 4 : A tool for (not only SUSY) model builders". In: *Comput. Phys. Commun.* 185 (2014), pp. 1773–1790. DOI: 10.1016/j.cpc.2014.02.018. arXiv: 1309.7223 [hep-ph].

[73] Florian Staub. "Exploring new models in all detail with SARAH". In: *Adv. High Energy Phys.* 2015 (2015), p. 840780. DOI: 10.1155/2015/840780. arXiv: 1503.04200 [hep-ph].

[74] Claudia Hagedorn et al. "Unification of Gauge Couplings in Radiative Neutrino Mass Models". In: *JHEP* 09 (2016), p. 111. DOI: 10.1007/JHEP09(2016)111. arXiv: 1605.03986 [hep-ph].

[75] S. Dimopoulos, S. Raby, and Frank Wilczek. "Supersymmetry and the Scale of Unification". In: *Phys. Rev. D* 24 (1981), pp. 1681–1683. DOI: 10.1103/PhysRevD.24.1681.

[76] Luis E. Ibanez and Graham G. Ross. “Low-Energy Predictions in Supersymmetric Grand Unified Theories”. In: *Phys. Lett. B* 105 (1981), pp. 439–442. DOI: 10.1016/0370-2693(81)91200-4.

[77] William J. Marciano and Goran Senjanovic. “Predictions of Supersymmetric Grand Unified Theories”. In: *Phys. Rev. D* 25 (1982), p. 3092. DOI: 10.1103/PhysRevD.25.3092.

[78] Steven Weinberg. “Baryon and Lepton Nonconserving Processes”. In: *Phys. Rev. Lett.* 43 (1979), pp. 1566–1570. DOI: 10.1103/PhysRevLett.43.1566.

[79] Ernest Ma. “Pathways to naturally small neutrino masses”. In: *Phys. Rev. Lett.* 81 (1998), pp. 1171–1174. DOI: 10.1103/PhysRevLett.81.1171. arXiv: hep-ph/9805219.

[80] Ernest Ma and Utpal Sarkar. “Neutrino masses and leptogenesis with heavy Higgs triplets”. In: *Phys. Rev. Lett.* 80 (1998), pp. 5716–5719. DOI: 10.1103/PhysRevLett.80.5716. arXiv: hep-ph/9802445.

[81] J. A. Casas and A. Ibarra. “Oscillating neutrinos and $\mu \to e, \gamma$”. In: *Nucl. Phys. B* 618 (2001), pp. 171–204. DOI: 10.1016/S0550-3213(01)00475-8. arXiv: hep-ph/0103065.

[82] M. Tanabashi et al. “Review of Particle Physics”. In: *Phys. Rev. D* 98 (3 Aug. 2018), p. 030001. DOI: 10.1103/PhysRevD.98.030001. URL: https://link.aps.org/doi/10.1103/PhysRevD.98.030001.

[83] M. Maniatis et al. “Stability and symmetry breaking in the general two-Higgs-doublet model”. In: *Eur. Phys. J. C* 48 (2006), pp. 805–823. DOI: 10.1140/epjc/s10052-006-0016-6. arXiv: hep-ph/0605184.

[84] Alexander Merle and Moritz Platscher. “Running of radiative neutrino masses: the scotogenic model — revisited”. In: *JHEP* 11 (2015), p. 148. DOI: 10.1007/JHEP11(2015)148. arXiv: 1507.06314 [hep-ph].

[85] Takashi Toma and Avelino Vicente. “Lepton Flavor Violation in the Scotogenic Model”. In: *JHEP* 01 (2014), p. 160. DOI: 10.1007/JHEP01(2014)160. arXiv: 1312.2840 [hep-ph].

[86] Avelino Vicente and Carlos E. Yaguna. “Probing the scotogenic model with lepton flavor violating processes”. In: *JHEP* 02 (2015), p. 144. DOI: 10.1007/JHEP02(2015)144. arXiv: 1412.2545 [hep-ph].

[87] David Tucker-Smith and Neal Weiner. “Inelastic dark matter”. In: *Phys. Rev. D* 64 (2001), p. 043502. DOI: 10.1103/PhysRevD.64.043502. arXiv: hep-ph/0101138.

[88] Sandy S. C. Law and Kristian L. McDonald. “A Class of Inert N-tuplet Models with Radiative Neutrino Mass and Dark Matter”. In: *JHEP* 09 (2013), p. 092. DOI: 10.1007/JHEP09(2013)092. arXiv: 1305.6467 [hep-ph].

[89] Juri Fiaschi, Michael Klasen, and Simon May. “Singlet-doublet fermion and triplet scalar dark matter with radiative neutrino masses”. In: *JHEP* 05 (2019), p. 015. DOI: 10.1007/JHEP05(2019)015. arXiv: 1812.11133 [hep-ph].

[90] Simon May. “Minimal dark matter models with radiative neutrino masses: From Lagrangians to observables”. Other thesis. Mar. 2020. arXiv: 2003.04157 [hep-ph].

[91] Marco Cirelli, Nicolao Fornengo, and Alessandro Strumia. “Minimal dark matter”. In: *Nucl. Phys. B* 753 (2006), pp. 178–194. DOI: 10.1016/j.nuclphysb.2006.07.012. arXiv: hep-ph/0512090.

[92] Werner Porod. “SPheno, a program for calculating supersymmetric spectra, SUSY particle decays and SUSY particle production at e+ e- colliders”. In: *Comput. Phys. Commun.* 153 (2003), pp. 275–315. DOI: 10.1016/S0010-4655(03)00222-4. arXiv: hep-ph/0301101.

[93] W. Porod and F. Staub. “SPheno 3.1: Extensions including flavour, CP-phases and models beyond the MSSM”. In: *Comput. Phys. Commun.* 183 (2012), pp. 2458–2469. DOI: 10.1016/j.cpc.2012.05.021. arXiv: 1104.1573 [hep-ph].

[94] Geneviève Bélanger et al. “micrOMEGAs5.0 : Freeze-in”. In: *Comput. Phys. Commun.* 231 (2018), pp. 173–186. DOI: 10.1016/j.cpc.2018.04.027. arXiv: 1801.03509 [hep-ph].

[95] Manfred Lindner, Alexander Merle, and Viviana Niro. “Enhancing Dark Matter Annihilation into Neutrinos”. In: *Phys. Rev. D* 82 (2010), p. 123529. DOI: 10.1103/PhysRevD.82.123529. arXiv: 1005.3116 [hep-ph].

[96] Yasaman Farzan. “Flavoring Monochromatic Neutrino Flux from Dark Matter Annihilation”. In: *JHEP* 02 (2012), p. 091. DOI: 10.1007/JHEP02(2012)091. arXiv: 1111.1063 [hep-ph].

[97] Chiara Arina, Suchita Kulkarni, and Joseph Silk. "Monochromatic neutrino lines from sneutrino dark matter". In: *Phys. Rev. D* 92.8 (2015), p. 083519. DOI: 10.1103/PhysRevD.92.083519. arXiv: 1506.08202 [astro-ph.HE].

[98] Chaimae El Aisati et al. "Prospects for discovering a neutrino line induced by dark matter annihilation". In: *JCAP* 10 (2017), p. 021. DOI: 10.1088/1475-7516/2017/10/021. arXiv: 1706.06600 [hep-ph].

[99] R. Bernabei et al. "Improved model-dependent corollary analyses after the first six annual cycles of DAMA/LIBRA-phase2". In: *Nucl. Phys. Atom. Energy* 20.4 (2019), pp. 317–348. DOI: 10.15407/jnpae2019.04.317. arXiv: 1907.06405 [hep-ph].

[100] Shmuel Nussinov, Lian-Tao Wang, and Itay Yavin. "Capture of Inelastic Dark Matter in the Sun". In: *JCAP* 08 (2009), p. 037. DOI: 10.1088/1475-7516/2009/08/037. arXiv: 0905.1333 [hep-ph].

[101] Arjun Menon et al. "Capture and Indirect Detection of Inelastic Dark Matter". In: *Phys. Rev. D* 82 (2010), p. 015011. DOI: 10.1103/PhysRevD.82.015011. arXiv: 0905.1847 [hep-ph].

[102] Jing Shu, Peng-fei Yin, and Shou-hua Zhu. "Neutrino Constraints on Inelastic Dark Matter after CDMS II". In: *Phys. Rev. D* 81 (2010), p. 123519. DOI: 10.1103/PhysRevD.81.123519. arXiv: 1001.1076 [hep-ph].

[103] Riccardo Catena and Fredrik Hellström. "New constraints on inelastic dark matter from IceCube". In: *JCAP* 10 (2018), p. 039. DOI: 10.1088/1475-7516/2018/10/039. arXiv: 1808.08082 [astro-ph.CO].

[104] Tsuyoshi Hashimoto and Daijiro Suematsu. "Inflation and DM phenomenology in a scotogenic model extended with a real singlet scalar". In: *Phys. Rev. D* 102.11 (2020), p. 115041. DOI: 10.1103/PhysRevD.102.115041. arXiv: 2009.13057 [hep-ph].

[105] M. G. Aartsen, et al. "The IceCube Neutrino Observatory: Instrumentation and Online Systems". In: *JINST* 12.03 (2017), P03012. DOI: 10.1088/1748-0221/12/03/P03012. arXiv: 1612.05093 [astro-ph.IM].

[106] Andrew Gould. "Resonant Enhancements in Weakly Interacting Massive Particle Capture by the Earth". In: *ApJ* 321 (Oct. 1987), p. 571. DOI: 10.1086/165653.

[107] W. H. Press and D. N. Spergel. “Capture by the sun of a galactic population of weakly interacting, massive particles”. In: *ApJ* 296 (Sept. 1985), pp. 679–684. DOI: 10.1086/163485.

[108] Sunghyun Kang, S. Scopel, and Gaurav Tomar. “Probing DAMA/LIBRA data in the full parameter space of WIMP effective models of inelastic scattering”. In: *Phys. Rev. D* 99.10 (2019), p. 103019. DOI: 10.1103/PhysRevD.99.103019. arXiv: 1902.09121 [hep-ph].

[109] Marat Freytsis and Zoltan Ligeti. “On dark matter models with uniquely spin-dependent detection possibilities”. In: *Phys. Rev. D* 83 (2011), p. 115009. DOI: 10.1103/PhysRevD.83.115009. arXiv: 1012.5317 [hep-ph].

[110] Michael E Peskin and Daniel V Schroeder. *An introduction to quantum field theory*. Includes exercises. Boulder, CO: Westview, 1995. URL: https://cds.cern.ch/record/257493.

[111] M. Cannoni. “On the formalism and upper limits for spin-dependent cross sections in dark matter elastic scattering with nuclei”. In: *Phys. Rev. D* 84 (2011), p. 095017. DOI: 10.1103/PhysRevD.84.095017. arXiv: 1108.4337 [hep-ph].

[112] Torsten Bringmann et al. “DarkSUSY 6 : An Advanced Tool to Compute Dark Matter Properties Numerically”. In: *JCAP* 07 (2018), p. 033. DOI: 10.1088/1475-7516/2018/07/033. arXiv: 1802.03399 [hep-ph].

[113] G. Belanger et al. “micrOMEGAs_3: A program for calculating dark matter observables”. In: *Comput. Phys. Commun.* 185 (2014), pp. 960–985. DOI: 10.1016/j.cpc.2013.10.016. arXiv: 1305.0237 [hep-ph].

[114] Mattias Blennow, Stefan Clementz, and Juan Herrero-Garcia. “The distribution of inelastic dark matter in the Sun”. In: *Eur. Phys. J. C* 78.5 (2018). [Erratum: Eur.Phys.J.C 79, 407 (2019)], p. 386. DOI: 10.1140/epjc/s10052-018-5863-4. arXiv: 1802.06880 [hep-ph].

[115] G. Bélanger et al. “Limits on dark matter proton scattering from neutrino telescopes using micrOMEGAs”. In: *JCAP* 12 (2015), p. 036. DOI: 10.1088/1475-7516/2015/12/036. arXiv: 1507.07987 [hep-ph].

[116] Alexander Belyaev, Neil D. Christensen, and Alexander Pukhov. "CalcHEP 3.4 for collider physics within and beyond the Standard Model". In: *Comput. Phys. Commun.* 184 (2013), pp. 1729–1769. DOI: 10.1016/j.cpc.2013.01.014. arXiv: 1207.6082 [hep-ph].

[117] Bugaev, Edgar and Montaruli, Teresa and Shlepin, Yuri and Sokalski, Igor A. "Propagation of tau neutrinos and tau leptons through the earth and their detection in underwater / ice neutrino telescopes". In: *Astropart. Phys.* 21 (2004), pp. 491–509. DOI: 10.1016/j.astropartphys.2004.03.002. arXiv: hep-ph/0312295.

[118] Simon May. "minimal-lagrangians: Generating and studying dark matter model Lagrangians with just the particle content". In: *Comput. Phys. Commun.* 261 (2021), p. 107773. DOI: 10.1016/j.cpc.2020.107773. arXiv: 2003.08037 [hep-ph].

[119] Marco Cirelli et al. "Spectra of neutrinos from dark matter annihilations". In: *Nucl. Phys. B* 727 (2005). [Erratum: Nucl.Phys.B 790, 338–344 (2008)], pp. 99–138. DOI: 10.1016/j.nuclphysb.2007.10.001. arXiv: hep-ph/0506298.

[120] Michael Klasen et al. "Scalar dark matter and fermion coannihilations in the radiative seesaw model". In: *JCAP* 04 (2013), p. 044. DOI: 10.1088/1475-7516/2013/04/044. arXiv: 1302.5298 [hep-ph].

[121] J. Harz et al. "Theoretical uncertainty of the supersymmetric dark matter relic density from scheme and scale variations". In: *Phys. Rev. D* 93.11 (2016), p. 114023. DOI: 10.1103/PhysRevD.93.114023. arXiv: 1602.08103 [hep-ph].

[122] Marcela Carena et al. "Invisible Z boson decays at e+ e- colliders". In: *Phys. Rev. D* 68 (2003), p. 113007. DOI: 10.1103/PhysRevD.68.113007. arXiv: hep-ph/0308053.

[123] Qing-Hong Cao, Ernest Ma, and G. Rajasekaran. "Observing the Dark Scalar Doublet and its Impact on the Standard-Model Higgs Boson at Colliders". In: *Phys. Rev. D* 76 (2007), p. 095011. DOI: 10.1103/PhysRevD.76.095011. arXiv: 0708.2939 [hep-ph].

[124] Erik Lundstrom, Michael Gustafsson, and Joakim Edsjo. "The Inert Doublet Model and LEP II Limits". In: *Phys. Rev. D* 79 (2009), p. 035013. DOI: 10.1103/PhysRevD.79.035013. arXiv: 0810.3924 [hep-ph].

[125] "Combination of searches for invisible Higgs boson decays with the ATLAS experiment". In: (Oct. 2020).

[126] Albert M Sirunyan et al. "Search for invisible decays of a Higgs boson produced through vector boson fusion in proton-proton collisions at $\sqrt{s} = 13$ TeV". In: *Phys. Lett. B* 793 (2019), pp. 520–551. DOI: 10.1016/j.physletb.2019.04.025. arXiv: 1809.05937 [hep-ex].

[127] E. Aprile et al. "Implications on Inelastic Dark Matter from 100 Live Days of XENON100 Data". In: *Phys. Rev. D* 84 (2011), p. 061101. DOI: 10.1103/PhysRevD.84.061101. arXiv: 1104.3121 [astro-ph.CO].

[128] E. Aprile et al. "Effective field theory search for high-energy nuclear recoils using the XENON100 dark matter detector". In: *Phys. Rev. D* 96.4 (2017), p. 042004. DOI: 10.1103/PhysRevD.96.042004. arXiv: 1705.02614 [astro-ph.CO].

[129] Xun Chen et al. "Exploring the dark matter inelastic frontier with 79.6 days of PandaX-II data". In: *Phys. Rev. D* 96.10 (2017), p. 102007. DOI: 10.1103/PhysRevD.96.102007. arXiv: 1708.05825 [hep-ex].

[130] E. Barbosa de Souza et al. "First search for a dark matter annual modulation signal with NaI(Tl) in the Southern Hemisphere by DM-Ice17". In: *Phys. Rev. D* 95.3 (2017), p. 032006. DOI: 10.1103/PhysRevD.95.032006. arXiv: 1602.05939 [physics.ins-det].

[131] G. Adhikari et al. "Search for a Dark Matter-Induced Annual Modulation Signal in NaI(Tl) with the COSINE-100 Experiment". In: *Phys. Rev. Lett.* 123.3 (2019), p. 031302. DOI: 10.1103/PhysRevLett.123.031302. arXiv: 1903.10098 [astro-ph.IM].

[132] J. Amare et al. "Annual Modulation Results from Three Years Exposure of ANAIS-112". In: (Mar. 2021). arXiv: 2103.01175 [astro-ph.IM].

[133] A. Albert et al. "Results from the search for dark matter in the Milky Way with 9 years of data of the ANTARES neutrino telescope". In: *Phys. Lett. B* 769 (2017). [Erratum: Phys.Lett.B 796, 253–255 (2019)], pp. 249–254. DOI: 10.1016/j.physletb.2017.03.063. arXiv: 1612.04595 [astro-ph.HE].

[134] M. G. Aartsen et al. "Search for Neutrinos from Dark Matter Self-Annihilations in the center of the Milky Way with 3 years of IceCube/DeepCore". In: *Eur. Phys. J. C* 77.9 (2017), p. 627. DOI: 10.1140/epjc/s10052-017-5213-y. arXiv: 1705.08103 [hep-ex].

[135] Felix Kahlhoefer et al. "Model-independent comparison of annual modulation and total rate with direct detection experiments". In: *JCAP* 05 (2018), p. 074. DOI: 10.1088/1475-7516/2018/05/074. arXiv: 1802.10175 [hep-ph].

[136] Sunghyun Kang et al. "DAMA/LIBRA-phase2 in WIMP effective models". In: *JCAP* 07 (2018), p. 016. DOI: 10.1088/1475-7516/2018/07/016. arXiv: 1804.07528 [hep-ph].

[137] Chiara Arina, Fu-Sin Ling, and Michel H. G. Tytgat. "IDM and iDM or The Inert Doublet Model and Inelastic Dark Matter". In: *JCAP* 10 (2009), p. 018. DOI: 10.1088/1475-7516/2009/10/018. arXiv: 0907.0430 [hep-ph].

[138] Carlos E. Yaguna. "Isospin-violating dark matter in the light of recent data". In: *Phys. Rev. D* 95.5 (2017), p. 055015. DOI: 10.1103/PhysRevD.95.055015. arXiv: 1610.08683 [hep-ph].

[139] Joseph Bramante et al. "Inelastic frontier: Discovering dark matter at high recoil energy". In: *Phys. Rev. D* 94.11 (2016), p. 115026. DOI: 10.1103/PhysRevD.94.115026. arXiv: 1608.02662 [hep-ph].

[140] Sebastian Baum, Katherine Freese, and Chris Kelso. "Dark Matter implications of DAMA/LIBRA-phase2 results". In: *Phys. Lett. B* 789 (2019), pp. 262–269. DOI: 10.1016/j.physletb.2018.12.036. arXiv: 1804.01231 [astro-ph.CO].

[141] G. Adhikari et al. "COSINE-100 and DAMA/LIBRA-phase2 in WIMP effective models". In: *JCAP* 06 (2019), p. 048. DOI: 10.1088/1475-7516/2019/06/048. arXiv: 1904.00128 [hep-ph].

[142] M. Antonello et al. "Characterization of SABRE crystal NaI-33 with direct underground counting". In: *Eur. Phys. J. C* 81.4 (2021), p. 299. DOI: 10.1140/epjc/s10052-021-09098-5. arXiv: 2012.02610 [physics.ins-det].

[143] Julio F. Navarro, Carlos S. Frenk, and Simon D. M. White. "The Structure of cold dark matter halos". In: *Astrophys. J.* 462 (1996), pp. 563–575. DOI: 10.1086/177173. arXiv: astro-ph/9508025.

[144] Gary Steigman, Basudeb Dasgupta, and John F. Beacom. "Precise Relic WIMP Abundance and its Impact on Searches for Dark Matter Annihilation". In: *Phys. Rev. D* 86 (2012), p. 023506. DOI: 10.1103/PhysRevD.86.023506. arXiv: 1204.3622 [hep-ph].

[145] Yasaman Farzan, Silvia Pascoli, and Michael A. Schmidt. "AMEND: A model explaining neutrino masses and dark matter testable at the LHC and MEG". In: *JHEP* 10 (2010), p. 111. DOI: 10.1007/JHEP10(2010)111. arXiv: 1005.5323 [hep-ph].

[146] Sarah Andreas, Michel H.G. Tytgat, and Quentin Swillens. "Neutrinos from Inert Doublet Dark Matter". In: *JCAP* 04 (2009), p. 004. DOI: 10.1088/1475-7516/2009/04/004. arXiv: 0901.1750 [hep-ph].

[147] A. Albert et al. "Search for Dark Matter Annihilation in the Earth using the ANTARES Neutrino Telescope". In: *Phys. Dark Univ.* 16 (2017), pp. 41–48. DOI: 10.1016/j.dark.2017.04.005. arXiv: 1612.06792 [hep-ex].

[148] Andrew Gould. "Cosmological density of WIMPs from solar and terrestrial annihilations". In: *Astrophys. J.* 388 (1992), pp. 338–344. DOI: 10.1086/171156.

[149] Michael Klasen, Martin Pohl, and Günter Sigl. "Indirect and direct search for dark matter". In: *Prog. Part. Nucl. Phys.* 85 (2015), pp. 1–32. DOI: 10.1016/j.ppnp.2015.07.001. arXiv: 1507.03800 [hep-ph].

[150] E. Aprile et al. "Light Dark Matter Search with Ionization Signals in XENON1T". In: *Phys. Rev. Lett.* 123.25 (2019), p. 251801. DOI: 10.1103/PhysRevLett.123.251801. arXiv: 1907.11485 [hep-ex].

[151] Francois-Xavier Josse-Michaux and Emiliano Molinaro. "Triplet scalar dark matter and leptogenesis in an inverse seesaw model of neutrino mass generation". In: *Phys. Rev. D* 87.3 (2013), p. 036007. DOI: 10.1103/PhysRevD.87.036007. arXiv: 1210.7202 [hep-ph].

[152] Najimuddin Khan. "Exploring the hyperchargeless Higgs triplet model up to the Planck scale". In: *Eur. Phys. J. C* 78.4 (2018), p. 341. DOI: 10.1140/epjc/s10052-018-5766-4. arXiv: 1610.03178 [hep-ph].

[153] T. Hambye et al. "Scalar Multiplet Dark Matter". In: *JHEP* 07 (2009). [Erratum: JHEP 05, 066 (2010)], p. 090. DOI: 10.1007/JHEP05(2010)066. arXiv: 0903.4010 [hep-ph].

[154] Pavel Fileviez Perez et al. "Triplet Scalars and Dark Matter at the LHC". In: *Phys. Rev. D* 79 (2009), p. 055024. DOI: 10.1103/PhysRevD.79.055024. arXiv: 0811.3957 [hep-ph].

[155] Timothy Cohen et al. "Singlet-Doublet Dark Matter". In: *Phys. Rev. D* 85 (2012), p. 075003. DOI: 10.1103/PhysRevD.85.075003. arXiv: 1109.2604 [hep-ph].

[156] Carlos E. Yaguna. "Singlet-Doublet Dirac Dark Matter". In: *Phys. Rev. D* 92.11 (2015), p. 115002. DOI: 10.1103/PhysRevD.92.115002. arXiv: 1510.06151 [hep-ph].

[157] Subhaditya Bhattacharya, Nirakar Sahoo, and Narendra Sahu. "Singlet-Doublet Fermionic Dark Matter, Neutrino Mass and Collider Signatures". In: *Phys. Rev. D* 96.3 (2017), p. 035010. DOI: 10.1103/PhysRevD.96.035010. arXiv: 1704.03417 [hep-ph].

[158] R. Enberg et al. "LHC and dark matter signals of improved naturalness". In: *JHEP* 11 (2007), p. 014. DOI: 10.1088/1126-6708/2007/11/014. arXiv: 0706.0918 [hep-ph].

[159] Kenny C. Y. Ng et al. "Solar Atmospheric Neutrinos: A New Neutrino Floor for Dark Matter Searches". In: *Phys. Rev. D* 96.10 (2017), p. 103006. DOI: 10.1103/PhysRevD.96.103006. arXiv: 1703.10280 [astro-ph.HE].

[160] Francesc Ferrer, Alejandro Ibarra, and Sebastian Wild. "A novel approach to derive halo-independent limits on dark matter properties". In: *JCAP* 09 (2015), p. 052. DOI: 10.1088/1475-7516/2015/09/052. arXiv: 1506.03386 [hep-ph].

[161] M. G. Aartsen et al. "Velocity Independent Constraints on Spin-Dependent DM-Nucleon Interactions from IceCube and PICO". In: *Eur. Phys. J. C* 80.9 (2020), p. 819. DOI: 10.1140/epjc/s10052-020-8069-5. arXiv: 1907.12509 [astro-ph.HE].

[162] Abdesslam Arhrib et al. "Radiative Model of Neutrino Mass with Neutrino Interacting MeV Dark Matter". In: *JCAP* 04 (2016), p. 049. DOI: 10.1088/1475-7516/2016/04/049. arXiv: 1512.08796 [hep-ph].

[163] Juri Fiaschi et al. "MeV neutrino dark matter: Relic density, lepton flavour violation and electron recoil". In: *JHEP* 11 (2019), p. 129. DOI: 10.1007/JHEP11(2019)129. arXiv: 1908.09882 [hep-ph].

[164] Manfred Lindner, Daniel Schmidt, and Thomas Schwetz. "Dark Matter and neutrino masses from global $\mathrm{U}(1)_{B-L}$ symmetry breaking". In: *Phys. Lett. B* 705 (2011), pp. 324–330. DOI: 10.1016/j.physletb.2011.10.022. arXiv: 1105.4626 [hep-ph].

[165] Cesar Bonilla et al. "Two-loop Dirac neutrino mass and WIMP dark matter". In: *Phys. Lett. B* 762 (2016), pp. 214–218. DOI: 10.1016/j.physletb.2016.09.027. arXiv: 1607.03931 [hep-ph].

[166] D. Aristizabal Sierra et al. "Dynamical flavor origin of $\mathbb{Z}_N$ symmetries". In: *Phys. Rev. D* 91.9 (2015), p. 096004. DOI: 10.1103/PhysRevD.91.096004. arXiv: 1412.5600 [hep-ph].

[167] Ernest Ma, Ivica Picek, and Branimir Radovčić. "New Scotogenic Model of Neutrino Mass with $U(1)_D$ Gauge Interaction". In: *Phys. Lett. B* 726 (2013), pp. 744–746. DOI: 10.1016/j.physletb.2013.09.049. arXiv: 1308.5313 [hep-ph].

[168] Vedran Brdar, Ivica Picek, and Branimir Radovcic. "Radiative Neutrino Mass with Scotogenic Scalar Triplet". In: *Phys. Lett. B* 728 (2014), pp. 198–201. DOI: 10.1016/j.physletb.2013.11.045. arXiv: 1310.3183 [hep-ph].

[169] Tong Li and Wei Chao. "Neutrino Masses, Dark Matter and B-L Symmetry at the LHC". In: *Nucl. Phys. B* 843 (2011), pp. 396–412. DOI: 10.1016/j.nuclphysb.2010.10.004. arXiv: 1004.0296 [hep-ph].

[170] Shu-Yu Ho, Takashi Toma, and Koji Tsumura. "Systematic $U(1)_{B–L}$ extensions of loop-induced neutrino mass models with dark matter". In: *Phys. Rev. D* 94.3 (2016), p. 033007. DOI: 10.1103/PhysRevD.94.033007. arXiv: 1604.07894 [hep-ph].

[171] Cesar Bonilla et al. "Dark matter stability and Dirac neutrinos using only Standard Model symmetries". In: *Phys. Rev. D* 101.3 (2020), p. 033011. DOI: 10.1103/PhysRevD.101.033011. arXiv: 1812.01599 [hep-ph].

[172] Julian Calle et al. “Minimal radiative Dirac neutrino mass models”. In: *Phys. Rev. D* 99.7 (2019), p. 075008. DOI: 10.1103/PhysRevD.99.075008. arXiv: 1812.05523 [hep-ph].

[173] Sudip Jana, P. K. Vishnu, and Shaikh Saad. “Minimal realizations of Dirac neutrino mass from generic one-loop and two-loop topologies at $d = 5$”. In: *JCAP* 04 (2020), p. 018. DOI: 10.1088/1475-7516/2020/04/018. arXiv: 1910.09537 [hep-ph].

[174] Arnab Dasgupta, Sin Kyu Kang, and Oleg Popov. “Radiative Dirac neutrino mass, neutrinoless quadruple beta decay, and dark matter in B-L extension of the standard model”. In: *Phys. Rev. D* 100.7 (2019), p. 075030. DOI: 10.1103/PhysRevD.100.075030. arXiv: 1903.12558 [hep-ph].

[175] Ernest Ma. “Leptonic Source of Dark Matter and Radiative Majorana or Dirac Neutrino Mass”. In: *Phys. Lett. B* 809 (2020), p. 135736. DOI: 10.1016/j.physletb.2020.135736. arXiv: 1912.11950 [hep-ph].

[176] Ernest Ma. “Gauged lepton number, Dirac neutrinos, dark matter, and muon g-2”. In: *Phys. Lett. B* 819 (2021), p. 136402. DOI: 10.1016/j.physletb.2021.136402. arXiv: 2104.10324 [hep-ph].

[177] Nicolás Bernal, Julián Calle, and Diego Restrepo. “Anomaly-free Abelian gauge symmetries with Dirac scotogenic models”. In: *Phys. Rev. D* 103.9 (2021), p. 095032. DOI: 10.1103/PhysRevD.103.095032. arXiv: 2102.06211 [hep-ph].

[178] Anson Hook, Eder Izaguirre, and Jay G. Wacker. “Model Independent Bounds on Kinetic Mixing”. In: *Adv. High Energy Phys.* 2011 (2011), p. 859762. DOI: 10.1155/2011/859762. arXiv: 1006.0973 [hep-ph].

[179] Juebin Lao et al. “Fermionic and scalar dark matter with hidden U(1) gauge interaction and kinetic mixing”. In: *Phys. Rev. D* 101.9 (2020), p. 095031. DOI: 10.1103/PhysRevD.101.095031. arXiv: 2003.02516 [hep-ph].

[180] Chia-Feng Chang, Ernest Ma, and Tzu-Chiang Yuan. “Multilepton Higgs Decays through the Dark Portal”. In: *JHEP* 03 (2014), p. 054. DOI: 10.1007/JHEP03(2014)054. arXiv: 1308.6071 [hep-ph].

[181] Suyong Choi, Sunghoon Jung, and P. Ko. “Implications of LHC data on 125 GeV Higgs-like boson for the Standard Model and its various extensions”. In: *JHEP* 10 (2013), p. 225. DOI: 10.1007/JHEP10(2013)225. arXiv: 1307.3948 [hep-ph].

[182] Kingman Cheung et al. “Bounds on Higgs-Portal models from the LHC Higgs data”. In: *JHEP* 10 (2015), p. 057. DOI: 10.1007/JHEP10(2015)057. arXiv: 1507.06158 [hep-ph].

[183] Kingman Cheung et al. “Higgs precision study of the 750 GeV diphoton resonance and the 125 GeV standard model Higgs boson with Higgs-singlet mixing”. In: *Phys. Rev. D* 94.3 (2016), p. 033010. DOI: 10.1103/PhysRevD.94.033010. arXiv: 1512.07853 [hep-ph].

[184] Paul Langacker. “The Physics of Heavy Z' Gauge Bosons”. In: *Rev. Mod. Phys.* 81 (2009), pp. 1199–1228. DOI: 10.1103/RevModPhys.81.1199. arXiv: 0801.1345 [hep-ph].

[185] Lotty Ackerman et al. “Dark Matter and Dark Radiation”. In: *Phys. Rev. D* 79 (2009). Ed. by Hans Volker Klapdor-Kleingrothaus and Irina V. Krivosheina, p. 023519. DOI: 10.1103/PhysRevD.79.023519. arXiv: 0810.5126 [hep-ph].

[186] Georges Aad et al. “Constraints on new phenomena via Higgs boson couplings and invisible decays with the ATLAS detector”. In: *JHEP* 11 (2015), p. 206. DOI: 10.1007/JHEP11(2015)206. arXiv: 1509.00672 [hep-ex].

[187] Bob Holdom. “Two U(1)’s and Epsilon Charge Shifts”. In: *Phys. Lett. B* 166 (1986), pp. 196–198. DOI: 10.1016/0370-2693(86)91377-8.

[188] M. Napsuciale, S. Rodríguez, and H. Hernández-Arellano. “Kinetic mixing, custodial symmetry, Z, Z' interactions and Z' production in hadron colliders”. In: (Sept. 2020). arXiv: 2009.10658 [hep-ph].

[189] Yann Mambrini. “The ZZ’ kinetic mixing in the light of the recent direct and indirect dark matter searches”. In: *JCAP* 07 (2011), p. 009. DOI: 10.1088/1475-7516/2011/07/009. arXiv: 1104.4799 [hep-ph].

[190] Biswajoy Brahmachari and Amitava Raychaudhuri. “Kinetic mixing and symmetry breaking dependent interactions of the dark photon”. In: *Nucl. Phys. B* 887 (2014), pp. 441–455. DOI: 10.1016/j.nuclphysb.2014.08.015. arXiv: 1409.2082 [hep-ph].

[191] Jun-Xing Pan et al. "Scrutinizing a massless dark photon: basis independence". In: *Nucl. Phys. B* 953 (2020), p. 114968. DOI: 10.1016/j.nuclphysb.2020.114968. arXiv: 1807.11363 [hep-ph].

[192] J. P. Lees et al. "Search for Invisible Decays of a Dark Photon Produced in e^+e^- Collisions at BaBar". In: *Phys. Rev. Lett.* 119.13 (2017), p. 131804. DOI: 10.1103/PhysRevLett.119.131804. arXiv: 1702.03327 [hep-ex].

[193] D. Banerjee et al. "Dark matter search in missing energy events with NA64". In: *Phys. Rev. Lett.* 123.12 (2019), p. 121801. DOI: 10.1103/PhysRevLett.123.121801. arXiv: 1906.00176 [hep-ex].

[194] Chuan-Hung Chen and Takaaki Nomura. "Influence of an inert charged Higgs boson on the muon $g-2$ and radiative neutrino masses in a scotogenic model". In: *Phys. Rev. D* 100.1 (2019), p. 015024. DOI: 10.1103/PhysRevD.100.015024. arXiv: 1903.03380 [hep-ph].

[195] Fred Jegerlehner and Andreas Nyffeler. "The Muon g-2". In: *Phys. Rept.* 477 (2009), pp. 1–110. DOI: 10.1016/j.physrep.2009.04.003. arXiv: 0902.3360 [hep-ph].

[196] Piotr H. Chankowski, Stefan Pokorski, and Jakub Wagner. "Z-prime and the Appelquist-Carrazzone decoupling". In: *Eur. Phys. J. C* 47 (2006), pp. 187–205. DOI: 10.1140/epjc/s2006-02537-3. arXiv: hep-ph/0601097.

[197] Robert Feger and Thomas W. Kephart. "LieART—A Mathematica application for Lie algebras and representation theory". In: *Comput. Phys. Commun.* 192 (2015), pp. 166–195. DOI: 10.1016/j.cpc.2014.12.023. arXiv: 1206.6379 [math-ph].

[198] Philip Ilten et al. "Serendipity in dark photon searches". In: *JHEP* 06 (2018), p. 004. DOI: 10.1007/JHEP06(2018)004. arXiv: 1801.04847 [hep-ph].

Acknowledgments

A number of people accompanied me during the time of writing this thesis and helped me in a number of ways. All these people deserve a big thank you.

First of all I would like to thank *Prof. Michael Klasen* for the opportunity to write this thesis, his constant support and the excellent collaboration.

A special thanks goes to *Sybrand Zeinstra* with whom I worked closely together. Thank you for the many explanations and all the fun time in the office. You were great to work with.

Further I would like to thank my other collaborators *Raffaela Busse*, *Alexander Kappes* and *Caroline Rodenbeck* for the productive work and their input on the experimental side.

I am thankful *Dr. Amin Abou Ibrahim* for all the helpful discussions and insights into BSM physics.

Finally I would like to thank all my colleagues for the overall fun time in the institute.

Declaration of academic integrity

I, *Thede de Boer*, hereby confirm that this thesis on “Verifiable dark matter with radiative neutrino masses” is solely my own work and that I have used no sources or aids other than the ones stated. All passages in my thesis for which other sources, including electronic media, have been used, be it direct quotes or content references, have been acknowledged as such and the sources cited.

Münster, September 7, 2021 ______________________________

(signature of student)

I, *Thede de Boer*, agree to have my thesis checked in order to rule out potential similarities with other works and to have my thesis stored in a database for this purpose.

Münster, September 7, 2021 ______________________________

(signature of student)